

An Investigation into the Effects of Microstructure and Texture on the High Strain Rate Behaviour of Ti-6Al-4V

DPhil Thesis

Euan Wielewski
Christ Church
Department of Engineering Science
University of Oxford

Supervised by: Dr Clive Siviour and Dr Nik Petrinic
Michaelmas Term 2011

An Investigation into the Effects of Microstructure and Texture on the High Strain Rate Behaviour of Ti-6Al-4V

Euan Wielewski, Christ Church, University of Oxford

For the degree of DPhil in Engineering Science, Michaelmas Term 2011

Abstract

The core aim of this research project was to improve understanding of the effects of microstructure and crystallographic texture on the high strain rate plastic deformation behaviour of the industrially important Titanium alloy, Ti-6Al-4V. To facilitate this study, four rolled plates of Ti-6Al-4V, with varying thermo-mechanical processing histories, were provided by TIMET Corp., the world's largest supplier of Titanium product.

To determine the nature of each plate's microstructure and the crystallographic texture of the dominant α phase, the four Ti-6Al-4V plates were microstructurally characterised using techniques such as optical microscopy and electron backscatter diffraction (EBSD).

To determine the effects of the measured microstructures and textures on the strain rate dependent plastic deformation behaviour of the four Ti-6Al-4V plates, uniaxial compression and tension tests were carried out in the three orthogonal material orientations at quasi-static (10^{-3} s^{-1}) and high strain rates (10^{3} s^{-1}) using a standard electro-mechanical test device and split-Hopkinson pressure bars (SHPB), respectively.

To provide further understanding of the effects of microstructure and texture on the plastic deformation behaviour of Ti-6Al-4V, this time under complex impact loading conditions, the classic Taylor impact experiment was adapted to include an optical measurement and geometry reconstruction technique. A novel experimental setup was designed that consists of an ultra-high speed camera and mirror arrangement, allowing the Taylor impact specimen to be viewed from multiple angles during the experiment. Using the previously mentioned optical measurement and geometry reconstruction technique, it was then possible to gain

valuable, previously unobtainable, data on the deformation history of Taylor impact specimens *in-situ*, such as the major/minor axes of the anisotropically deforming elliptical specimen cross-sections as a function of time and axial position, true strain as a function of time and axial position, and the true strain rate as a function of axial position. The technique was verified by testing a specimen cut from the in-plane material orientation of a clock-rolled high purity Zirconium plate. The output measurements from a post-deformation image frame were compared with measurements of the recovered specimen made using a coordinate measurement machine (CMM), with analysis showing excellent agreement between the two techniques. The experiment was then carried out on specimens cut from the two orthogonal in-plane material orientations of one of the four Ti-6Al-4V plates. Analysis of the data from these experiments gave significant insight into the plastic deformation behaviour of macroscopically textured Ti-6Al-4V under complex impact loading.

Recovered Ti-6Al-4V specimens from the outlined Taylor impact experiments were then sectioned along specific planes and microstructurally characterised using EBSD, with comparisons made between the pre and post-deformation microstructures. From this analysis, and the previously discussed geometry reconstruction technique, insight was gained into the effects of micro-texture on the general anisotropic plastic deformation behaviour of Ti-6Al-4V plate materials and in particular the role of micro-texture on the formation of deformation twins.

Finally, the understanding gained from these experiments, and a detailed review of the literature, was used to inform a novel, physically based material modelling framework, capable of capturing the effects of microstructure and texture on the strain rate and temperature dependent plastic deformation behaviour of Ti-6Al-4V. The model was implemented in the computational software package, MATLAB, and verified by comparison with the mechanical characterisation results from one of the Ti-6Al-4V plates. A number of frameworks are discussed for implementing the new Ti-6Al-4V model within finite element (FE) analysis software packages, such as ABAQUS, LS-DYNA and DEFORM. It is hoped that the new Ti-6Al-4V model can be used to optimise the design of Ti-6Al-4V components and structures for impact loading scenarios.

CONTENTS

ABSTRACT

CONTENTS I

LIST OF TABLES VII

LIST OF FIGURES VIII

NOMENCLATURE XV

PUBLICATIONS AND CONFERENCES XVIII

ACKNOWLEDGEMENTS XIX

1 INTRODUCTION 1

1.1 THE ROLE OF TITANIUM ALLOYS IN THE GAS TURBINE ENGINE 1

1.2 MOTIVATION FOR RESEARCHING THE HIGH STRAIN RATE BEHAVIOUR OF TITANIUM ALLOYS 2

1.3 PROJECT OUTLINE 2

2 LITERATURE REVIEW 5

2.1 FUNDAMENTALS OF TI-6AL-4V 5

2.2 CRYSTALLOGRAPHY OF TI-6AL-4V 5

2.2.1 Crystallographic Indices 5

2.2.2 Crystal Structure of the α Phase 6

2.2.3 Crystal Structure of the β Phase 7

2.3 PRODUCTION AND THERMO-MECHANICAL PROCESSING OF TI-6AL-4V 7

2.3.1 Sponge Production 7

2.3.2 Melting 8

2.3.3 Primary Processing 8

2.3.4 Secondary Processing 9

2.4 MICROSTRUCTURE OF TI-6AL-4V 9

2.4.1 Overview ... *9*

2.4.2 Fully Lamellar Microstructures ... *9*

2.4.3 Bi-Modal (Duplex) Microstructures ... *10*

2.4.4 Fully Equiaxed Microstructures ... *11*

2.5 TEXTURE IN TI-6AL-4V ... 12

2.5.1 Overview ... *12*

2.5.2 Micro-Texture ... *12*

2.5.3 Macro-Texture ... *16*

2.6 GENERAL DEFORMATION BEHAVIOUR OF METALS ... 18

2.7 ELASTIC DEFORMATION OF TI-6AL-4V ... 19

2.8 PLASTIC DEFORMATION OF TI-6AL-4V ... 20

2.8.1 Slip ... *20*

2.8.2 Deformation Twinning ... *23*

2.9 THE EFFECT OF TEMPERATURE AND STRAIN RATE ON PLASTIC FLOW STRESS ... 25

2.9.1 Overview ... *25*

2.9.2 The Motion of Dislocations in a Crystalline Solid ... *25*

2.9.3 Temperature Dependence ... *25*

2.9.4 Strain Rate Dependence ... *26*

3 EXPERIMENTAL TECHNIQUES ... 31

3.1 OVERVIEW ... 31

3.2 MECHANICAL CHARACTERISATION OVER A RANGE OF STRAIN RATES ... 31

3.2.1 Range of Strain Rates and Experimental Techniques ... *31*

3.2.2 Conventional Cross-Head Device ... *32*

3.2.3 Split-Hopkinson Pressure Bars ... *34*

3.2.4 Taylor Impact ... *38*

3.3 MICROSCOPY TECHNIQUES ... 40

3.3.1 Overview ... *40*

3.3.2 Optical Microscopy ... *40*

3.3.3 Scanning Electron Microscopy *41*

3.3.4 Electron Back-Scatter Diffraction *41*

3.3.5 Sample Preparation *43*

4 MICROSTRUCTURAL CHARACTERISATION OF TI-6AL-4V 45

4.1 OVERVIEW 45

4.2 MATERIAL ORIENTATIONS 46

4.3 CHEMICAL COMPOSITION 46

4.4 MICROSTRUCTURE 47

4.5 MICRO-TEXTURE 53

4.6 MACRO-TEXTURE 59

4.7 MICROSTRUCTURAL PARAMETERS 61

4.8 CONCLUSIONS 62

5 UNIAXIAL MECHANICAL CHARACTERISATION OF TI-6AL-4V 63

5.1 OVERVIEW 63

5.2 SPECIMEN PREPARATION 63

5.3 QUASI-STATIC AND HIGH STRAIN RATE TESTING RESULTS 64

5.4 COMPARISON OF FLOW STRESS DATA 69

5.5 RATIO-BASED ANALYSIS OF FLOW STRESS DATA 71

5.5.1 Material Orientation Dependence of the Flow Stress *71*

5.5.2 Strain Rate Dependence of the Flow Stress *73*

5.5.3 Compression/Tension Asymmetry of the Flow Stress *75*

5.6 GENERAL PLASTIC FLOW BEHAVIOUR OF TI-6AL-4V PLATES 77

5.7 FRACTURE SURFACES 80

5.8 PREFERENTIAL FAILURE PLANES 87

5.9 DUCTILITY 89

5.10 CONCLUSIONS 90

6 TAYLOR IMPACT OF TI-6AL-4V 92

6.1 OVERVIEW 92

6.2 BACKGROUND 93
6.3 EXPERIMENTAL SETUP AND OPTICAL MEASUREMENT TECHNIQUE 95
6.4 TRIAL TAYLOR IMPACT EXPERIMENTS ON CP-ZR 98
6.4.1 Overview 98
6.4.2 Characterisation of High Purity Clock-Rolled Zirconium Plate 99
6.4.3 Trial Experimental Results 102
6.4.4 Validation 104
6.4.5 Discussion 105
6.4.6 Conclusions 105
6.5 TAYLOR IMPACT EXPERIMENTS ON TI-6AL-4V 106
6.5.1 Overview 106
6.5.2 Experimental Results from Taylor Impact on Ti-6Al-4V 107
6.5.3 Discussion 110
6.5.4 Conclusions 112
6.6 MICROSTRUCTURE AND MICRO-TEXTURE EVOLUTION OF TI-6AL-4V DURING A TAYLOR IMPACT 113
6.6.1 Overview 113
6.6.2 EBSD of Sectioned Taylor Impact Specimens 114
6.6.3 Taylor Factor Maps 117
6.6.4 Discussion 119
6.6.5 Conclusions 126
6.7 CONCLUSIONS 127
7 MODELLING THE EFFECTS OF MICROSTRUCTURE AND TEXTURE ON THE FLOW STRESS OF TI-6AL-4V 129
7.1 OVERVIEW 129
7.2 PHENOMENOLOGICAL MATERIAL MODELS 130
7.2.1 Overview 130
7.2.2 Johnson-Cook Model 130

7.3 PHYSICALLY BASED MATERIAL MODELS 132
7.3.1 Overview 132
7.3.2 Thermally Activated Dislocation Motion 132
7.3.3 Mechanical Threshold Stress Model 137
7.4 TI-6AL-4V MODEL 138
7.4.1 Overview 138
7.4.2 Effect of Aluminium Content on the Yield Stress of α Phase Titanium 141
7.4.3 Effect of Dislocation Density on the Yield Stress of α Phase Titanium 143
7.4.4 Resolved Yield Stress of Primary α Grains 146
7.4.5 Resolved Yield Stress of α/β Lath Colonies 147
7.4.6 Effect of Primary α Grain Size and α/β Colony Size on Resolved Yield Stress 148
7.4.7 Effect of Volume Fraction Primary α on the Yield Stress of Ti-6Al-4V 149
7.4.8 Effect of Macro-Texture on Uniaxial Flow Stress of Ti-6Al-4V 150
7.4.9 Complete Model Framework 151
7.5 COMPARISON WITH EXPERIMENTAL RESULTS 152
7.5.1 Overview 152
7.5.2 Physically Based Model Parameters 152
7.5.3 Aluminium Content 153
7.5.4 Volume Fraction Primary α Grains 153
7.5.5 Primary α Grain Size 154
7.5.6 α Colony Size 154
7.5.7 Dislocation Density 155
7.5.8 Taylor Factor 156
7.5.9 Comparison with Uniaxial Flow Stress Data 157
7.5.10 Effect of Temperature on the Ti-6Al-4V Model 159
7.5.11 The Effect of Volume Fraction Primary α on the Ti-6Al-4V Model 160
7.5.12 Other Ti-6Al-4V Microstructures 162
7.6 IMPLEMENTATION IN A FINITE ELEMENT FRAMEWORK 162
7.6.1 Overview 162

7.6.2 Anisotropic Yield *163*

7.6.3 Tension/Compression Asymmetry of Yield Stress *163*

7.7 CONCLUSIONS 165

8 DISCUSSION 167

8.1 OUTLINE 167

8.2 THE EFFECTS OF MICROSTRUCTURE AND TEXTURE 167

8.2.1 General *167*

8.2.2 Solute Atom Content *169*

8.2.3 Micro-Mechanical Testing of Microstructural Features *170*

8.2.4 Dislocation Density *170*

8.2.5 Micro-Texture *171*

8.2.6 Deformation Twinning *171*

8.3 CONCLUSIONS 173

9 CONCLUSIONS 174

9.1 OVERVIEW 174

9.2 MICROSTRUCTURAL CHARACTERISATION 174

9.3 MECHANICAL CHARACTERISATION 175

9.4 TAYLOR IMPACT EXPERIMENTS 176

9.5 MODELLING THE EFFECTS OF MICROSTRUCTURE AND TEXTURE 178

9.6 FINAL REMARKS 179

10 BIBLIOGRAPHY 180

LIST OF TABLES

TABLE 3.1 - TI-6AL-4V SAMPLE PREPARATION ROUTE FOR EBSD 44

TABLE 4.1 - CHEMICAL COMPOSITION OF THE FOUR DEVELOPMENT PLATES 47

TABLE 5.1 - PLATE 1 - TRUE FLOW STRESS AT 5% TRUE PLASTIC STRAIN 69

TABLE 5.2 - PLATE 2 - TRUE FLOW STRESS AT 5% TRUE PLASTIC STRAIN 70

TABLE 5.3 - PLATE 3 - TRUE FLOW STRESS AT 5% TRUE PLASTIC STRAIN 70

TABLE 5.4 - PLATE 4 - TRUE FLOW STRESS AT 5% TRUE PLASTIC STRAIN 70

TABLE 5.5 - MATERIAL ORIENTATION RATIOS IN TENSION AND COMPRESSION AT QUASI-STATIC AND HIGH STRAIN RATES 71

TABLE 5.6 - STRAIN RATE RATIOS IN TENSION AND COMPRESSION IN MATERIAL ORIENTATION 1, 2 AND 3 73

TABLE 5.7 – COMP/TENS RATIOS AT QUASI-STATIC AND HIGH STRAIN RATES IN MATERIAL ORIENTATIONS 1 AND 2 75

TABLE 5.8 - PERCENTAGE ELONGATION TO FAILURE VALUES IN TENSION AT QUASI-STATIC AND HIGH STRAIN RATES 89

LIST OF FIGURES

FIGURE 1.1 - MATERIALS USED IN A TYPICAL GAS TURBINE ENGINE [4] 1

FIGURE 2.1 - HEXAGONAL CLOSE-PACKED STRUCTURE: (A) ABAB STACKING SEQUENCE OF ATOMS ON THE BASAL PLANES PERPENDICULAR TO THE *C*-AXIS, (B) PRIMITIVE UNIT CELL, (C) HEXAGONAL UNIT CELL WITH LABELLED AXES [5] 6

FIGURE 2.2 - BODY CENTRED CUBIC STRUCTURE [5] 7

FIGURE 2.3 - EXAMPLE OF A FULLY LAMELLAR MICROSTRUCTURE [1] 10

FIGURE 2.4 - EXAMPLE OF A BI-MODAL (DUPLEX) MICROSTRUCTURE [1] 11

FIGURE 2.5 - EXAMPLE OF A FULLY EQUIAXED MICROSTRUCTURE [1] 11

FIGURE 2.6 - IDEALISED SKETCHES OF MICRO-TEXTURE IN A POLYCRYSTALLINE METAL: (A) MACRO-ZONE, (B) DIFFERENT SIZE CLASS FOR A SPECIFIC ORIENTATION AND (C) SPECIFIC ORIENTATION AT THE EDGE OF A SPECIMEN [6] 13

FIGURE 2.7 - INVERSE POLE FIGURE MAP OF TI-6AL-4V, SHOWING MACRO-ZONES OF CRYSTALLOGRAPHIC ORIENTATION 15

FIGURE 2.8 - STAGES OF MICROSTRUCTURE IN TI-6AL-4V COOLING FROM THE ABOVE THE B TRANSUS [2] 15

FIGURE 2.9 - POSITION OF THE (0001) POLE OF A HCP UNIT CELL ON THE UNIT REFERENCE SPHERE [6]. 17

FIGURE 2.10 - FIGURE SHOWING THE STAGES OF STEREOGRAPHIC PROJECTION OF A CUBIC UNIT CELL: (A) ORIENTATION OF THE UNIT CELL IN THE UNIT SPHERE, (B) PROJECTION OF THE POLES ONTO THE EQUATORIAL PLANE AND (C) THE FINAL POLE FIGURE, WITH POLE FIGURE ANGLES HIGHLIGHTED [6] 17

FIGURE 2.11 - EXAMPLE POLE FIGURES FROM A HEAVILY TEXTURED COMMERCIAL TI-6AL-4V PLATE 18

FIGURE 2.12 – TYPICAL UNIAXIAL TENSILE DEFORMATION BEHAVIOUR OF METALS [8] 19

FIGURE 2.13 - ELASTIC MODULUS OF SINGLE CRYSTAL A PHASE TITANIUM AS A FUNCTION OF DECLINATION ANGLE [1] 20

FIGURE 2.14 - MOTION OF A DISLOCATION THROUGH A SIMPLE CRYSTAL LATTICE 20

FIGURE 2.15 - SLIP SYSTEMS IN *HCP* A PHASE TITANIUM [1] 21
FIGURE 2.16 - CRSS OF BASAL, PRISMATIC AND C + A TYPE SLIP IN *HCP* TITANIUM [1], [11] 23
FIGURE 2.17 – TWINNING SYSTEMS OBSERVED IN *HCP* TITANIUM [15] 24
FIGURE 2.18 - DISLOCATION VELOCITY VS RESOLVED SHEAR STRESS: (I) THERMALLY ACTIVATED DISLOCATION MOTION, (II) DRAG CONTROLLED DISLOCATION MOTION AND (III) RELATIVISTIC EFFECTS CONTROLLED DISLOCATION MOTION [17] 27
FIGURE 2.19 - TRUE STRESS VS TRUE STRAIN FOR CP-TI OVER A WIDE RANGE OF STRAIN RATES [13] .. 28
FIGURE 3.1 - RANGE OF STRAIN RATES AND EXPERIMENTAL TECHNIQUES 32
FIGURE 3.2 - SCHEMATIC OF A COMPRESSION SPLIT-HOPKINSON PRESSURE BAR SETUP [29] 35
FIGURE 3.3 - LAGRANGIAN WAVE PROPAGATION DIAGRAM FOR A TYPICAL COMPRESSION SHPB SETUP [29] 35
FIGURE 3.4 - SCHEMATIC OF THE CLASSIC TAYLOR IMPACT EXPERIMENT 38
FIGURE 3.5 - EXAMPLE KIKUCHI PATTERN FROM EBSD OF TI-6AL-4V PLATE MATERIAL 42
FIGURE 3.6 - (A) SCHEMATIC OF A TYPICAL EBSD SYSTEM [44], (B) EBSD SETUP USED IN THIS STUDY 43
FIGURE 4.1 - MATERIAL ORIENTATIONS RELATIVE TO PLATE AND ROLLING DIRECTION 46
FIGURE 4.2 - OPTICAL MICROGRAPH: PLATE 1 – LONGITUDINAL/THROUGH-THICKNESS 49
FIGURE 4.3 - OPTICAL MICROGRAPH: PLATE 1 – TRANSVERSE/THROUGH-THICKNESS 49
FIGURE 4.4 - OPTICAL MICROGRAPH: PLATE 2 – LONGITUDINAL/THROUGH-THICKNESS 50
FIGURE 4.5 - OPTICAL MICROGRAPH: PLATE 2 – TRANSVERSE/THROUGH-THICKNESS 50
FIGURE 4.6 - OPTICAL MICROGRAPH: PLATE 3 – LONGITUDINAL/THROUGH-THICKNESS 51
FIGURE 4.7 - OPTICAL MICROGRAPH: PLATE 3 – TRANSVERSE/THROUGH-THICKNESS 51
FIGURE 4.8 - OPTICAL MICROGRAPH: PLATE 4 – LONGITUDINAL/THROUGH-THICKNESS 52
FIGURE 4.9 - OPTICAL MICROGRAPH: PLATE 4 – TRANSVERSE/THROUGH-THICKNESS 52
FIGURE 4.10 - INVERSE POLE FIGURE MAP (500X500MM): PLATE 1 – LONGITUDINAL/THROUGH-THICKNESS 55
FIGURE 4.11 - INVERSE POLE FIGURE MAP (100X100MM): PLATE 1 – LONGITUDINAL/THROUGH-THICKNESS 55
FIGURE 4.12 - INVERSE POLE FIGURE MAP (500X500MM): PLATE 2 – LONGITUDINAL/THROUGH-THICKNESS 56

FIGURE 4.13 - INVERSE POLE FIGURE MAP (100X100MM): PLATE 2 – LONGITUDINAL/THROUGH-THICKNESS 56
FIGURE 4.14 - INVERSE POLE FIGURE MAP (500X500MM): PLATE 3 – LONGITUDINAL/THROUGH-THICKNESS 57
FIGURE 4.15 - INVERSE POLE FIGURE MAP (100X100MM): PLATE 3 – LONGITUDINAL/THROUGH-THICKNESS 57
FIGURE 4.16 - INVERSE POLE FIGURE MAP (500X500MM): PLATE 4 – LONGITUDINAL/THROUGH-THICKNESS 58
FIGURE 4.17 - INVERSE POLE FIGURE MAP (100X100MM): PLATE 4 – LONGITUDINAL/THROUGH-THICKNESS 58
FIGURE 4.18 - POLE FIGURES: (A) PLATE 1, (B) PLATE 2, (C) PLATE 3 AND (D) PLATE 4 60
FIGURE 5.1 - UNIAXIAL MECHANICAL TESTING SPECIMEN ORIENTATIONS RELATIVE TO PLATE 64
FIGURE 5.2 - PLATE 1 - MECHANICAL CHARACTERISATION RESULTS IN (A) COMPRESSION AND (B) TENSION 65
FIGURE 5.3 - PLATE 2 - MECHANICAL CHARACTERISATION RESULTS IN (A) COMPRESSION AND (B) TENSION 66
FIGURE 5.4 - PLATE 3 - MECHANICAL CHARACTERISATION RESULTS IN (A) COMPRESSION AND (B) TENSION 67
FIGURE 5.5 - PLATE 4 - MECHANICAL CHARACTERISATION RESULTS IN (A) COMPRESSION AND (B) TENSION 68
FIGURE 5.6 - CHART OF MATERIAL ORIENTATION RATIOS IN TENSION AT QUASI-STATIC AND HIGH STRAIN RATES 72
FIGURE 5.7 - CHART OF MATERIAL ORIENTATION RATIOS IN COMPRESSION AT QUASI-STATIC AND HIGH STRAIN RATES 72
FIGURE 5.8 - CHART OF STRAIN RATE RATIOS IN TENSION IN MATERIAL ORIENTATIONS 1 AND 2 74
FIGURE 5.9 - CHART OF STRAIN RATE RATIOS IN COMPRESSION IN MATERIAL ORIENTATIONS 1 AND 2.. 74
FIGURE 5.10 - CHART OF COMP/TENS RATIOS AT QUASI-STATIC STRAIN RATES IN MATERIAL ORIENTATIONS 1 AND 2 76
FIGURE 5.11 - CHART OF COMP/TENS RATIOS AT HIGH STRAIN RATES IN MATERIAL

ORIENTATIONS 1 AND 2 76
FIGURE 5.12 - (A) DIAGRAM SHOWING FRACTURE SURFACE IN RELATION TO TENSILE SPECIMEN 80
FIGURE 5.13 - PLATE 1 - LONGITUDINAL DIRECTION - FRACTURE SURFACE - CENTRE OF SPECIMEN 81
FIGURE 5.14 - PLATE 1 - LONGITUDINAL DIRECTION - FRACTURE SURFACE - EDGE OF SPECIMEN 81
FIGURE 5.15 - PLATE 2 - LONGITUDINAL DIRECTION - FRACTURE SURFACE - CENTRE OF SPECIMEN 82
FIGURE 5.16 - PLATE 2 - LONGITUDINAL DIRECTION - FRACTURE SURFACE - EDGE OF SPECIMEN 82
FIGURE 5.17 - PLATE 3 - LONGITUDINAL DIRECTION - FRACTURE SURFACE - CENTRE OF SPECIMEN 83
FIGURE 5.18 - PLATE 3 - LONGITUDINAL DIRECTION - FRACTURE SURFACE - EDGE OF SPECIMEN 83
FIGURE 5.19 - PLATE 4 - LONGITUDINAL DIRECTION - FRACTURE SURFACE - CENTRE OF SPECIMEN 84
FIGURE 5.20 - PLATE 4 - LONGITUDINAL DIRECTION - FRACTURE SURFACE - EDGE OF SPECIMEN 84
FIGURE 5.21 - PLATE 4 - HIGH STRAIN RATE - LONGITUDINAL DIRECTION - FRACTURE SURFACE - CENTRE OF SPECIMEN 85
FIGURE 5.22 - PLATE 4 - HIGH STRAIN RATE - LONGITUDINAL DIRECTION - FRACTURE SURFACE - EDGE OF SPECIMEN 85
FIGURE 5.16 – PREFERENTIAL FAILURE PLANE FOR COMPRESSION SPECIMENS 87
FIGURE 5.17 - PREFERENTIAL FAILURE PLANES IN TENSION, RELATIVE TO ORIGINAL MATERIAL ORIENTATIONS 88
FIGURE 6.1 - TAYLOR IMPACT EXPERIMENTAL SETUP 95
FIGURE 6.2 - CROSS-SECTIONAL VIEW OF THE TAYLOR IMPACT EXPERIMENTAL SETUP 96
FIGURE 6.3 - ELLIPTICAL CROSS-SECTION AND TANGENTS WITH CONSTRAINTS 98
FIGURE 6.4 - ZR PLATE ORIENTATION, ROLLING DIRECTIONS AND SPECIMEN ORIENTATIONS 99
FIGURE 6.5 - ZR - MICROSTRUCTURE, MICRO-TEXTURE AND MACRO-TEXTURE 100
FIGURE 6.6 - ZR - MECHANICAL CHARACTERISATION RESULTS IN COMPRESSION AT HIGH STRAIN RATES 101
FIGURE 6.7 - IMAGES FROM A TAYLOR IMPACT EXPERIMENT CARRIED OUT ON A REPRESENTATIVE ZR SPECIMEN [53] 102
FIGURE 6.8 - RECONSTRUCTED MAJOR/MINOR AXES OF A REPRESENTATIVE ZR TAYLOR IMPACT SPECIMEN [53] 103
FIGURE 6.9 - RECONSTRUCTED AREA STRAIN OF A REPRESENTATIVE ZR TAYLOR IMPACT SPECIMEN . 103

FIGURE 6.10 - RECONSTRUCTED MAJOR/MINOR AXES AND CMM DATA FOR THE REPRESENTATIVE ZR SPECIMEN 105
FIGURE 6.11 - PLATE 3 MATERIAL ORIENTATIONS, ROLLING DIRECTION AND TAYLOR IMPACT SPECIMEN ORIENTATIONS 107
FIGURE 6.12 - MAJOR/MINOR AXES OF THE ELLIPTICAL CROSS-SECTION AS A FUNCTION OF TIME OF A TAYLOR IMPACT SPECIMEN CUT FROM THE LONGITUDINAL MATERIAL ORIENTATION OF TI-6AL-4V PLATE 3 107
FIGURE 6.13 - MAJOR/MINOR AXES OF THE ELLIPTICAL CROSS-SECTION AS A FUNCTION OF TIME OF A TAYLOR IMPACT SPECIMEN CUT FROM THE TRANSVERSE MATERIAL ORIENTATION OF A TI-6AL-4V PLATE 3 108
FIGURE 6.14 - TRUE STRAIN AS A FUNCTION OF TIME AND AXIAL POSITION IN A REPRESENTATIVE TAYLOR IMPACT SPECIMEN CUT FROM THE LONGITUDINAL MATERIAL ORIENTATION .. 109
FIGURE 6.15 - TRUE STRAIN AS A FUNCTION OF TIME AND AXIAL POSITION IN A REPRESENTATIVE TAYLOR IMPACT SPECIMEN CUT FROM THE TRANSVERSE MATERIAL ORIENTATION 109
FIGURE 6.16 - STRAIN RATE AS A FUNCTION OF AXIAL POSITION FOR REPRESENTATIVE TAYLOR IMPACT SPECIMENS IN THE LONGITUDINAL AND TRANSVERSE MATERIAL ORIENTATIONS 110
FIGURE 6.17 - SECTIONED POST-DEFORMATION LONGITUDINAL TAYLOR IMPACT SPECIMEN 114
FIGURE 6.18 - EBSD ANALYSIS RESULTS FOR AN UNDEFORMED LONGITUDINAL TAYLOR IMPACT SPECIMEN FROM PLATE 3 115
FIGURE 6.19 - EBSD ANALYSIS RESULTS FOR A DEFORMED LONGITUDINAL TAYLOR IMPACT SPECIMEN FROM PLATE 3 115
FIGURE 6.20 - EBSD ANALYSIS RESULTS FOR AN UNDEFORMED TRANSVERSE TAYLOR IMPACT SPECIMEN FROM PLATE 3 116
FIGURE 6.21 - EBSD ANALYSIS RESULTS FOR A DEFORMED TRANSVERSE TAYLOR IMPACT SPECIMEN FROM PLATE 3 116
FIGURE 6.22 - TAYLOR FACTOR MAP OF THE DEFORMED LONGITUDINAL TAYLOR IMPACT SPECIMEN FROM PLATE 3 118
FIGURE 6.23 - TAYLOR FACTOR MAP OF THE DEFORMED TRANSVERSE TAYLOR IMPACT SPECIMEN FROM PLATE 3 118

FIGURE 6.24 - NUMBER FRACTION OF MISORIENTATIONS BETWEEN GRAINS IN AN UNDEFORMED TAYLOR IMPACT SPECIMEN CUT FROM THE LONGITUDINAL MATERIAL ORIENTATION .. 121
FIGURE 6.25 - NUMBER FRACTION OF MISORIENTATIONS BETWEEN GRAINS IN A DEFORMED TAYLOR IMPACT SPECIMEN CUT FROM THE LONGITUDINAL MATERIAL ORIENTATION 121
FIGURE 6.26 – IPF PROJECTIONS OF "GRAIN-TO-GRAIN" MISORIENTATIONS OF A LONGITUDINAL TAYLOR IMPACT SPECIMEN OVER THE RANGES OF 35±5° AND 85±5° 121
FIGURE 6.27 – HIGH-RESOLUTION IPF MAP AND MISORIENTATION PROFILE FOR A DEFORMED LONGITUDINAL TAYLOR IMPACT SPECIMEN FROM PLATE 3 123
FIGURE 6.28 - NUMBER FRACTION OF MISORIENTATIONS BETWEEN GRAINS IN AN UNDEFORMED TAYLOR IMPACT SPECIMEN CUT FROM THE TRANSVERSE MATERIAL ORIENTATION 125
FIGURE 6.29 - NUMBER FRACTION OF MISORIENTATIONS BETWEEN GRAINS IN A DEFORMED TAYLOR IMPACT SPECIMEN CUT FROM THE TRANSVERSE MATERIAL ORIENTATION 125
FIGURE 6.30 - IPF PROJECTIONS OF "GRAIN-TO-GRAIN" MISORIENTATIONS OF A TRANSVERSE TAYLOR IMPACT SPECIMEN OVER THE RANGES OF 85±5° 125
FIGURE 7.1 - OVERCOMING OF SHORT-RANGE BARRIERS TO DISLOCATION MOTION BY THERMAL + MECHANICAL ENERGY [5] 133
FIGURE 7.2 - TYPICAL SHAPES OF BARRIERS TO DISLOCATION MOTION - RECTANGULAR, HYPERBOLIC AND SINUSOIDAL [17] 136
FIGURE 7.3 - IDEALISED TI-6AL-4V BI-MODAL MICROSTRUCTURE 139
FIGURE 7.4 - OUTLINE OF TI-6AL-4V MODELLING FRAMEWORK 140
FIGURE 7.5 - SHEAR STRESS VS TEMPERATURE FOR DIFFERENT CONTENTS OF ALUMINIUM IN TITANIUM 142
FIGURE 7.6 - PLOT SHOWING FIT OF YIELD STRESS DATA TO MTS MODEL 143
FIGURE 7.7 - ORTHOGONAL MATERIAL ORIENTATIONS AND YIELD STRESSES RELATIVE TO ROLLED PLATE 151
FIGURE 7.8 - IMAGEJ PROCESS USED TO MEASURE THE VOLUME FRACTION OF PRIMARY A GRAINS IN TI-6AL-4V 154
FIGURE 7.9 - COMPARISON OF MODEL RESULTS WITH EXPERIMENTAL RESULTS FOR PLATE 1 - DIRECTION 1 158

FIGURE 7.10 - COMPARISON OF MODEL RESULTS WITH EXPERIMENTAL RESULTS FOR PLATE 1 - DIRECTION 2 158
FIGURE 7.11 - EFFECT OF TEMPERATURE ON MODEL OUTPUT COMPARED WITH EXPERIMENTAL RESULTS FROM LITERATURE 160
FIGURE 7.12 - EFFECT OF VOLUME FRACTION PRIMARY A ON MODEL OUTPUT 161

NOMENCLATURE

Ti-6Al-4V	Titanium alloy (6% Aluminium, 4% Vanadium by weight)
CP-Ti	Commercially pure Titanium
CP-Zr	Commercially pure Zirconium
Al	Aluminium
V	Vanadium
Fe	Iron
C	Carbon
O_2	Oxygen
N_2	Nitrogen
hcp	Hexagonal close-packed crystal structure
bcc	Body-centred cubic crystal structure
fcc	Face-centred cubic crystal structure
α	Titanium phase (*hcp*)
β	Titanium phase (*bcc*)
P1	Plate 1
P2	Plate 2
P3	Plate 3
P4	Plate 4
VAR	Vacuum arc re-melt
EBCHM	Electron beam cold hearth melting
SEM	Scanning electron microscope
TEM	Transmission electron microscope
EBSD	Electron backscatter diffraction
PF	Pole figure
IPF	Inverse pole figure
QS	Quasi-static, in this study defined as a strain rate of 10^{-3} s^{-1}
HR	High strain rate, in this study defined as a strain rate of 10^{3} s^{-1}
SHPB	Split-Hopkinson pressure bar/s
CCD	Charge coupled device
CMOS	Complimentary metal oxide semi-conductor (active pixel sensor)
CMM	Coordinate measuring machine

VISAR	Velocity interferometer system for any reflector
D1	Longitudinal (rolling direction) orthogonal material orientation of a plate material
D2	Transverse (transverse to the rolling direction) orthogonal material orientation of a plate material
D3	Through-thickness orthogonal material orientation of a plate material
RD	Rolling direction
TRAN	Transverse direction
TT	Through-thickness direction
MTS	Mechanical threshold stress
GND	Geometrically necessary dislocation
FE	Finite element
CRSS	Critically resolved shear stress
LiF	Lithium fluoride
s	Nominal stress
e	Nominal strain
σ	True stress or True flow stress
σ_0	True yield stress
ε	True strain
$\dot{e}$	Strain rate
l_0	Original specimen gauge length
l	Instantaneous specimen gauge length
A_0	Original specimen cross-sectional area
A	Instantaneous specimen cross-sectional area
ε_I	Strain due to input wave in SHPB experiment
ε_R	Strain due to reflected wave in SHPB experiment
ε_T	Strain due to transmitted wave in SHPB experiment
c_b	Wave speed
K *or* B	Strength coefficient (Johnson-Cook model)
C	Strain rate dependence coefficient (Johnson-Cook model)
n	Strain hardening exponent (Johnson-Cook model)
T_m	Melting temperature (Johnson-Cook model)
T_r	Reference temperature (Johnson-Cook model)
ε_0	Reference strain rate (Johnson-Cook model)
τ	Resolved shear stress

γ	Shear strain
$\dot{\gamma}$	Shear strain rate
$\dot{\gamma}_0$	Reference shear strain rate
b	Burgers vector
ΔG_0	Helmholtz free energy
ΔG	Gibbs free energy of activation
ρ	Dislocation density
k	Boltzmann's constant
$\tau_{athermal}$	Temperature and strain rate independent shear stress
$\tau_{thermal}$	Temperature and strain rate dependent shear stress
μ	Shear modulus
τ_0	Mechanical threshold stress
g_0	Normalised activation energy
V	Volume fraction primary α
M	Taylor factor
σ_i	Material orientation dependent flow stress
M_i	Material orientation dependent Taylor factor
τ_α	Resolved yield stress in primary α
$\tau_{\alpha/\beta}$	Resolved yield stress in α/β colony
C_{Al}	Concentration of Aluminium atoms
$\tau_{dislocations}$	Back-stress due to dislocations
A	Strain hardening coefficient (Taylor model)
λ	Mean free path
ρ_{forest}	Forest dislocation density
B	Ratio of forest dislocations to total dislocations
τ_{HP}	Hall-Petch back stress due to grain boundary strengthening
k	Hall-Petch strengthening coefficient
d	Mean grain diameter
τ_{macro}	Hall-Petch back stress due to macrozone / α colony boundaries
$\tau_{\alpha\text{-}grain}$	Hall-Petch back stress due to primary α grain boundaries

PUBLICATIONS AND CONFERENCES

Publications

Some of the work that constitutes this thesis has been previously published in peer-reviewed academic journals and conference proceedings. A list of those publications is given below in chronological order:

E. Wielewski *et al*., "On the Correlation between Macrozones and Twinning in Ti-6Al-4V at Very High Strain Rates", Scripta Materialia, Vol. 67, pg 229-232 (2012).

E. Wielewski *et al.*, "Electron Back-Scatter Diffraction of Pre and Post-Deformation Ti-6Al-4V Taylor Impact Specimens", AIP Conf. Pro. (2012).

C. R. Siviour, M. Arthington, E. Wielewski and N. Petrinic, "Increasing Data from High Rate Characterization Experiments using Optical Reconstruction", AIP Conf. Pro. (2012).

E. Wielewski *et al.*, "A method for the *in-situ* measurement of evolving elliptical cross-sections in initially cylindrical Taylor impact specimens", J. of Strain A. for Eng. Des., Vol. 45, pg 429-437 (2010).

E. Wielewski *et al.*, "Texture Dependency of High Strain Rate Properties of Ti-6Al-4V", Shock Compression of Condensed Matter - 2009, Pts 1 and 2, AIP Conf. Pro., Vol. 1195, pg 1109-1112 (2009).

E. Wielewski *et al.*, "Taylor impact experiments on Ti-6Al-4V specimens using 3D geometry reconstruction and instrumented target rods", DYMAT 2009 Conf. Pro., Vol. 1, pg 257-263 (2009).

Conferences

During the course of this study, a number of conferences and workshops have been attended. A list of those conferences and workshops is given below in chronological order:

2008	Testing at the Microscale (BSSM) – London, UK
2008	Materials for Armour Systems (IOM^3) – London, UK
2009	DYMAT International Conference – Brussels, Belgium
2009	Shock Compression of Condensed Matter (APS) – Nashville, USA
2010	Electron Backscatter Diffraction Meeting (RMS) – Derby, UK
2010	Challenges in EBSD Analysis of Titanium Workshop – Derby, UK
2011	Shock Compression of Condensed Matter (APS) – Chicago, USA

ACKNOWLEDGEMENTS

A special thank you goes to my supervisor and mentor, Dr Clive Siviour. Throughout this project his infectious joy for the wonders of science have been a never-ending inspiration. Special thanks also goes to my supervisor, Dr Nik Petrinic. Without his support this project would not have been possible.

The members of the Solid Mechanics and Materials Engineering Group have always been on hand to help me, and for that I shall always be grateful. Rather than invariably miss someone out, I will just thank you all as a whole, you know who you are. That being said, I would like to single out Dr Matt Arthington, who was always been there for guidance, support and a relevant .m file. Thanks also go to Dr Matt Thomas, Prof. Dave Rugg and Dr Ben Britton, who have always been at hand to discuss my many questions about the often-confusing world of Titanium and EBSD analysis. Without you all, this thesis would not have been possible.

This research was financially sponsored by the Engineering and Physical Research Council (EPSRC), Rolls-Royce Plc. and TIMET Corp., who also supplied the material used in this study. Experimental equipment, such as high speed cameras and flashes, were provided by the EPSRC Instrument Pool for the initial “proof of concept” of the Taylor impact work.

In the interests of openness, it should be acknowledged that the Taylor impact experiments on the studied Ti-6Al-4V plates were carried out by Mr Josh Eggleston as part of his final year project, for which I was his supervisor and present for all experiments. Also, the EBSD analysis of the CP-Zr plate used in Chapter 6 was carried out by Dr Ben Britton.

During my time at Oxford, I was fortunate enough to be appointed the role of College Lecturer in Engineering Science at Oriel College. I found this role extremely rewarding and I am very grateful that Dr Douglas Hamilton and Dr John Huber gave me this opportunity.

Finally, I would like to give a special thank you to my family and friends who have supported me throughout this journey. In particular, I would like to thank my Mum and Dad, for always pushing me to aim higher and being there to lift my spirits when I needed it.

1 INTRODUCTION

1.1 The Role of Titanium Alloys in the Gas Turbine Engine

Titanium alloys have found extensive use within the aerospace industry due to their high specific strength and resistance to corrosion [1–3]. Over the last few decades they have become a vital material in the design of aerospace components and structures. Titanium alloys have found particularly strong usage in gas turbine engines. As can be seen in Figure 1.1, Titanium alloys are extensively used in the front section of gas turbine engines, where low to moderate temperatures are experienced. Typical components made from Titanium alloys include; fan blades, compressor blades, stator vanes, compressor discs and containment casings [4].

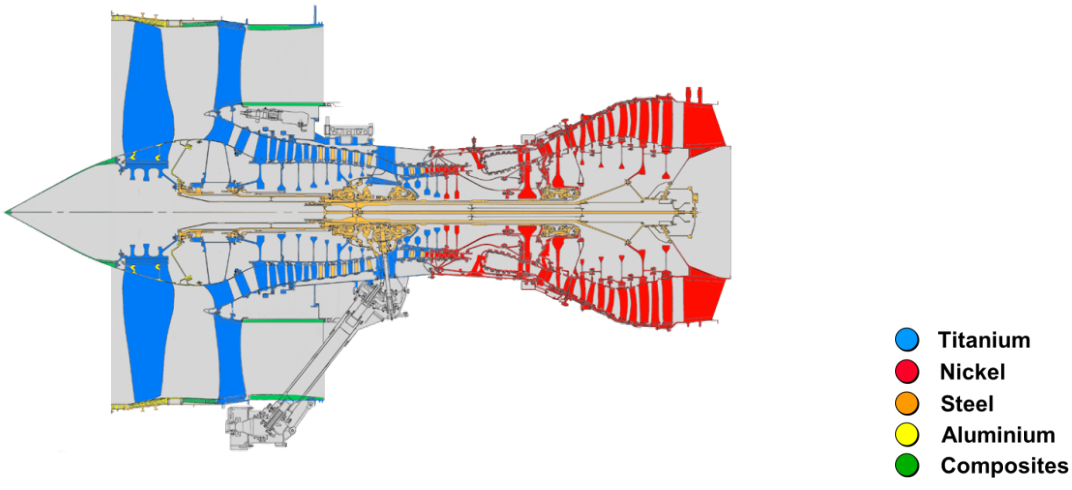


Figure 1.1 - Materials used in a typical gas turbine engine [4]

1.2 Motivation for Researching the High Strain Rate Behaviour of Titanium Alloys

Components and structures made from Titanium alloys, such as fan blades and containment casings in gas turbine engines, can on occasions be subjected to complex dynamic loading. Typical impact scenarios that result in complex dynamic loading of Titanium alloy components include; “bird strike”, where a bird is ingested into the engine and impacts the leading fan blades, and a “blade-off”, where a fan blade becomes detached from the disk and impacts the containment casing [4]. These scenarios result in the material being loaded to large strains over a wide range of strain rates.

It is common for materials to exhibit strain rate dependent mechanical behaviour. For example, the plastic flow stress of metals increases with increasing strain rate [5]. This makes the strain rate dependent behaviour of Titanium alloys of great interest to both the aerospace industry and academia. Of particular interest is the mechanical response of Titanium alloys at high strain rates. However, due to the extreme nature of high strain rate loading, it poses significant experimental and theoretical challenges to researchers studying the mechanical behaviour of materials.

1.3 Project Outline

Key mechanical properties of Titanium alloys, such as yield stress, plastic flow stress, ductility and anisotropy, are defined by microstructure and crystallographic orientation, also known as texture [1–3]. It is vital that greater knowledge is developed of the effects of microstructure and texture on the high strain rate behaviour of Titanium alloys, thus allowing engineers and material scientists to optimise material selection and component design for impact scenarios. Increased knowledge of the underlying mechanisms of deformation in

Titanium alloys at high strain rates also has the potential to be used to inform the development of Titanium alloys specifically tailored for high strain rate loading applications.

To facilitate this study into understanding the effects of microstructure and texture on the high strain rate behaviour of Titanium alloys, TIMET Corp. have supplied four plates of development level unidirectionally rolled Ti-6Al-4V, the most widely used of the Titanium alloys [1–3]. Each plate has undergone a different thermo-mechanical processing route, resulting in four different microstructures.

The microstructure and texture of these four plates will be characterised using a range of microscopy techniques, with particular focus being placed on understanding the nature of microstructural and micro-textural features such as zones of preferentially oriented grains/laths, known as "α colonies" or "macro-zones".

Uniaxial mechanical characterisation of the four plates, over applied strain rates ranging from 10^{-3} s^{-1} to 10^{3} s^{-1}, will be completed to determine the effects of microstructure and texture on the uniaxial mechanical behaviour of rolled Ti-6Al-4V plate.

To gain further insight, novel experimental techniques will be developed and implemented to investigate the high strain rate behaviour of Ti-6Al-4V under complex impact loading scenarios, such as the Taylor impact test.

Post-deformation microstructural and micro-textural analysis will be carried out on recovered Taylor impact specimens as a means of understanding the effects of microstructure and texture on the mechanisms of plastic deformation in Ti-6Al-4V at high strain rates.

The understanding gained from these experiments will then be used to inform a new physically based Ti-6Al-4V modelling framework, capable of capturing the effects of both microstructure and texture on the strain rate and temperature dependent plastic flow stress behaviour of Ti-6Al-4V.

Original contributions to engineering knowledge will be given through improved understanding of the mechanisms of plastic deformation in Ti-6Al-4V at high strain rates and the ability to predict the effects of varying microstructural parameters on the plastic flow stress behaviour of Ti-6Al-4V using the new Ti-6Al-4V modelling framework. It is hoped that this tool will allow engineers and material scientists to optimise the microstructure and texture of Ti-6Al-4V for application in critical aerospace components that have the potential to undergo impact loading.

2 LITERATURE REVIEW

2.1 Fundamentals of Ti-6Al-4V

Titanium is an allotropic element: it can exist in more than one crystallographic form. The α phase is a hexagonal close-packed (*hcp*) structure and is stable at room temperature. Above 883°C this structure transforms into a body-centred cubic (*bcc*) structure known as the β phase. Ti-6Al-4V is an α+β alloy in which the alloying elements, Aluminium and Vanadium, are included as α and β phase stabilisers, respectively, such that both the α and β phases are present at room temperature [1–3].

Due to the *hcp* structure of the α phase, Titanium and its alloys can often exhibit highly anisotropic mechanical properties. Ti-6Al-4V products undergo a wide variety of thermo-mechanical processing routes that produce a large variety of complex microstructures with varying levels of crystallographic texturing, directly affecting mechanical properties and the level of anisotropy [1].

2.2 Crystallography of Ti-6Al-4V

2.2.1 Crystallographic Indices

Miller-Bravais indices will be used when referring to the *hcp* crystal structure and standard Miller indices used when referring to the *bcc* crystal structure.

2.2.2 Crystal Structure of the α Phase

Using the hard-sphere representation of atoms, atoms constituting the α phase of Titanium closely pack together in the ABAB stacking sequence shown in Figure 2.1 (a), resulting in the primitive unit cell shown in Figure 2.1 (b). To highlight the hexagonal symmetry of the lattice, it is common for the structure to be represented by the hexagonal prism shown in Figure 2.1 (c). The hexagonal prism is a combination of three primitive unit cells and should not be considered a true unit cell. Using the Miller-Bravais indices and labelling the axes as shown in Figure 2.1 (c), it is possible to uniquely define any plane, $(hkil)$ with $h+k+i=0$, and any direction, $[uvtw]$ with $u+t+v=0$, of the hexagonal crystal lattice [5]. The density of packing in the *hcp* lattice can be quantified by taking the ratio between the length of the ***c***-axis and ***a***-axis. Titanium has a *c*/*a* ratio of 1.587 [1].

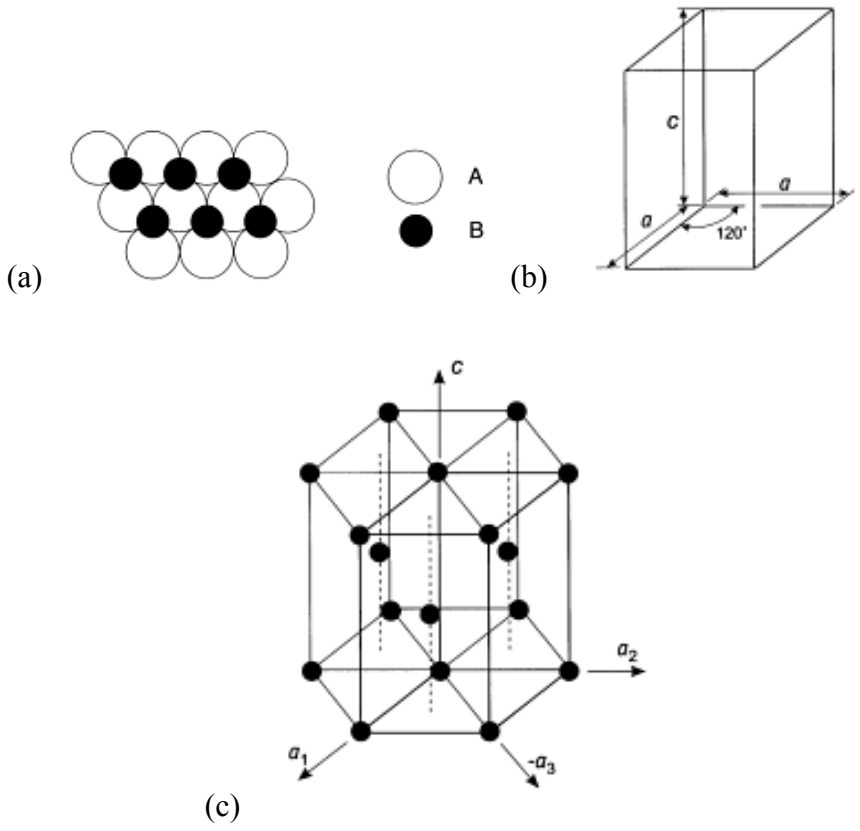


Figure 2.1 - Hexagonal close-packed structure: (a) ABAB stacking sequence of atoms on the basal planes perpendicular to the *c*-axis, (b) primitive unit cell, (c) hexagonal unit cell with labelled axes [5]

2.2.3 Crystal Structure of the β Phase

Atoms in the β phase of Titanium arrange into a *bcc* structure, as shown in Figure 2.2, with atoms touching along the close-packed $\langle 111 \rangle$ direction, using standard Miller indices [1].

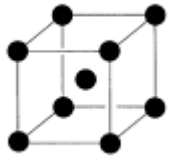


Figure 2.2 - Body centred cubic structure [5]

2.3 Production and Thermo-Mechanical Processing of Ti-6Al-4V

2.3.1 Sponge Production

Titanium is the fourth most abundant metal in the Earth's crust with the starting ore found in either its rutile (TiO_2) or ilmentile ($FeTiO_3$) forms. The extraction of Titanium from its ores is a difficult process that can be split into five stages [1–3]:

- The ore is first chlorinated to produce $TiCl_4$.
- The $TiCl_4$ is then distilled by fractional distillation to remove impurities.
- The now purified $TiCl_4$ is reduced by the Kroll process to produce metallic Titanium (known as sponge).
- The sponge is then purified to remove by-products from the reduction process, this is most commonly done by the vacuum distillation process.
- The final stage of sponge production is to crush and size the purified sponge to create a product ready for undergoing subsequent melting into commercially pure Titanium and Titanium alloys.

2.3.2 Melting

The melting stage of the processing route is used to formulate Titanium alloys and produce the ingots that are the starting point for milled products. It is important that this stage of the processing is well monitored to ensure the number of defects present in the final product are kept to a minimum. Molten Titanium is exceptionally reactive and as a result special methods have been developed to produce the ingots. The two commercially feasible methods for production of Titanium and Titanium alloy ingots are Vacuum Arc Re-melt (VAR) and Electron Beam Cold Hearth Melting (EBCHM). VAR has been used for over 50 years and a large body of empirical knowledge has been built up on the best methods to produce high quality products. EBCHM, on the other hand, is a technology still in its infancy and is currently only used for rotor grade material. Despite the relative lack of empirical knowledge on EBCHM, it still offers a number of advantages over VAR. The most significant improvement lies in use of gravity to remove high-density inclusions such as Tungsten (one of the main categories of defect that occurs during the melting stage) [1–3].

2.3.3 Primary Processing

During the primary processing stage, it is common for the ingot to undergo a β phase field homogenisation by heating the ingot to 200-450°C above the β transus for 20-30 hours before it is conditioned to create a smooth surface, free of stress concentrations. This is usually done by either grinding or lathe turning, with great care taken not to increase the local surface temperature, so as to avoid interstitial stabilised regions. A series of alternate forging processes above and below the β transus are then carried out to reduce the size of the β grains and work the material into a manageable shape, ready for secondary processing [1], [2].

2.3.4 Secondary Processing

Secondary processing involves altering forging and rolling parameters, such as the working temperature, the cooling rate and the amount of longitudinal/transverse strain, to produce the desired microstructure and texture. Once again, this process is mainly based on empirical knowledge. A great deal of research is being performed to understand how to control these parameters and produce specific microstructures and textures.

In a typical secondary processing route the material is mechanically worked either above or below the β transus, depending on the final product requirements, before a solution heat treatment is performed to produce the specified volume fraction of primary α grains. A low temperature aging heat treatment is then carried out to relieve stresses in the material and provide some further precipitation hardening [1], [2].

2.4 Microstructure of Ti-6Al-4V

2.4.1 Overview

The microstructure of a metal is defined by the size, shape and distribution of grains within the polycrystalline aggregate. As previously mentioned, Ti-6Al-4V is an α+β alloy, which means that both the α and β phase are present at room temperature. A number of complex multiphase microstructures can be formed that mostly fall into three distinct categories. The following sections give a brief review of these three main categories of microstructures.

2.4.2 Fully Lamellar Microstructures

The characteristic feature of the fully lamellar microstructure are colonies of α lamellae (or α platelets) surrounded by the remaining β matrix lamellae with a layer of α at the prior β grain boundaries. The most important part of the thermo-mechanical processing for

this microstructure is the cooling rate, as this determines features such as α lamellae size, α colony size and the thickness of the α layers at the prior β grain boundaries [1]. An example of this microstructure can be seen in Figure 2.3, where α phase is the light areas and β phase is the dark areas.

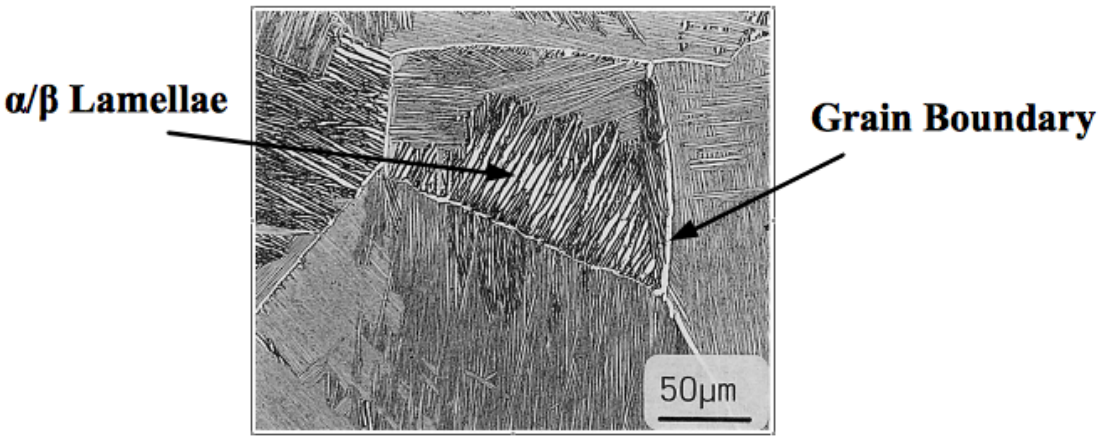


Figure 2.3 - Example of a fully lamellar microstructure [1]

2.4.3 Bi-Modal (Duplex) Microstructures

As with the fully lamellar microstructure, the bi-modal (or duplex) microstructure consists of α lamellae surrounded by the remaining β matrix lamellae, with a layer of α at the prior β grain boundaries. A further annealing stage is added to the thermo-mechanical processing in which primary α grains are nucleated at triple points between prior β grains [1]. The process used to break-up the lamellae structure can lead to significant "texturing" of both the α and β phases, this will be discussed further in the next section [1], [2]. An example of a bi-modal microstructure can be seen in Figure 2.4.

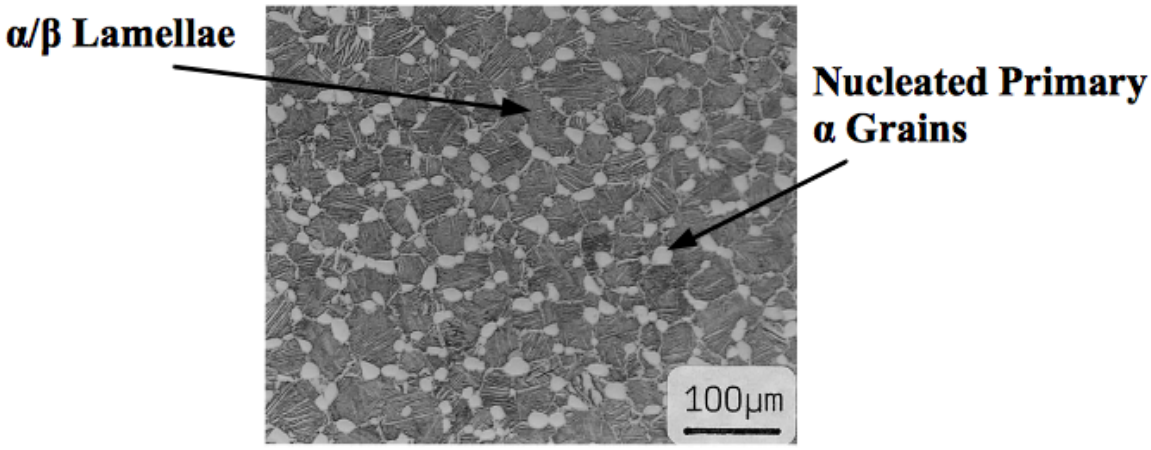


Figure 2.4 - Example of a bi-modal (duplex) microstructure [1]

2.4.4 Fully Equiaxed Microstructures

The fully equiaxed microstructure consists of connected primary α grains in a β matrix, unlike the bi-modal and fully lamellar microstructures; there are no α/β lamellae. Altering parameters, such as the cooling rate after re-crystallisation, allows the size of the primary α grains to be controlled [1]. An example of a fully equiaxed microstructure can be seen in Figure 2.5.

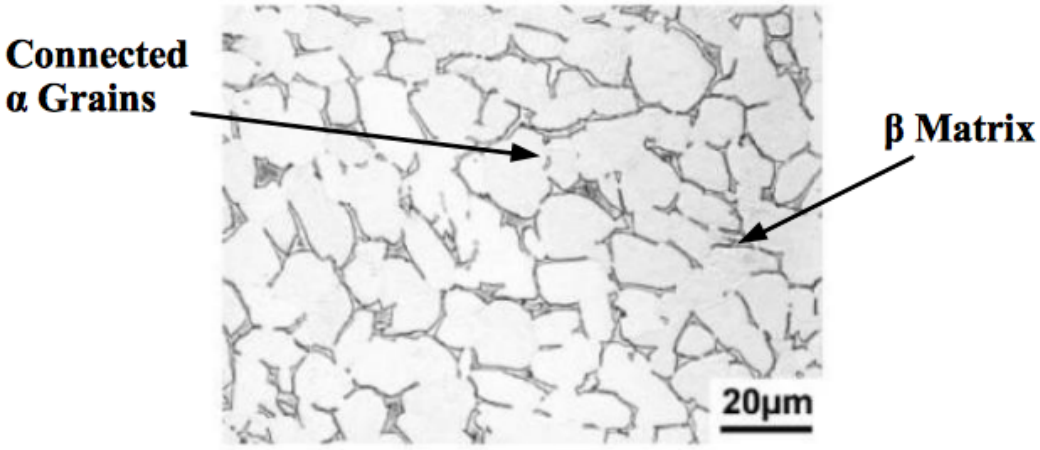


Figure 2.5 - Example of a fully equiaxed microstructure [1]

2.5 Texture in Ti-6Al-4V

2.5.1 Overview

Ti-6Al-4V is a polycrystalline material, meaning that it is composed of an aggregate of single crystals (or grains/laths), each having their own specific crystallographic orientation. The effects of non-random crystallographic orientation, more commonly known as texture, can have significant effects on mechanical material properties such as:

- Young's modulus
- Poisson's ratio
- Yield stress
- Ductility
- Toughness

It is common for texture to be thought of in terms of micro-texture, consisting of local grain-to-grain interactions, and macro-texture, the combined crystallographic agglomeration of all grains [6], [7]. The following sections will provide an overview of both micro and macro-texture, with particular focus being placed on Ti-6Al-4V.

2.5.2 Micro-Texture

By mapping the spatial location and crystallographic orientation of each individual grain in a polycrystalline metal, it is possible to understand the interconnected effects of grain morphology and crystallographic orientation on mechanical behaviour [6], [7]. Figure 2.6 presents three idealised sketches of typical polycrystalline microstructures. In these simplified cases, grains marked with a star have a spread of crystallographic orientations of only 15º, whereas all other grains have a random orientation.

A sketch of a common micro-texture seen in Titanium alloys is shown in Figure 2.6 (a), where a group of grains with the same crystallographic texture cluster together [1].

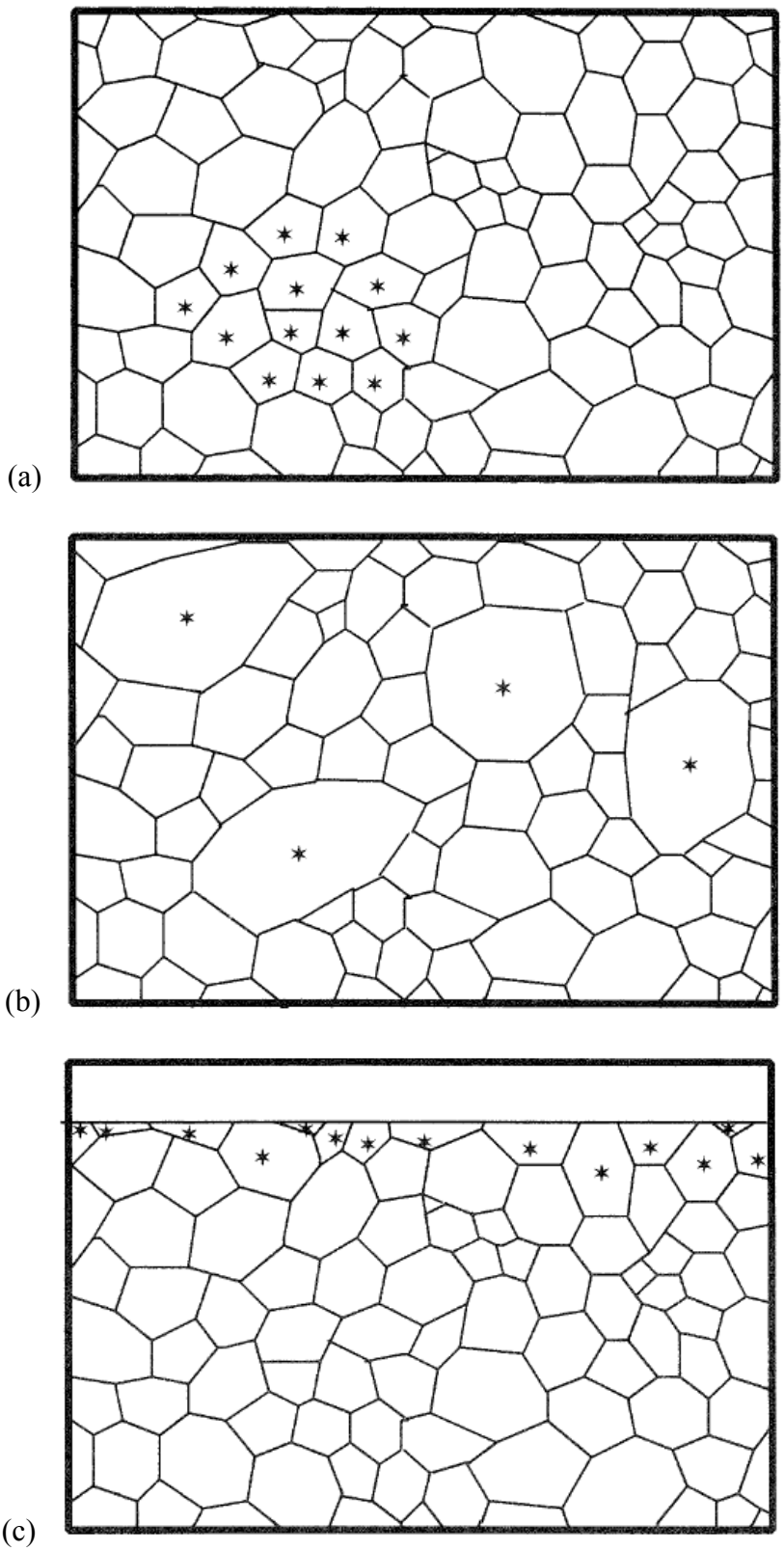


Figure 2.6 - Idealised sketches of micro-texture in a polycrystalline metal: (a) macro-zone, (b) different size class for a specific orientation and (c) specific orientation at the edge of a specimen [6]

Another idealised sketch of a typical micro-texture seen in polycrystalline metals is shown in Figure 2.6 (b), this time highlighting a difference in grain size class connected to crystallographic orientation. In low symmetry metals, such as Titanium alloys, this feature of micro-texture is seen when a material is processed at low temperature, leading "soft" orientated grains to be deformed around "hard" orientated grains, relative to the direction of loading [1]. Finally, Figure 2.6 (c) presents an idealised sketch of a micro-texture feature of a specimen cut from a heavily processed polycrystalline metal in which the grains located near the specimen surface are preferentially aligned. This may lead to features such as a hard surface skin on the material.

As will be discussed later in this chapter, the plastic deformation of metals is mainly accommodated by the glide of dislocations along preferential crystallographic planes in preferential directions [5]. If grains are preferentially orientated in a specific zone, as shown in Figure 2.6 (a), dislocations can easily transfer across grain boundaries [7]. These zones of preferentially orientated grains can have a significant effect on the mechanical properties of low symmetry polycrystalline metals, such as Ti-6Al-4V.

An example of an inverse pole figure (IPF) map of the α phase of a commercial, rolled Ti-6Al-4V plate material is presented in Figure 2.7, where each colour represents a different crystallographic orientation of the *hcp* unit cell. As can be seen from Figure 2.7, it is common for Ti-6Al-4V to contain regions of preferentially orientated grains, known as "α colonies" or "macro-zones". A well-established Burgers relationship exists between the prior β crystallographic orientation and the α phase orientation, which states that:

$$(110)_\beta \parallel (0001)_\alpha$$

$$[111]_\beta \parallel [11\bar{2}0]_\alpha$$

From this relationship, a *bcc* crystal can have 12 possible *hcp* variants, each with a different crystallographic orientation [1].

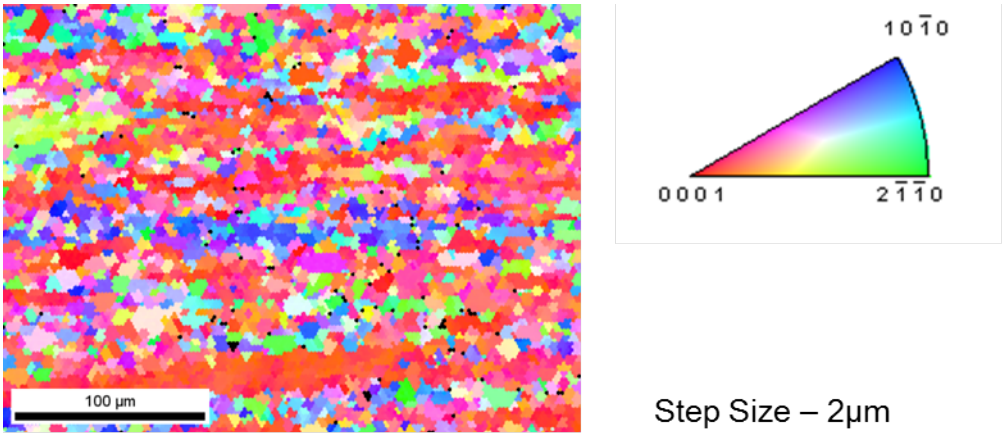


Figure 2.7 - Inverse pole figure map of Ti-6Al-4V, showing macro-zones of crystallographic orientation

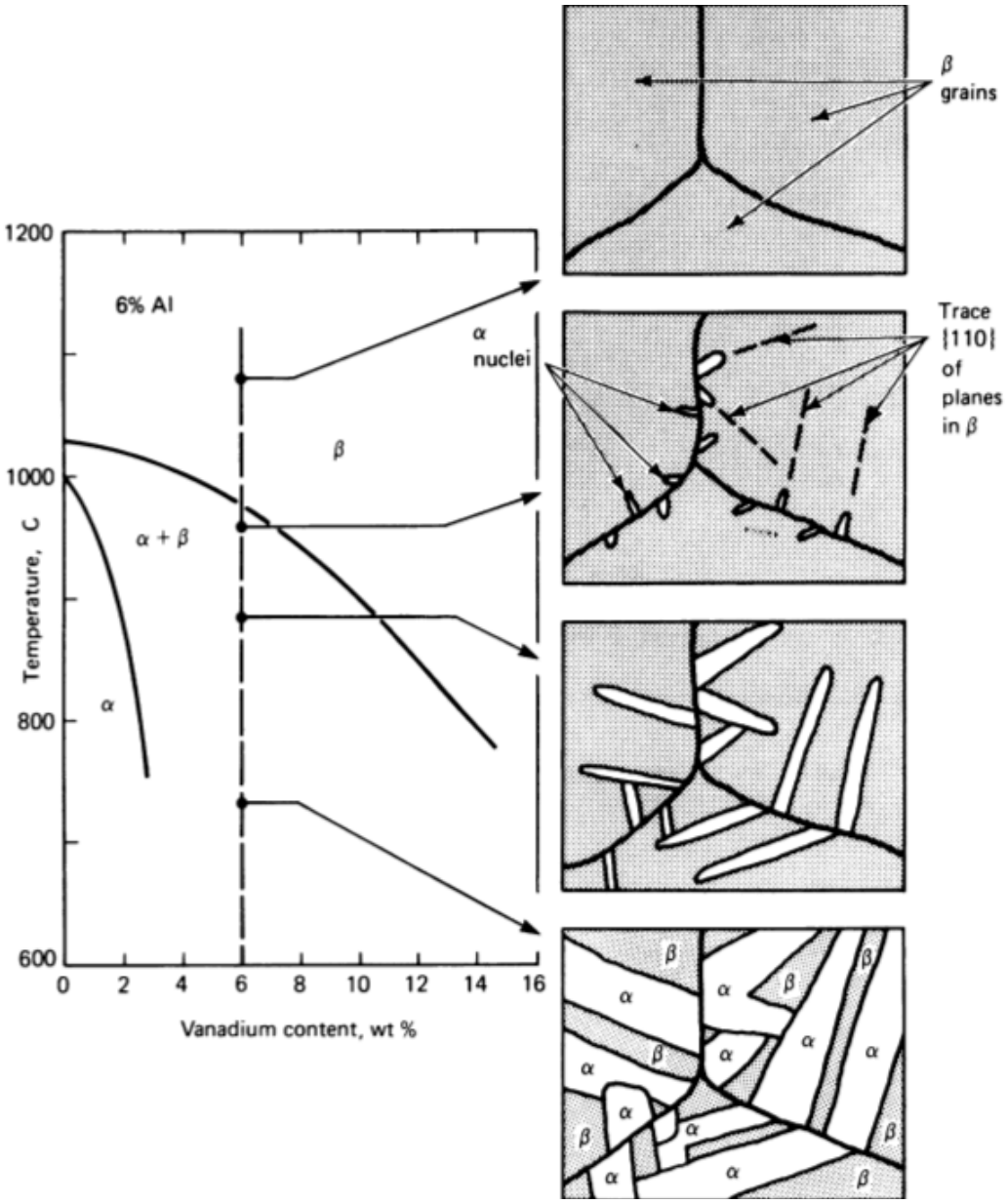


Figure 2.8 - Stages of microstructure in Ti-6Al-4V cooling from the above the β transus [2]

As illustrated in Figure 2.8, on cooling from above the β transus, α phase first grows along the β grain boundaries resulting in a layer of α with a specific crystallographic orientation relating to the prior β grain orientation. α laths then grow from the α phase layer at the β grain boundaries, maintaining the crystallographic orientation of the α at the prior β grain boundaries [2]. These colonies of α laths with the same crystallographic orientation result in α colonies and macro-zones like those shown in Figure 2.6 (a) and Figure 2.7.

2.5.3 Macro-Texture

Macro-texture can be described as the non-random, preferred crystallographic orientation distribution of the material. A heavily macro-textured material can have significantly anisotropic mechanical behaviour, as previously discussed. The inherently three-dimensional crystallographic orientation of a material is typically represented in two-dimensions by a stereographic projection. The normal of a given crystallographic plane can be described by a single point on the surface of the unit reference sphere, as shown in Figure 2.9. However, it should be noted that to obtain the full three-dimensional orientation of a crystal, two crystallographic planes must be defined. The individual points on the reference sphere are then projected onto a pole figure, as shown in Figure 2.10. In the case shown, the cubic unit cell orientation is projected from the reference sphere onto a pole figure. The azimuth of the projected pole is defined by the angle α, where α = 0º is the north pole of the reference sphere. The rotation of the pole around the polar axis is defined by the angle β, where β = 0º is a reference direction. Typically the reference directions are related to the processing geometry of the material, for example the rolling direction in a plate material [6], [7].

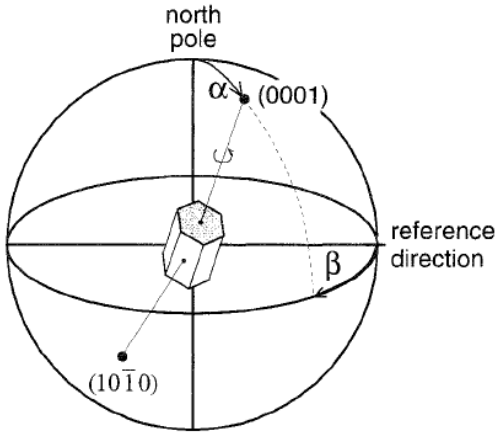


Figure 2.9 - Position of the (0001) pole of a hcp unit cell on the unit reference sphere [6]

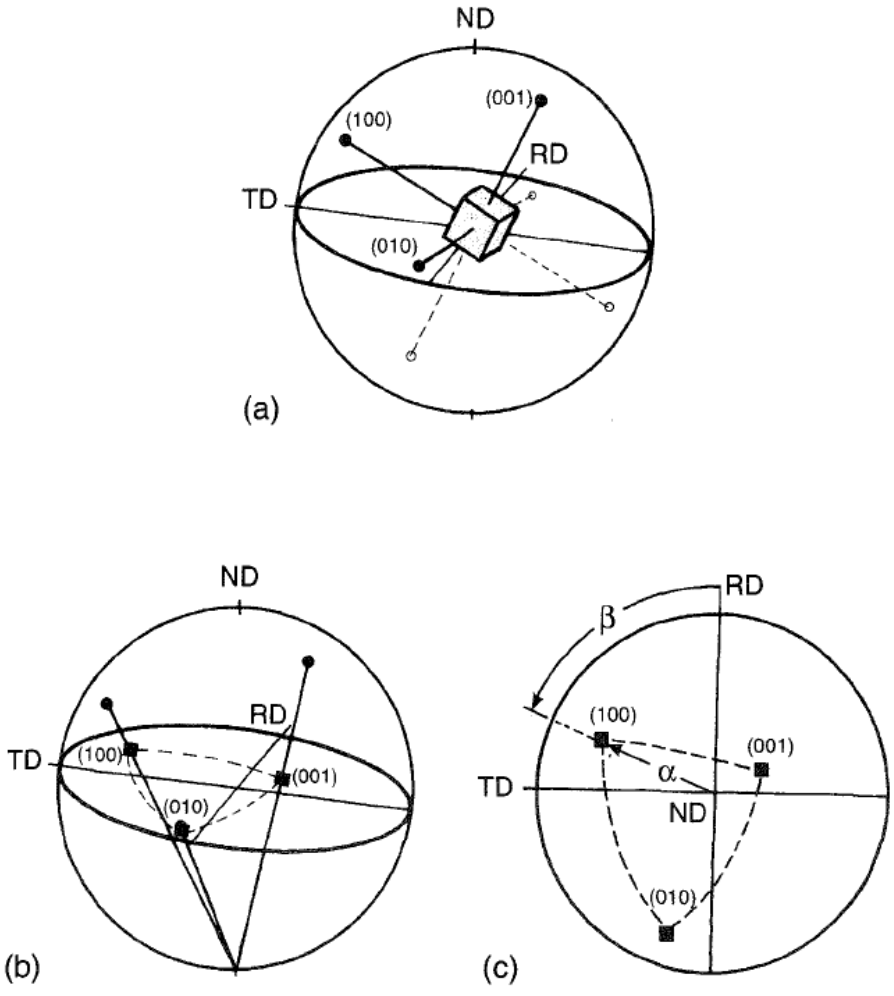


Figure 2.10 - Figure showing the stages of stereographic projection of a cubic unit cell: (a) orientation of the unit cell in the unit sphere, (b) projection of the poles onto the equatorial plane and (c) the final pole figure, with pole figure angles highlighted [6]

The macro-texture of a polycrystalline material can then be mapped by plotting the crystallographic orientation of a specific plane of each spatial point in the polycrystalline aggregate, resulting in a pole figure intensity plot [6], [7]. As an example, pole figures of the (0001) and $\{11\bar{2}0\}$ planes of the α phase from the heavily textured commercial Ti-6Al-4V plate shown in Figure 2.7 are presented in Figure 2.11. In such plots, the orientation data is presented in relation to a random orientation distribution. For example, in Figure 2.11, the maximum intensity is "x4.59" random, whereas a random distribution would have a uniform intensity of "x1" random. The data can then be contoured to highlight intensities in orientation. All pole figure intensity plots in this thesis use a linear contour spacing.

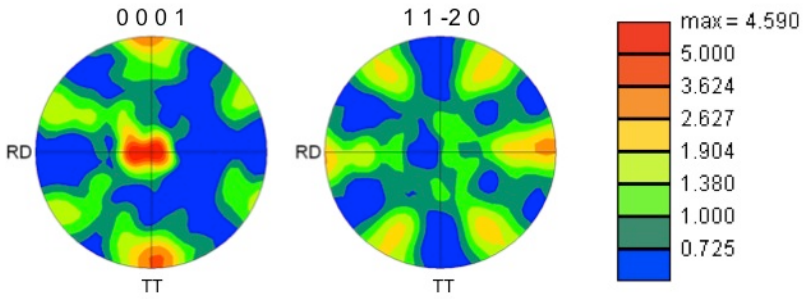


Figure 2.11 - Example pole figures from a heavily textured commercial Ti-6Al-4V plate

2.6 General Deformation Behaviour of Metals

In general, metals undergoing uniaxial tensile deformation, as seen in a typical tensile mechanical characterisation test, first deform by the conservative stretching of the inter-atomic bonds between atoms forming the metals crystal structure, this is know as the *elastic* response of the material [8]. As shown in Figure 2.12, metals typically have a linear elastic response. After a certain amount of elastic deformation, the elastic limit (or yield strength) of the material is reached. After this point, the non-conservative motion of defects in the metals crystal structure results in the permanent *plastic* deformation of the material [8]. As shown in Figure 2.12, this behaviour continues until the ultimate tensile strength (UTS) is reached,

subsequently followed by fracture. The typical elastic and plastic response of Titanium and its alloys will now be outlined in the following sections.

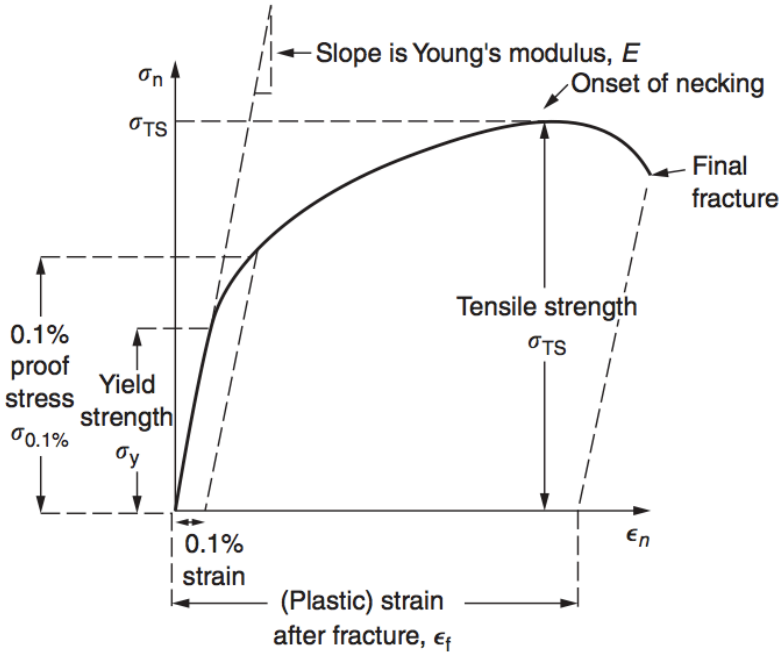


Figure 2.12 – Typical uniaxial tensile deformation behaviour of metals [8]

2.7 Elastic Deformation of Ti-6Al-4V

The modulus of elasticity of single crystal α phase Titanium is heavily dependent on the orientation of the crystal lattice relative to the direction of loading, due to the intrinsic anisotropy of the *hcp* crystal structure. An example of this can be seen in Figure 2.13, where the modulus of elasticity of single crystal commercially pure α phase Titanium is shown as a function of the declination angle of the ***c***-axis of the hexagonal unit cell [1].

The effect of the anisotropic *hcp* crystal structure is far less pronounced in a polycrystalline aggregate, with variation in the elastic modulus being heavily dependent on the extent of macroscopic crystallographic texturing [1]. The *bcc* β phase is generally thought to have a lower elastic modulus than the *hcp* α phase. However, this can be difficult to show in practise, as the β phase is not stable at room temperature [1].

The addition of Aluminium as an α phase stabiliser has the effect of increasing the elastic modulus. In contrast, the addition of Vanadium as a β phase stabiliser has the effect of reducing the elastic modulus. This is due to the Vanadium disturbing and reducing the lattice bonding force. A typical value for the elastic modulus of an α+β Titanium alloy, such as Ti-6Al-4V, is approximately 115 GPa [1].

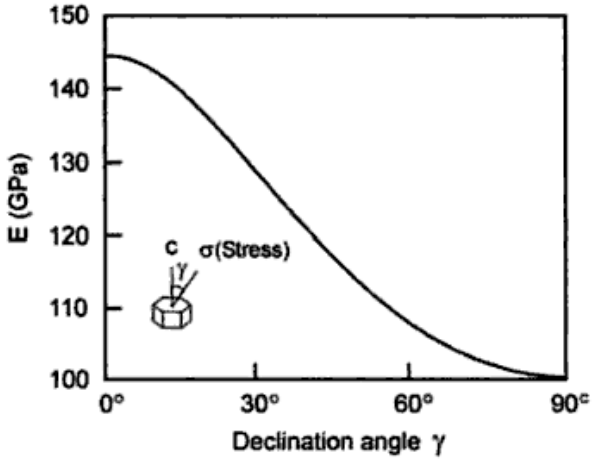


Figure 2.13 - Elastic modulus of single crystal α phase Titanium as a function of declination angle [1]

2.8 Plastic Deformation of Ti-6Al-4V

2.8.1 Slip

Slip occurs in crystalline materials when defects, known as *dislocations*, in the crystal lattice glide along preferential planes, known as slip planes, and in preferential directions, known as slip directions [5]. This can be thought of as the sliding, or successive displacement, of one plane of atoms over another, as illustrated in Figure 2.14.

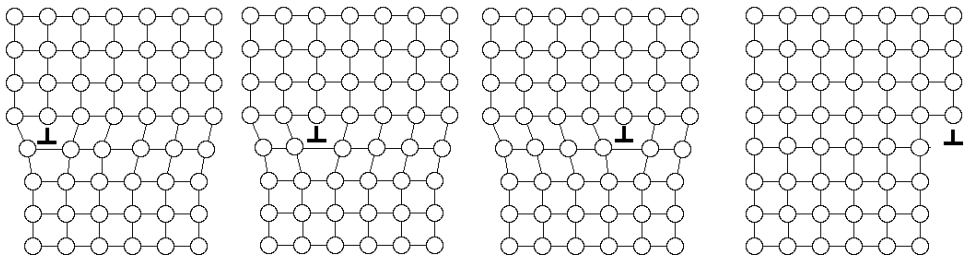


Figure 2.14 - Motion of a dislocation through a simple crystal lattice

The crystal structures on either side of the slip plane remain undistorted, with further deformation occurring by continued movement on an existing slip plane or the formation of new dislocations. The combination of a slip plane and a slip direction is known as a slip system. These slip planes are normally the planes containing the highest density of atoms with the slip direction corresponding to the shortest lattice translation vector, typically the direction where the atoms are most closely spaced [5]. As with the majority of crystalline solids, slip is the most common mechanism of plastic deformation in Ti-6Al-4V and will now be discussed for both the *hcp* α phase and the *bcc* β phase.

The main slip directions in α phase Titanium are the close-packed directions of type $\langle 11\bar{2}0\rangle$, commonly known as $\langle \boldsymbol{a} \rangle$ type Burgers vectors. The slip planes containing these $\langle \boldsymbol{a} \rangle$ type Burgers vectors are the (0001), the three $\{10\bar{1}0\}$ and the six $\{10\bar{1}1\}$ planes. These are also respectively known are the Basal, Prismatic and Pyramidal planes [1–3], [5]. A diagram of a *hcp* unit cell showing the various slip planes and slip directions for α phase Titanium (and *hcp* metals in general) can be seen in Figure 2.15.

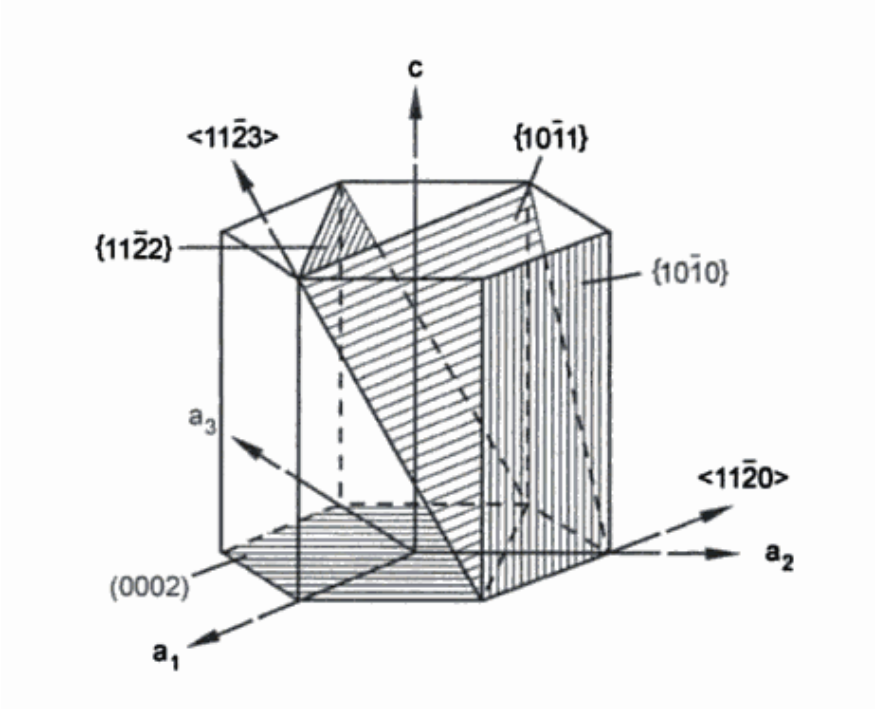


Figure 2.15 - Slip systems in *hcp* α phase Titanium [1]

For a single crystal grain in a polycrystalline aggregate to undergo sufficient homogeneous plastic deformation to accommodate the shape changes imposed by neighbouring grains, von Mises' criterion states that at least five independent slip systems are required [5]. The combination of the three slip planes and all possible slip directions in the *hcp* unit cell gives a total of twelve slip systems, reducing to only four independent slip systems [1]. The von Mises criterion for homogeneous plastic deformation can only be fulfilled when a further slip system is operative. Transmission Electron Microscope (TEM) observations have been made of deformed Titanium alloys, showing the presence of so-called $\langle \boldsymbol{c}+\boldsymbol{a} \rangle$ type dislocations. $\langle \boldsymbol{c}+\boldsymbol{a} \rangle$ type dislocations glide along the Pyramidal plane in the $\langle 11\bar{2}3 \rangle$ direction [1]. It has been proposed that these $\langle \boldsymbol{c}+\boldsymbol{a} \rangle$ type dislocations provide the required fifth independent slip system to satisfy von Mises' criterion [1], [9]. However, an independent slip system must have its own independent dislocation source and the relationship between $\langle \boldsymbol{c} \rangle$ and $\langle \boldsymbol{a} \rangle$ with $\langle \boldsymbol{c}+\boldsymbol{a} \rangle$ type dislocations is currently unclear, raising the questions of whether they offer the fifth independent slip system or whether a fifth independent slip system is even required [9]. This has led to a number of researchers arguing that internal stresses set up at grain boundaries (when inelastic strains are not compatible) may be relieved by deformation twinning, as will be discussed in the next section [9], [10].

Each of the Basal, Prismatic and Pyramidal $\langle \boldsymbol{a} \rangle$ type slip systems and the $\langle \boldsymbol{c}+\boldsymbol{a} \rangle$ type slip systems have different critically resolved shear stresses (CRSS). Paton *et al.* [11] have studied the temperature dependent resolved shear stresses of the different slip systems. The results of this study are given in Figure 2.16. As can be seen from the data in Figure 2.16, the $\langle \boldsymbol{c}+\boldsymbol{a} \rangle$ type slip system has a significantly higher CRSS.

The *bcc* β phase is a far simpler case and is in general agreement with the observed slip modes in *bcc* metals, namely the $\{110\}$, $\{112\}$ and $\{123\}$ slip planes, all with the same $\langle 111 \rangle$ slip direction [1].

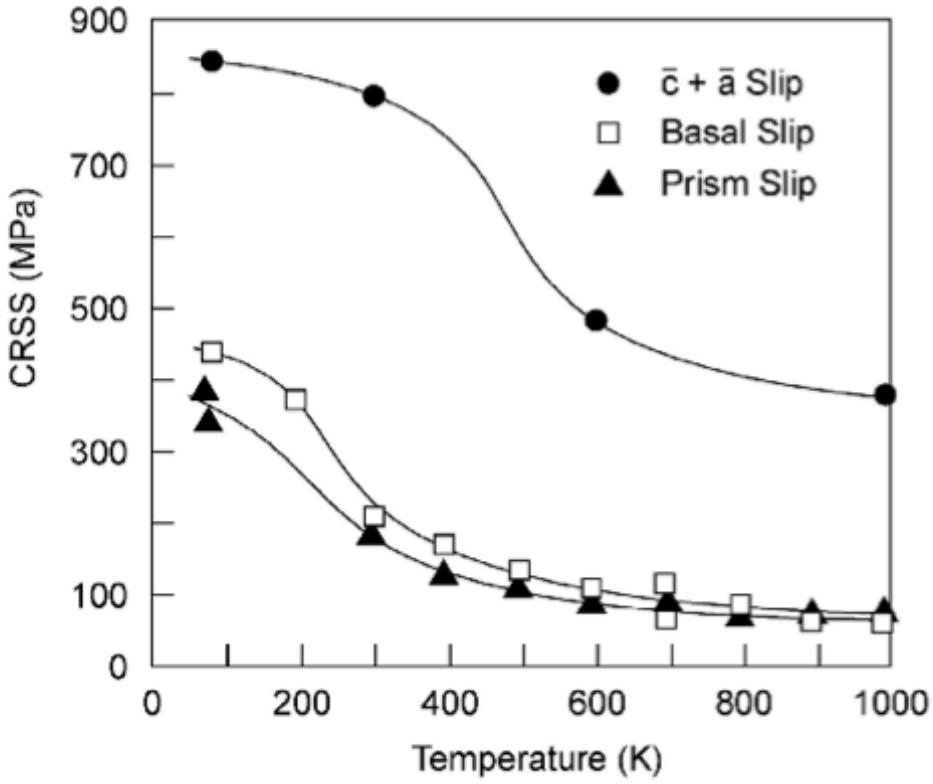


Figure 2.16 - CRSS of Basal, Prismatic and $\langle c + a \rangle$ type slip in *hcp* Titanium [1], [11]

2.8.2 Deformation Twinning

Twinning is an important mode of deformation in *hcp* metals and plays a significant role in defining fracture strength and ductility. Twinning occurs when crystals share lattice points in a symmetrical manner such that an applied shear stress causes the parent crystal to re-orientate into a mirror orientation [9].

The twinning modes most commonly seen in commercially pure, single crystal α phase Titanium are $\{10\bar{1}2\}$, $\{11\bar{2}1\}$ and $\{11\bar{2}2\}$, as shown in Figure 2.17. These are particularly important for plastic deformation when the axis of loading is parallel to the ***c***-axis of the *hcp* crystal structure, due to the lack of available slip systems in this orientation. Tensile loading along the ***c***-axis leads to activation of the $\{10\bar{1}2\}$ and $\{11\bar{2}1\}$ twins, whereas compressive loading along the ***c***-axis leads to activation of the $\{11\bar{2}2\}$ and $\{10\bar{1}1\}$ twins [1], [9], [10]. In Figure 2.17 the misorientation angle between the ***c***-axis of the twinned and parent

crystal is also clearly highlighted. This allows the type of twin to be identified using crystallographic orientation analysis techniques, some of which will be outlined in the next chapter.

It has been widely reported that loading at low homologous temperatures or high strain rates increases the density of twin formation in *hcp* metals [9], [12], [13]. It has also been noted that increasing the concentration of solute atoms, such as Aluminium, greatly suppresses the propensity of α phase Titanium to twin [1]. Due to this, it is often proposed that Ti-6Al-4V does not undergo twinning during deformation. However, experimental evidence highlighting twin formation in Ti-6Al-4V during high strain rate loading shows that this is a generalisation that should not be made lightly [14]. It is clear that microstructure, texture, strain rate and temperature have a significant effect on twin formation, with much work is needed to fully understand the mechanisms of activation.

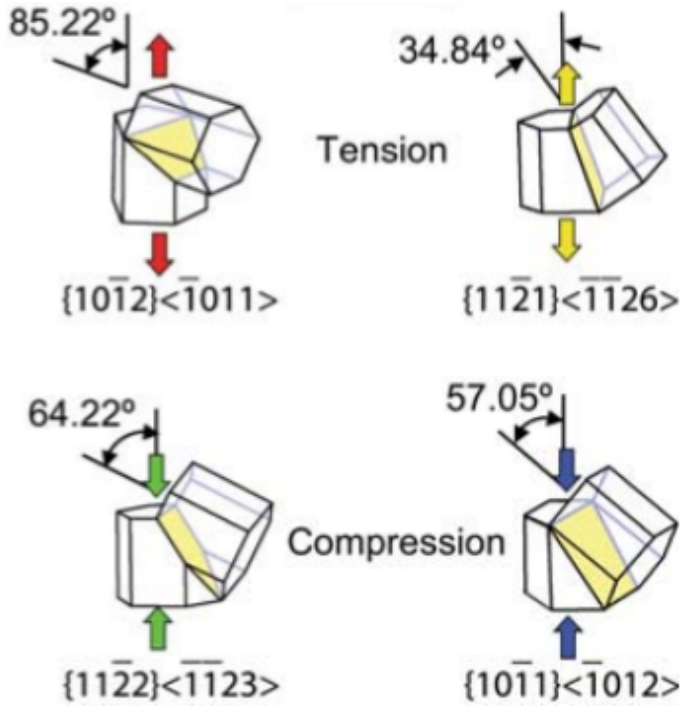


Figure 2.17 – Twinning systems observed in *hcp* Titanium [15]

2.9 The Effect of Temperature and Strain Rate on Plastic Flow Stress

2.9.1 Overview

To understand the behaviour of homogeneous polycrystalline materials that plastically deform principally by the glide of dislocations, we must first understand how such materials derive their strength. It has been experimentally observed that the yield stress and plastic flow stress of polycrystalline metals are dependent on crystal structure, crystal orientation, alloy composition, temperature, strain rate and grain size [5]. Since the 1930's, dislocation theory has provided a robust framework for the analysis of the plastic deformation of polycrystalline metals and has had significant success in understanding the source of the dependence of the yield stress and plastic flow stress on the previously mentioned factors [5]. The following sections will provide a brief overview of some of the key factors affecting the yield stress and plastic flow stress of polycrystalline metals in general, as well as providing more detailed information on Ti-6Al-4V.

2.9.2 The Motion of Dislocations in a Crystalline Solid

Plastic deformation in polycrystalline metals, such as Ti-6Al-4V, is predominantly accommodated by the glide of dislocations along preferential planes of the crystal lattice. The plastic flow stress of such a material is determined by the inherent lattice resistance and barriers to dislocation motion, which typically distort the lattice and increase the shear stress required for dislocation glide to occur [5]. Examples of barriers to dislocation motion include; solute atoms, interstitial atoms, precipitates and grain boundaries [5].

2.9.3 Temperature Dependence

The dependence of the plastic flow stress on temperature and applied strain rate is determined by the energy needed for dislocations to overcome the barriers to their motion. In

the case of temperature dependence, increased thermal vibrations of the crystal lattice may assist a dislocation in overcoming barriers to its motion. This results in the observed macroscopic response of decreasing plastic flow stress with increasing temperature [5]. It should be noted that phase changes and/or microstructural evolution, due to changes in temperature, can have a significant effect on the plastic flow stress of a metal. Although temperature dependence of the flow stress of Ti-6Al-4V is very important, the focus of this study will be on strain rate dependence at low homologous temperatures, i.e. room temperature.

2.9.4 Strain Rate Dependence

The first study of dislocation dynamics were presented in the ground breaking paper by Gilman and Johnston [16], where they used an ingenious etch pit technique to measure the velocity of dislocations in LiF. Since that study, the dynamic behaviour of dislocations has been extensively documented [5], [17]. It has been found that the behaviour of dislocations can be split into three distinct stages; thermally activated dislocation motion, drag controlled dislocation motion and relativistic effects controlled dislocation motion [17], as shown in Figure 2.18, with the velocity of dislocations tending towards the shear wave speed. All the work detailed in this research will be in the thermally activated dislocation glide regime.

It has been shown that the time taken for a given dislocation to travel between barriers is small compared with the time spent waiting at a given barrier [5], [17]. Therefore, the strain rate dependence of a metals yield stress is principally dependent on the time dislocations wait to overcome given barriers. If the strain rate is increased, the time available for a dislocation to overcome a short-range barrier is reduced, thus the stress must increase to increase the probability that the dislocation will overcome that barrier to its motion and achieve the dislocation velocity required to maintain plastic flow at the increased strain rate [5], [17]. This will be covered in more detail in Chapter 7.

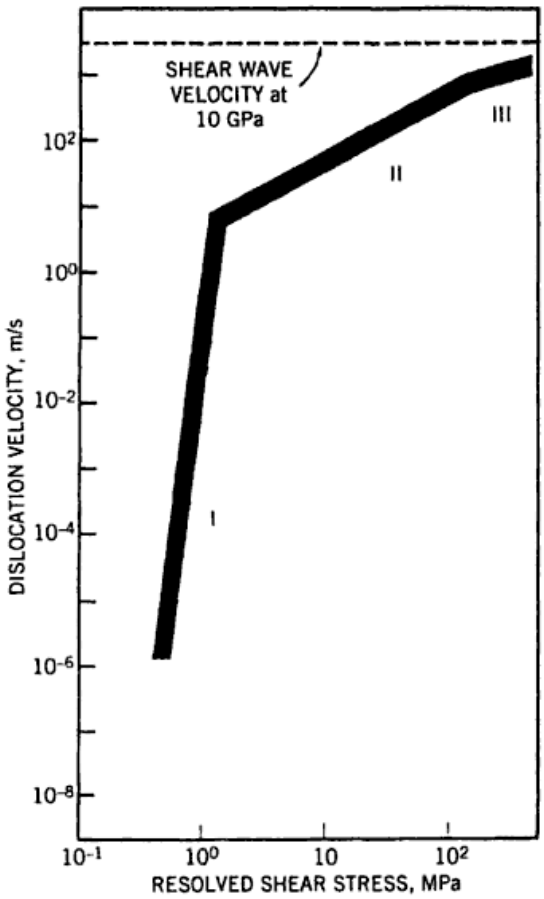


Figure 2.18 - Dislocation velocity vs resolved shear stress: (I) thermally activated dislocation motion, (II) drag controlled dislocation motion and (III) relativistic effects controlled dislocation motion [17]

The macroscopic effect of strain rate on the plastic flow stress of metals has been extensively studied for both face-centred cubic (*fcc*) and *bcc* metals. Ramesh [12] notes that the basic strain rate dependent behaviour of *fcc* and *bcc* metals consists of three key features:

- Increasing flow stress with increasing strain rate
- Rate dependence of the strain hardening in *fcc* metal; but not in *bcc* metals
- Strong rate history effects, due to the development of dislocation substructures

It is also noted that for most cubic metals a sudden increase in the strain hardening occurs around a strain rate of ~10^{3} s^{-1} [17]. Follansbee and Kocks [18] have argued that this is

due to the fact that high strain rate experiments are incapable of providing accurate flow stress data before significant microstructural evolution has occurred, making it extremely difficult to measure the strain rate dependence of the flow stress at a constant structure.

Although a significant amount of research has been carried out on *fcc* and *bcc* metals, the same cannot be said for *hcp* metals [12]. Very little information is available on the effects of high strain rates on the plastic flow stress of Ti-6Al-4V. This is compounded by the fact that compositional, microstructural and textural data are often not included in research papers studying behaviour at high strain rates, making it impossible to meaningfully compare results. However, there are sufficient data available to make general observations of some key features of the strain rate dependent flow stress behaviour of Ti-6Al-4V and the simpler case of commercially pure, α phase Titanium (CP-Ti).

Chicilli *et al.* [13] investigated the strain rate dependence of the flow stress of CP-Ti over a wide range of strain rates using a number of different experimental techniques. Typical true stress vs true strain plots from their study can be seen in Figure 2.19. Similar results have been reported by Harding [19] and Meyers *et al.* [20].

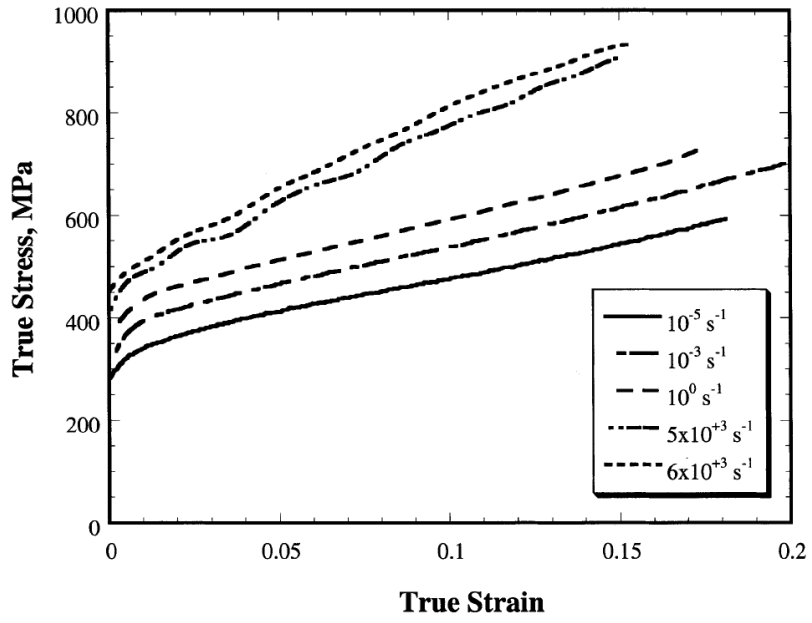


Figure 2.19 - True stress vs true strain for CP-Ti over a wide range of strain rates [13]

From Figure 2.19, it can be seen that both the flow stress and the strain hardening rate increase with strain rate. The previously mentioned step change in strain hardening, in this case between 10^0 s^{-1} and 10^3 s^{-1}, can clearly be seen. This feature of the mechanical behaviour has been linked with an observed increase in deformation twinning at high strain rates [13]. It is also worth noting the slight upward trend seen in the strain hardening of the quasi-static data, a feature often seen in *hcp* materials in general. This has been shown to be due to deformation twinning increasing the rate of strain hardening by twinning planes acting as barriers to dislocation motion i.e. reducing the effective slip length [13], [21–23]. Ramesh [12] also postulates that this behaviour may be linked to the evolution of texture during deformation. Recently, Gurao *et al.* [24] studied the effects of strain rate and material orientation on the formation of compressive and tensile twinning systems in heavily textured CP-Ti, noting that different material orientations had different strain hardening profiles, as well as different densities of compressive and tensile twins.

Experimental results reported by Follansbee and Gray show an increase in the rate of strain hardening around a strain rate of 10^3 s^{-1} for Ti-6Al-4V [25], as seen in previous CP-Ti results and results for *fcc* metals. Detailed microstructural data is provided but the authors do not record the texture of the material or the orientation of the specimens relative to the bulk material. Lee *et al.* have presented a number of results detailing the effects of strain rate and temperature on Ti-6Al-4V [26]. However, very little microstructural information is provided and no data of the texture/specimen orientations are provided.

MacDougall and Harding [27] measured the temperature rise observed in Ti-6Al-4V during room temperature high strain rate tension and torsion testing, reporting that the proportion of work converted to heat increased from ~0.2 at a plastic shear strain of ~10% to ~0.7 at a plastic shear strain of 35%. Temperature rises of ~50 °C were observed during the

high strain rate torsion tests. No microstructural or textural data is presented for the alloy under investigation.

Sarsfield *et al.* [28] report both tensile and compressive data over a range of strain rates for three Titanium alloys, including Ti-6Al-4V, but do not provide information on the initial microstructure, texture or specimen orientations. All studies report an increase in flow stress with strain rate.

3 EXPERIMENTAL TECHNIQUES

3.1 Overview

In this chapter the experimental apparatus and techniques used to characterise the mechanical behaviour of Ti-6Al-4V over a range of strain rates will be described, with particular focus placed on the strengths and weaknesses of each technique. Further to this, the equipments and techniques used to microstructurally and texturally characterise Ti-6Al-4V will be described.

3.2 Mechanical Characterisation over a Range of Strain Rates

3.2.1 Range of Strain Rates and Experimental Techniques

For the purpose of this study, the range of relevant strain rates has been split into the four categories shown in Figure 3.1; quasi-static, intermediate strain rates, high strain rates and ultra-high strain rates. These categories relate to typical in-service scenarios and more specifically the experimental equipment and techniques needed to achieve these strain rates under well-controlled laboratory conditions.

Significant progress has been made over the last fifty years in characterising materials over a wide range of strain rates. However, limitations are still present. Particularly problematic is the so-called intermediate strain rate range, where wave-propagation must be considered but cannot easily be accounted for [29].

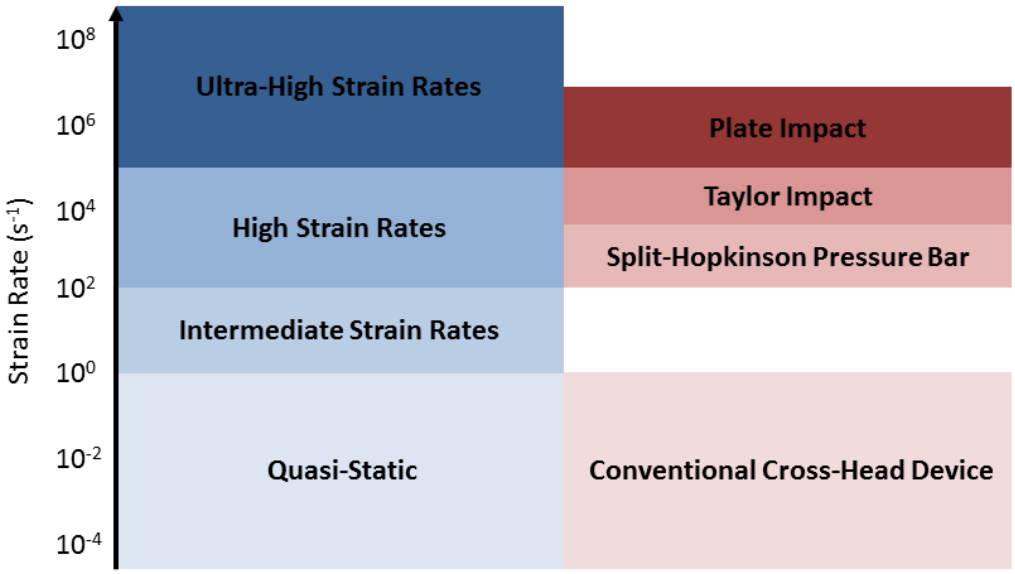


Figure 3.1 - Range of strain rates and experimental techniques

The following sections will describe the equipment, techniques and analysis used in this study: conventional crosshead device testing, split-Hopkinson pressure bar testing and Taylor impact testing. Recent reviews of high strain rate material testing are provided by Field *et al.*, Gray III and Ramesh [29–31].

3.2.2 Conventional Cross-Head Device

A conventional electro-mechanically driven crosshead device was used to mechanically characterise the Ti-6Al-4V plate materials in both tension and compression in the quasi-static strain rate range. The crosshead was moved at a constant speed with the uniaxial load applied to the specimen being measured using a 10 kN load cell. Displacements were measured by using a laser extensometer to track stripes painted on the gauge section, in the case of tensile specimens, and stripes painted on the ends of the compression anvils, in the case of compression specimens. The tensile specimens had a cylindrical gauge section 8 mm in length and 3 mm in diameter. The compression specimens were cylindrical with a length of 3.5 mm and a diameter of 3 mm.

Once the load/displacement curve is measured for a specimen, it is then possible to calculate the stress/strain curve. Nominal stress, also known as engineering stress, is defined as:

$$s = \frac{F}{A_0} \tag{3.1}$$

where s is the nominal stress, F is the uniaxial force acting on the specimen and A_0 is the original cross-sectional area of the gauge section of the specimen. Nominal strain, also known as engineering strain, is defined as:

$$e = \frac{dl}{l_0} \tag{3.2}$$

where e is the nominal strain, l_0 is the original gauge length of the specimen and dl is the change in length of the gauge section of the specimen.

However, if the material is pulled in tension the cross-sectional area reduces, where as when the material is compressed the cross-sectional area increases. This results in an artificial asymmetry in the stress/strain response when comparing tension and compression, which is particularly prevalent when dealing with large plastic deformations. To directly compare the stress response of a material in tension and compression, we must consider stress due to the force applied to the *instantaneous* cross-sectional area:

$$\sigma = \frac{F}{A} \tag{3.3}$$

where A is the instantaneous cross-sectional area and σ is known as the true stress. Now, to compare the strain response we must consider the fact that for a given displacement in tension, the equivalent displacement in compression will result in a much larger strain.

However, by considering small strain increments we can say that:

$$d\varepsilon = \frac{dl}{l} \tag{3.4}$$

where $d\varepsilon$ is a small increment of strain and l is the instantaneous length of the specimen. We can then write the true strain for both tension and compression as:

$$\varepsilon = \int_{l_0}^{l} \frac{dl}{l} = \ln\left(\frac{l}{l_0}\right) \tag{3.5}$$

We are now in a position to accurately compare the stress/strain response of materials in both tension and compression [8]. It should be noted that the conditions assumed when calculating true stress and true strain no longer hold after points of plastic instability, such as necking or shear banding.

The strain rate is defined as:

$$\dot{e} = \frac{de}{dt} = \frac{v}{l_0} \tag{3.6}$$

where $\dot{e}$ is the strain rate and v is the speed of deformation [29], in this case the speed of the cross-head.

3.2.3 Split-Hopkinson Pressure Bars

Compression and tension Split-Hopkinson Pressure Bars (SHPB), also known as Kolsky bars, were used to mechanically characterise the Ti-6Al-4V plate materials in the high strain rate range. The basic setup of a compression SHPB can be seen in Figure 3.2.

A typical SHPB consists of two long bars, designated the input and output bars, as shown in Figure 3.2. These bars are designed to remain elastic throughout testing. In the case of the experimental setup used for the testing of Ti-6Al-4V specimens, maraging steel bars of length 500mm and diameter 25 mm were used. A small specimen, which is expected to

undergo plastic deformation, is sandwiched between the two bars. The free end of the input bar is then impacted by a cylindrical projectile of the same material and diameter as the input bar, thus generating an elastic compressive stress wave that propagates down the input bar and into the specimen. Several reverberations of the stress wave occur in the specimen, with a stress wave propagating into the output bar and a reflected wave being transmitted back up the input bar [29], [31]. A Lagrangian wave propagation diagram for a typical compression SHPB setup is shown in Figure 3.3.

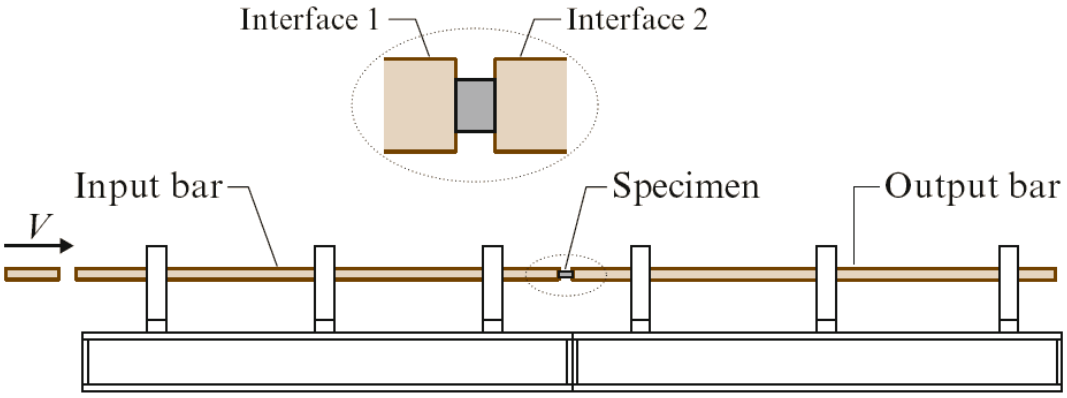


Figure 3.2 - Schematic of a compression split-Hopkinson pressure bar setup [29]

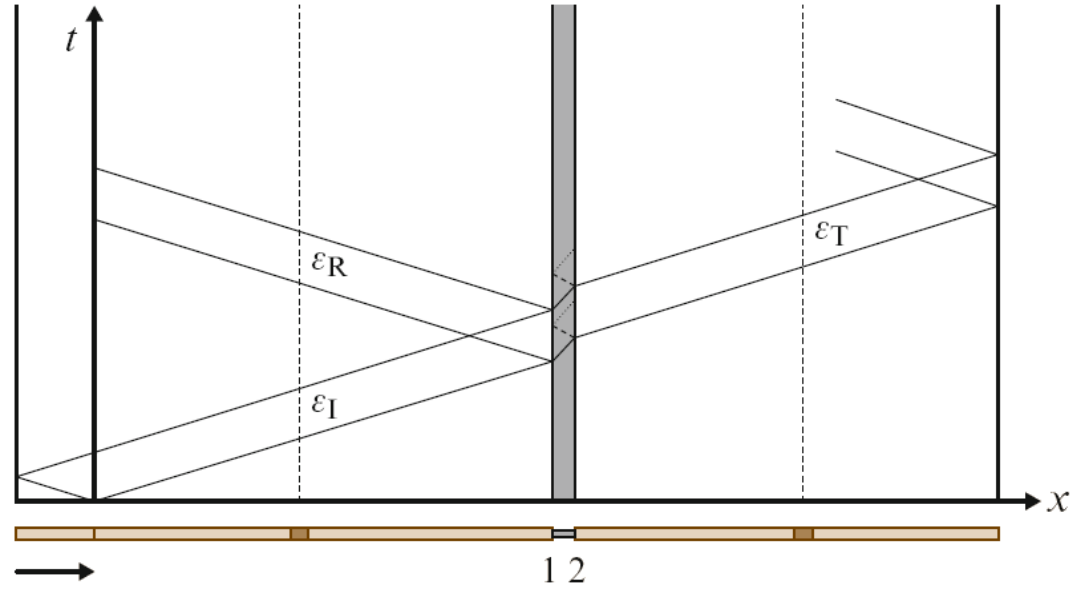


Figure 3.3 - Lagrangian wave propagation diagram for a typical compression SHPB setup [29]

Resistance strain gauges are used to measure the elastic strains due to the input, ε_I, reflected, ε_R, and transmitted, ε_T, waves, as shown in Figure 3.3. Ideally these gauges are located such that the input and reflected waves do not overlap. However, in the equipment setup used for testing the Ti-6Al-4V plate material, this is not the case. As a result, a wave separation routine was used to separate the input and reflected waves using two sets of gauges on the input bar, allowing longer experimental durations. The signals from the strain gauges were recorded using a Wheatstone bridge, an amplifier and a data acquisition tower, which were calibrated quasi-statically using a conventional electromechanically driven crosshead device.

If we assume the induced stress wave propagates down the bars as a one-dimensional elastic wave, the characteristic wave relationships tell us that the particle velocity at the interface between the specimen and the input bar is given by:

$$v_1(t) = c_b\left(\varepsilon_I - \varepsilon_R\right) \tag{3.7}$$

Likewise, the particle velocity at the interface between the specimen and the output bar is given by:

$$v_2(t) = c_b\varepsilon_T \tag{3.8}$$

where ε_I, ε_R and ε_T are defined as previously and c_b is the wave speed in the bar.

As the strains in the elastic bars are known, and since the Young's modulus of the bars is known, it is possible to then calculate the stresses in the bars and thus the normal forces acting at the interface between the specimen and the input bar:

$$P_1 = E_b\left(\varepsilon_I + \varepsilon_R\right)A_b \tag{3.9}$$

and at the interface between the specimen and the output bar:

$$P_2 = E_b\left(\varepsilon_T\right)A_b \tag{3.10}$$

Once equilibrium in the specimen has been achieved, i.e. $P_1 \approx P_2$, the analysis simplifies and it can be estimated that:

$$\varepsilon_I + \varepsilon_R = \varepsilon_T \tag{3.11}$$

therefore, it can be said that:

$$\dot{e}(t) = -\frac{2c_b}{l_0}\varepsilon_R(t) \tag{3.12}$$

$$e(t) = \int_0^t \dot{e}(\tau)\ d\tau \tag{3.13}$$

$$s(t) = \frac{E_b A_b}{A_0}\varepsilon_T(t) \tag{3.14}$$

where l_0 is defined as in the previous section. It can then be shown that:

$$\varepsilon(t) = -\ln\left[1-e(t)\right] \tag{3.15}$$

$$\sigma(t) = s(t)\left[1-e(t)\right] \tag{3.16}$$

Although requiring a more complicated design of apparatus, the concept and analysis of a tensile SHPB setup is exactly the same as that described above [29]. For both the compressive and tensile SHPB testing, the specimen designs were the same as those used in compressive and tensile quasi-static testing.

3.2.4 Taylor Impact

The classic 1948 papers by Taylor, Whiffin, and Carrington and Gayler [32–34] detail what is now known as the Taylor impact experiment. In the classic Taylor impact experiment, a right circular cylinder is impacted at a high velocity against a rigid anvil. The recovered specimens are found to have deformed plastically over a segment of the specimen close to the impact end, resulting in an increase in cross-sectional area and a decrease in length, as shown in Figure 3.4.

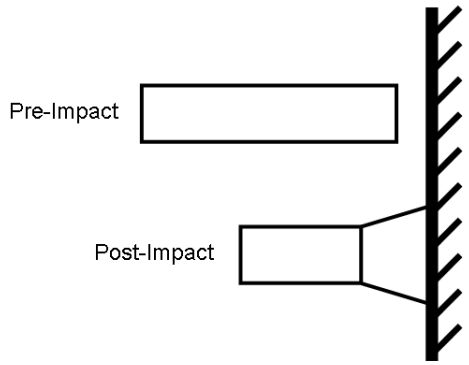


Figure 3.4 - Schematic of the classic Taylor impact experiment

Based on the assumption that the material behaves in a rigid-perfectly plastic manner, Taylor used a one-dimensional analysis to derive a method of determining a material's dynamic yield stress by measuring the dimensions of specimens before and after impact. Various researchers have proposed a number of improvements to this original analysis, including Lee and Tupper [35] and Hawkyard [36]. However, the advent of more accurate and reliable methods of high strain rate material characterisation, e.g. the split-Hopkinson pressure bar, has meant that the Taylor impact experiment is now rarely used for this purpose.

Despite this, the Taylor impact experiment is still widely used, as it provides an excellent method for validating constitutive material models used in finite element (FE) simulations, because of the complex stress states as well as variety of strain rates and final strains imposed on the material during the experiment. This has led to the development of

new methods of instrumentation with examples including high-speed photography [37], a velocity interferometer system for any reflector (VISAR) [38] and X-ray tomography [39]. These instrumentation techniques, combined with more detailed analyses of recovered specimens, have enabled key aspects of the deformation process to be quantified, such as the void nucleation in deformed specimens, the evolution of deformation along the length of a specimen, and the specimen diameter for specimens with circular cross-sections, as functions of time. A reader requiring more detailed discussion of the experimental techniques listed above is referred to the papers by Chapman *et al.* [40] and Field *et al.* [30].

Recently, the classic Taylor impact experiment has been used to great effect as a method of verifying constitutive material models for strongly textured metals that exhibit anisotropic plastic deformation. Work published by Maudlin *et al.* [41] and Plunkett *et al.* [42] has focused on the modelling of *hcp* metals, such as strongly textured high-purity clock-rolled Zirconium plate, with particular attention paid to the effects of the evolution of texture due to slip and twinning. Recovered specimens from these Taylor impact experiments were digitally scanned using an optical comparator along the major and minor axes of the elliptically deformed cross-sections. An optical reference specimen was then used to allow comparisons to be made with the final deformed shapes predicted by FE simulations.

In order to validate these models better, methods for characterising anisotropic deformation during the Taylor impact experiment are required. Chapter 6 describes in detail the application of a novel optical measurement technique to the classic Taylor impact experimental set-up. The technique provides quantitative data indispensable for the verification of key model parameters. The technique is first validated by applying it to the testing of strongly textured high-purity clock-rolled Zirconium plate before being used to gain greater insight into the deformation behaviour of the development level Ti-6Al-4V plates.

3.3 Microscopy Techniques

3.3.1 Overview

From the discussions in Chapter 3 it is clear that characterising the microstructure and texture of Ti-6Al-4V is vital to understanding its mechanical behaviour, providing valuable information for researchers wishing to develop constitutive material models for Ti-6Al-4V or optimise Titanium alloys for specific applications. This section will detail the microscopy techniques used to characterise the microstructure and texture of the four development level Ti-6Al-4V plates tested in this study.

3.3.2 Optical Microscopy

Optical microscopy is the most widely used microscopy technique due to its ease of use and low running costs. The design of optical microscopes varies hugely but the basic concept is very simple. An optical microscope consists of a bright light source to illuminate the specimen and a series of lenses used to magnify the image of the specimen in the focal plane, with a precision stage used to position the specimen. The image is either directly viewed via eyepieces or digitally captured using a CCD or CMOS detector. The maximum magnification of a modern optical microscope is in the order of 1500x [43].

Optical microscopy is an important technique for the characterisation of Titanium alloys, as a large amount of data has been built up over the years on the various different microstructures seen from different processing routes [1], [2]. Polishing and etching of the specimen surface allows the grain structure of the alloy to be observed, giving valuable data such as grain size, grain shape, percentages of α/β phases and microstructural development. Typical Ti-6Al-4V microstructures imaged using optical microscopy were shown in Figure 2.3, Figure 2.4 and Figure 2.5.

3.3.3 Scanning Electron Microscopy

The scanning electron microscope (SEM) is a relatively modern scientific instrument used to image specimens at the micron or nanometre scale. Despite initially prohibitive costs, the SEM is now widely used in both academia and industry. As with the optical microscope, the design of a SEM can vary hugely. However, the concept of its operation is very simple. A high-energy beam of electrons is scanned along the surface of the specimen in a raster manner. The electrons interact with the specimen and signals; such as secondary electrons, backscattered electrons, characteristic X-rays and transmitted electrons, give information on the specimen's topography, composition and many other properties. SEMs are characterised by a very large depth of field, allowing the capture of detailed topographic information, as can be seen in later sections of this study focussing on fracture surfaces. The maximum magnification of a modern SEM is in the order of 500,000x [43]. All SEM analyses in this study were carried out using a Carl Zeiss Evo LS15 Variable Pressure Scanning Electron Microscope equipped with a LaB6 electron gun.

3.3.4 Electron Back-Scatter Diffraction

Electron Backscatter Diffraction (EBSD) is a diffraction technique used to determine the microscopic crystallographic orientation of materials. For many years EBSD remained a specialist technique, due to the lack of availability of SEMs and commercial EBSD systems. However, with the advent of the wide spread availability of SEMs, the last decade has seen EBSD become the most widely used method for characterising the micro and macro-texture of engineering materials such as Ti-6Al-4V. EBSD is now applied to crystal orientation mapping, phase identification, grain morphology studies, micro-strain studies and much more.

EBSD patterns, or Kikuchi patterns, are generated by the backscatter diffraction of electrons from a stationary beam of high-energy electrons interacting with a volume of crystalline material, such as in a SEM, being projected onto a Phosphor screen. Kikuchi

patterns are characterised by a regular arrangement of bright bands, as shown in Figure 3.5. The Kikuchi pattern can be thought of as the gnomonic projection of the crystal lattice structure onto the two-dimensional Phosphor screen [6], [44].

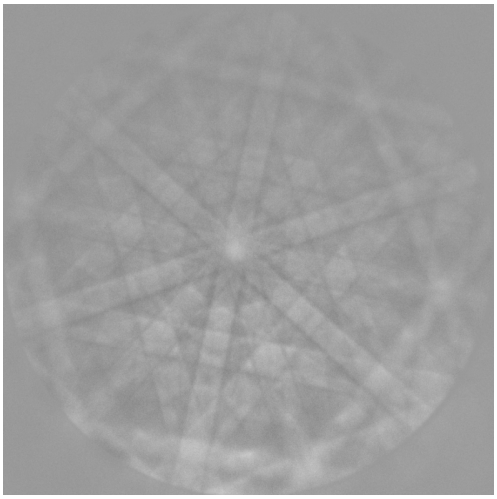


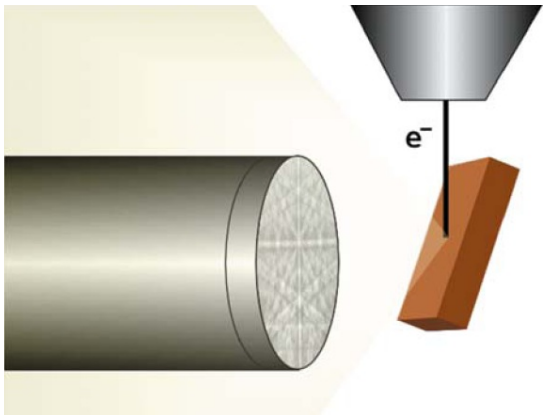
Figure 3.5 - Example Kikuchi pattern from EBSD of Ti-6Al-4V plate material

A typical automated EBSD system consists of the SEM, the pattern acquisition device and the software. The specimen is tilted to an angle of 70º, so that the interacting electrons diffract in such a way as to be projected onto the Phosphor screen. A schematic of a typical EBSD system setup is shown in Figure 3.6, as well as the setup used in this study. A CCD camera then records the pattern produced on the Phosphor screen. The software is used to sort the bands of the recorded Kikuchi patterns according to their intensities and width. Theoretical values for the inter-planar angles (the angle between Kikuchi bands) and the inter-planar spacings (the width of the Kikuchi bands) are then compared with the recorded Kikuchi patterns. The 4-5 most intense bands are then indexed. This is done by considering the first 3-4 families of crystallographic planes, such that the Kikuchi pattern is uniquely solved for a specific crystallographic orientation [6], [44].

By raster scanning the surface of the specimen, typically in a hexagonal grid, and collecting Kikuchi patterns at each point, the crystallographic orientation of a specimen can be mapped across the scanned surface. This gives valuable information such as macro-texture,

micro-texture, grain size and grain misorientations, which can be used to generate numerous plots highlighting different microstructural features [6], [7], [44].

All EBSD data used in this study was gathered using an EDAX OIM XM 4 Hikari System equipped with a DigiView IV Camera and OIM Data Collection Software, mounted on the previously mentioned Carl Zeiss Evo LS15 Variable Pressure SEM. Analysis of the EBSD data was carried out using the EDAX Data Analysis software package.

(a) 

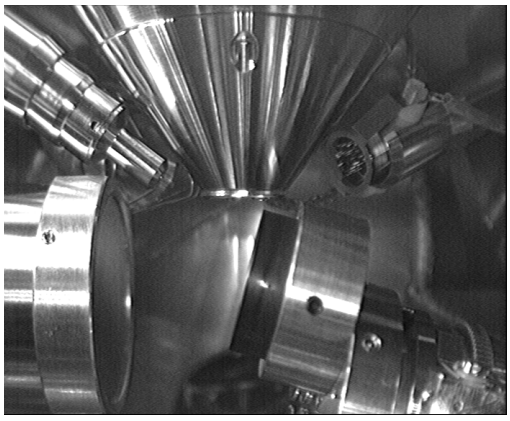
(b) 

Figure 3.6 - (a) Schematic of a typical EBSD system [44]**, (b) EBSD setup used in this study**

3.3.5 Sample Preparation

To microscopically study materials using techniques such as optical microscopy and EBSD, samples must first be prepared in the correct manner. In this study, samples were first hot mounted in a conductive epoxy resin. A Struers TegraForce 15 automated polishing/grinding wheel, with the Struers magnetic disc system, was then used to prepare the surfaces of the specimens for EBSD. The precise preparation route can be seen in Table 3.1. For optical microscopy a final etching stage was added by submerging the sample surface in Kroll's Reagent (2ml HF, 10ml HNO_3 and 88ml distilled water) for 5 seconds [1], [2].

Stage	Type	Disc	Lubricant	Time
1	Grinding	MD-Piano 220	Water	5mins
2	Polishing	MD-Largo	DiaPro Largo	5mins
3	Polishing	MD-Chem	Colloidal Silica (90%) + Hydrogen Peroxide (10%)	30mins

Table 3.1 - Ti-6Al-4V sample preparation route for EBSD

4 MICROSTRUCTURAL CHARACTERISATION OF Ti-6Al-4V

4.1 Overview

As discussed in Chapter 2, chemical composition, microstructure and texture play a fundamental role in defining the mechanical properties of Ti-6Al-4V. In this chapter, a range of techniques will be used to microstructurally characterise the four plates of development level Ti-6Al-4V supplied by TIMET Corp. for investigation. The characterisation carried out in this chapter will be used to compare the four different plate materials and infer relationships between key microstructural/textural parameters and mechanical behaviour.

Little is known about the different thermo-mechanical processing routes undergone by the four development level Ti-6Al-4V plates supplied by TIMET Corp. However, it is known that all four plates come from a standard 3xVacuum Arc Re-melt (VAR) melting route and have been unidirectionally rolled during secondary processing.

The four development plates have been designated Plate 1, Plate 2, Plate 3 and Plate 4, in no particular order.

4.2 Material Orientations

Before beginning microstructural characterisation, we must first define the material orientations of the four development plates. As is standard with rolled plate materials, the direction of primary rolling is defined as the longitudinal axis, 1, the direction perpendicular to the rolling direction is defined as the transverse axis, 2, and the direction normal to the plane of the plate is defined as the through thickness axis, 3. A diagram showing the material orientations relative to the plate and rolling direction can be seen in Figure 4.1.

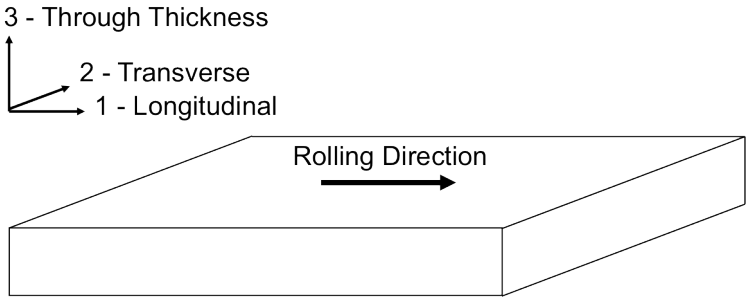


Figure 4.1 - Material orientations relative to plate and rolling direction

4.3 Chemical Composition

The inclusion of alloying elements in the composition of a metal can be used to significantly improve its mechanical behaviour. However, during processing, unwanted elements can be included in the chemical composition as a result of production methods. For example, the inclusion of elements such as Oxygen and Nitrogen in Ti-6Al-4V during thermo-mechanical processing can lead to severe degradation of the alloy's mechanical properties, due to Oxygen and Nitrogen atoms becoming solute within the crystal lattice, increasing strength but severely decreasing ductility [1].

As a result, it is vital that the composition of any Ti-6Al-4V plate is characterised before testing, such that valid comparisons can be made between different microstructures of the same alloy. TIMET Corp. carried out a compositional analysis on all four development plates,

the results of which can be seen in Table 4.1. All four plates show similar alloying element, Oxygen, Nitrogen and trace element content, allowing valid comparisons to be made between the mechanical behaviour of the four plates.

Element	P1	P2	P3	P4	
Al	6.404	6.385	6.428	6.346	% weight
Fe	0.147	0.149	0.16	0.143	
V	3.935	3.948	3.985	3.913	
C	-	-	-	-	
O_2	1980	2025	1938	1858	ppm
N_2	62	60	73	68	

Table 4.1 - Chemical composition of the four development plates

4.4 Microstructure

Optical microscopy was carried out by TIMET Corp. on the four development plates along the longitudinal\through-thickness plane and the transverse\through-thickness plane, in the centre of the plate. The images obtained can be used to qualitatively define the microstructures of the four development plates by comparing them with the vast library of Ti-6Al-4V microstructures available in the literature [1], [2]. Further, a large body of empirical data is available on the mechanical behaviour of given Ti-6Al-4V microstructures, making comparison with previous studies a valuable exercise. This will be done in Chapter 5.

The optical micrographs for Plate 1 are shown in Figure 4.2 and Figure 4.3. From these optical micrographs it can be seen that Plate 1 has a classic bi-modal microstructure consisting of α laths in a matrix of β, with nucleated primary α also clearly seen. The similarities between microstructures in the longitudinal/through-thickness and transverse/through-thickness planes indicate that the plate may have undergone some cross-rolling during thermo-mechanical processing.

The optical micrographs for Plate 2 are shown in Figure 4.4 and Figure 4.5. As with Plate 1, the optical micrographs of Plate 2 show that it has a bi-modal microstructure consisting of α laths in a matrix of β, with nucleated primary α grains. Plate 2 appears to have a slightly higher percentage of nucleated primary α when compared with Plate 1, although further analysis would need to be carried out to confirm this. Comparison between optical micrographs of Plate 2 in the longitudinal/through-thickness and transverse/through-thickness planes shows significant differences in microstructure. In the longitudinal/through-thickness plane, long bands of primary α can be seen, as well as spheroidised primary α, whereas in the transverse/through-thickness plane, the nucleated primary α grains are all relatively well spheroidised. This indicates that Plate 2 has undergone unidirectional rolling along the longitudinal direction.

The optical micrographs for Plate 3 are shown in Figure 4.6 and Figure 4.7. These micrographs show that Plate 3 has a well-developed bi-modal microstructure consisting of a high percentage of α in a matrix of β. Comparison between the longitudinal/through-thickness and transverse/through-thickness planes shows very little difference, indicating a degree of cross-rolling has occurred during thermo-mechanical processing, as with Plate 1.

The optical micrographs for Plate 4 are shown in Figure 4.8 and Figure 4.9. It can be seen from these micrographs that Plate 4 has a very well-developed bi-modal microstructure consisting of a high percentage of primary α in a matrix of β. Comparisons with Plate 3 show a larger relative nucleated primary α grain size. Comparison between the longitudinal/through-thickness and transverse/through-thickness planes shows significant differences in microstructure. The longitudinal direction consists of large spheroidised primary α, as well as long bands of primary α. In contrast, the transverse/through-thickness plane mainly consists of large spheroidised primary α, indicating that unidirectional rolling has occurred along the longitudinal direction.

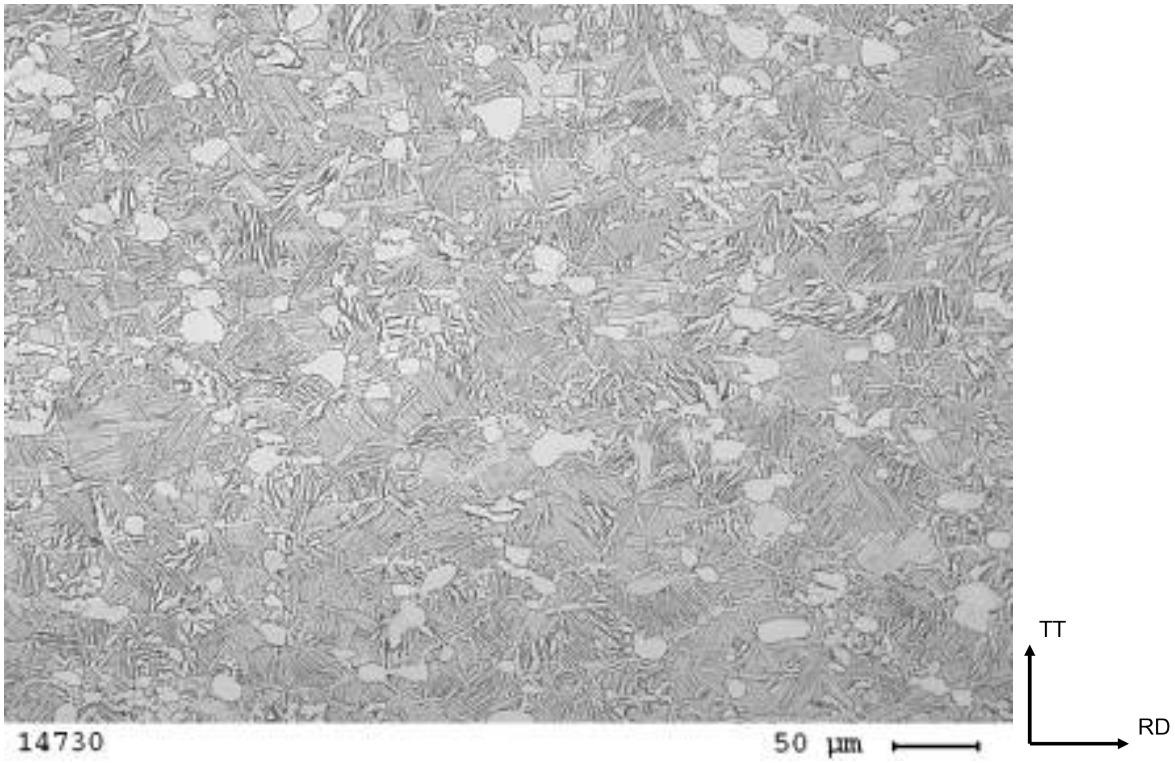


Figure 4.2 - Optical micrograph: Plate 1 – Longitudinal/Through-Thickness

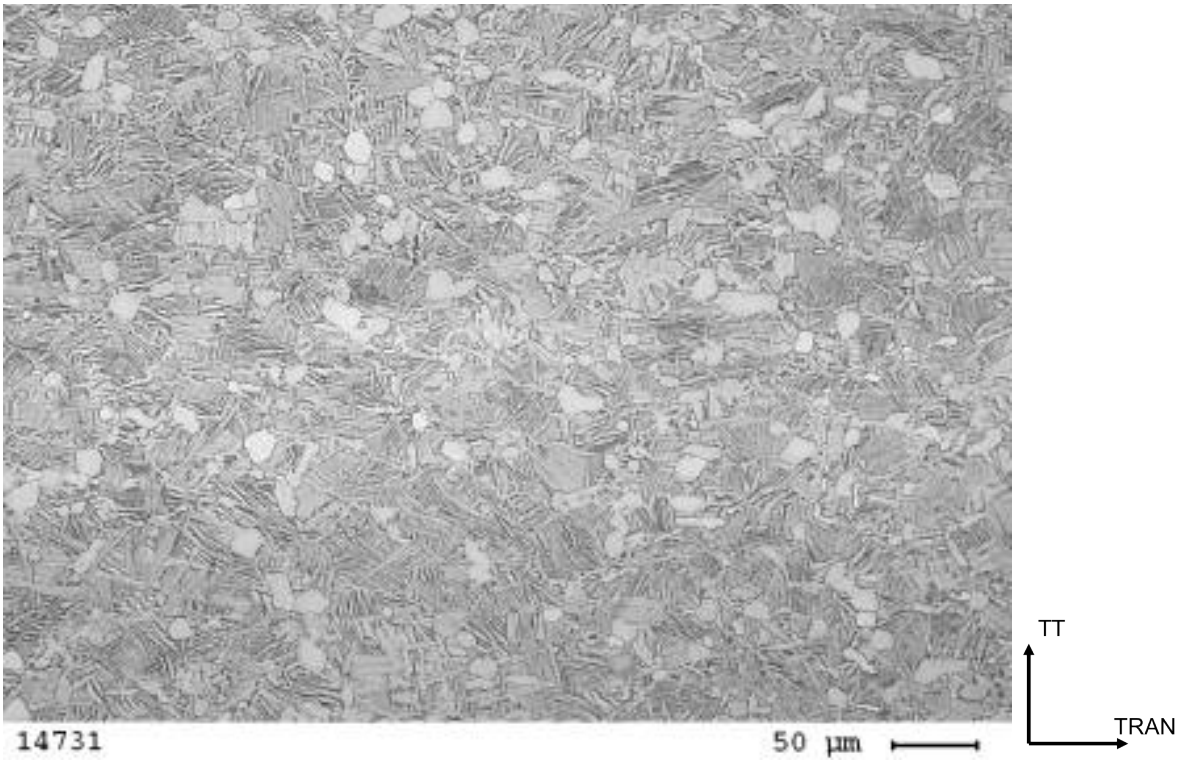


Figure 4.3 - Optical micrograph: Plate 1 – Transverse/Through-Thickness

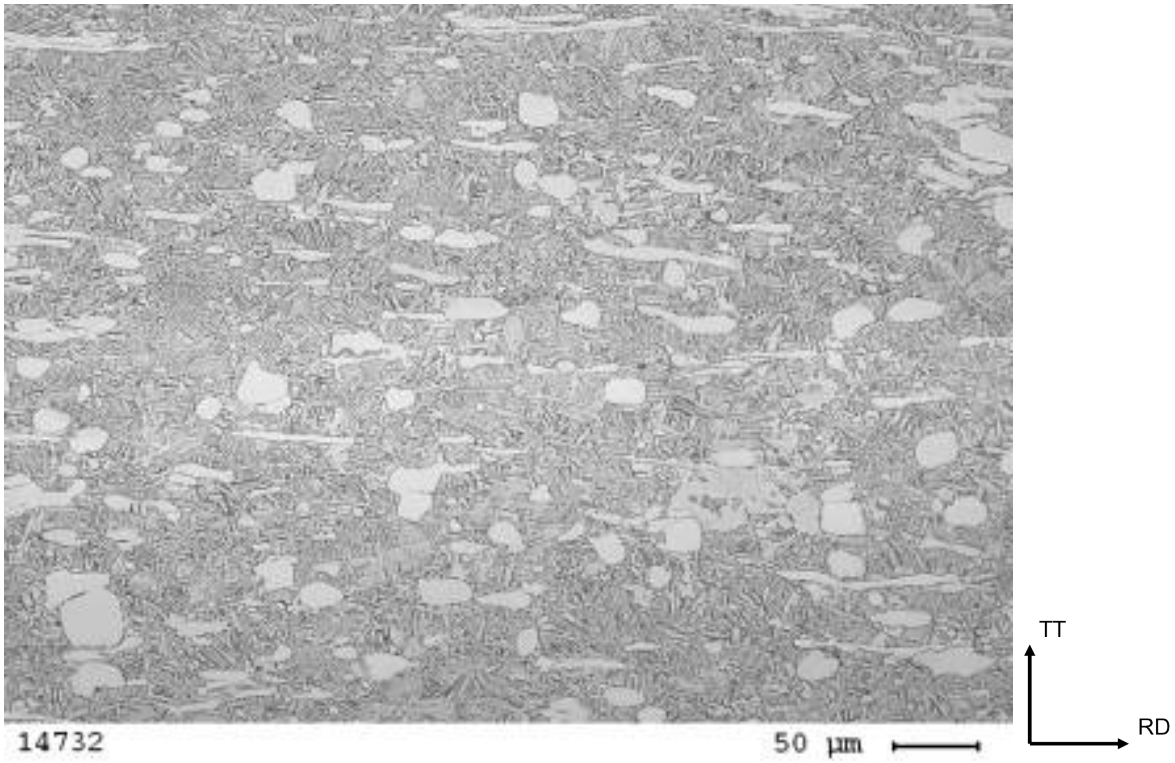


Figure 4.4 - Optical micrograph: Plate 2 – Longitudinal/Through-Thickness

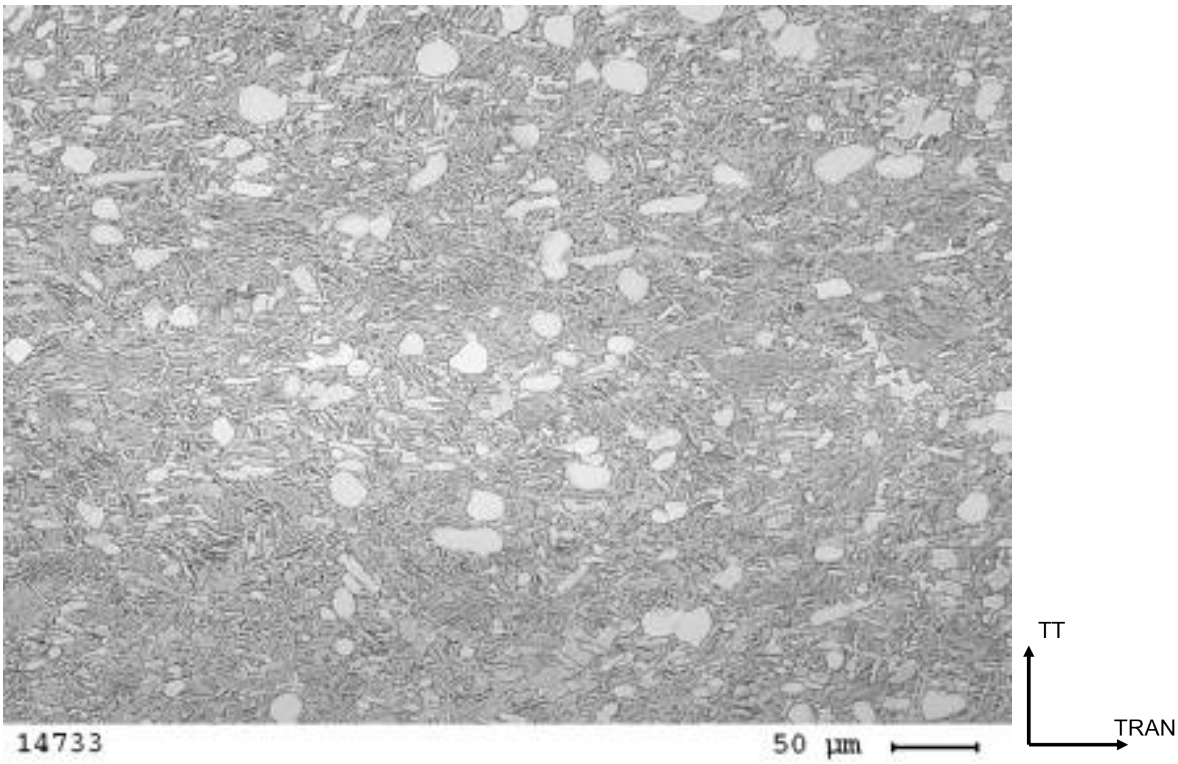


Figure 4.5 - Optical micrograph: Plate 2 – Transverse/Through-Thickness

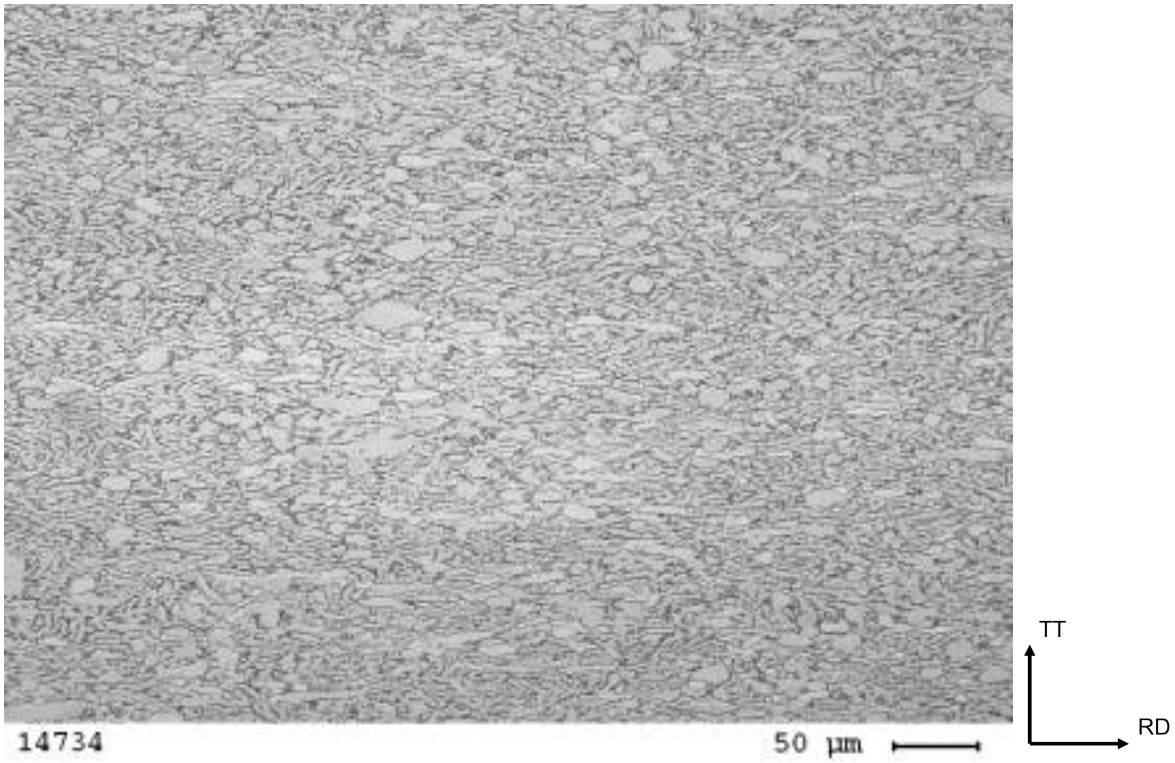


Figure 4.6 - Optical micrograph: Plate 3 – Longitudinal/Through-Thickness

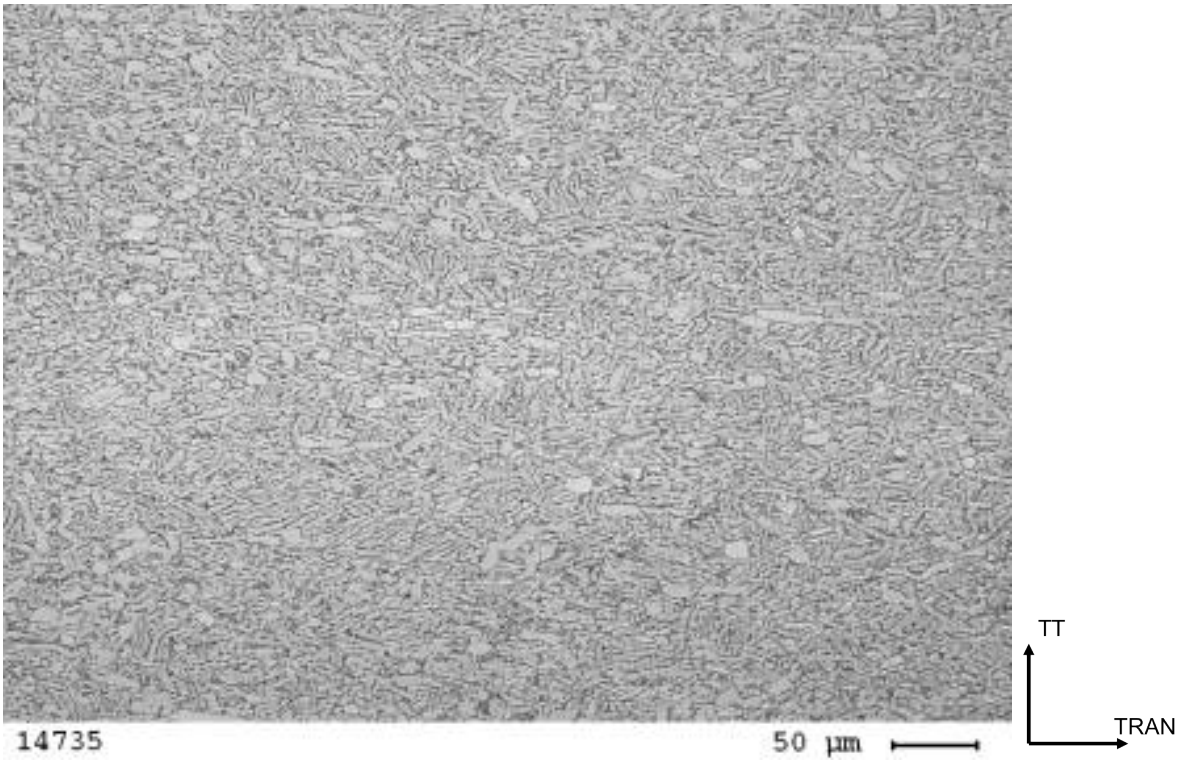


Figure 4.7 - Optical micrograph: Plate 3 – Transverse/Through-Thickness

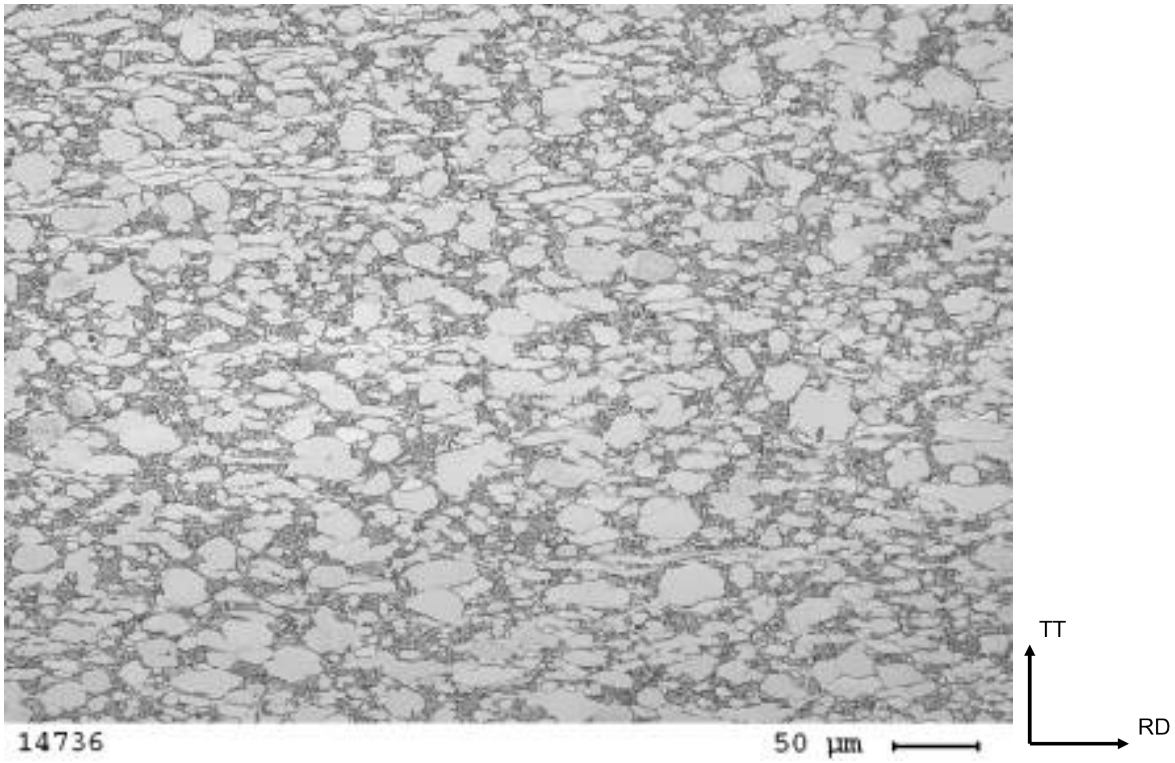


Figure 4.8 - Optical micrograph: Plate 4 – Longitudinal/Through-Thickness

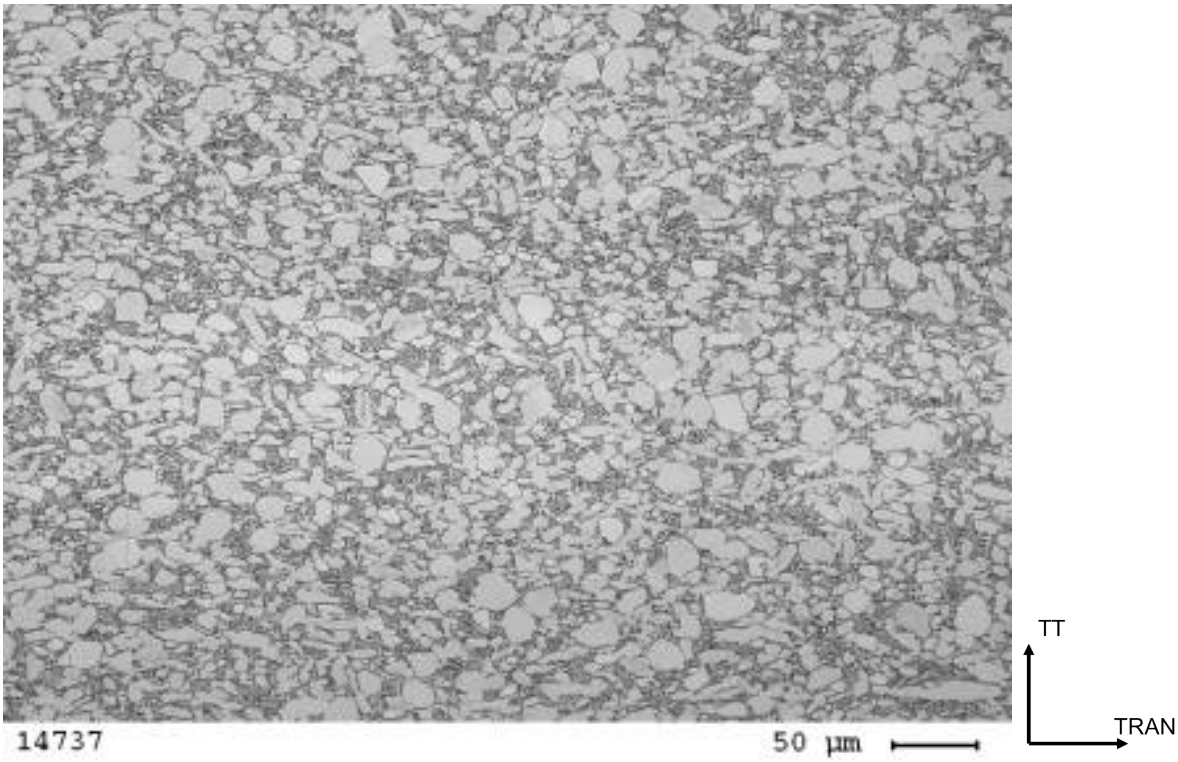


Figure 4.9 - Optical micrograph: Plate 4 – Transverse/Through-Thickness

4.5 Micro-Texture

Due to the limited number of slip systems available in the *hcp* unit cell of α phase Titanium, it is vital that the micro-texture of Ti-6Al-4V is characterised to better understand the role it plays in defining mechanical behaviour. Key to understanding the effects of micro-texture on the mechanics of deformation are the interactions between so called "soft" grains/laths and "hard" grains/laths, in other words, grains/laths preferentially orientated for slip and grains/laths that are poorly orientated for slip, relative to the direction of loading.

In this section, the results from electron backscatter diffraction (EBSD) studies on all four development level Ti-6Al-4V plates will be presented with comparisons made between the different plates and relevant observations made. All EBSD analyses were carried out as described in Chapter 3. Scans were carried out on the longitudinal\through-thickness planes of all four plates over two areas; 500x500μm with a step size of 2μm and 100x100μm with a step size of 0.5μm. Inverse pole figure (IPF) maps were plotted for each of the plates, with a standard 15° misorientation criterion used to define the grain boundaries.

IPF maps of the EBSD results for Plate 1 are shown in Figure 4.10 and Figure 4.11. From Figure 4.10 it can be seen that the orientation of the *hcp* α phase in Plate 1 is relatively well distributed. However, in the area scanned there are clearly visible zones of preferred crystallographic orientation. The well-distributed α phase orientations of Plate 1 indicate that it has undergone a significant amount of thermo-mechanical work along both the longitudinal and transverse directions, as was concluded from analysis of the optical micrographs from this plate. A small number of spheroidised primary α grains can be seen, once again in agreement with the optical microscopy. However, the micro-texture and microstructure are dominated by α colony structures.

IPF maps of the EBSD results for Plate 2 are shown in Figure 4.12 and Figure 4.13. From Figure 4.13 it can be seen that Plate 2, like Plate 1, also exhibits an α colony-based microstructure. In Figure 4.12, it can be seen that Plate 2 has significant preferred crystallographic orientation at the microscopic level, consisting of zones of α grains/laths with preferred crystallographic orientation and large elongated α grains. A larger volume of spheroidised primary α is also clearly visible, when compared with Plate 1.

IPF maps of the EBSD results for Plate 3 are shown in Figure 4.14 and Figure 4.15. Due to a well-developed microstructure, Plate 3 consists of a large volume fraction of α grains/laths in a matrix of β, with significant macro-zones of α grains/laths of non-random orientation seen in both Figure 4.14 and Figure 4.15. In Figure 4.15 it can clearly be seen that the level of micro-texturing is such that in some areas the misorientation criteria for defining a grain/lath boundary does not select individual grains/laths but instead selects large groups of grains/laths with the same orientation.

IPF maps of the EBSD results for Plate 4 are shown in Figure 4.16 and Figure 4.17. Once again, due to the well-developed microstructure of α grains/laths, we see very different results to that seen in Plates 1 and 2. In Figure 4.16, significant macro-zones of preferred crystallographic orientation can be seen. However, unlike Plate 3, there are large primary α grains dispersed through out the microstructure. Inspection of the crystallographic orientation of the grains shows that the large primary α grains are poorly orientated for slip in the direction of reduction during rolling, the through-thickness direction. This is further highlighted in Figure 4.17, where is can be seen that grains and macro-zones preferentially orientated for slip in the direction of reduction have deformed around the “hard” orientated large primary α grains, which appear to have acted like hard precipitates in a deforming matrix during the rolling stage of thermo-mechanical processing.

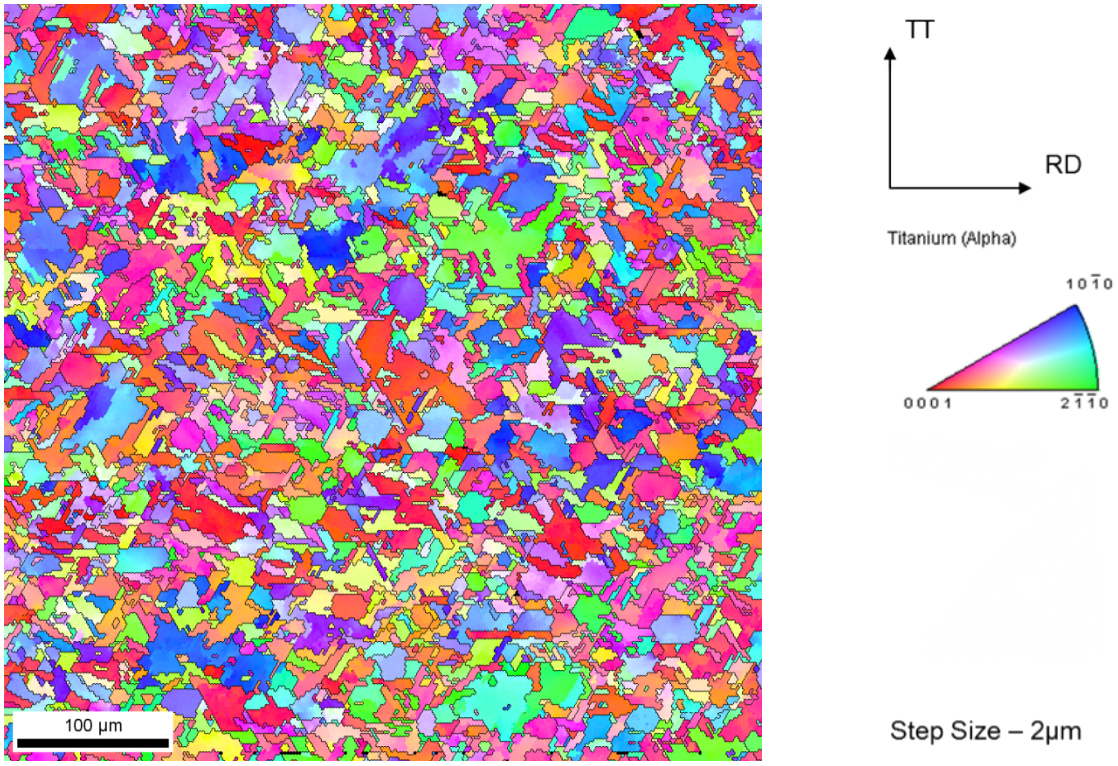


Figure 4.10 - Inverse Pole Figure Map (500x500µm): Plate 1 – Longitudinal/Through-Thickness

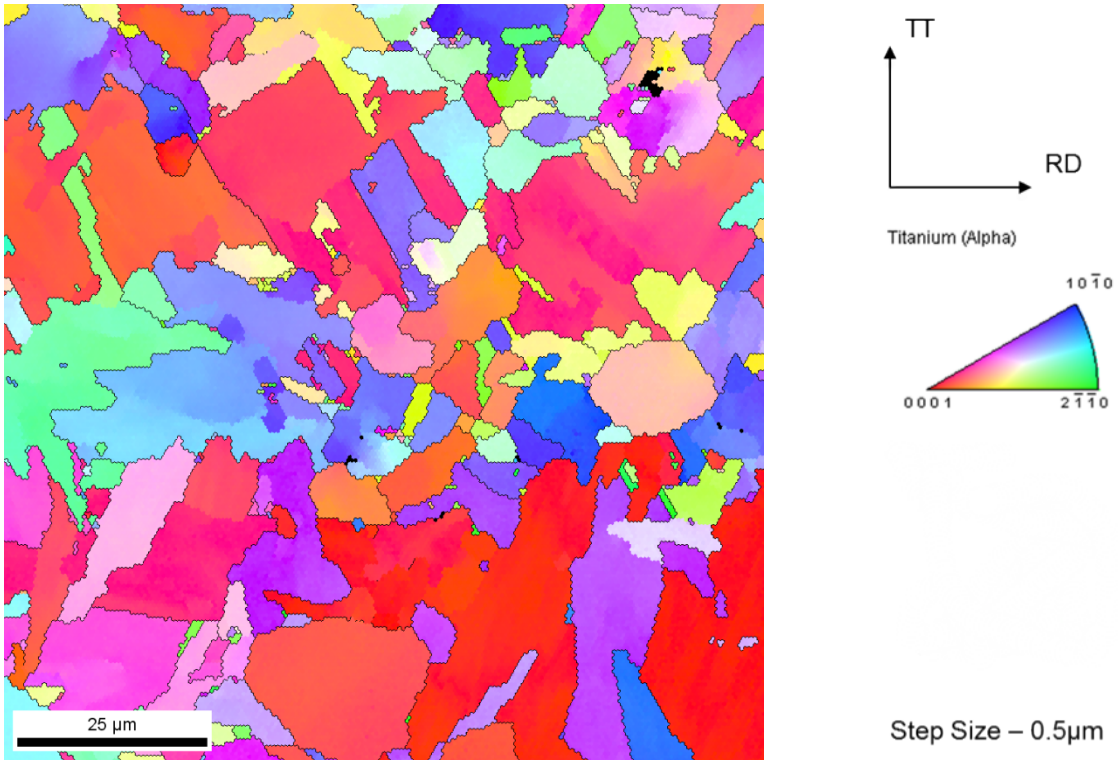


Figure 4.11 - Inverse Pole Figure Map (100x100µm): Plate 1 – Longitudinal/Through-Thickness

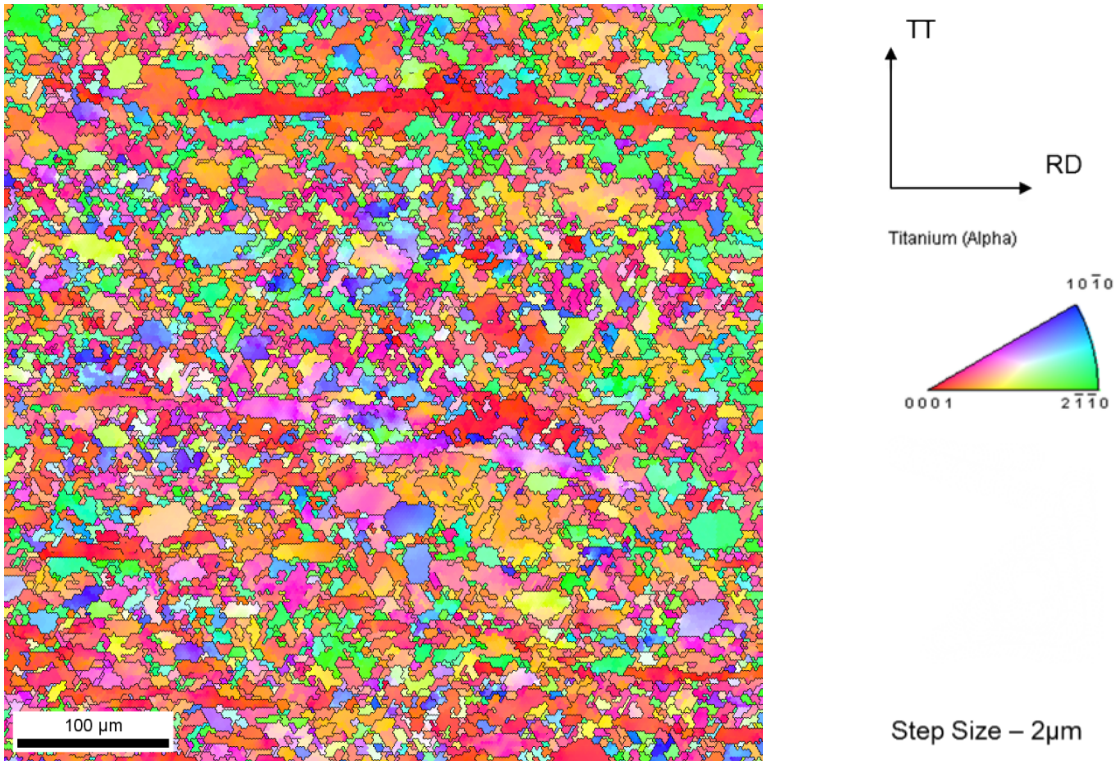


Figure 4.12 - Inverse Pole Figure Map (500x500µm): Plate 2 – Longitudinal/Through-Thickness

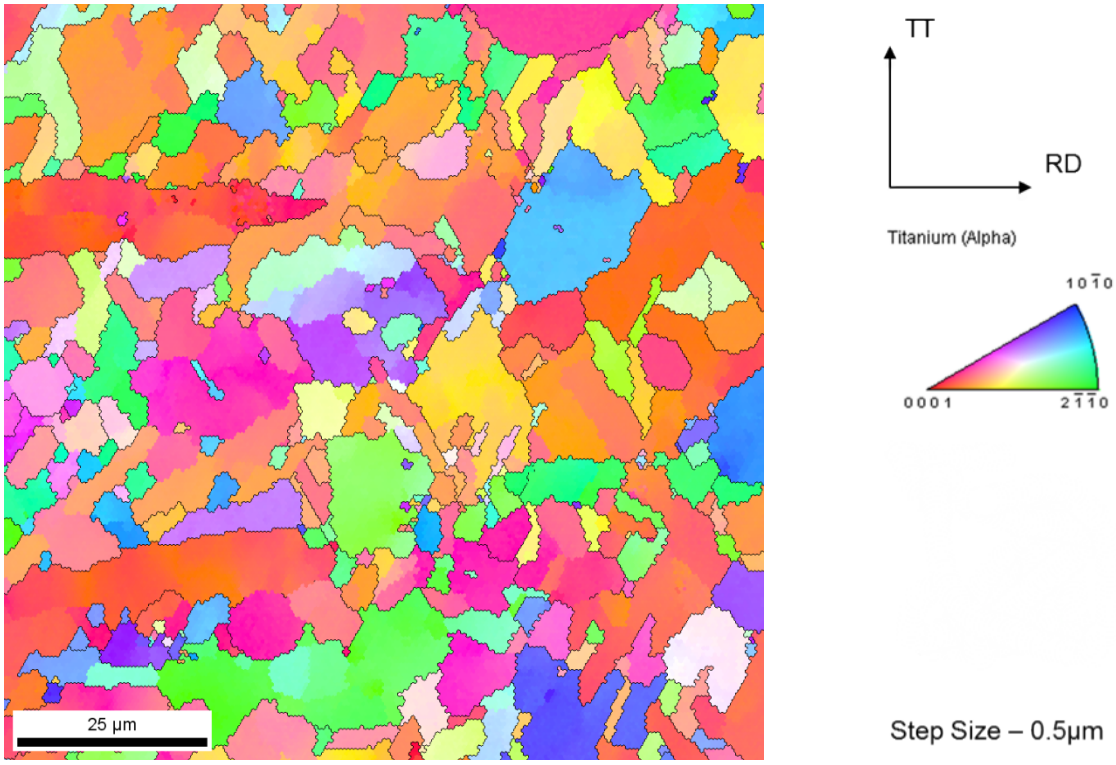


Figure 4.13 - Inverse Pole Figure Map (100x100µm): Plate 2 – Longitudinal/Through-Thickness

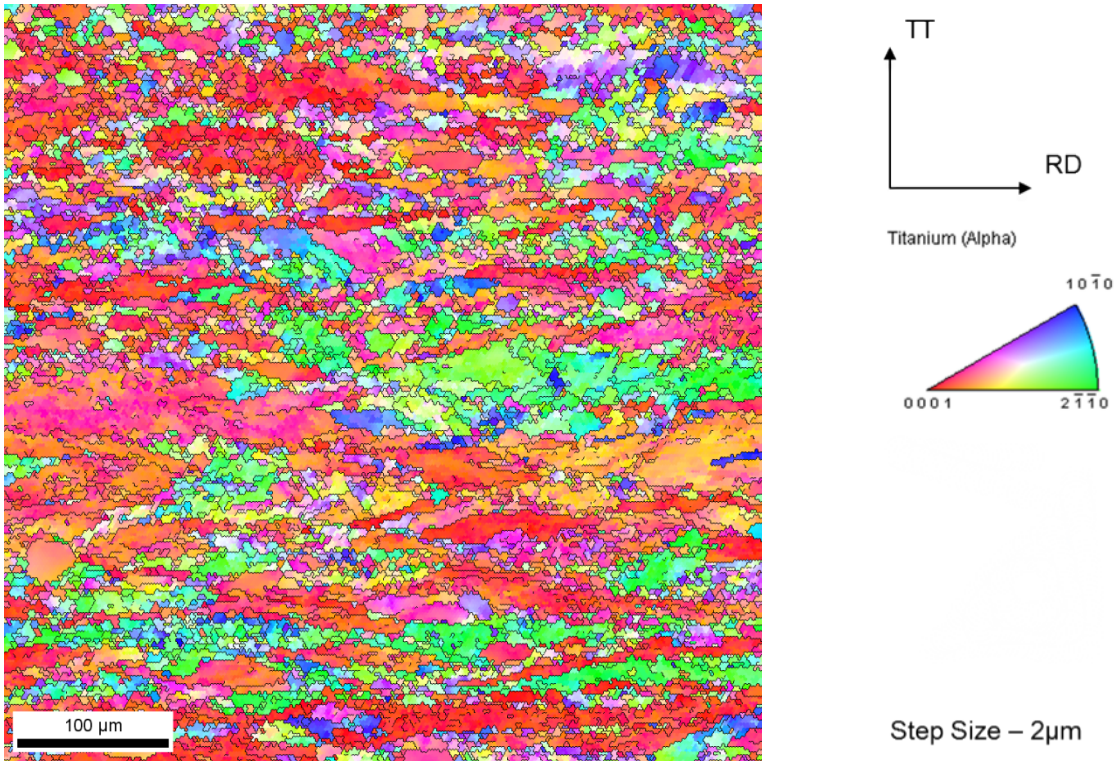


Figure 4.14 - Inverse Pole Figure Map (500x500µm): Plate 3 – Longitudinal/Through-Thickness

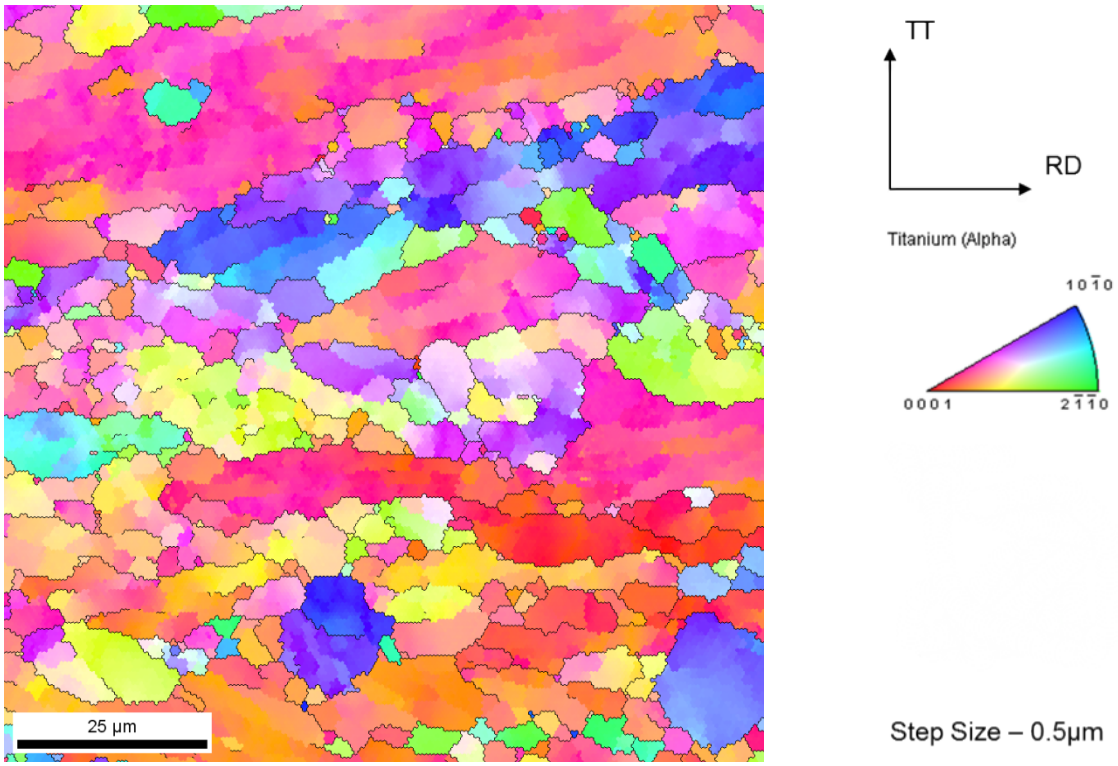


Figure 4.15 - Inverse Pole Figure Map (100x100µm): Plate 3 – Longitudinal/Through-Thickness

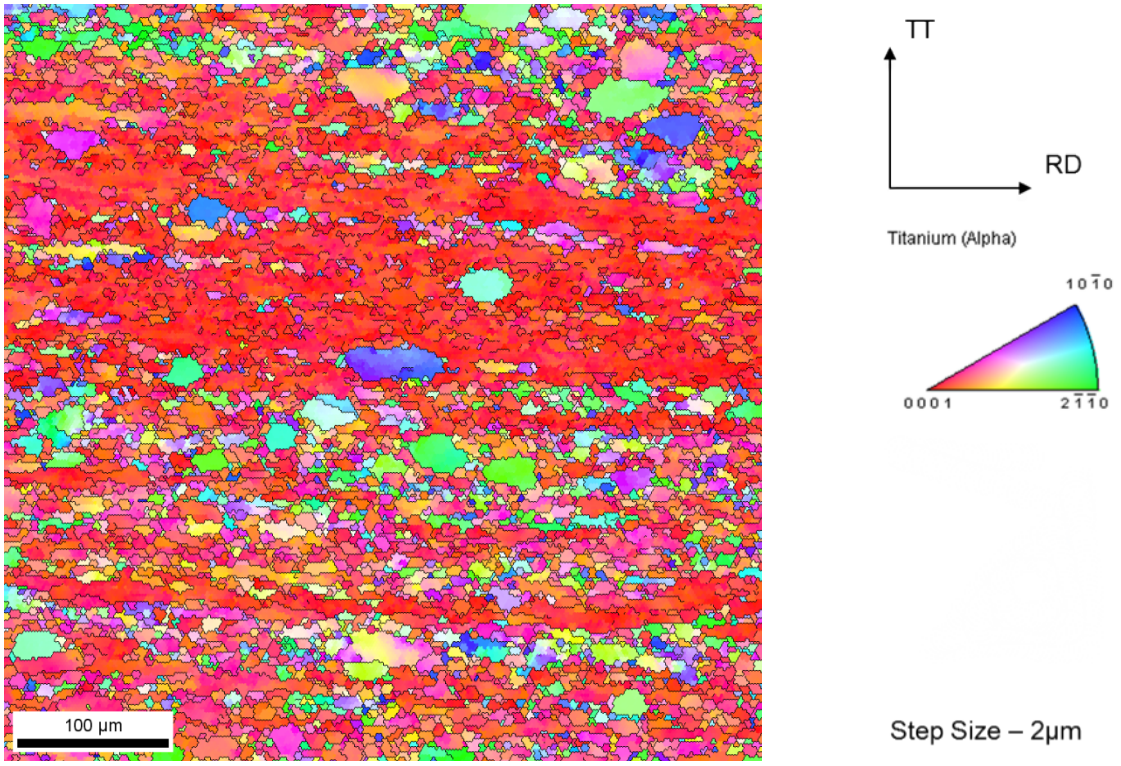


Figure 4.16 - Inverse Pole Figure Map (500x500µm): Plate 4 – Longitudinal/Through-Thickness

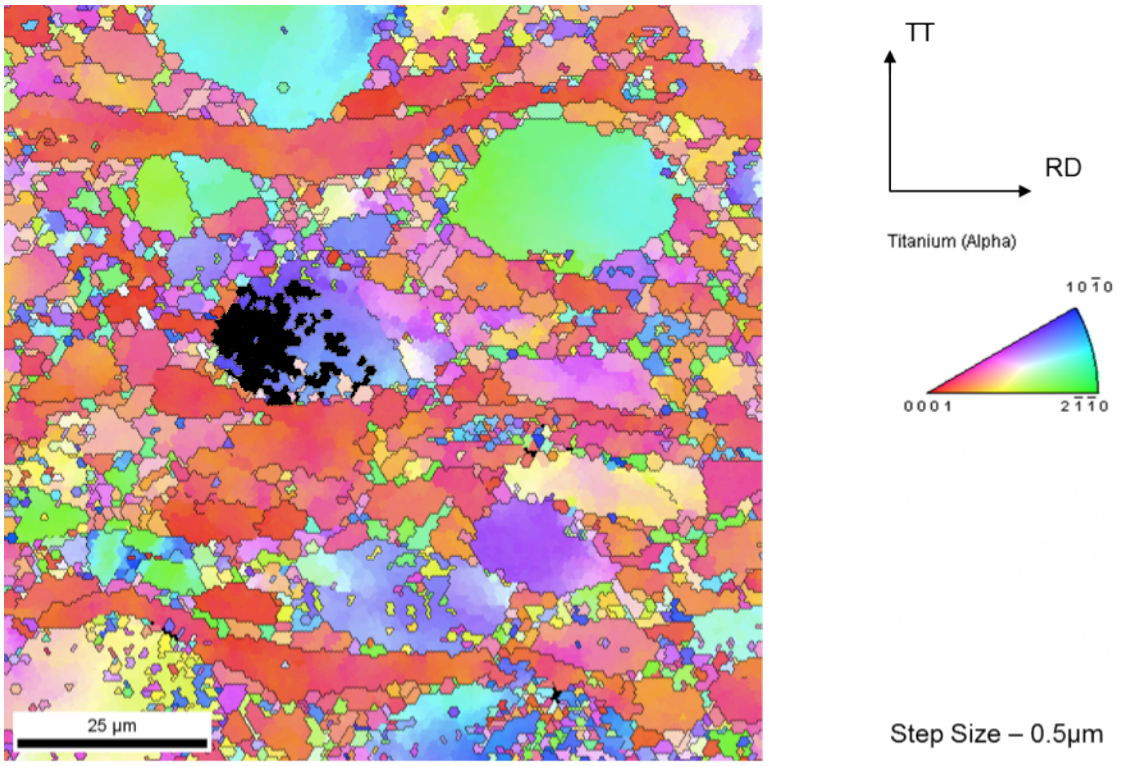


Figure 4.17 - Inverse Pole Figure Map (100x100µm): Plate 4 – Longitudinal/Through-Thickness

4.6 Macro-Texture

The previous section highlighted the variation in the micro-texture of the four development level Ti-6Al-4V plates. In this section, the crystallographic orientations will be "averaged" over a large area to understand the macroscopic nature of preferred crystallographic orientation, commonly known as macro-texture. The macro-textures of the four Ti-6Al-4V development plates were measured by carrying out EBSD over a large area, typically 2 mm x 2 mm, with a step size of 10 μm. As is customary when studying macro-texture, the "averaged" crystallographic orientations of the Ti-6Al-4V plates will be represented by a contoured pole figure (PF) plot, as described in Chapter 2. When representing the orientation of the *hcp* α phase, two planes need to be projected onto PFs to fully resolve the "averaged" crystallographic orientation, typically the (0001) and another non-basal plane are used [6].

The (0001) and $\{10\bar{1}0\}$ PFs for Plates 1, 2, 3, and 4 are shown in Figure 4.18. From these PFs it can be seen that all four plates are significantly macro-textured. All four plates have a strong basal/transverse texture, i.e. for the majority of grains, the normal of the (0001) plane is pointing in the transverse material direction.

Plate 1 has a slightly more distributed texture compared with the other three plates, with some of the normals of the (0001) plane pointing in the longitudinal and through thickness directions. The orientation of the $\{10\bar{1}0\}$ planes around the normal to the (0001) is relatively smeared.

Plates, 2, 3 and 4 all have very similar macro-texture, with the normal to the (0001) pointing predominately in the transverse direction but with some smearing in the through-thickness direction. In all three plates the *hcp* unit cell also exhibits macro-texturing around the *c*-axis, as is seen in the $\{10\bar{1}0\}$ PFs.

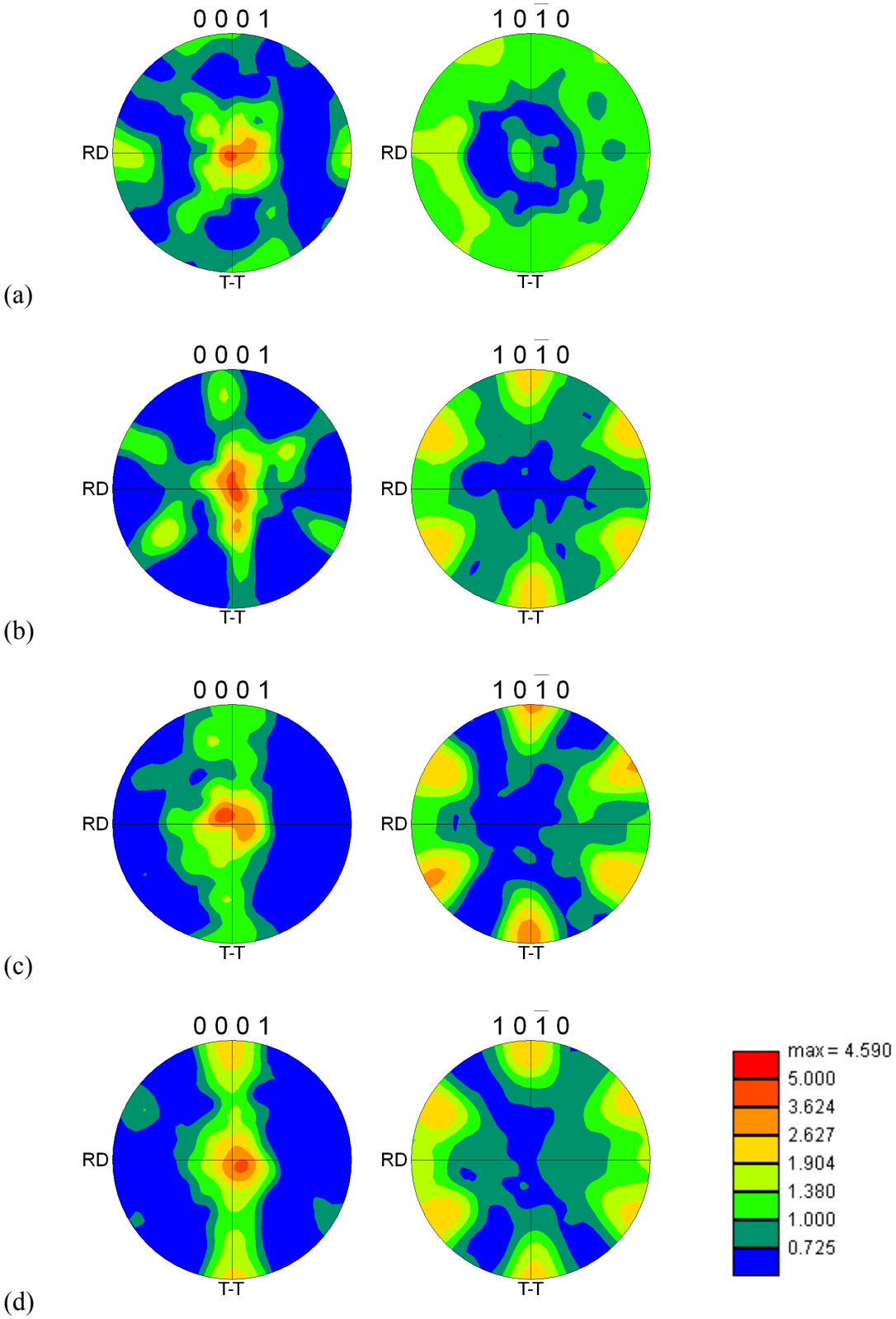


Figure 4.18 - Pole Figures: (a) Plate 1, (b) Plate 2, (c) Plate 3 and (d) Plate 4

4.7 Microstructural Parameters

Due to the complex bimodal (duplex) microstructures seen in all four development level Ti-6Al-4V plates under investigation, it is not possible to give a clear grain size distribution plot as would be done for most single phase and many dual phase metals. For example, due to the lath and macro-zone dominated structure of Plates 1, 2, 3 and 4, it is not appropriate to use grain size as a structural parameter. Instead, the structural parameter of importance is the α colony size, or macro-zone size, and potentially the lath spacing in the case of martensitic type microstructures [1]. For example, consider the case of neighbouring laths with the same crystallographic orientation forming part of an α colony, dislocations can easily cross the boundaries between these neighbouring laths, making lath spacing or thickness a poor microstructural parameter to compare between microstructures, unless it is linked with the micro-texture.

Defining quantitative measures for the microstructures studied is complicated even further when the interspersed nucleated primary α grains seen in all four plates are considered. As is seen in the four development plates, colonies or macro-zones of α grains and laths with the same crystallographic orientation are interspersed with primary α grains, typically with different crystallographic orientations, meaning that defining grain boundaries in this case may also be of limited use, due to the fact that dislocations can easily transfer across the boundaries between grains/laths in the macro-zone but not boundaries between the primary α grains and macro-zone α grains.

As a result of this complexity and the difficulty of comparing widely varying microstructures with interlinked microstructural features in a meaningful way, much of the analysis will be kept to a qualitative level, with a quantitative analysis of Plate 1 being carried out in Chapter 7 to obtain microstructural parameters for use in a material modelling framework.

4.8 Conclusions

The microstructures of the four development level Ti-6Al-4V plates under investigation have been characterised using a range of techniques, including chemical compositional analysis, optical microscopy and EBSD.

It has been shown that all four plates have complex bimodal microstructures consisting of colonies, or macro-zones, of α/β laths and α grains interspersed with nucleated primary α grains. Varying levels of primary α grain nucleation are seen between the plates as well as a range of grain sizes and shapes. All four plates have significant crystallographic texturing at the macroscopic and microscopic levels.

The difficulty of analysing and comparing the widely varying microstructures of the four development plates was discussed. As a result, analysis and comparison of the four plates was kept to qualitative level. A quantitative analysis of Plate 1 will be carried out in Chapter 7 to obtain microstructural parameters for use in a material modelling framework.

5 UNIAXIAL MECHANICAL CHARACTERISATION OF Ti-6Al-4V

5.1 Overview

This chapter will present results from uniaxial mechanical characterisation experiments carried out on the four development level Ti-6Al-4V plates using experimental techniques capable of accessing a range of strain rates. Uniaxial testing was carried out in the three orthogonal material orientations in compression and the two in-plane orthogonal material orientations in tension, at quasi-static (10^{-3} s^{-1}) and high strain rates (10^{3} s^{-1}).

The results from these experiments will then be analysed using a ratio method to gain qualitative and quantitative understanding of the effects of strain rate, material orientation and direction of loading on the mechanical behaviour of Ti-6Al-4V.

The effects of strain rate and material orientation on failure mechanisms in Ti-6Al-4V will then be analysed by studying the orientation and topography of fracture surfaces using a scanning electron microscope (SEM).

5.2 Specimen Preparation

Specimens were cut from the four Ti-6Al-4V plates in the three orthogonal material orientations for compression and two in-plane orthogonal material orientations for tension, as shown in Figure 5.1. Specimens were manufactured to the geometries defined in Chapter 3.

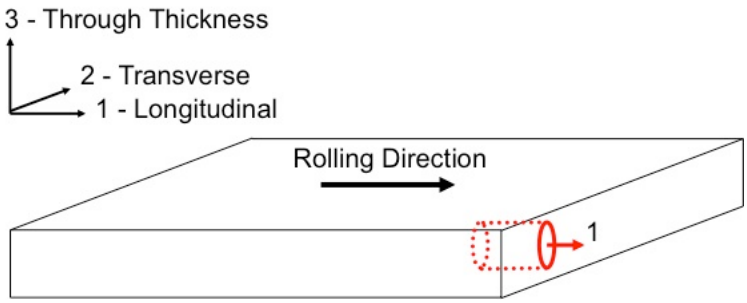


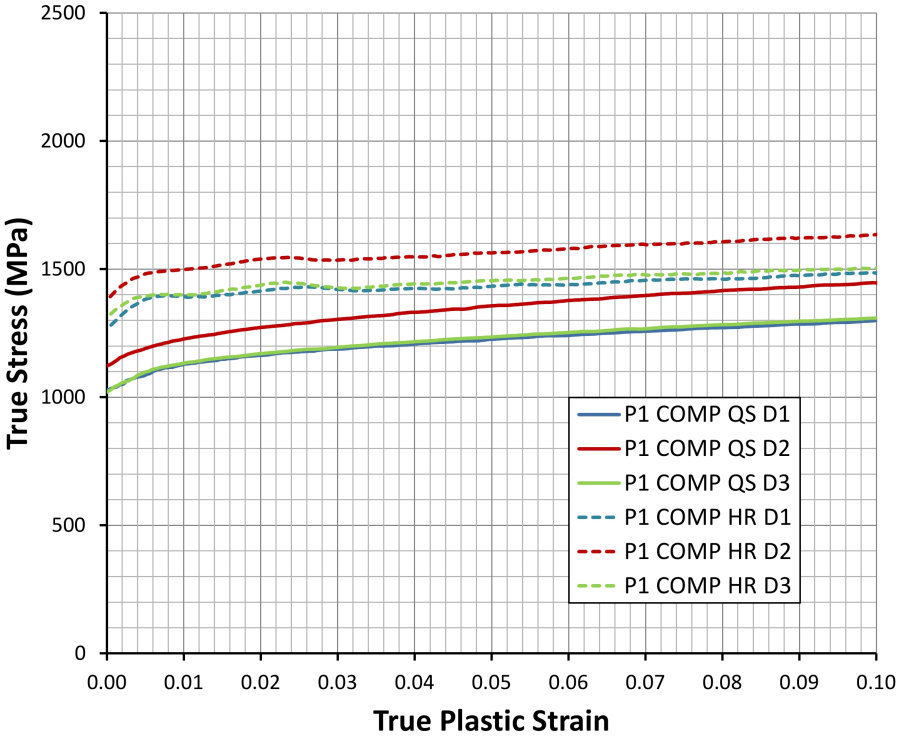
Figure 5.1 - Uniaxial mechanical testing specimen orientations relative to plate

5.3 Quasi-Static and High Strain Rate Testing Results

Mechanical testing was carried out at quasi-static and high strain rates using the experimental procedures described in Chapter 3. For quasi-static testing, an electro-mechanical test device was used to achieve strain rates of 10^{-3} s^{-1} in both tension and compression, whereas, for high strain rate testing, compressive and tensile split-Hopkinson pressure bars (SHPB) were used to achieve strain rates of ~10^{3} s^{-1}. Three specimens were tested for each experimental condition.

Representative data from the mechanical characterisation results for Plates 1, 2, 3 and 4 are presented in Figure 5.2, Figure 5.3, Figure 5.4 and Figure 5.5, respectively. Characterisation results are presented in the form of true stress vs true plastic strain plots. Each plate material was characterised in compression in the longitudinal (D1), transverse (D2) and through thickness (D3) material orientations at quasi-static (QS) and high strain rates (HR), as defined in the previous section. Due to the limit of the as received plate thicknesses, it was not possible to cut tensile test specimens from the through thickness direction. As a result, each plate material was characterised in tension in the longitudinal (D1) and transverse (D2) material orientations at quasi-static (QS) and high strain rates (HR).

(a)



(b)

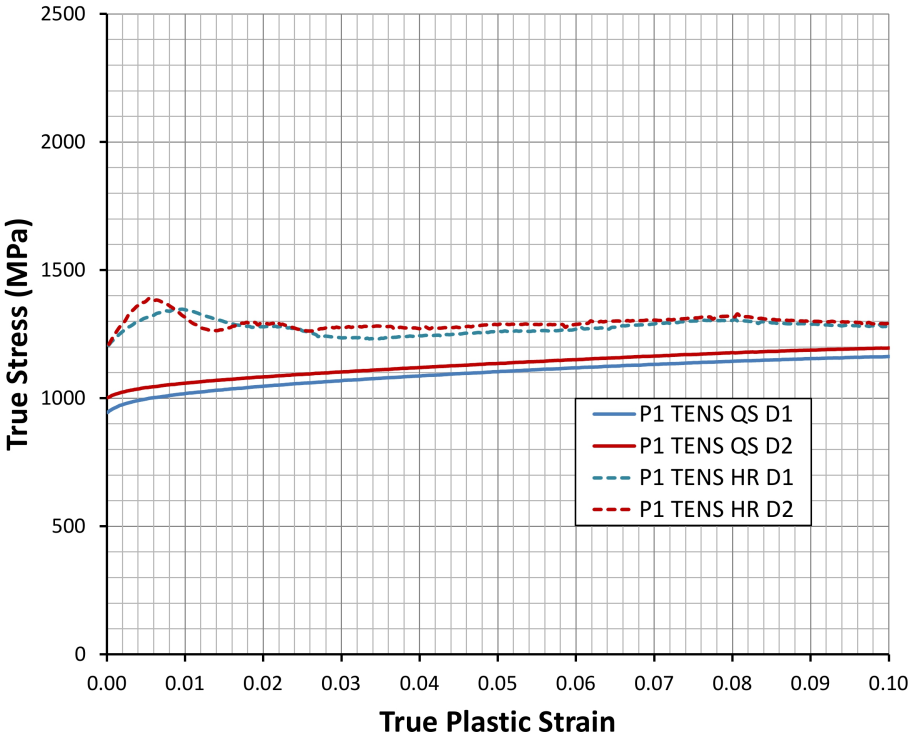
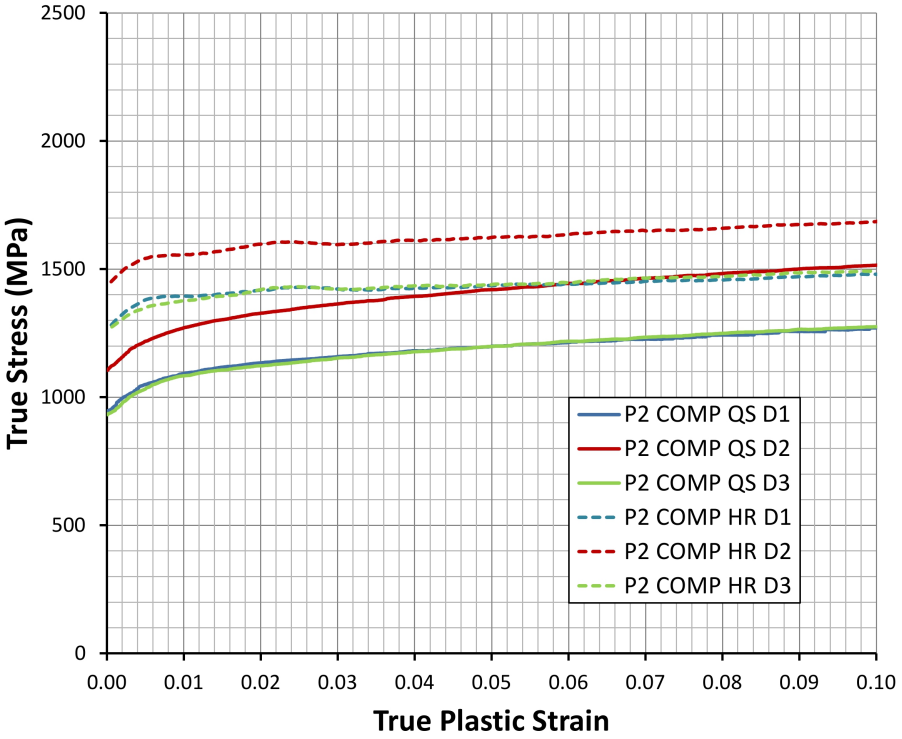


Figure 5.2 - Plate 1 - Mechanical characterisation results in (a) compression and (b) tension

(a)



(b)

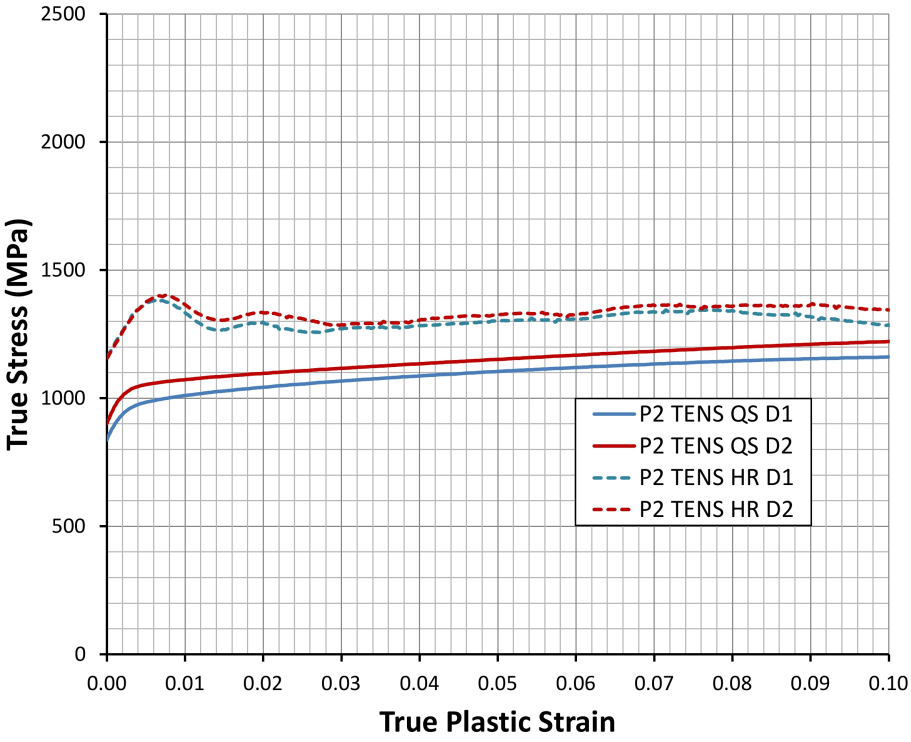
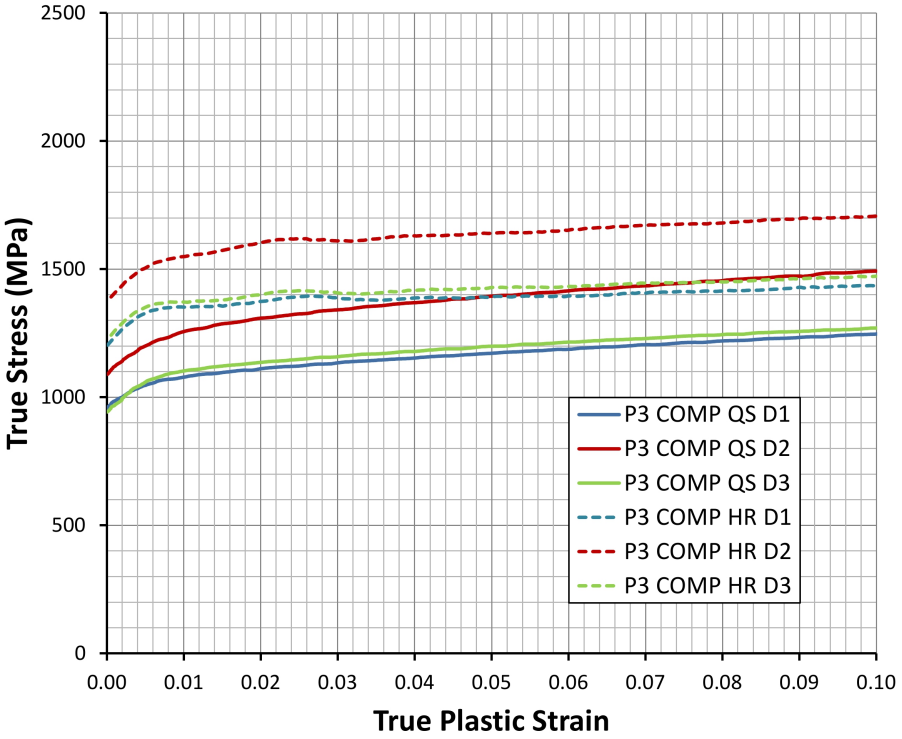


Figure 5.3 - Plate 2 - Mechanical characterisation results in (a) compression and (b) tension

(a)



(b)

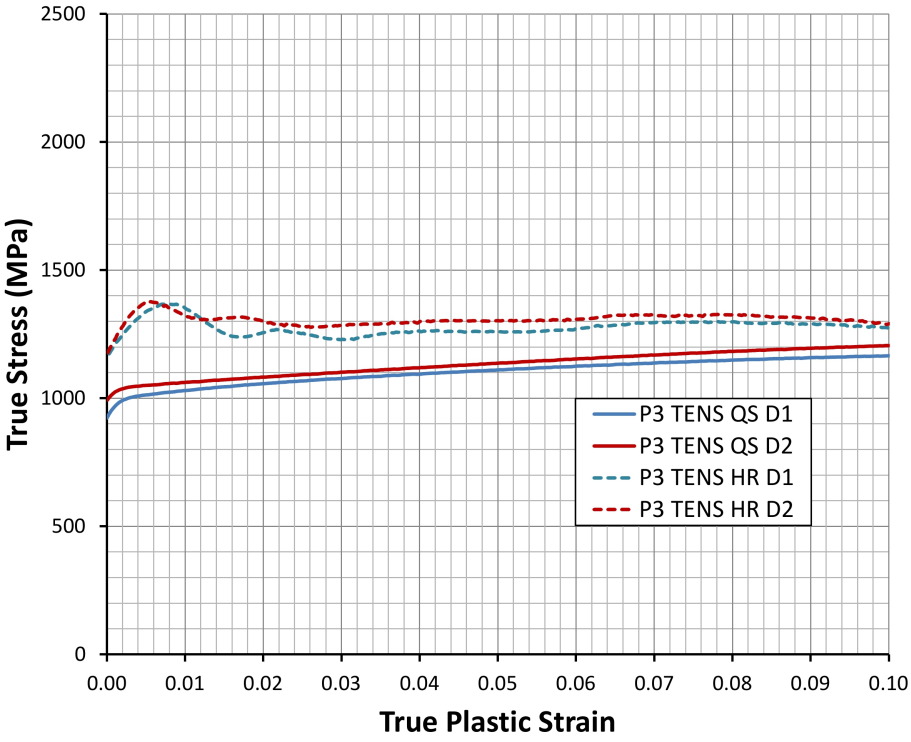
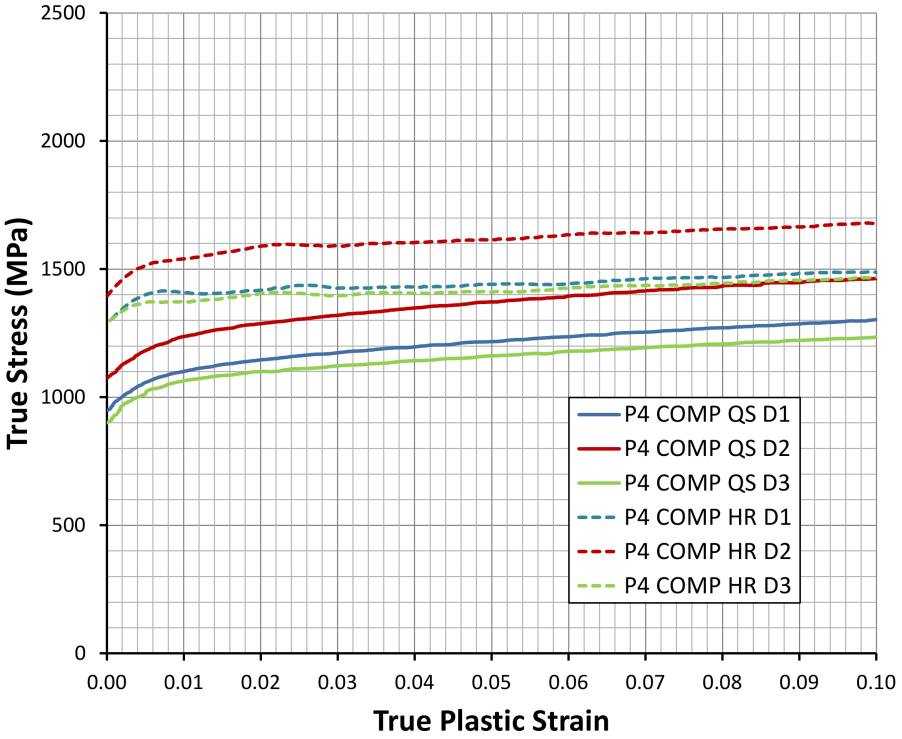


Figure 5.4 - Plate 3 - Mechanical characterisation results in (a) compression and (b) tension

(a)



(b)

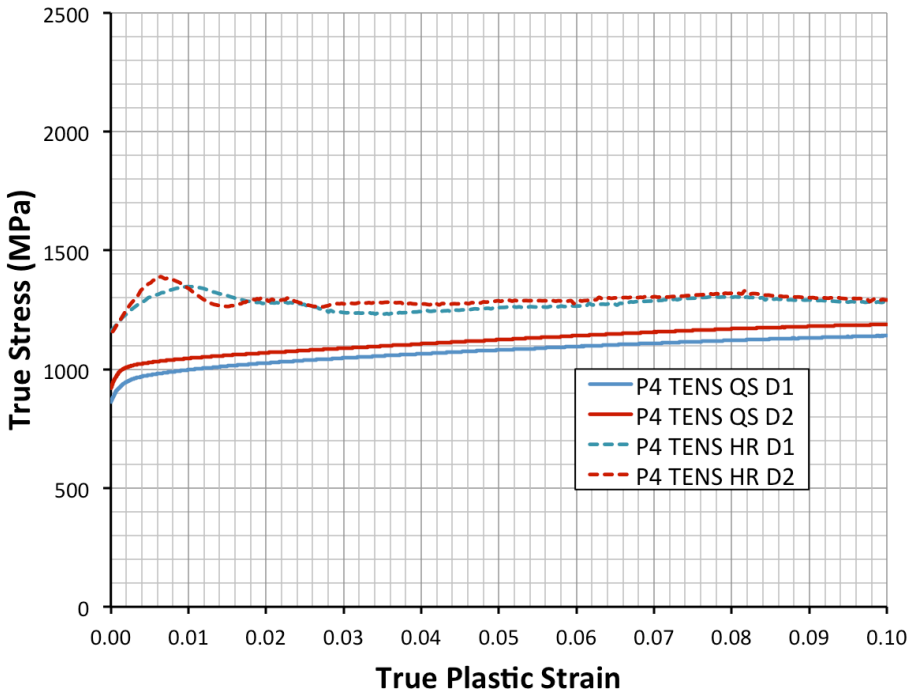


Figure 5.5 - Plate 4 - Mechanical characterisation results in (a) compression and (b) tension

5.4 Comparison of Flow Stress Data

To determine the relative mechanical behaviour of metals, it is useful to compare well-defined points of a material's behaviour, such as the yield stress. Due to the gradual yielding observed in Ti-6Al-4V, it is more appropriate to use a "proof stress" at a given value of strain. The most commonly used value is 0.1% true strain. However, because of the need to ensure that equilibrium has been reached in high strain rate experiments, the following comparisons will use a proof stress taken at 5% true plastic strain. As this stress is clearly post-yield, it is more accurately described as the true flow stress at 5% true plastic strain and from now on will simply be referred to as the flow stress.

Flow stresses from the mechanical characterisation results for Plates 1, 2, 3 and 4 are presented in Table 5.1, Table 5.2, Table 5.3 and Table 5.4, respectively. The errors in the flow stresses were taken to be the maximum deviation from the flow stress of the representative specimen. For each plate the flow stress is given for compression in the longitudinal (D1), transverse (D2) and through thickness (D3) material orientations at quasi-static and high strain rates. Further, representative flow stresses are given for tension in the longitudinal (D1) and transverse (D2) material orientations at quasi-static and high strain rates.

	Quasi-Static					
	Tension			Compression		
	D1	D2	D3	D1	D2	D3
Flow Stress (MPa)	1080 ± 7	1124 ± 8	N/A	1217 ± 6	1372 ± 5	1162 ± 6

	High Strain Rate					
	Tension			Compression		
	D1	D2	D3	D1	D2	D3
Flow Stress (MPa)	1260 ± 10	1286 ± 11	N/A	1441 ± 8	1618 ± 7	1411 ± 10

Table 5.1 - Plate 1 - True flow stress at 5% true plastic strain

	Quasi-Static					
	Tension			Compression		
	D1	D2	D3	D1	D2	D3
Flow Stress (MPa)	1104 ± 8	1152 ± 7	N/A	1198 ± 4	1420 ± 5	1199 ± 9

	High Strain Rate					
	Tension			Compression		
	D1	D2	D3	D1	D2	D3
Flow Stress (MPa)	1302 ± 8	1325 ± 10	N/A	1436 ± 7	1608 ± 9	1441 ± 6

Table 5.2 - Plate 2 - True flow stress at 5% true plastic strain

	Quasi-Static					
	Tension			Compression		
	D1	D2	D3	D1	D2	D3
Flow Stress (MPa)	1111 ± 6	1137 ± 9	N/A	1172 ± 5	1395 ± 4	1199 ± 6

	High Strain Rate					
	Tension			Compression		
	D1	D2	D3	D1	D2	D3
Flow Stress (MPa)	1260 ± 10	1303 ± 12	N/A	1393 ± 5	1641 ± 7	1429 ± 8

Table 5.3 - Plate 3 - True flow stress at 5% true plastic strain

	Quasi-Static					
	Tension			Compression		
	D1	D2	D3	D1	D2	D3
Flow Stress (MPa)	1068 ± 5	1112 ± 7	N/A	1180 ± 7	1311 ± 5	1123 ± 5

	High Strain Rate					
	Tension			Compression		
	D1	D2	D3	D1	D2	D3
Flow Stress (MPa)	1236 ± 11	1277 ± 8	N/A	1429 ± 7	1596 ± 8	1406 ± 7

Table 5.4 - Plate 4 - True flow stress at 5% true plastic strain

5.5 Ratio-Based Analysis of Flow Stress Data

Using a ratio-based analysis, much like the so-called Lankford Coefficients [7], the effects of material orientation, strain rate and direction of loading on the deformation behaviour of Ti-6Al-4V will be quantified. As in the previous section, the true flow stress at 5% true plastic strain will be used for all comparisons.

5.5.1 Material Orientation Dependence of the Flow Stress

A comparison can be made between the flow stress of specimens loaded in the different material orientations by taking the ratio of the representative flow stress in the longitudinal (D1), σ_1, and transverse (D2), σ_2, material orientations:

$$X = \frac{\sigma_2}{\sigma_1} \tag{5.1}$$

Table 5.5, Figure 5.6 and Figure 5.7 present the material orientation flow stress ratios for the 4 development Ti-6Al-4V plates in tension/compression at quasi-static and high strain rates.

		Tension		Compression	
		QS	HR	QS	HR
D2/D1 Ratio	P1	1.04	1.02	1.12	1.12
	P2	1.04	1.02	1.19	1.12
	P3	1.02	1.03	1.19	1.18
	P4	1.04	1.03	1.11	1.12

Table 5.5 - Material orientation ratios in tension and compression at quasi-static and high strain rates

From the data presented in Table 5.5 and Figure 5.6, it can be seen that for all 4 plates undergoing tensile loading, at both quasi-static and high strain rates, $\sigma_2 > \sigma_1$ by approximately 2-4%. However, Table 5.5 and Figure 5.7 show that when undergoing compressive loading, at both quasi-static and high strain rates, $\sigma_2 > \sigma_1$ by approximately 12-19%.

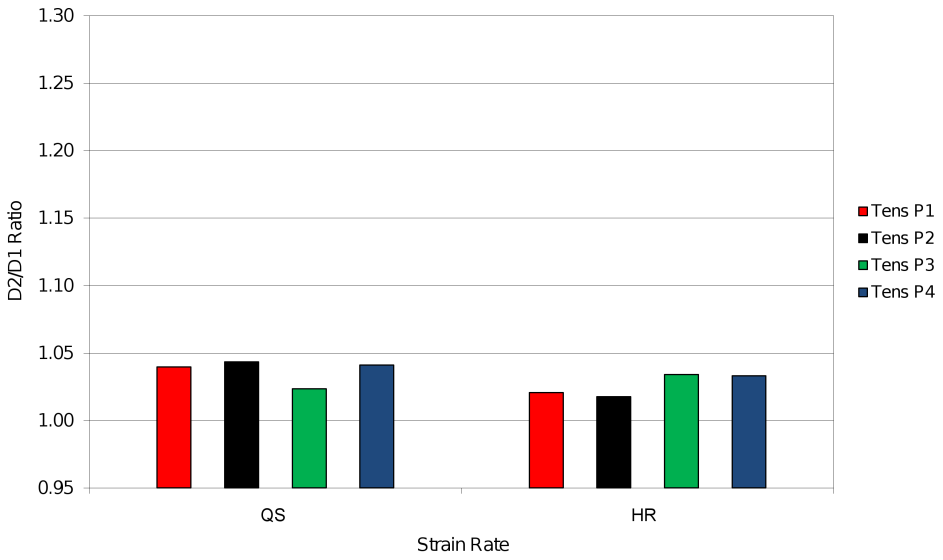


Figure 5.6 - Chart of material orientation ratios in tension at quasi-static and high strain rates

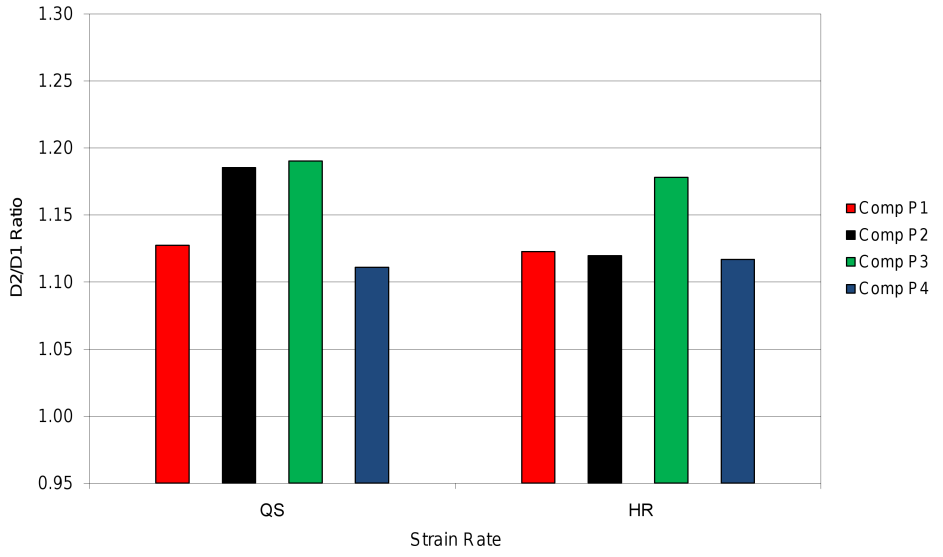


Figure 5.7 - Chart of material orientation ratios in compression at quasi-static and high strain rates

5.5.2 Strain Rate Dependence of the Flow Stress

A comparison can be made between the flow stress of specimens loaded at different strain rates, in both tension and compression, by taking the ratio of the representative flow stress at quasi-static strain rates, σ_{QS}, and high strain rates, σ_{HR}:

$$Y = \frac{\sigma_{HR}}{\sigma_{QS}} \tag{5.2}$$

Table 5.6, Figure 5.8 and Figure 5.9 present the strain rate dependent flow stress ratios for the 4 plates in tension/compression for the longitudinal (D1) and transverse (D2) material orientations.

		Tension			Compression		
		D1	**D2**	**D3**	**D1**	**D2**	**D3**
HR/QS Ratio	**P1**	1.17	1.14	N/A	1.18	1.18	1.21
	P2	1.18	1.15	N/A	1.20	1.13	1.20
	P3	1.13	1.15	N/A	1.19	1.18	1.19
	P4	1.16	1.15	N/A	1.21	1.22	1.25

Table 5.6 - Strain rate ratios in tension and compression in material orientation 1, 2 and 3

Table 5.6 and Figure 5.8 show that for all 4 plates undergoing tensile loading in the longitudinal (D1) material orientation, $\sigma_{HR} > \sigma_{QS}$ by approximately 13-18%. However, for tensile loading in the transverse (D2) material orientation, less variation is seen between the plates, with $\sigma_{HR} > \sigma_{QS}$ by approximately 14-15%.

Likewise, Table 5.6 and Figure 5.8 show that for all 4 plates undergoing compressive loading in the longitudinal (D1), transverse (D2) and through thickness material (D3) orientation, $\sigma_{HR} > \sigma_{QS}$ by approximately 18-25%.

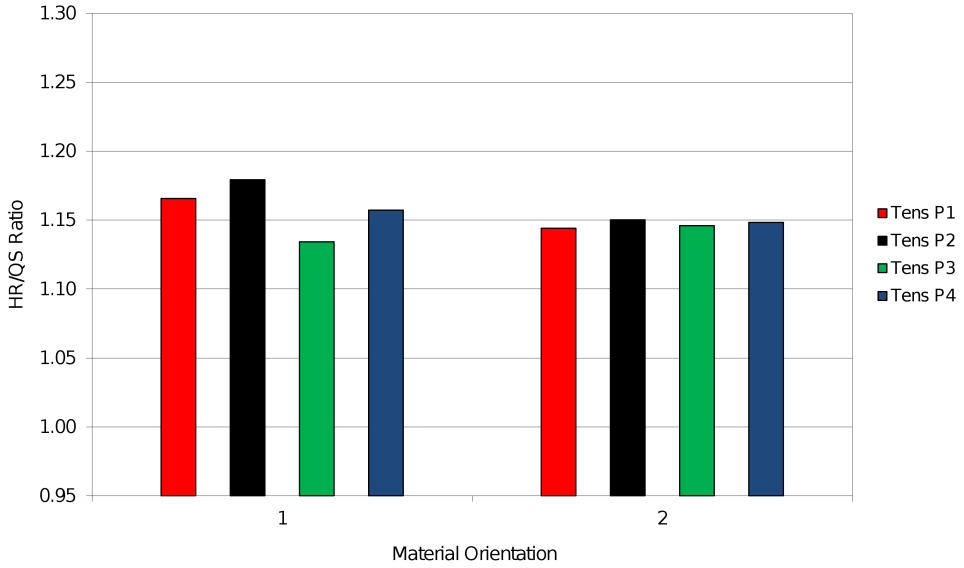


Figure 5.8 - Chart of strain rate ratios in tension in material orientations 1 and 2

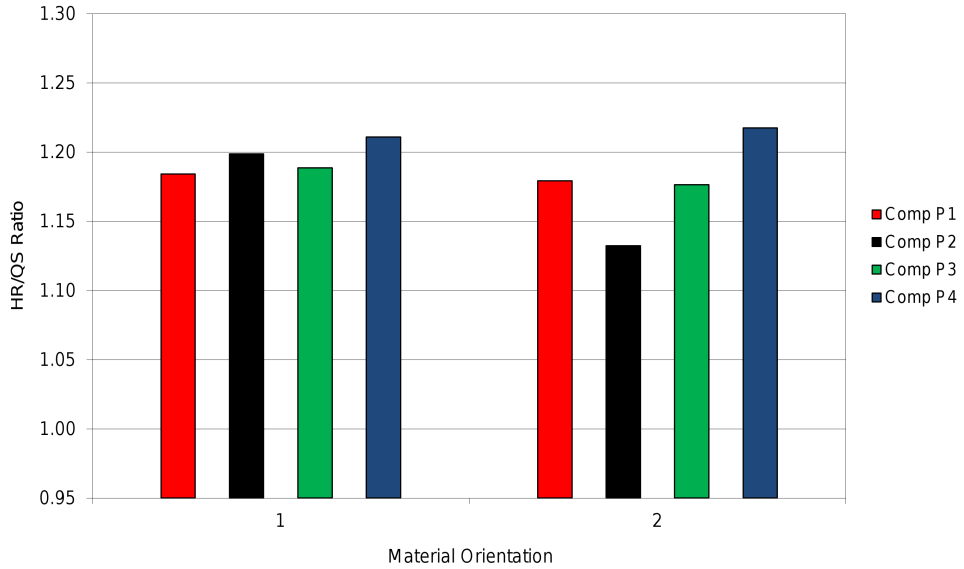


Figure 5.9 - Chart of strain rate ratios in compression in material orientations 1 and 2

5.5.3 Compression/Tension Asymmetry of the Flow Stress

A comparison can be made between the flow stress of specimens loaded in compression and tension at different strain rates by taking the ratio of the representative flow stress in compression, σ_C, and tension, σ_T:

$$Z = \frac{\sigma_C}{\sigma_T} \tag{5.3}$$

Table 5.7, Figure 5.10 and Figure 5.11 present the direction of loading dependent flow stress ratio for the 4 plates in compression/tension for the longitudinal (D1) and transverse (D2) material orientations at quasi-static and high strain rates.

		Quasi-Static Strain Rate			High Strain Rate		
		D1	D2	D3	D1	D2	D3
Comp/Tens Ratio	P1	1.13	1.22	N/A	1.14	1.26	N/A
	P2	1.09	1.23	N/A	1.10	1.21	N/A
	P3	1.06	1.23	N/A	1.11	1.26	N/A
	P4	1.11	1.18	N/A	1.16	1.25	N/A

Table 5.7 – Comp/tens ratios at quasi-static and high strain rates in material orientations 1 and 2

The data presented in Table 5.7 and Figure 5.10 show that for all 4 plates loaded at quasi-static strain rates, in the longitudinal (D1) material orientation, $\sigma_C > \sigma_T$ by approximately 6-13%, whereas in the transverse (D2) material orientation, $\sigma_C > \sigma_T$ by approximately 18-22%.

Likewise, Table 5.7 and Figure 5.11 show that for all 4 plates loaded at high strain rates, in the longitudinal (D1) material orientation, $\sigma_C > \sigma_T$ by approximately 11-16%, whereas in the transverse (D2) material orientation, $\sigma_C > \sigma_T$ by approximately 21-26%.

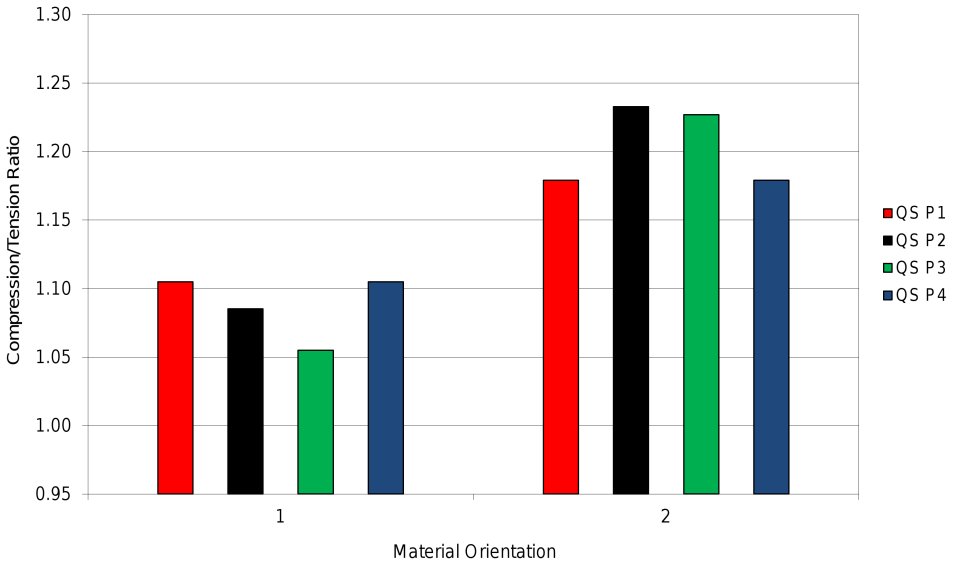


Figure 5.10 - Chart of comp/tens ratios at quasi-static strain rates in material orientations 1 and 2

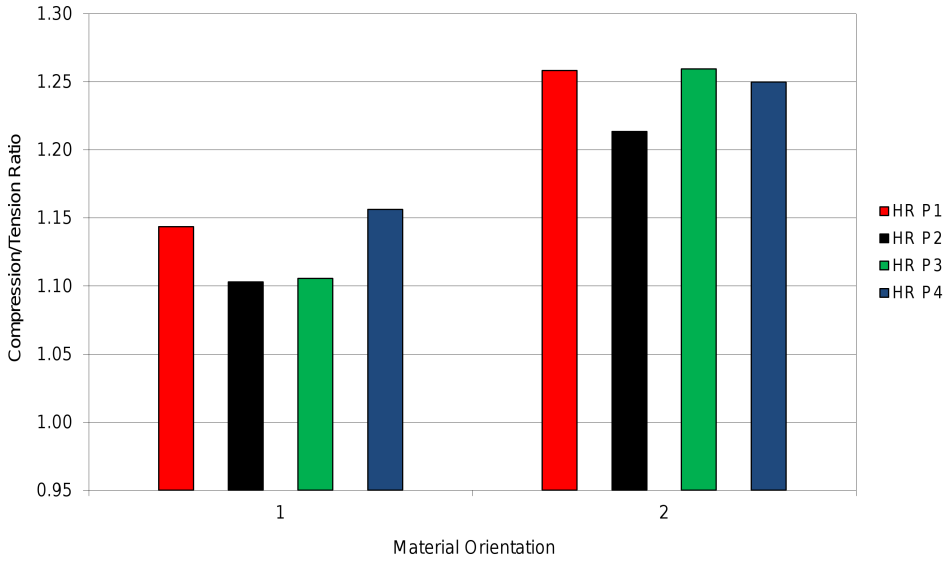


Figure 5.11 - Chart of comp/tens ratios at high strain rates in material orientations 1 and 2

5.6 General Plastic Flow Behaviour of Ti-6Al-4V Plates

From the data presented in Table 5.1, Table 5.2, Table 5.3 and Table 5.4, and the analysis carried out in the preceding section, its is clear that material orientation, strain rate and direction of loading have a significant affect on flow stress behaviour in all four development level Ti-6Al-4V plates.

Due to the complex interlinked nature of the microstructural and textural features seen in Ti-6Al-4V, it can be difficult to isolate the effects of different features on the plastic flow stress behaviour. Carefully selected materials and well-designed experiments are required to isolate specific microstructural and textural features, thus allowing the effects of those features on the plastic flow behaviour to be determined. Unfortunately, the widely varying microstructures and micro-textures studied as part of this project do not allow such an analysis to be carried out. However, from the completed microstructural and mechanical characterisation of the four development level Ti-6Al-4V plates, it is possible to gain a more general insight into the effects, or lack of effects, caused by different microstructures and textures.

For example, it is interesting to note that all four plates exhibit significant tension/compression asymmetry of flow stress. A number of studies have shown that slip in Titanium has an inherent tension/compression asymmetry [45–47], possibly resulting from the pressure dependence of $\langle \boldsymbol{c} + \boldsymbol{a} \rangle$ type slip [46], [47]. However, the tension/compression asymmetries observed in the mechanical characterisation results are too large to be accounted for by this. Tension/compression asymmetries have also been seen due to the apparent tension/compression asymmetry of deformation twinning [9]. As the twinning content is typically low at quasi-static strain rates, and a large tension/compression asymmetry is still observed in the quasi-static characterisation results, it is unlikely the behaviour is due to this.

The most likely reason for the observed tension/compression asymmetry is that during processing, large compressive residual stresses are locked into the material [48].

However, the effects of twinning at high strain rates and in the transverse material orientation cannot be ruled out. The slight observed strain rate dependence of the tension/compression asymmetry in the transverse material orientation is evidence that at high strain rates in compression, and in particular the transverse material orientation, twinning becomes significant, resulting in an increase in the yield and flow stress through the Hall-Petch effect [21], [22]. Microstructural evidence of deformation twinning during complex, high strain rate compressive loading is given in Chapter 6. However, to confirm that twinning is the mechanism that results in the observed strain rate dependence of the tension/compression asymmetry in the transverse material orientation, a significant study of post-deformation microstructures of uniaxial test specimens would be required.

The material orientation dependence of the tension/compression asymmetry would be adequately explained by the presence of an anisotropic residual stress. In the case of these unidirectionally rolled Ti-6Al-4V plates, it highly likely that secondary processing will result in an anisotropic residual stress, with the effects of texture playing a role due to the mechanical and thermal anisotropy of the *hcp* crystal structure [48].

A study of the residual stresses in the characterised plates is outwith the scope of this project. However, techniques such as X-ray diffraction and neutron diffraction are widely available and could be used to determine the magnitude and orientations of the residual stress tensor [49].

The material orientation dependence of the flow stress is clearly due to the significant macro and micro-texture observed in all four Ti-6Al-4V plates. As the easy glide of dislocations occurs along $\langle \boldsymbol{a} \rangle$ type slip systems i.e. slip systems with slip directions on the Basal plane, it is intuitive that material orientations with the majority of α grains/laths

orientated with the ***c***-axis of the *hcp* unit cell lying parallel to the direction of loading will have a higher flow stress than those with the ***c***-axis of the *hcp* unit cell lying perpendicular to the direction of loading, as is the case for all four plates.

Rather than the increase in strain hardening at high strain rates observed by many researchers [23], [50–52], all four plates show lower strain hardening at high strain rates. As shown by MacDougall and Harding [27], during high strain rate deformation, relatively large increases in temperature can occur due to the conversion of mechanical work to heat. MacDougall and Harding recorded an increase in temperature of ~30°C during homogeneous plastic deformation in a torsional SHPB test at a strain rate of ~600 s^{-1}. It is likely that the observed softening at high strain rates is due to this increase in temperature compared with quasi-static experiments, resulting in lower strain hardening through thermal softening of the flow stress. However, further work would be needed to confirm this hypothesis.

Of significant interest is the effect, or lack of effect, of microstructure on the strain hardening behaviour of the four Ti-6Al-4V plates. It is surprising to observe that, despite having significantly different microstructures and micro-textures, the four Ti-6Al-4V plates have effectively the same strain hardening response. From the results in Table 5.1, Table 5.2, Table 5.3 and Table 5.4, it is clear that microstructure has an affect on the yield behaviour of Ti-6Al-4V. However, the strain hardening response appears to be independent of microstructure. This will be discussed further in Chapter 7, where a possible mechanism to account for this will be proposed and implemented within a modelling framework.

From the results in this chapter and Chapter 4, it is not possible to systematically determine the contribution of different microstructural and micro-textural features on the plastic flow behaviour of Ti-6Al-4V. The complex interactions of microstructure and texture, and their subsequent effects on the plastic flow behaviour of Ti-6Al-4V, will be discussed in more detail in Chapter 7.

5.7 Fracture Surfaces

Images of the fracture surfaces of representative tensile specimens from each of the four Ti-6Al-4V plates, loaded at quasi-static strain rates in the longitudinal material orientation until failure, were taken using a SEM in secondary electron imaging mode. The fractured tensile specimens were mounted on standard stubs using conductive tape and placed in the SEM chamber. Images were then taken of the fracture surfaces at a number of different magnifications and two different locations on the fracture surface, the “centre” and the “edge” of the fracture surface, as shown in Figure 5.12.

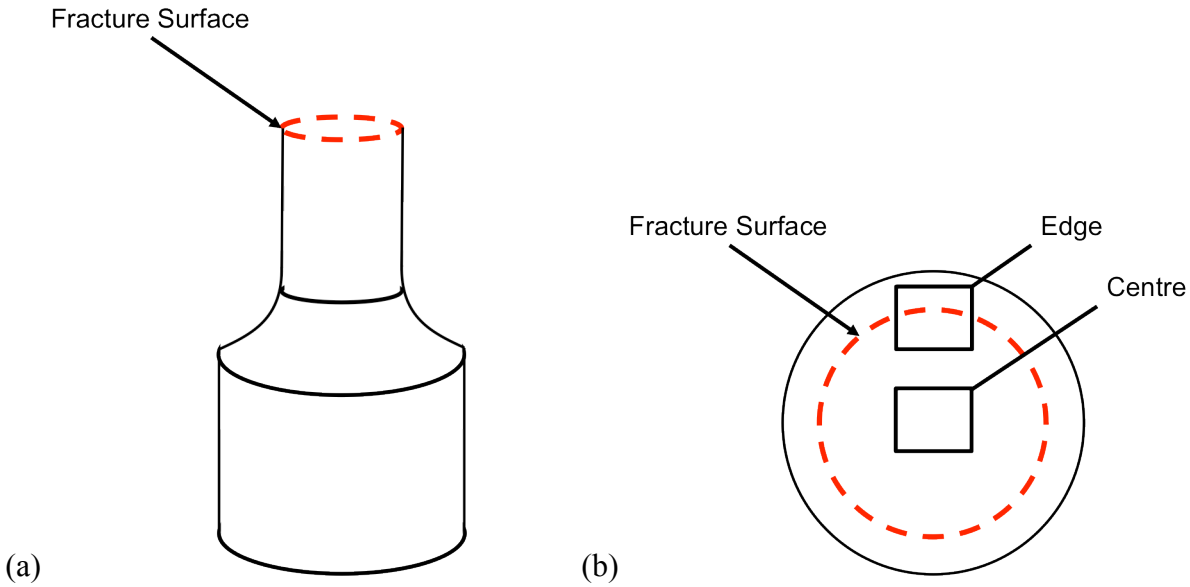


Figure 5.12 - (a) Diagram showing fracture surface in relation to tensile specimen

(b) plan view of fracture surface showing locations of "centre" and "edge" SEM images

When qualitatively comparing the fracture surfaces of the four plates, it can be seen that there is a difference in the size and shape of the dimples formed during fracture. When compared with the original microstructures of the four plates, it can be seen that there is a correlation between the size and shape of the dimples on the fracture surface and the microstructure of the plates. This correlation between dimple size/shape and microstructure is particularly clear when comparing the fracture surface and microstructure of Plate 4, as shown in Figure 4.8 and Figure 5.19.

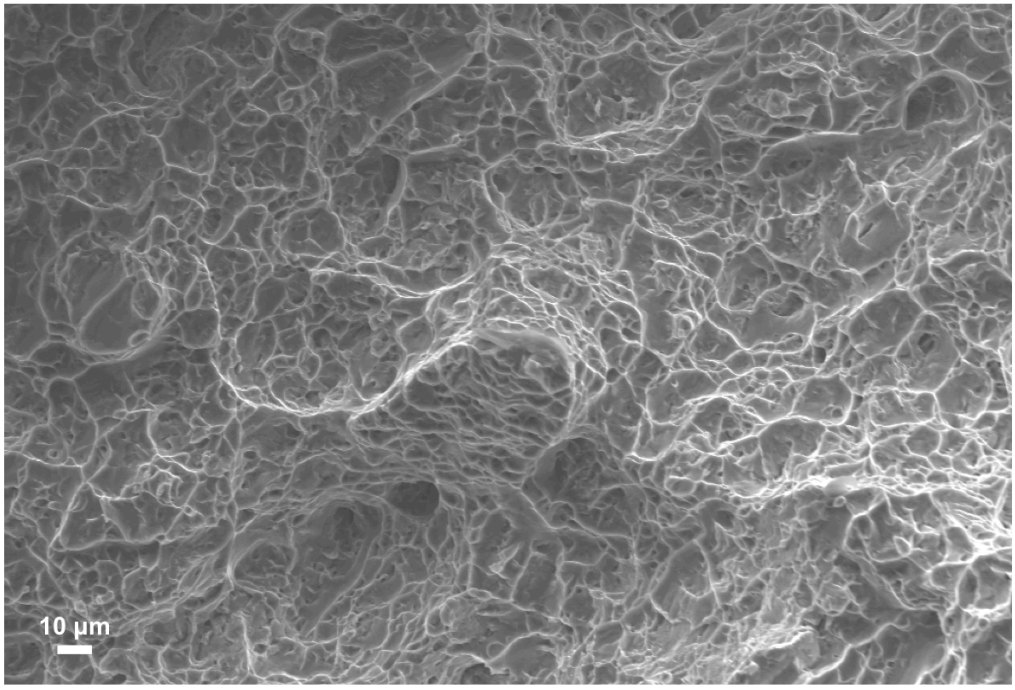


Figure 5.13 - Plate 1 - Longitudinal direction - Fracture surface - Centre of specimen

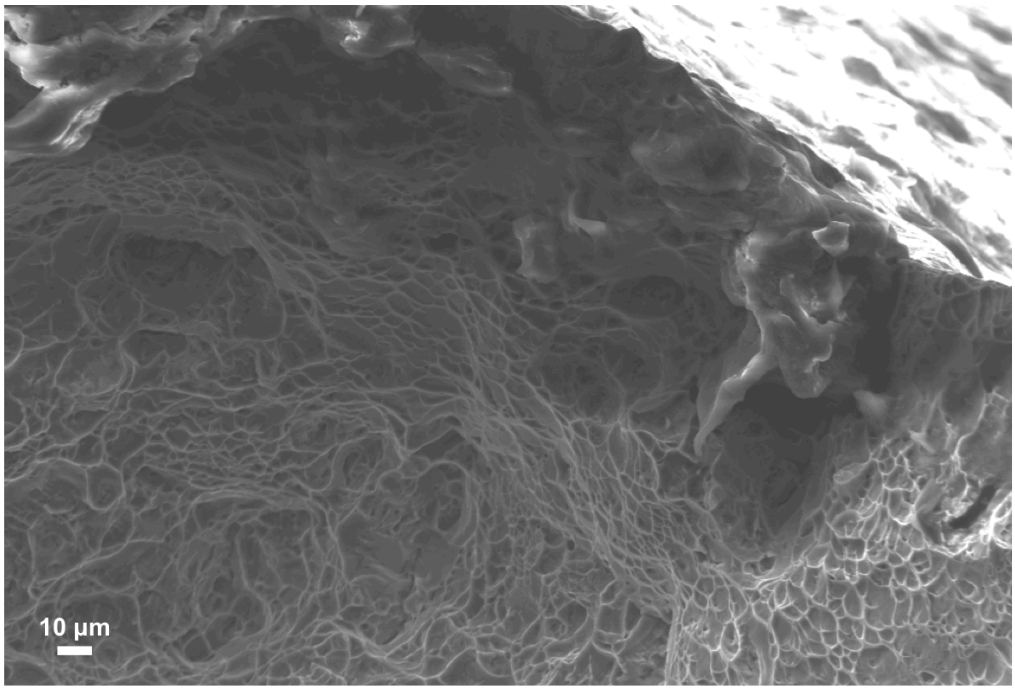


Figure 5.14 - Plate 1 - Longitudinal direction - Fracture surface - Edge of specimen

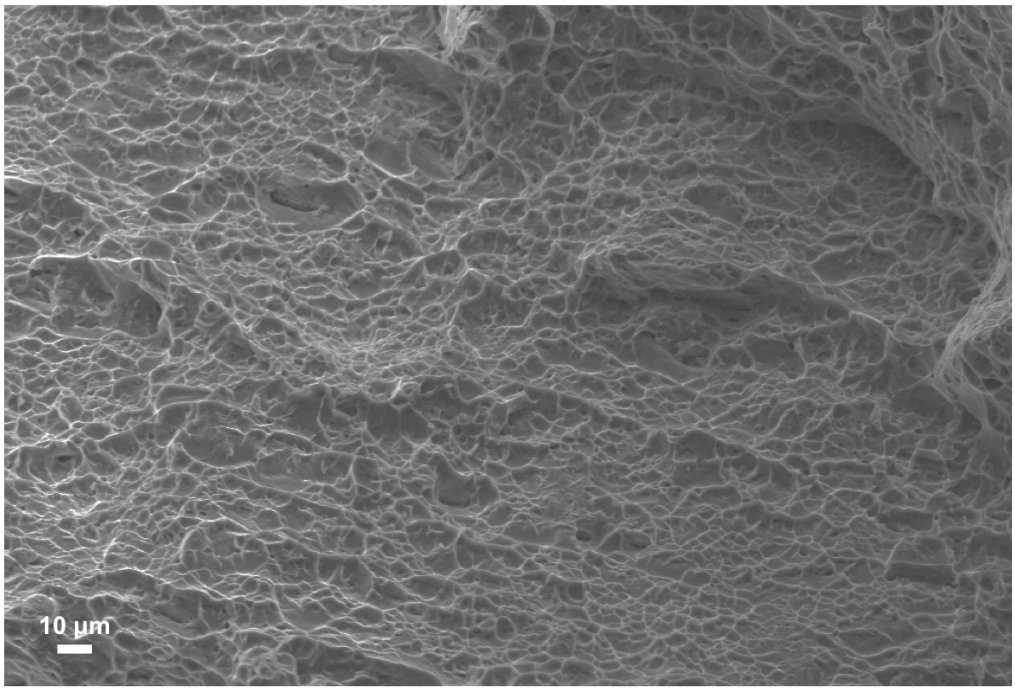


Figure 5.15 - Plate 2 - Longitudinal direction - Fracture surface - Centre of specimen

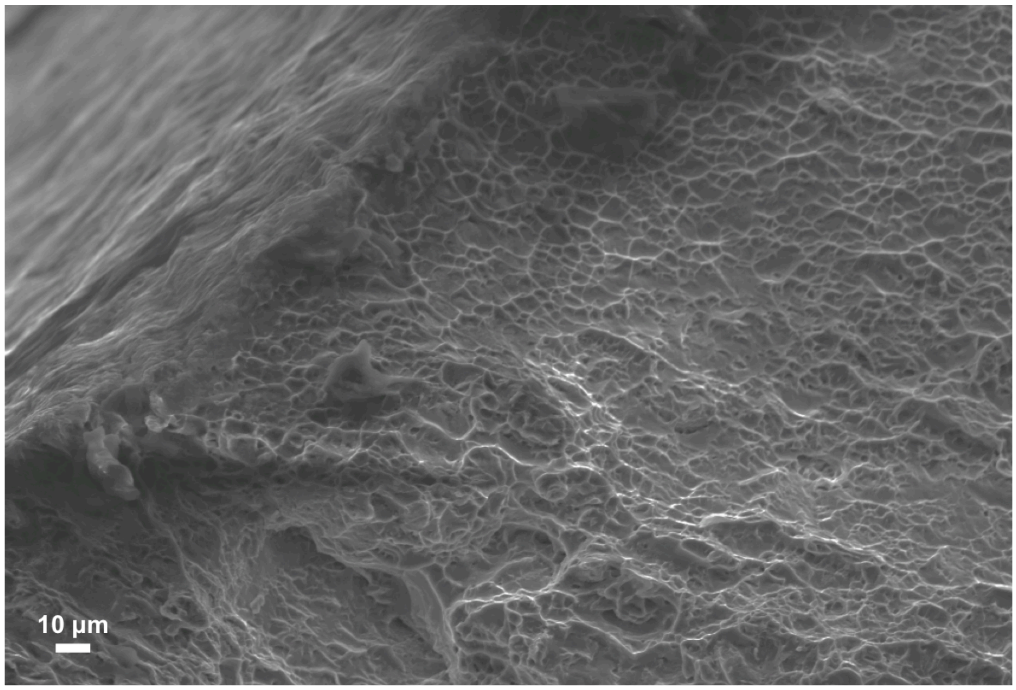


Figure 5.16 - Plate 2 - Longitudinal direction - Fracture surface - Edge of specimen

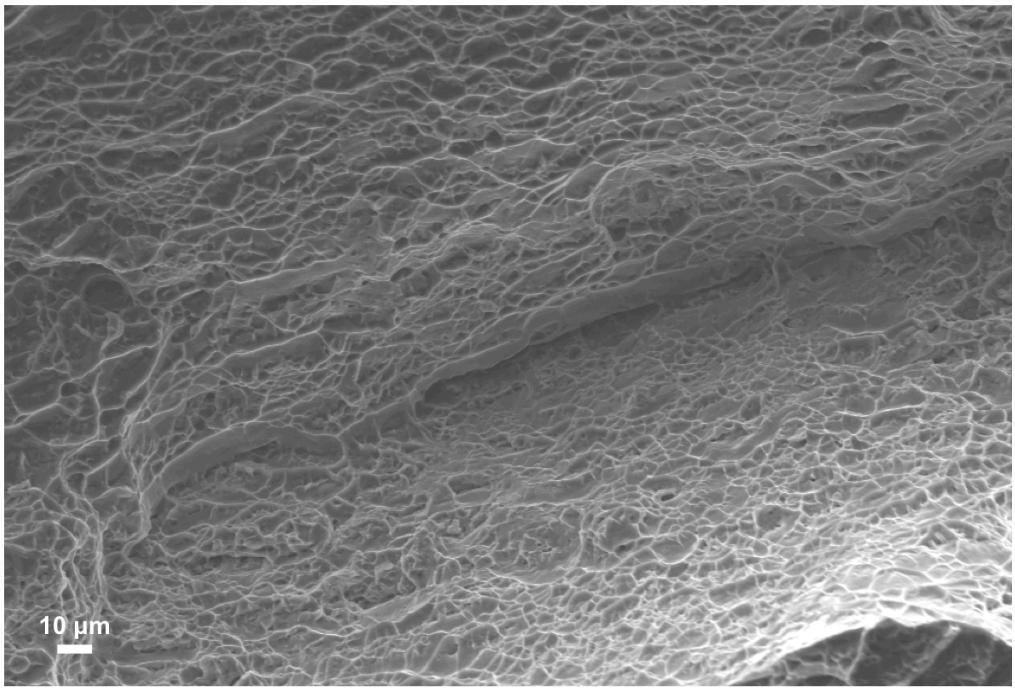


Figure 5.17 - Plate 3 - Longitudinal direction - Fracture surface - Centre of specimen

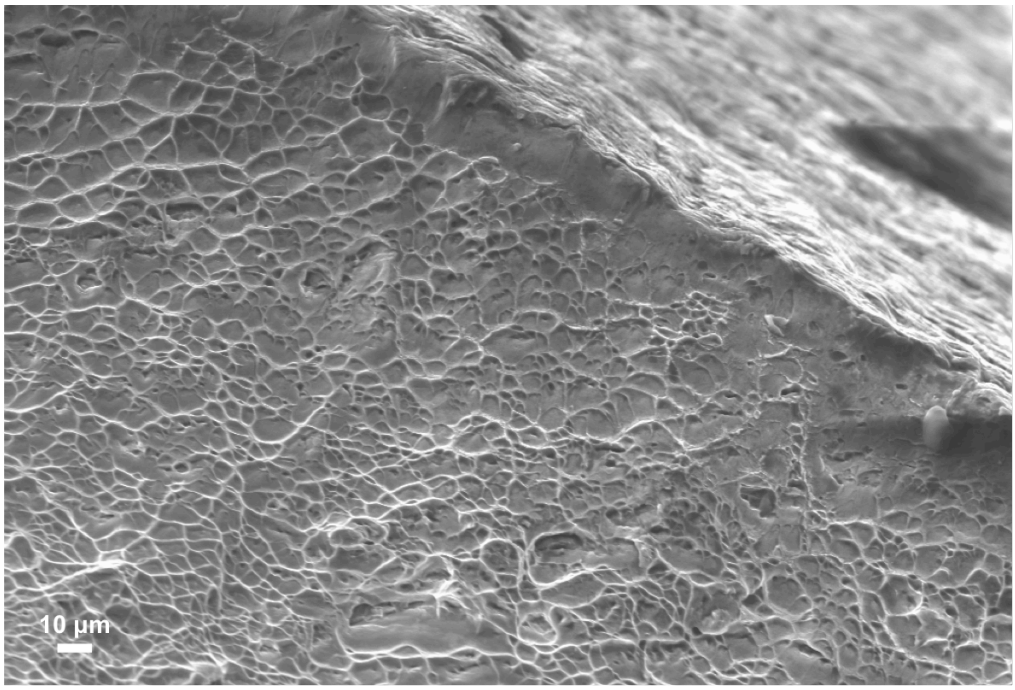


Figure 5.18 - Plate 3 - Longitudinal direction - Fracture surface - Edge of specimen

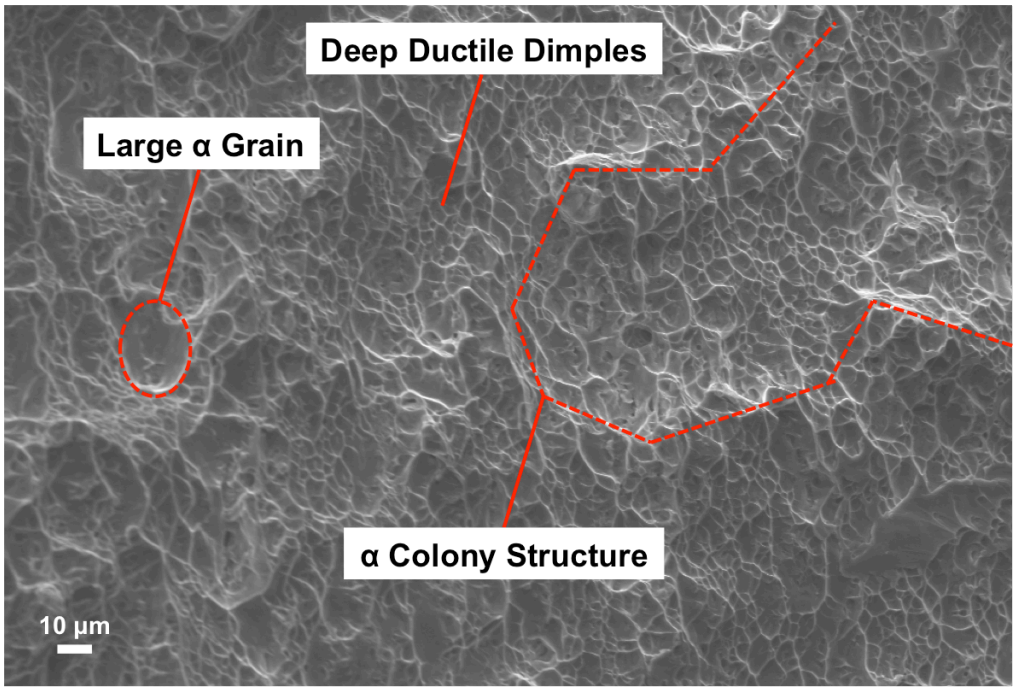


Figure 5.19 - Plate 4 - Longitudinal direction - Fracture surface - Centre of specimen

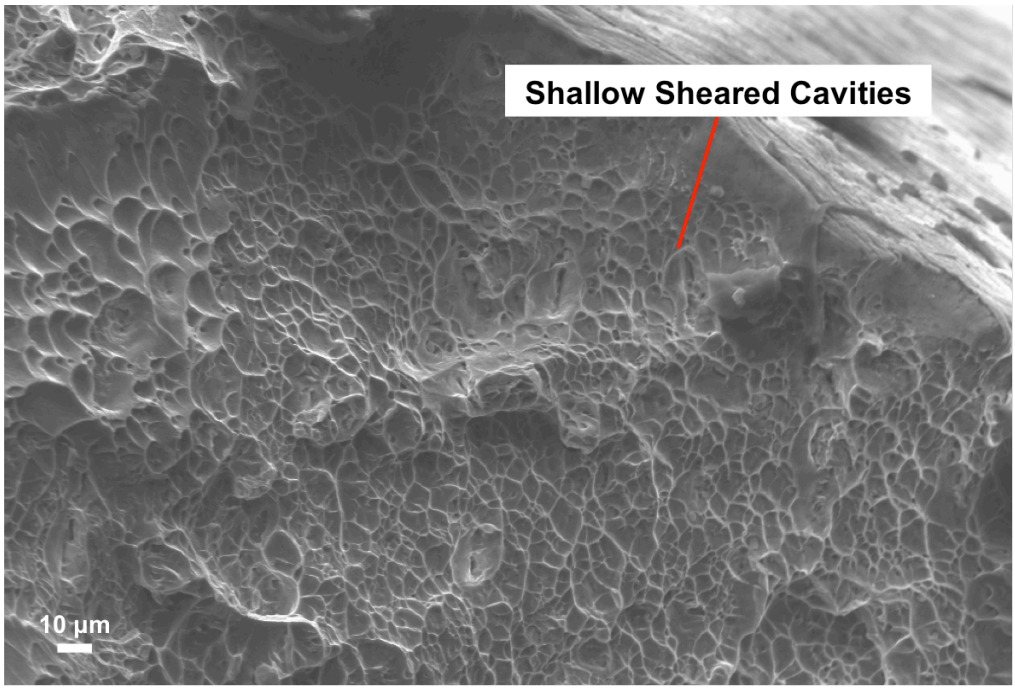


Figure 5.20 - Plate 4 - Longitudinal direction - Fracture surface - Edge of specimen

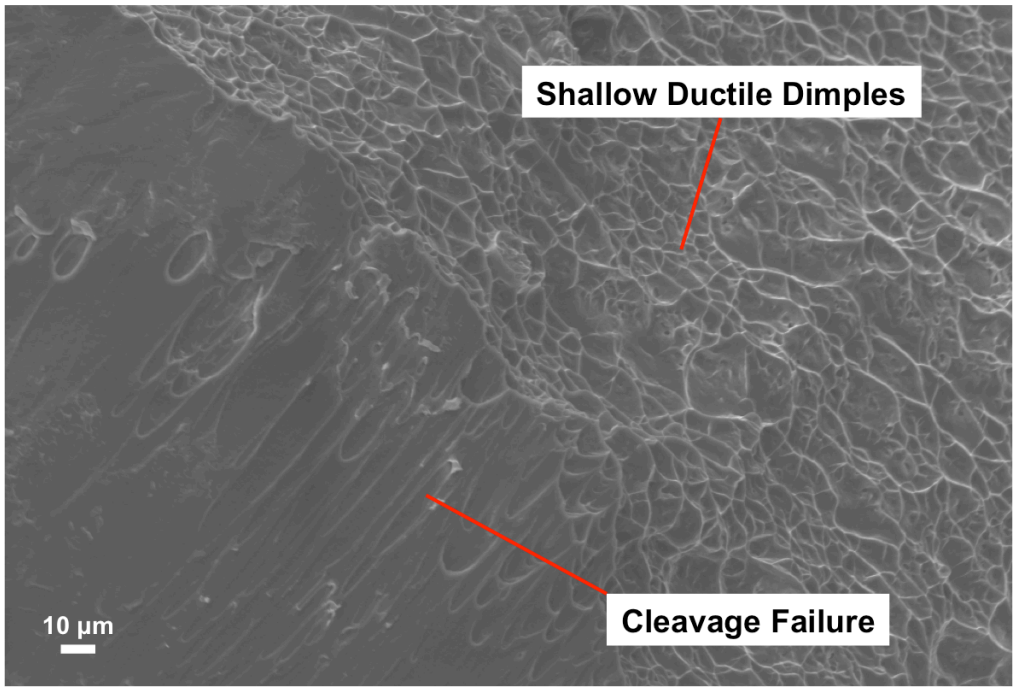


Figure 5.21 - Plate 4 - High Strain Rate - Longitudinal direction - Fracture surface - Centre of specimen

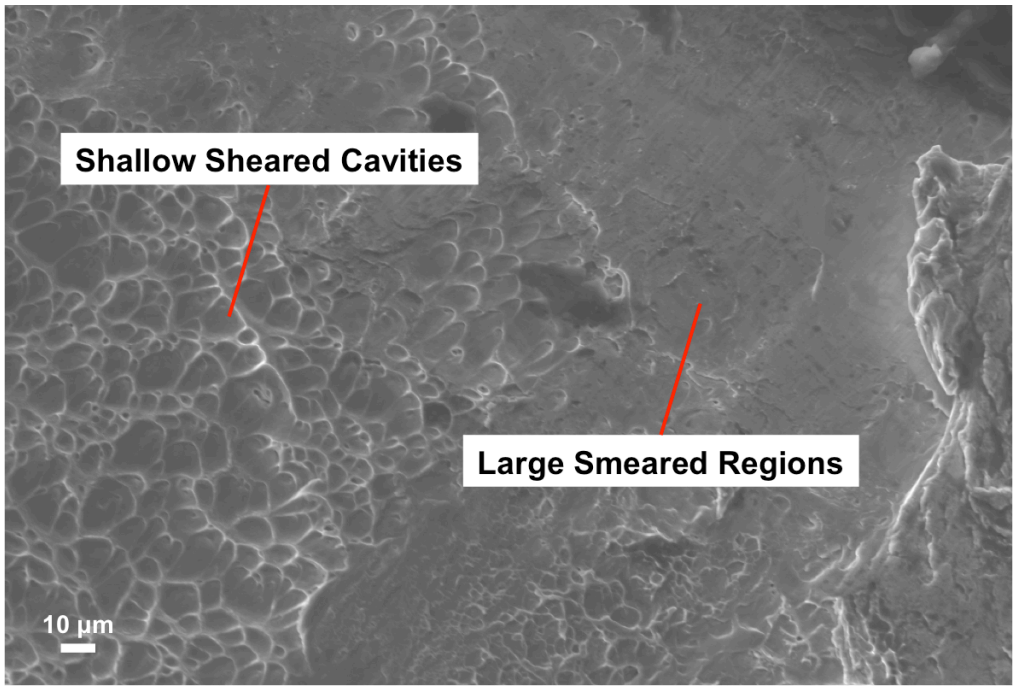


Figure 5.22 - Plate 4 - High Strain Rate - Longitudinal direction - Fracture surface - Edge of specimen

It has been shown in previous studies that the formation of dimples roughly the same size as the α grain size are due to voids forming and then coalescing at the interface between the α grains and the β matrix [28]. The fracture surfaces seen in this study appear to agree with this hypothesis. However, more detailed examination of the imaged fracture surfaces shows significant correlation, not only with the α grain size, but also with other key features of the individual plate's starting microstructure and micro-texture.

Once again, this can be most clearly seen by comparing the initial microstructure and micro-texture of Plate 4, as shown in Figure 4.8, Figure 4.9, Figure 4.16, and Figure 4.17, with the fracture surface from Plate 4, given in Figure 5.19 and Figure 5.20. As highlighted on Figure 5.19 and Figure 5.20, as well as the correlation between the α grain size, larger dimples can clearly be seen that correlate well with the larger α grains seen in the microstructure of Plate 4. Further, large regions of dimples on the fracture surface of Plate 4 appear to be pronounced or recessed. These regions of dimples appear to correlate well with the α colony structures seen in the micro-texture results from Plate 4, indicating that micro-texture has an effect on fracture characteristics and thus ductility.

Fracture surface images from a Plate 4 specimen loaded at high strain rates are presented in Figure 5.21 and Figure 5.22. By comparing the fracture surfaces of a specimen loaded quasi-statically with a specimen loaded at high strain rates, an understanding can be gained of the effects of strain rate on fracture characteristics.

From Figure 5.21 and Figure 5.22, it can clearly be seen that at high strain rates smearing of the fracture surface occurs near the edge of the specimen, with shallow sheared cavities also observed. These features indicate that adiabatic shear banding is occurring in this region. It can also be seen that the ductile dimples in the centre of the specimen are shallower than those seen at quasi-static strain rates. Finally, it can be observed that in the centre of the specimen there are areas of cleavage fracture, something not seen at quasi-static strain rates. All of these features indicate a predominately shear-based failure mechanism at high strain rates, compared with a more classical void nucleation and growth, ductile-based failure mechanism at quasi-static strain rates.

5.8 Preferential Failure Planes

Faint lines were scored onto the surface of the specimens during preparation such that it was possible to determine the material orientation of the specimen relative to the original plate. It was observed that all specimens failed along specific planes relative to the original plate orientation. These preferential failure planes for the compression specimens are shown in Figure 5.23. At quasi-static strain rates compression specimens failed due to shear fracture, whereas at high strain rates adiabatic shear banding was observed.

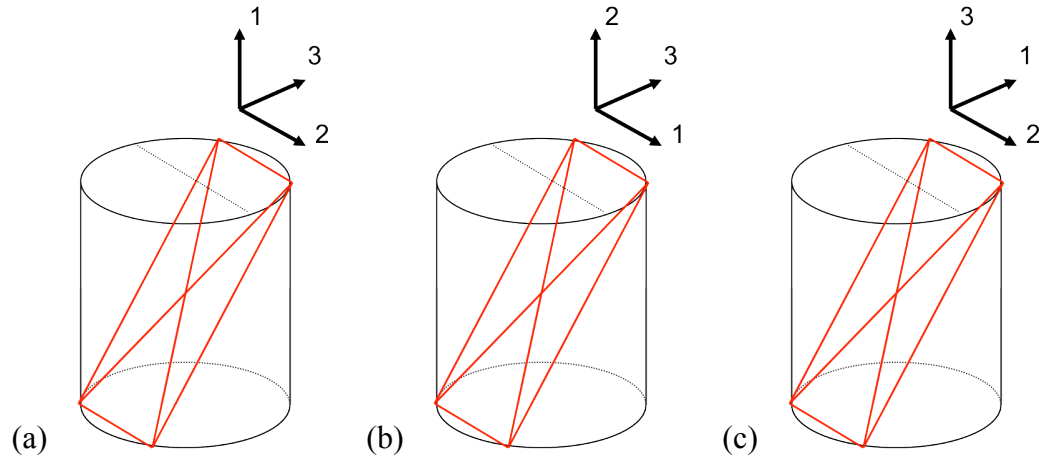
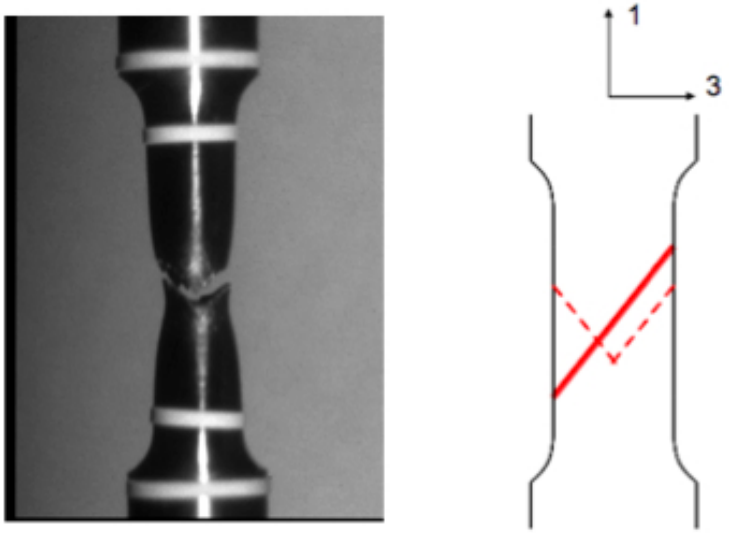


Figure 5.23 – Preferential failure plane for compression specimens loaded in the (a) longitudinal, (b) transverse and (c) through-thickness material orientations

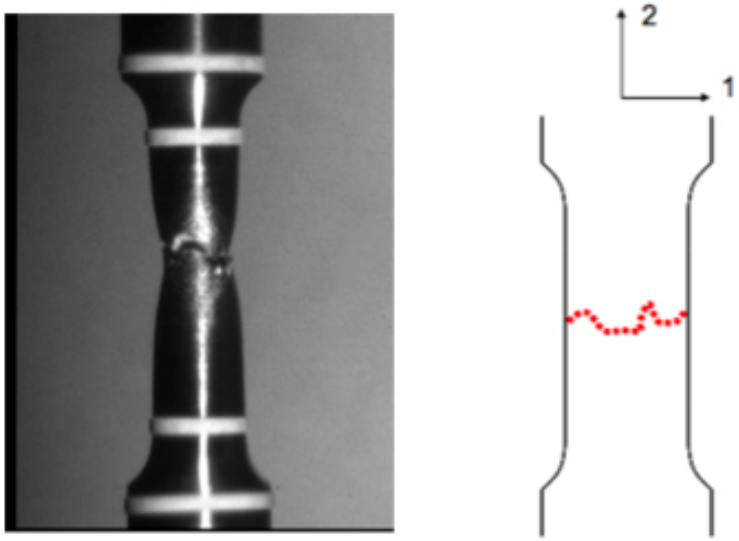
A similar trend was seen in tension with specimens loaded along the longitudinal material direction failing due to well-defined shear bands along specific planes relative to the material orientations, as shown in Figure 5.24 (a). However, when loaded along the transverse material direction, it was noted that failure was either of the classic "cup and cone" type or had no specific failure characteristics, Figure 5.24 (b).

These observed failure mechanisms are clearly due to anisotropy of yield, caused by the macro-texture of the four studied Ti-6Al-4V plates. Rather than being an inherent behaviour of the material, the observed failure mechanisms are due to geometric effects imposed by the anisotropy of yield. For example, in the case of a tensile test in the longitudinal direction, as

the material deforms, an elliptical cross-section is formed, with the major and minor axes of the ellipse relating to the transverse and through-thickness material orientations, respectively. This geometry change effectively forces shear failure to occur along the observed planes. In the case of a tensile test in the transverse direction, the yield stresses balance, resulting in a circular cross-section and a random failure mechanism.



(a)



(b)

Figure 5.24 - Preferential failure planes in tension, relative to original material orientations

5.9 Ductility

To quantify the ductility of the four different Ti-6Al-4V plates, the percentage elongation to failure was calculated for all tensile experiments at quasi-static (10^{-3} s^{-1}) and high strain rates (10^{3} s^{-1}). Elongation to failure results from representative specimens under all conditions are given in Table 5.8, with the error in the elongation to failure results taken as the maximum deviation from the representative specimen.

From the results in Table 5.8, it can be seen that, despite having different flow stresses and significantly different microstructures, the four Ti-6Al-4V plates have very similar percentage elongation to failure values, with very little variation between specimens tested under the same conditions. It can also be seen that for all four plates, ductility decreases with increasing strain rate.

Plate 3 has the lowest ductility of the four plates, which corresponds with the fact that it has the highest flow stress. Plate 1 and Plate 4 have near identical levels of ductility.

Of significant interest is the observation that Plate 2 has higher ductility in the transverse material orientation compared with the longitudinal material orientation, at both quasi-static and high strain rates. It is unclear where this feature of the material behaviour arises. One possible feature of the Plate 2 microstructure that may be a potential cause of this behaviour are the elongated α grain structures seen in the transverse/through-thickness plane but not in the longitudinal/through-thickness plane. However, this is merely a hypothesis, with a detailed study required to isolate the source of this observed behaviour.

	Quasi-Static Ductility (% elong.)				High Rate Ductility (% elong.)			
	P1	P2	P3	P4	P1	P2	P3	P4
D1	23 ± 1	21 ± 1	22 ± 2	23 ± 1	18 ± 2	17 ± 3	17 ± 2	17 ± 2
D2	23 ± 2	24 ± 2	22 ± 1	22 ± 1	18 ± 3	20 ± 2	16 ± 2	18 ± 2

Table 5.8 - Percentage elongation to failure values in tension at quasi-static and high strain rates

5.10 Conclusions

4 development level plates of Ti-6Al-4V, each with a different microstructure, have been tested at quasi-static and high strain rates under tensile and compressive loading in the three orthogonal material orientations relating to the rolling direction of the plates. The data has been used to compare the effects of microstructure, texture, strain rate, material orientation and the direction of loading on the mechanical behaviour of Ti-6Al-4V by comparing the true flow stress at a true plastic strain of 5%. From the comparison of this data, a number of general conclusions can be made about the mechanical behaviour of rolled Ti-6Al-4V plate with a strong basal/transverse macro-texture:

- The flow stress is material orientation dependent, with the flow stress in compression showing greater material orientation dependence than the flow stress in tension, at both quasi-static and high strain rates.

- The flow stress is strain rate dependent, with the flow stress in compression showing greater strain rate dependence than the flow stress in tension in the longitudinal, transverse and through-thickness material orientations.

- The flow stress is direction of loading dependent (tension/compression), with the flow stress in the transverse material orientation showing greater tension/compression asymmetry than the flow stress in the longitudinal material orientation. Tension/compression asymmetry of the flow stress increases with increasing strain rate in the transverse material orientation.

Reasons for these observed behaviours have been discussed. Further to these key points, it has been shown that the failure behaviour of rolled Ti-6Al-4V is dependent on material orientation, with failure occurring along preferential planes relative to the original plate material orientations. Fracture surfaces from tensile specimens showed varying fracture

surface topography dependant on the material microstructure, with the size and shape of ductile fracture dimples seen to be dependent on grain/α colony size. Adiabatic shear banding was observed at high strain rates.

Although these generalisations can be made about the mechanical behaviour of rolled Ti-6Al-4V plate materials exhibiting basal/transverse macroscopic texturing, it is clear from the presented results that microstructural and micro-textural crystallographic features affect the nature of this generalised mechanical behaviour. Although fully understanding the effects of these microstructural and micro-textural crystallographic features is outwith the scope of this thesis, attempts will be made in Chapter 7 to put forward evidence-based arguments for the interaction of key deformation mechanisms with microstructural and micro-textural crystallographic features of Ti-6Al-4V.

6 TAYLOR IMPACT OF Ti-6Al-4V

6.1 Overview

Current understanding of the deformation mechanisms of Titanium alloys under complex high strain rate loading is limited. In order to improve understanding in this area, post-deformation microstructural analyses of Titanium alloys loaded under well controlled, but complex, high strain rate loading conditions are required.

To facilitate this aim, this chapter presents the development of an extension to the classic Taylor impact test that uses high speed photography and a novel optical measurement technique to define the strain path history of an anisotropically deforming Taylor impact specimen as a function of time [53]. The experimental technique is validated using a specimen cut from a heavily textured clock-rolled high purity Zirconium plate. The results are compared with measurements of the recovered specimen made using a coordinate measurement machine (CMM), with excellent agreement shown between the measurement techniques.

The new experimental technique is then applied to specimens cut from the longitudinal and transverse material orientations of one of the four previously characterised Ti-6Al-4V plates (Plate 3). The application of this technique to the Taylor impact testing of Plate 3 provides significant insight into the effects of macro-texture on the high strain rate deformation of Ti-6Al-4V under complex loading scenarios.

Finally, electron backscatter diffraction (EBSD) analysis was performed on the pre and post-deformation specimens from Plate 3, in both the longitudinal and transverse material orientations. Comparisons are made between the deformed and undeformed microstructures, providing further insight into the role of texture on the high strain rate deformation of Ti-6Al-4V, this time at the microscopic scale.

6.2 Background

As described in Chapter 3, the classic Taylor impact experiment involves a right circular cylinder being impacted at a high velocity against a rigid anvil. The recovered specimens are found to have deformed plastically over a segment of the specimen close to the impact end, resulting in an increase in cross-sectional area and a decrease in length [32–34].

Despite no longer being used for its original purpose of determining the dynamic strength of materials, the Taylor impact experiment is still widely used, as it provides an excellent method for validating constitutive material models used in finite element (FE) simulations due to the complex stress states as well as variety of strain rates and final strains imposed on the material during the experiment. This has led to the development of new methods of instrumentation, with examples including high-speed photography [37], a velocity interferometer system for any reflector (VISAR) [38] and X-ray tomography [39]. These instrumentation techniques, combined with more detailed analyses of recovered specimens, have enabled the key aspects of the deformation process to be quantified, such as void nucleation in deformed specimens, the evolution of deformation along the length of a specimen and the specimen diameter for specimens with circular cross-sections, as functions of time. Detailed discussions of the experimental techniques listed above can be found in the review articles by Chapman *et al.* [40] and Field *et al.* [30].

Recently the classic Taylor impact experiment has been used to great effect as a method

of verifying constitutive material models for strongly textured metals that exhibit anisotropic plastic deformation. This work, published by Maudlin *et al.* [41] and Plunkett *et al.* [42], has focused on the modelling of *hcp* metals, such as strongly textured high-purity clock-rolled Zirconium plate, with particular attention being paid to the effects of the evolution of texture due to slip and twinning. This evolution of texture during the deformation process leads to an evolution in the yield surface, causing a change in the level of plastic anisotropy during deformation [54], [55]. Recovered specimens from these Taylor impact experiments were digitally scanned using an optical comparator along the major and minor axes of the elliptically deformed cross-sections. An optical reference specimen was then used to allow comparisons to be made with the final deformed shapes predicted by FE simulations.

In order to better validate these models, in particular in terms of texture evolution, and better understand the role of texture on the deformation of *hcp* metals in general, methods for characterising anisotropic deformation during the course of the Taylor impact experiment are required. Single-aspect high-speed photography allows optical measurements of specimen diameters to be made. This is sufficient for isotropic materials that retain circular cross-sections during deformation. However, the information that can be obtained from a single aspect is incomplete for samples that exhibit anisotropy, as such samples form cross-sections that are elliptical.

This section describes the application of high-speed photography and an optical measurement technique to the classic Taylor impact experiment. The technique is capable of reconstructing the elliptical cross-sections of a Taylor impact specimen as a function of time and axial position, from the images collected by high-speed photography. This approach provides quantitative data indispensable for the verification of key model parameters, such as the major and minor axes of the elliptically deformed cross-sections, as functions of time and the axial position. By providing access to this previously unobtainable data, the application of

the newly proposed technique to the classic Taylor impact experiment opens the prospect for a more rigorous verification method of anisotropic constitutive material models, as well as providing significant insight into the effects of texture and microstructure on the deformation of *hcp* metals under complex high strain rate loading.

6.3 Experimental Setup and Optical Measurement Technique

A gas gun and sabot were used to accelerate the specimens to the required impact speed, with the speed measured using light gates and an electronic timer. An end-hardened silver steel rod, of diameter 25mm and length 500mm, was mounted on V-notch bearings and used as a target, analogous to the output bar of an SHPB system, so as to allow space for the required mirror arrangement, flashes and high speed camera. A schematic of the experimental setup can be seen in Figure 6.1.

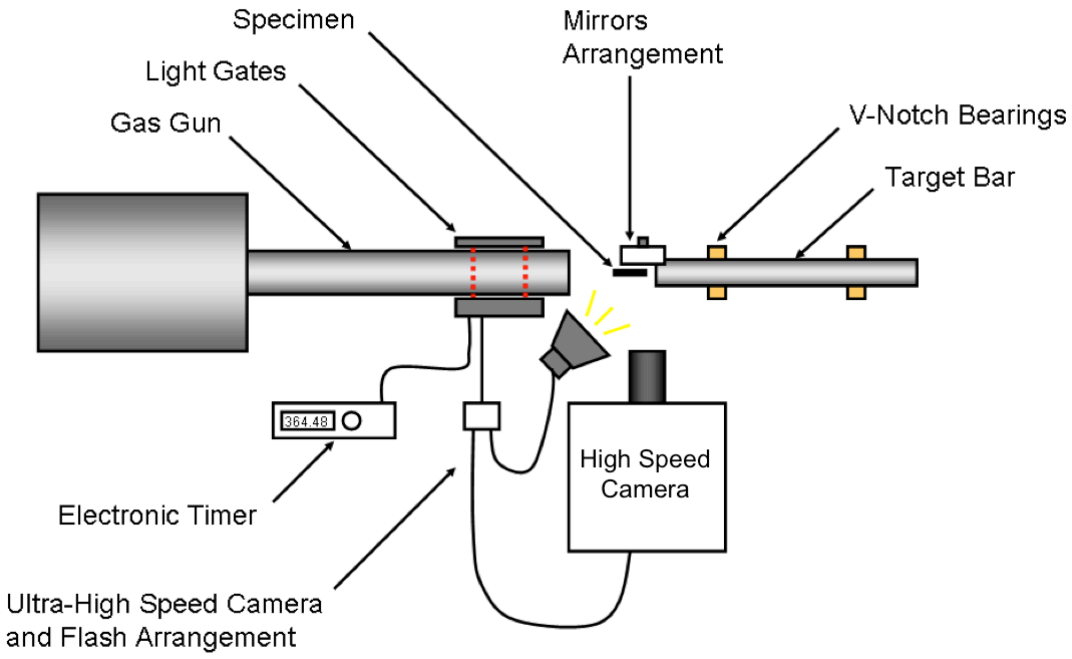


Figure 6.1 - Taylor impact experimental setup

A Specialised Imaging SIM-X high speed digital camera and two mirrors were used to capture images at -120°, 0° and 120° around the centre-line of the Taylor impact specimens,

as shown in Figure 6.2. Two 500J Bowens Gemini flashes were used to light the specimens such that they were reverse lit in all views, providing good contrast of the specimen edges.

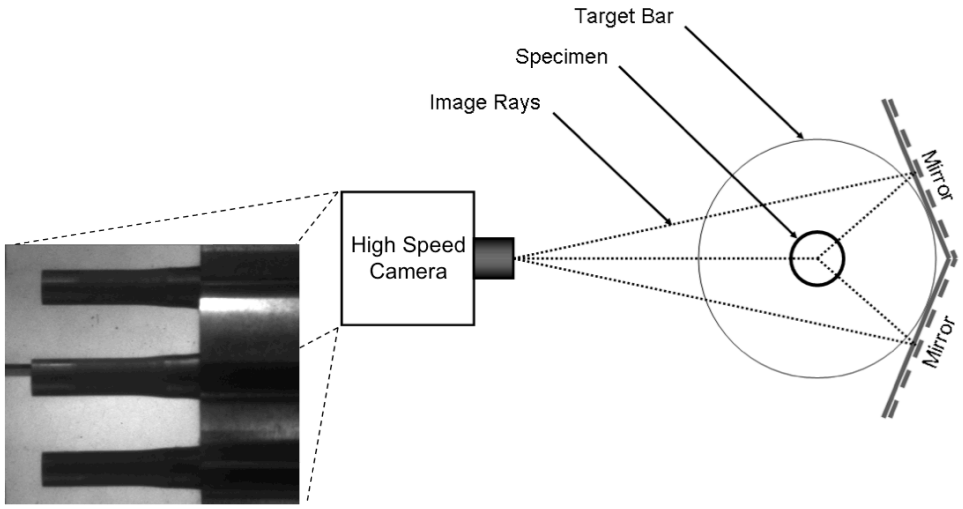


Figure 6.2 - Cross-sectional view of the Taylor impact experimental setup

Images from the SIM-X camera were intrinsically calibrated using the MATLAB Camera Calibration Toolbox and extrinsically calibrated by measuring the angles between the camera and mirrors to determine the camera position relative to a reference cylinder. To simplify extrinsic calibration, it was assumed that the camera was infinitely far away from the specimen, as validated by Arthington *et al.* [56].

The edges of the specimens were detected by a sub-pixel edge detection algorithm using a one-dimensional maximum gradient detector, allowing two edges from each view to be determined for each column of pixels. Having detected the positions of the edges in the image and knowing the position of the camera, vectors can then be calculated that are tangential to the specimen surface. It can be assumed that each of these tangential vectors lies on a cross-sectional plane at every distinguishable axial position, such that each tangential vector provides a constraint in radial position and orientation at a point on the surface of the specimen. As there are three views of the specimen, each giving two constraints on its surface, there are a total of six constraints on a given cross-sectional plane at every

distinguishable axial position. Choosing an appropriate coordinate system, each of the six constraints is of the form:

$$y = m_i x + c_i, \quad i = 1,...,6 \tag{6.1}$$

Assuming that the circumference of the specimen cross-section is elliptical, the conic equation of the ellipse in the space of the six defined constraints can be derived as:

$$f = Ax^2 + Bxy + Cy^2 + Dx + Ey + 1 = 0 \tag{6.2}$$

As shown in Figure 6.3, at the points (X_i, Y_i) where the constraints meet the ellipse, the tangent points, the gradients of the constraints, and the ellipse have equal directions according to:

$$\nabla f_i = \begin{bmatrix} 2AX_i + BY_i + D \\ BX_i + 2CY_i + E \end{bmatrix} = \lambda \begin{bmatrix} m_i \\ -1 \end{bmatrix} \tag{6.3}$$

where λ is an arbitrary scalar. Equations (1) to (3) can be combined, such that the ellipse is defined by any five of the six tangential constraints:

$$\begin{aligned} f_i &= f(m_i, c_i) \\ &= A\omega^2 + B\omega(m_i\omega + c_i) + C(m_i\omega + c_i)^2 + D\omega + E(m_i\omega + c_i) + 1 \\ &= 0 \end{aligned} \tag{6.4}$$

where:

$$\omega = \frac{1}{2} \frac{Bc_i + 2Cm_i c_i + Em_i + D}{A + Bm_i + Cm_i^2} \tag{6.5}$$

As there are six constraints and only five parameters (A, B, C, D, and E), a least-squares solution can be used to find the closest fit. For the results shown, a Gauss–Newton procedure was used to minimize:

$$\sum_i f_i^2 \tag{6.6}$$

The initial estimates of the parameters for all time steps (except the first) were taken as the parameters from the previous time step, assuming small changes in shape between time steps. The initial estimates for the parameters in the first time step were taken to be circles. A detailed description of the development, application and validation of the discussed optical measurement and geometry reconstruction technique is provided by Arthington [57].

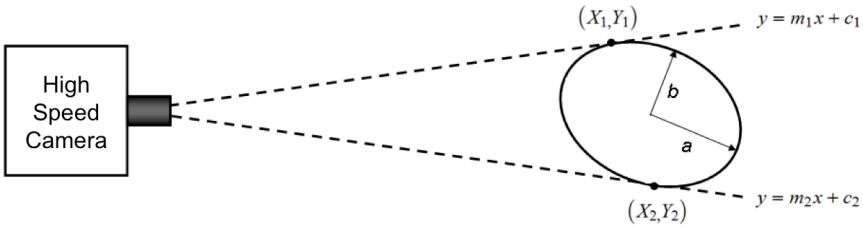


Figure 6.3 - Elliptical cross-section and tangents with constraints

6.4 Trial Taylor Impact Experiments on CP-Zr

6.4.1 Overview

A series of trial experiments were carried out to validate the experimental technique outlined in the previous section. It was decided that the experiments should be carried out on high purity clock-rolled Zirconium plate, due to its *hcp* crystal structure, strain rate dependence, anisotropic yield behaviour, high ductility and the large body of literature available on its behaviour under impact loading, in particular the classic Taylor impact test studies by Plunkett *et al.* [42] and Maudlin *et al.* [41] focussing on the effects of texture on plastic deformation.

The following section outlines the microstructural and mechanical characterisation of the as received high purity clock-rolled Zirconium plate (from here on referred to simply as Zr) and the results of the Taylor impact experiments carried out on the material using the previously discussed optical measurement and geometry reconstruction technique.

6.4.2 Characterisation of High Purity Clock-Rolled Zirconium Plate

Overview

A program of work was carried out to mechanically and microstructurally characterise the Zr plate material before beginning Taylor impact testing. The plate was first designated orthogonal material orientations, as shown in Figure 6.4.

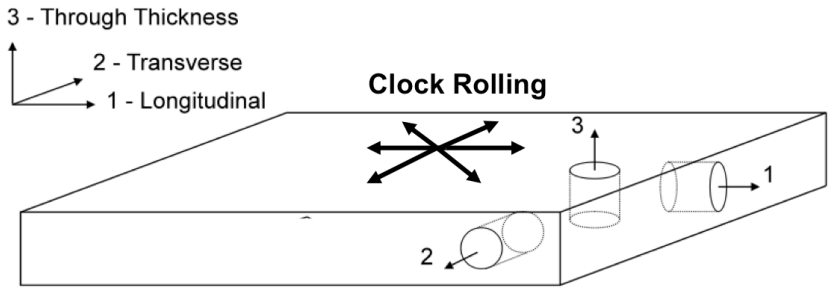


Figure 6.4 - Zr plate orientation, rolling directions and specimen orientations

Microstructure, Micro-Texture and Macro-Texture Characterisation

To characterise the microstructure and texture of the Zr plate, the electron back-scatter diffraction (EBSD) method was used, as previously outlined in Chapter 4. A slower, less abrasive polishing method was used due to the very soft nature of commercially pure Zr, with the specimen being polished overnight on a vibratory polishing wheel in a low concentration Colloidal-Silica slurry.

The results of the EBSD analysis are presented in Figure 6.5. From these results it can be seen that the Zr plate has a polycrystalline microstructure with an average grain size of ~50 μm. There does not appear to be any zones of micro-texture. However, the plate does exhibit strong macro-texture, as can be seen from the pole figure plot in Figure 6.5. From this plot it can be seen that the *hcp* unit cell of the majority of grains is orientated with the ***c***-axis roughly pointing parallel, with some smearing, to the though-thickness direction. As with the results seen in the previously tested Ti-6Al-4V plates that exhibited strong macro-texture, it is expected that this macro-texture will result in anisotropic plastic deformation.

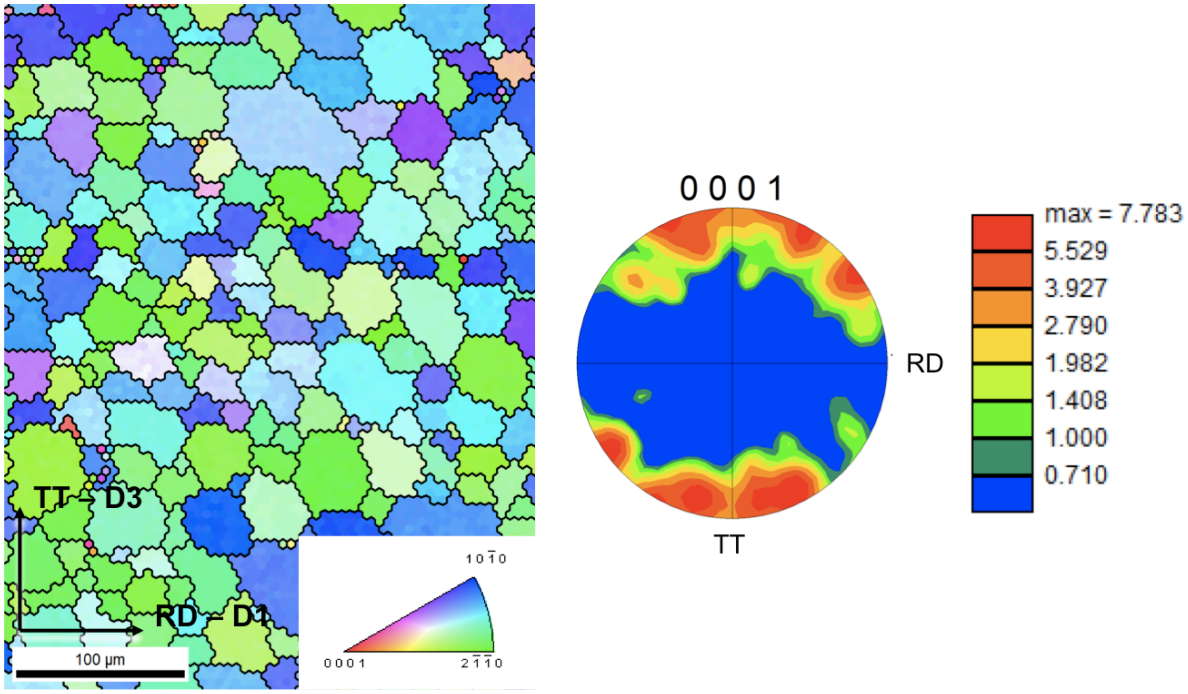


Figure 6.5 - Zr - Microstructure, micro-texture (IPF map) and macro-texture (PF plot)

Mechanical Characterisation

Compression specimens, of cylindrical design, were cut from the Zr plate in the longitudinal (D1) and through-thickness (D3) material orientations with a diameter of 3 mm and a height of 3.5 mm. Compressive split-Hopkinson pressure bars, using the same procedure as those used in Chapter 5, were then used to mechanically characterise the Zr plate material in the longitudinal and through thickness material orientations at a strain rate of 10^3 s^{-1}.

Representative experimental results in terms of true stress and true strain can be seen in Figure 6.6 for both material orientations. From these results it can be seen that the Zr plate exhibits strong anisotropy of plastic deformation, with the through-thickness material orientation having a flow stress nearly double that of the longitudinal material orientation.

At this point it is worth noting the difference in strain hardening seen in the different material orientations. The longitudinal material orientation has a nearly instantaneous transition to plastic flow, with the classic easy-glide, linear strain hardening response of *hcp*

metals deforming by $\langle \boldsymbol{a} \rangle$ type slip. However, the through-thickness material orientation has a very different response. Initial yield occurs at roughly the same point as the longitudinal material orientation followed by significant strain hardening, with the material eventually reaching steady state plastic flow at a higher stress, relative to the longitudinal flow stress.

This difference is most likely due to the relative availability of easy slip systems in the different material orientations. For example, in the longitudinal material orientation, for the majority of grains, easy slip can occur on the $\langle \boldsymbol{a} \rangle$ type slip systems. However, in the through-thickness material orientation there are very few grains available for easy slip. For compatible plastic flow to occur, the grains poorly orientated for slip must re-orientate through deformation twinning such that they are preferentially orientated for easy slip [58], [59]. This re-orientation of grains through deformation twinning is what is seen during the initial stages of plastic deformation in the through-thickness material orientation. It should also be noted that the twin boundaries formed result in strong barriers to dislocation motion, leading to an increased plastic flow stress through the Hall-Petch phenomenon [21].

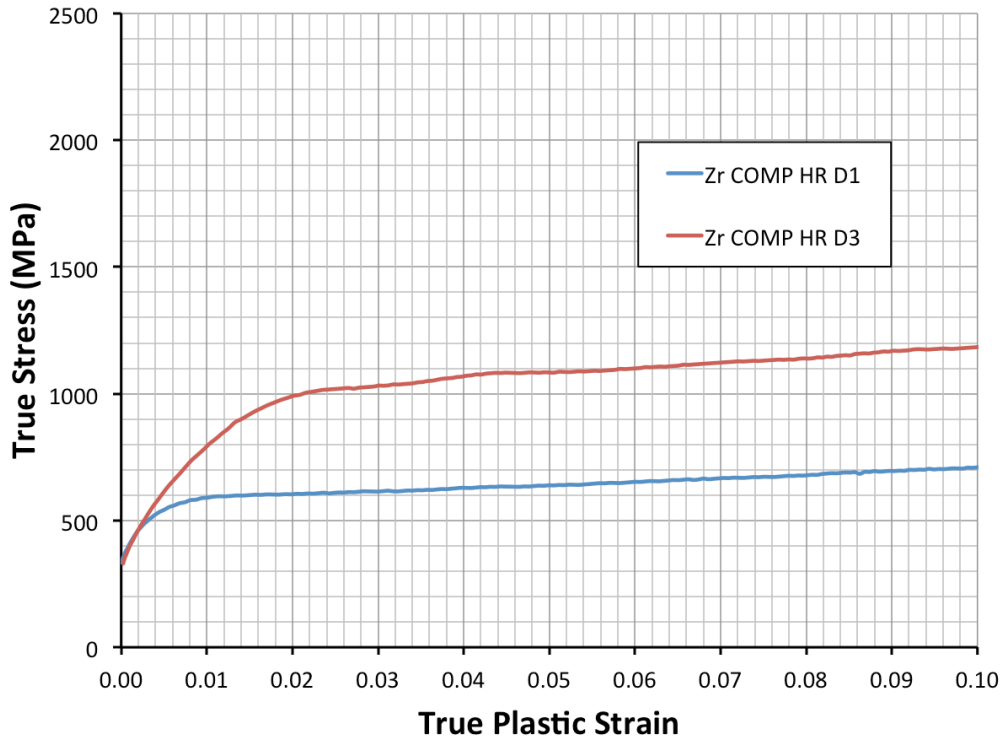


Figure 6.6 - Zr - Mechanical characterisation results in compression at high strain rates

6.4.3 Trial Experimental Results

In this section, results will be detailed from the trial Taylor impact experiments on high purity Zr plate using the previously outlined optical method for reconstructing the deforming geometry of the Taylor impact specimen as a function of time and axial position. A representative specimen will be used to illustrate the application of the technique and highlight some key data that can be obtained from the experimental technique.

Cylindrical specimens, of diameter 5 mm and length 25 mm, were cut from the in-plane directions of the Zr plate and lightly scored along their base such that it was possible to determine their original material orientations post-impact. The representative specimen chosen for this study had an impact velocity of 206 m s^{-1}. Using the experimental setup outlined previously, images were recorded with an inter-frame time of 7 μs and an exposure time of 1 μs.

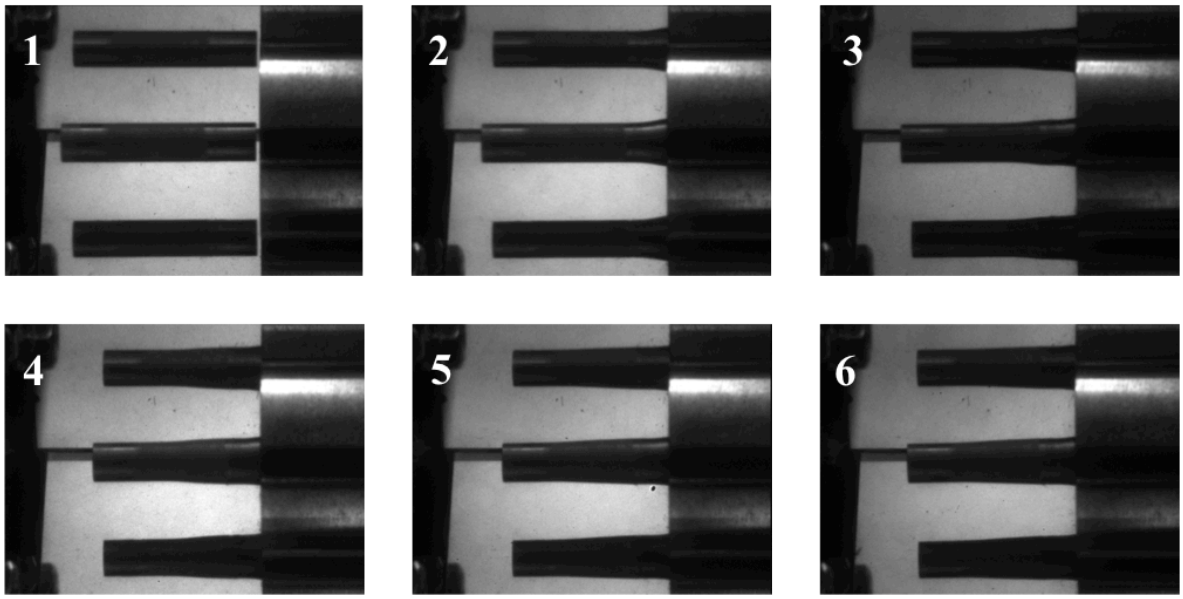


Figure 6.7 - Images from a Taylor impact experiment carried out on a representative Zr specimen [53]

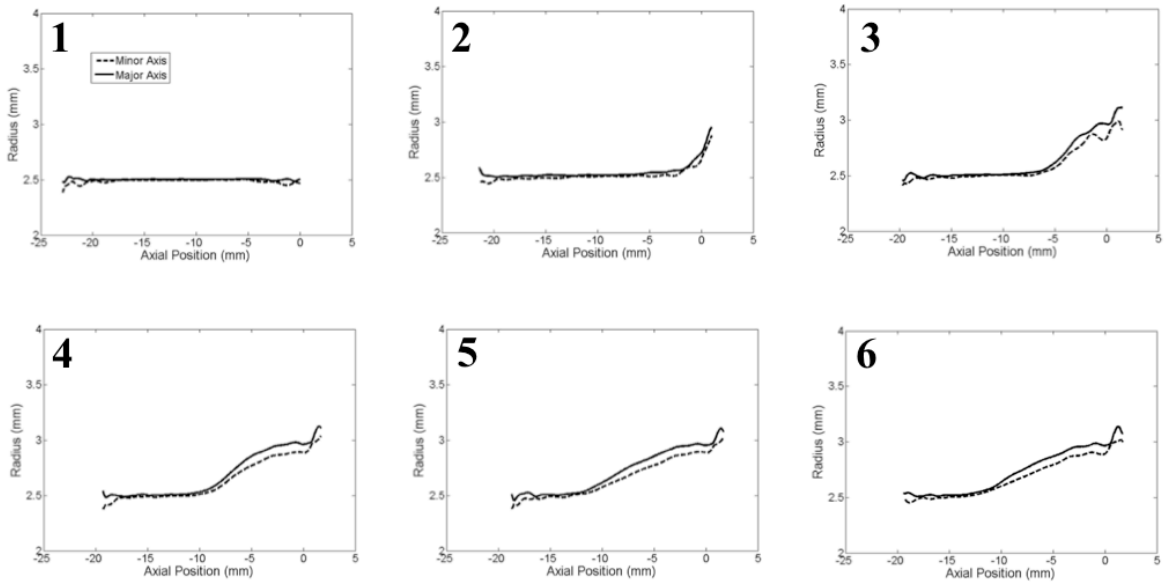


Figure 6.8 - Reconstructed major/minor axes of a representative Zr Taylor impact specimen [53]

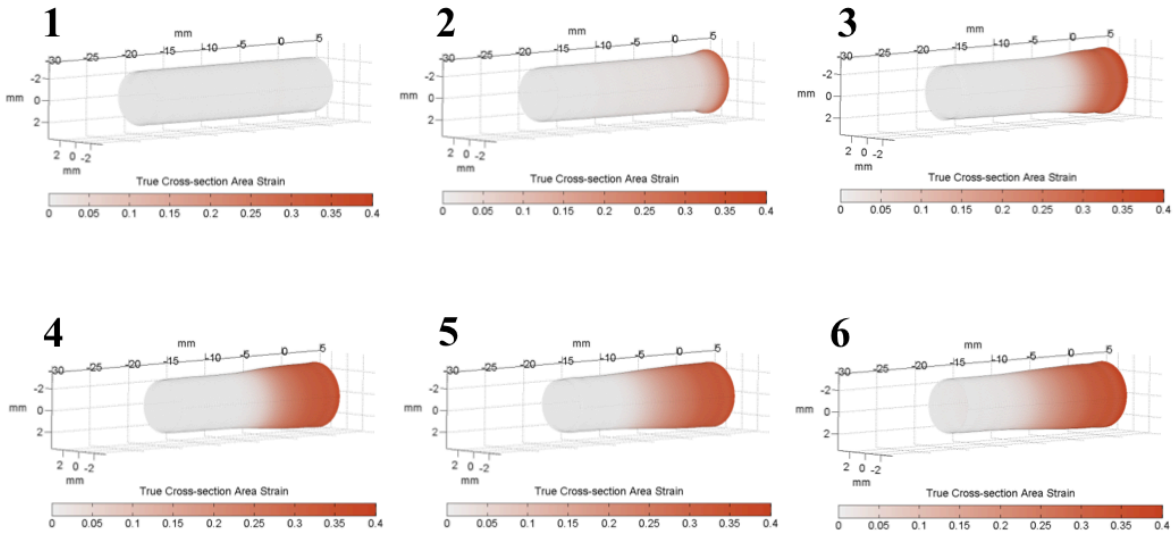


Figure 6.9 - Reconstructed area strain of a representative Zr Taylor impact specimen

The data obtained from the optical measurement and cross-section reconstruction technique can be used to give a number of useful plots. Figure 6.7 shows six out of a total of eight images from the experiment carried out on the representative specimen. One of the pre-impact images is not shown; a further post-impact image will be used later for validation purposes. These images were reconstructed using the optical measurement technique to produce two dimensional plots of the semi-major and semi-minor axes of the elliptical cross-

sections resulting from angular anisotropic deformation (Figure 6.8), as functions of time and axial position, and three dimensional plots of the true cross-sectional area strain, as a function of time (Figure 6.9).

6.4.4 Validation

To validate the reconstruction, the recovered specimen shape was measured using a Mitutoyo Series 191 coordinate measurement machine (CMM). Approximately 250 points were measured around the circumference of the recovered specimen at 1 mm intervals along its axial length. An ellipse was then fitted through the cross-sectional data points using a least-squares method. To ensure that the assumption of an elliptical cross-section was correct, the geometric distance between each CMM data point and the fitted ellipse at all measured axial positions was calculated. For example, at 5 mm from the impact face, the mean geometric distance was calculated to be less than the precision of the CMM, with a maximum geometric distance of 3.5 μm, indicating that an ellipse provides a good fit for the cross-sectional data. The lengths of the semi-major and semi-minor axes at each axial position were calculated and compared with the data from the image reconstructions of the same Taylor impact experiment, using the final post-impact frame as a reference. Any elastic recovery after this frame is negligible.

As can be seen in Figure 6.10, the data obtained from the optical measurements correlate very well with those of the CMM. The accuracy of CMM measurement declared by the manufacturer is of the order of ±2 μm. Comparing the CMM and optical measurements (ignoring the erroneous data at the ends of the specimen), a mean error in the lengths of the semi-major and semi-minor axes of 7μm is calculated for the optical measurements, with a maximum error of 19 μm.

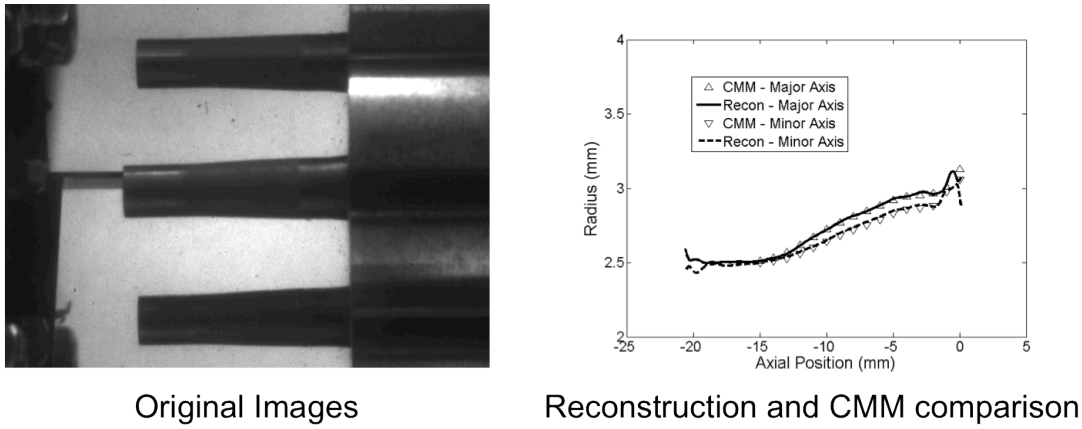


Figure 6.10 - Reconstructed major/minor axes and CMM data for the representative Zr specimen

6.4.5 Discussion

The results reported demonstrate that the optical measurement technique for Taylor impact specimen characterization provides a means of specimen shape characterisation that possesses suitably high resolution to detect small deviations from circular shape (ellipticity). It is interesting to note that the CMM measurements of a recovered specimen revealed that the cross-sectional shape was indeed well represented by an ellipse.

The results obtained show that the difference is surprisingly small between the semi-major and semi-minor ellipse axes of the deformed cross-sections, despite the sample being strongly textured. Although this result may seem counter-intuitive, similar results were obtained by Maudlin *et al.* [41] and Plunkett *et al.* [42], with evidence suggesting that this behaviour is due to complex texture evolution caused by twinning. However, further studies are required to fully understand the role of twinning on the high strain rate behaviour of Zr in complex stress state scenarios such as the Taylor impact experiment.

6.4.6 Conclusions

An optical measurement technique capable of reconstructing elliptical cross-sections along the axial length of a specimen during the classic Taylor impact experiment has been presented. The application of this technique to the Taylor impact experiment has enabled the

measurement of previously unobtainable data on the anisotropic deformation of specimens cut from strongly textured high purity Zr plate, such as the cross-sectional area strain and the semi-major and semi-minor axes of the deformed elliptical cross-sections that arise due to material anisotropy. The results were obtained as functions of time and the cylindrical axial position.

The surface geometry of a recovered specimen was measured using a CMM and compared with the reconstructed data from a post-impact image frame of the same Taylor impact experiment. Excellent agreement was seen between the CMM data and the data obtained using the optical measurement technique.

6.5 Taylor Impact Experiments on Ti-6Al-4V

6.5.1 Overview

In this section, results will be detailed from Taylor impact tests carried out on specimens cut from the in-plane material orientations of a rolled Ti-6Al-4V plate, designated Plate 3 in Chapter 5. The previously described and validated optical measurement technique will be used to determine the strain path and strain rate history of the specimens, giving access to key information on the effects of microstructure and texture on the evolution of anisotropic plastic deformation during the complex loading of a Taylor impact test.

Exactly the same procedure was used for the Taylor impact tests carried out on the Ti-6Al-4V specimens as was used for the Zr specimens outlined in the preceding section. Specimens were cut from the longitudinal and transverse material orientations of Plate 3 into right circular rods, with a length of 25 mm and a diameter of 5 mm. An illustration showing the longitudinal and transverse specimens relative to the original plate material orientations is given in Figure 6.11. The ends of the specimens were lightly scored such that it was possible to determine the original material orientations of the recovered specimens.

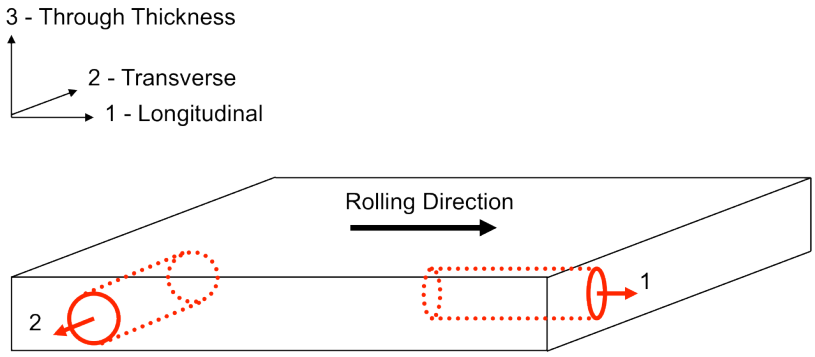


Figure 6.11 - Plate 3 material orientations, rolling direction and Taylor impact specimen orientations

Results from a representative specimen in the longitudinal and transverse material orientation, both with impact velocities of 160 m s^{-1}, will be given the next section, followed by a detailed discussion of key features of the results. Images from the high speed camera were taken with an inter-frame time of 5 μs and an exposure time of 0.25 μs.

6.5.2 Experimental Results from Taylor Impact on Ti-6Al-4V

The major/minor axes of the representative longitudinal and transverse Taylor impact specimen's elliptical cross-sections as a function of time and axial position are given in Figure 6.12 and Figure 6.13, respectively.

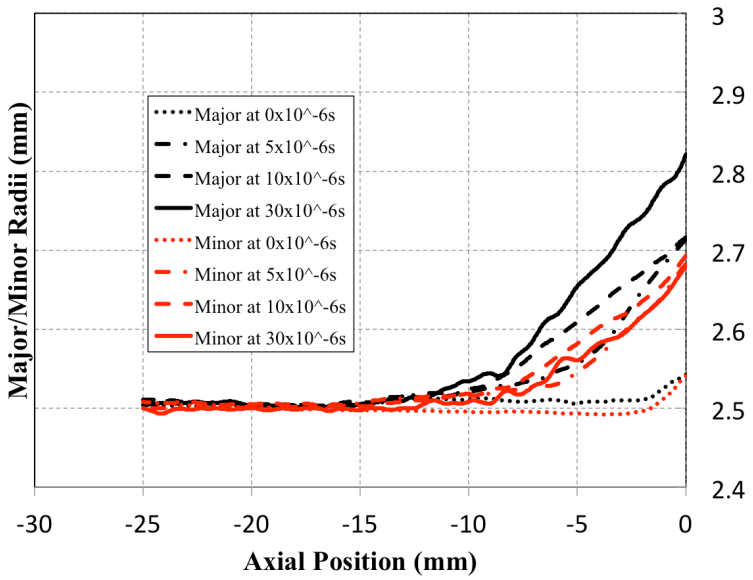


Figure 6.12 - Major/minor axes of the elliptical cross-section as a function of time of a Taylor impact specimen cut from the longitudinal material orientation of Ti-6Al-4V Plate 3

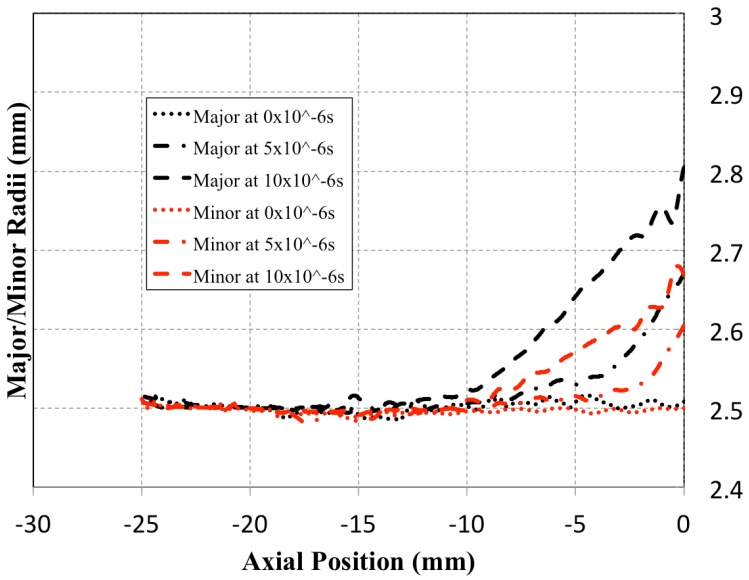


Figure 6.13 - Major/minor axes of the elliptical cross-section as a function of time of a Taylor impact specimen cut from the transverse material orientation of a Ti-6Al-4V Plate 3

The major/minor axes of the elliptical cross-sections were then used to calculate the area of the ellipses at each axial position and each individual time step. Assuming that plane sections remain plane and that volume is conserved, it can then be said that:

$$\varepsilon = ln\left(\frac{L}{L_0}\right) = \ln\left(\frac{A_0}{A}\right) \tag{6.7}$$

where ε is the true strain, L is the current length of an element, L_0 is the original length of the element, A is the current area of the element and A_0 is the original area of the element. Using the calculated areas of the elliptical cross-sections at each axial position, it is then possible to calculate the true areal strain, and thus the true effective strain, in the representative Taylor impact specimens as a function of axial position and time, as shown in Figure 6.14 and Figure 6.15.

As the true strain has been calculated as a function of time and axial position, it is then possible to calculate the true strain rate as a function of axial position by noting that:

$$\dot{\varepsilon} = \frac{d\varepsilon}{dt} = \frac{d\left(ln\left(\frac{A_0}{A}\right)\right)}{dt} \tag{6.8}$$

where $\dot{\varepsilon}$ is the true strain rate.

A plot showing the true strain rate as a function of axial position for both the longitudinal and transverse material orientations over the initial two inter-frame time steps is given in Figure 6.16.

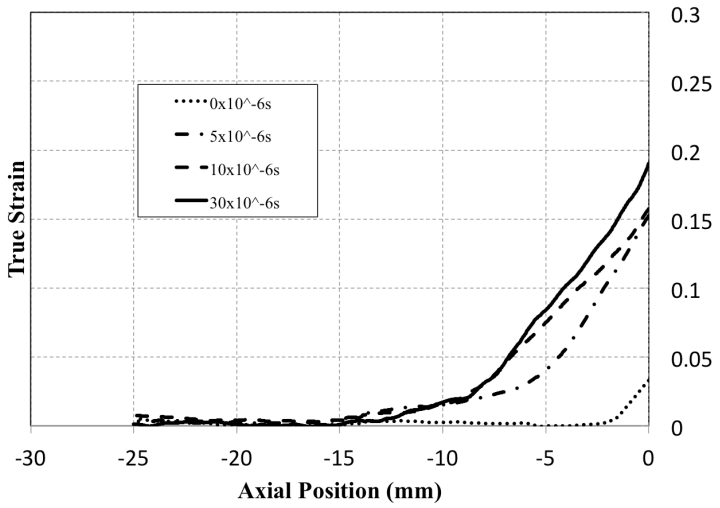


Figure 6.14 - True strain as a function of time and axial position in a representative Taylor impact specimen cut from the longitudinal material orientation

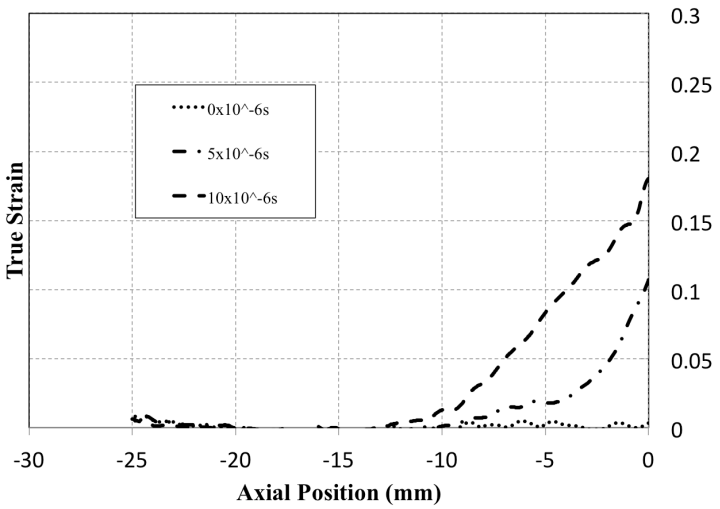


Figure 6.15 - True strain as a function of time and axial position in a representative Taylor impact specimen cut from the transverse material orientation

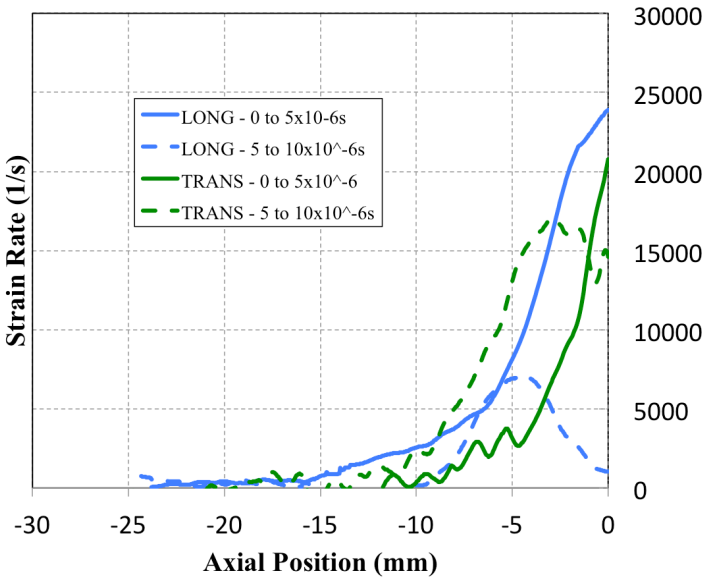


Figure 6.16 - Strain rate as a function of axial position for representative Taylor impact specimens in the longitudinal and transverse material orientations

6.5.3 Discussion

The major/minor axes of cross-sectional deformation as a function of time and axial position are given in Figure 6.12 and Figure 6.13 for Taylor impact specimens cut from the longitudinal and transverse material orientation, respectively, of a Ti-6Al-4V plate (Plate 3) previously characterised in Chapters 4 and 5. Both specimens had an impact velocity of ~160 m s^{-1}. From these plots it is clear that these representative specimens cut from orthogonal material orientations of the same plate have very different deformation histories.

In Chapter 5 the effects of macro-texture on the uniaxial plastic deformation of Plate 3 were outlined. It was shown that the preferred crystallographic orientation resulted in significant differences in the behaviour of specimens cut from the three different orthogonal material orientations, particularly in compression. The transverse material orientation had a flow stress ~18% higher than the flow stress in the longitudinal and through-thickness material orientations, at strain rates of ~10^3 s^{-1}.

In the results for the representative longitudinal Taylor impact specimen shown in Figure 6.12, the effect of the difference in yield stress between the longitudinal and transverse material orientations can clearly be seen by comparing the major and minor axes of the deforming specimen cross-sections. During the initial 5 μs of the experiment, there is very little difference between the major and minor axes. However, after 10 μs, the minor axis has stopped straining and all the remaining strain is taken by the major axis. Studying the recovered specimen, which had been marked to indicate its original orientation relative to the plate, showed that the major axis of cross-sectional deformation was parallel with the through-thickness material orientation, whereas the minor axis of cross-sectional deformation was parallel with the transverse material orientation. This correlates well with the observation that the flow stress in the transverse material orientation is significantly higher than the flow stress in the through-thickness material orientation.

Similarly, in the results for the Taylor impact specimen cut from the transverse material orientation, there are clear differences between the major and minor axes of the deforming specimens cross-section. The uniaxial characterisation results from Plate 3 showed that there was very little difference between the flow stress in the through-thickness and longitudinal material orientations, making the differences seen in the Taylor impact results an interesting feature of the specimen's deformation history.

One hypothesis that would explain this result is that during the initial stages of the impact, large stresses result in significant and rapid texture evolution in which grains are re-orientated to accommodate easy slip. This would also explain why during the initial stages of deformation in the longitudinal Taylor impact specimen there is very little difference in the major and minor axes of cross-sectional deformation. Possible sources for this rapid texture evolution and evidence of specific mechanisms will be discussed later in this chapter.

Another interesting result from these experiments can be seen by comparing Figure 6.14 and Figure 6.15, which show the true strain as a function of time and axial position for both the longitudinal and transverse specimens, respectively. Despite having very different deformation paths and durations of deformation, it is surprising to see that the final true strains in both specimens are almost identical. This can be explained by considering that for a given velocity, and thus a given kinetic energy, the material is capable of accommodating a given amount of plastic strain in the three orthogonal material orientations, resulting in different deformation paths but the same total plastic strain.

Figure 6.16 shows the true strain rate as a function of axial position for both the longitudinal and transverse Taylor impact specimens over the initial two inter-frame time steps. The propagation of the plastic deformation front can clearly be seen in both the longitudinal and transverse material orientations. As well as having different strain histories, the results in Figure 6.16 show that the specimens have very different strain rate histories. Due to easy dislocation glide in the longitudinal and through-thickness material orientations, the specimen cut from the transverse material orientation can accommodate a higher strain rate for longer, resulting in the same dissipation of kinetic energy over a shorter period of time. Comparing with the specimen cut from the longitudinal material orientation, it can be seen that despite an initially high strain rate, the strain rate in the longitudinal specimen quickly reduces. It is worth noting that the strain rates in one of the orthogonal material orientations may be high, despite a relatively low total cross-sectional area strain rate.

6.5.4 Conclusions

The results of an investigation into the effects of texture on the deformation of Ti-6Al-4V Taylor impact specimens have been presented. An optical measurement and reconstruction technique was used to give detailed information about the deformation of the Taylor impact specimens as a function of time and axial position. From this analysis, many

useful data can be obtained, such as the major/minor axes of the deforming specimens cross-section as functions of time and axial position, the true effective strain as a function of time and axial position and the true effective strain rate as a function of axial position.

It has been shown that different strain paths and strain rate histories are obtain for specimens cut from the longitudinal and transverse material orientation of a textured Ti-6Al-4V plate and that initial texturing can result in significant differences to the major and minor axes of the deforming specimens cross-sections.

It is clear from these results that the deformation of Ti-6Al-4V under complex high strain rate loading, like the classic Taylor impact test, is a difficult process to understand through macroscopic observation alone. Multiple mechanisms of deformation at the microscopic level interact in complex ways to produce the observed macroscopic response. In the following section, an initial attempt will be made to quantify these mechanisms.

6.6 Microstructure and Micro-Texture Evolution of Ti-6Al-4V During a Taylor Impact

6.6.1 Overview

It is clear from the previous analysis that studying the evolution of microstructure and micro-texture as a function of strain and strain rate is key to understanding the effects of microstructure and texture on the plastic deformation of Ti-6Al-4V during complex, high strain rate loading scenarios such as the Taylor impact test. To facilitate this study, EBSD analysis was carried out on the pre and post-deformation microstructures of the Ti-6Al-4V Taylor impact specimens tested in the previous section.

6.6.2 EBSD of Sectioned Taylor Impact Specimens

A pre-deformation specimen was cut from the longitudinal material orientation of Plate 3, sectioned along the longitudinal/though-thickness plane and prepared for EBSD analysis as outlined in Chapter 4. The results from this analysis are presented as an IPF map in Figure 6.18. The recovered deformed specimen from the longitudinal material orientation of Plate 3, which had it's strain path history analysed in the previous section, was sectioned along the longitudinal/though-thickness plane, as shown in Figure 6.17, and prepared for EBSD analysis. The EBSD analysis was carried out 200 μm from the impact face. The results from this analysis can be seen in Figure 6.19, where a "Confidence Index" threshold of 0.2 was used to remove poorly indexed points.

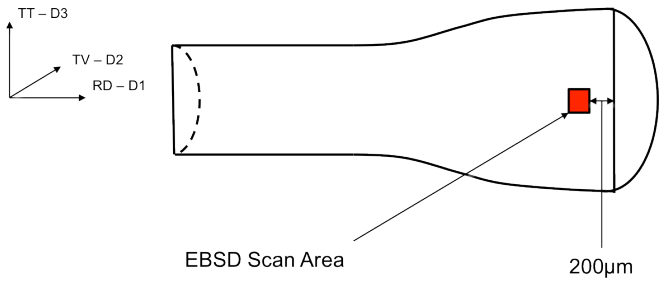


Figure 6.17 - Sectioned post-deformation longitudinal Taylor impact specimen

The same was then done for a specimen cut from the transverse material orientation of Plate 3. However, this time the specimen was sectioned along the transverse/though-thickness plane before being prepared for EBSD analysis as outlined in Chapter 4. The results from this analysis are presented as an IPF map in Figure 6.21. As done for the specimen cut from the longitudinal material orientation, a deformed specimen from the transverse material orientation of Plate 3, which had it's strain path history analysed in the previous section, was sectioned along the transverse/though-thickness plane and prepared for EBSD analysis. The EBSD analysis was carried out 200 μm from the impact face. The results from this analysis can be seen in Figure 6.21, where a "Confidence Index" threshold of 0.2 was again used.

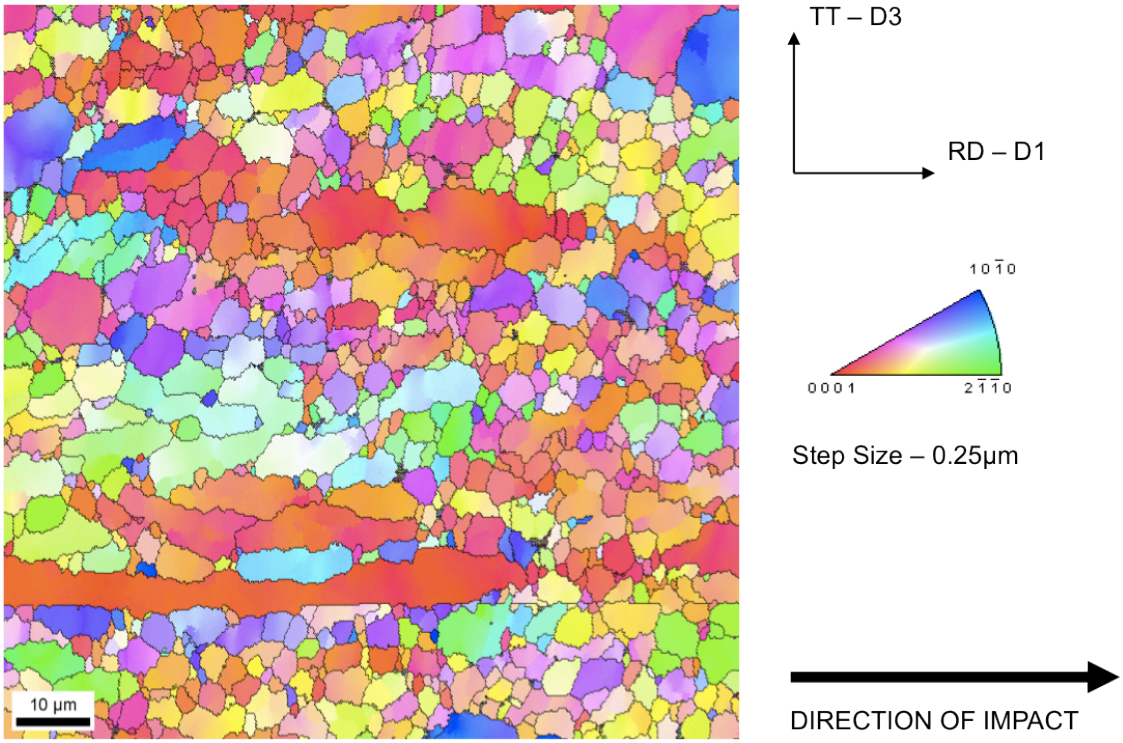


Figure 6.18 - EBSD analysis results for an undeformed longitudinal Taylor impact specimen from Plate 3

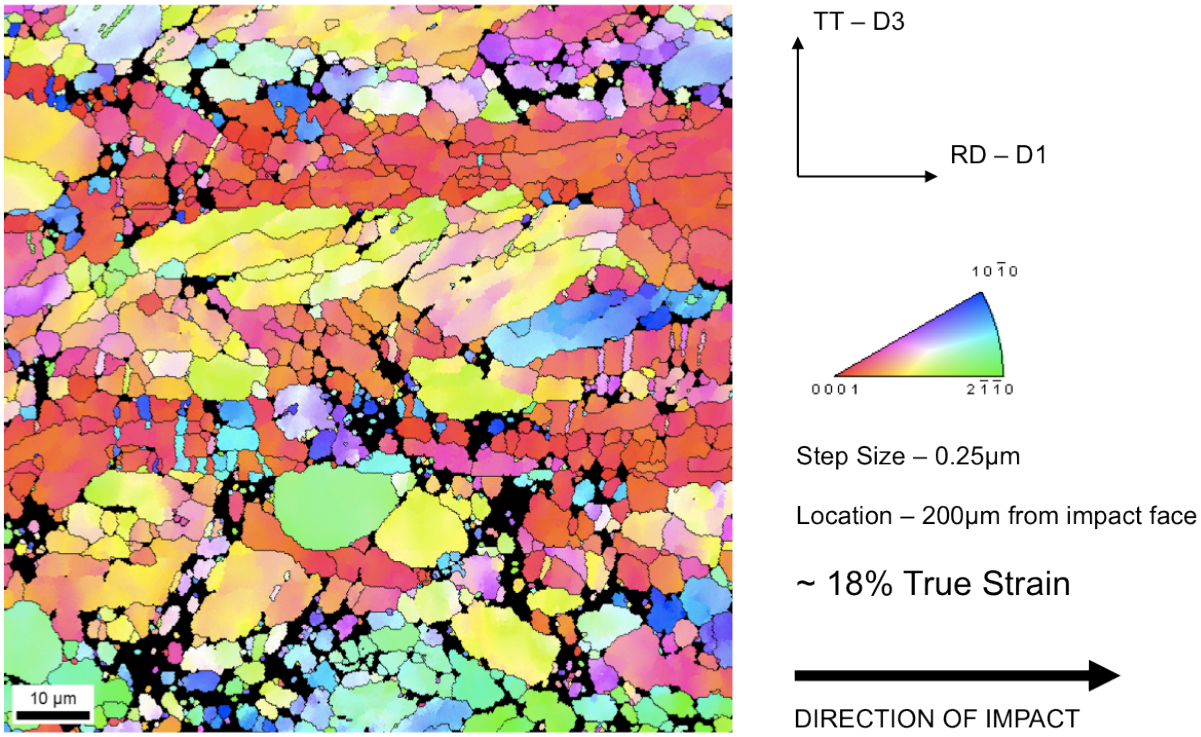


Figure 6.19 - EBSD analysis results for a deformed longitudinal Taylor impact specimen from Plate 3

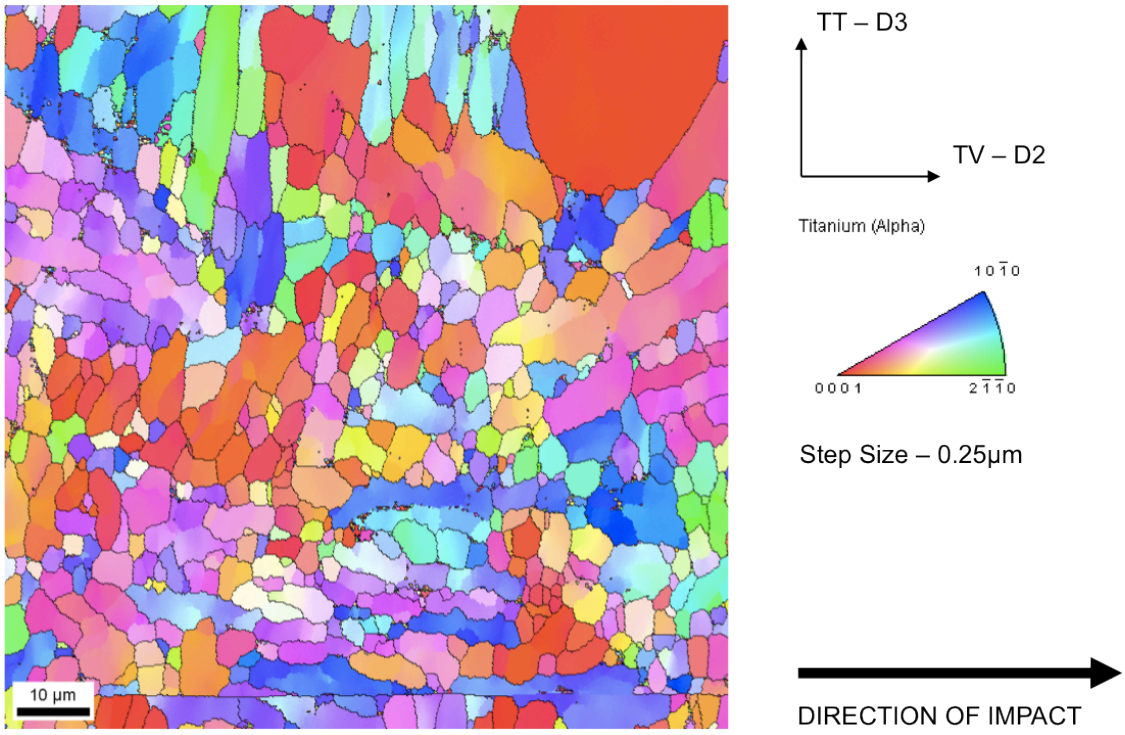


Figure 6.20 - EBSD analysis results for an undeformed transverse Taylor impact specimen from Plate 3

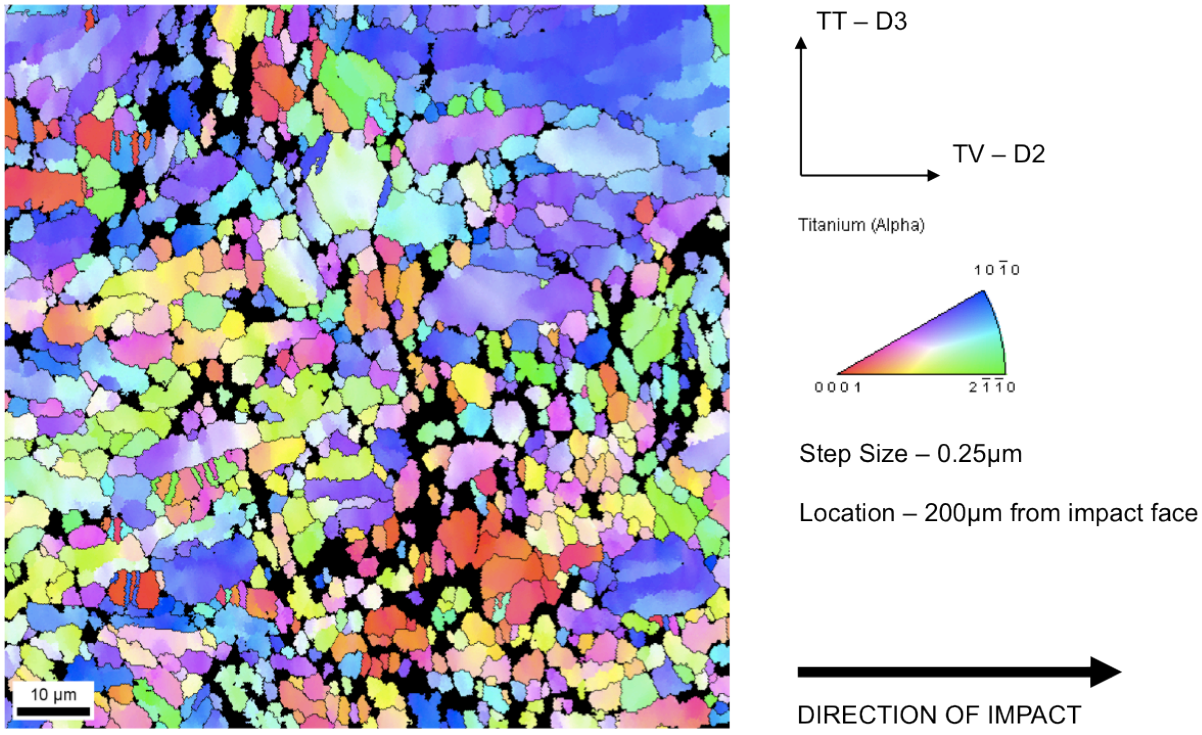


Figure 6.21 - EBSD analysis results for a deformed transverse Taylor impact specimen from Plate 3

6.6.3 Taylor Factor Maps

Due to the highly anisotropic nature of plastic deformation in the *hcp* crystal structure at a single crystal level, and the varying orientation of grains in a polycrystalline material, there can be significant differences in the applied load required to yield specific grains. Although IPF maps give an indication of the relative stresses required to yield specific grains comprising the polycrystalline aggregate, it is far more informative to map the orientation of the grains in relation to the active slip systems and applied loading condition.

The most widely used method of linking the orientation of a crystal to the active slip systems and applied loading condition is through either a Schmidt or Taylor factor. It was decided that for this study a Taylor factor approach should be used, as this encompasses all the information given by the Schmidt factor, with the added usefulness of providing a link between the critically resolved shear stress and the macroscopic yield stress.

The analysis required to calculate the Taylor factor of each grain comprising a polycrystal will not be outlined in detail. For the purposes of this work, it is enough to understand that the Taylor factor is calculated by assuming that a uniform strain is applied to the polycrystalline material under investigation. The stress is then calculated by considering the most favourable slip system for each of the grains, with the assumption of uniform strain rigidly imposing compatibility between the grains [7], [75].

For the Taylor factor analysis it was assumed that the only active slip systems were the Prismatic and Basal $\langle \boldsymbol{a} \rangle$ type slip systems, which were assumed to have the same critically resolved shear stress, and that the deformation matrix for a compression test in the direction of impact is representative of the classic Taylor impact test. The EDAX OIM Data Analysis software package was then used to calculate a Taylor factor for each of the recorded points from the previously analysed deformed microstructures. The results of these analyses were plotted as Taylor factor maps, as shown in Figure 6.22 and Figure 6.23.

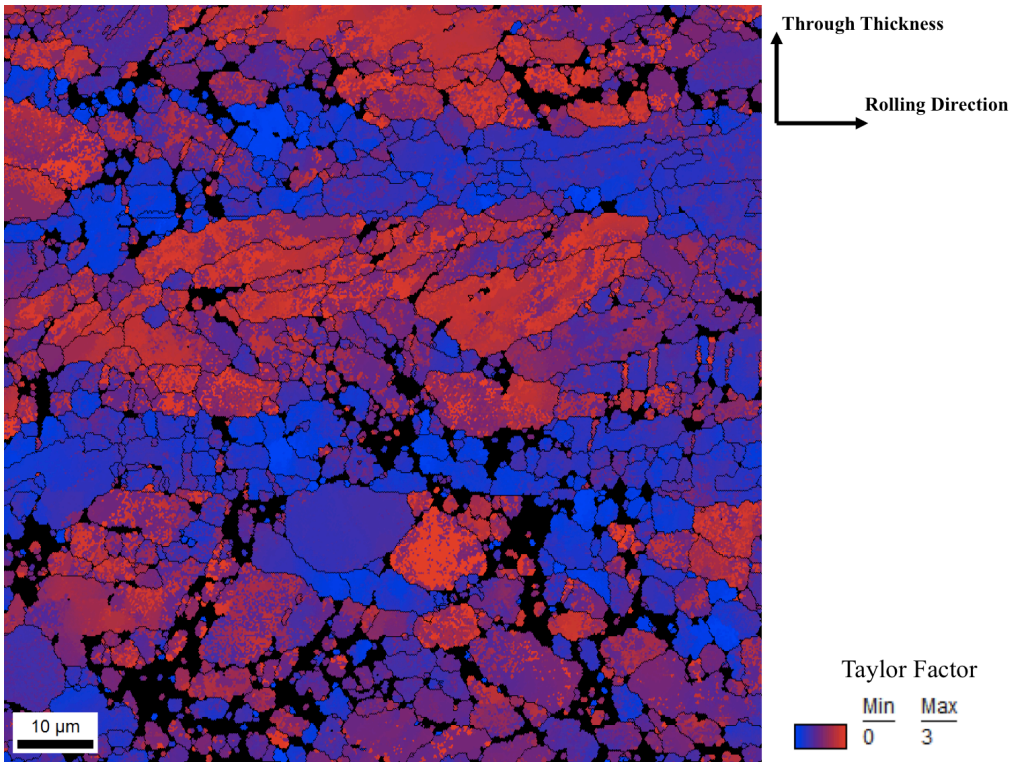


Figure 6.22 - Taylor factor map of the deformed longitudinal Taylor impact specimen from Plate 3

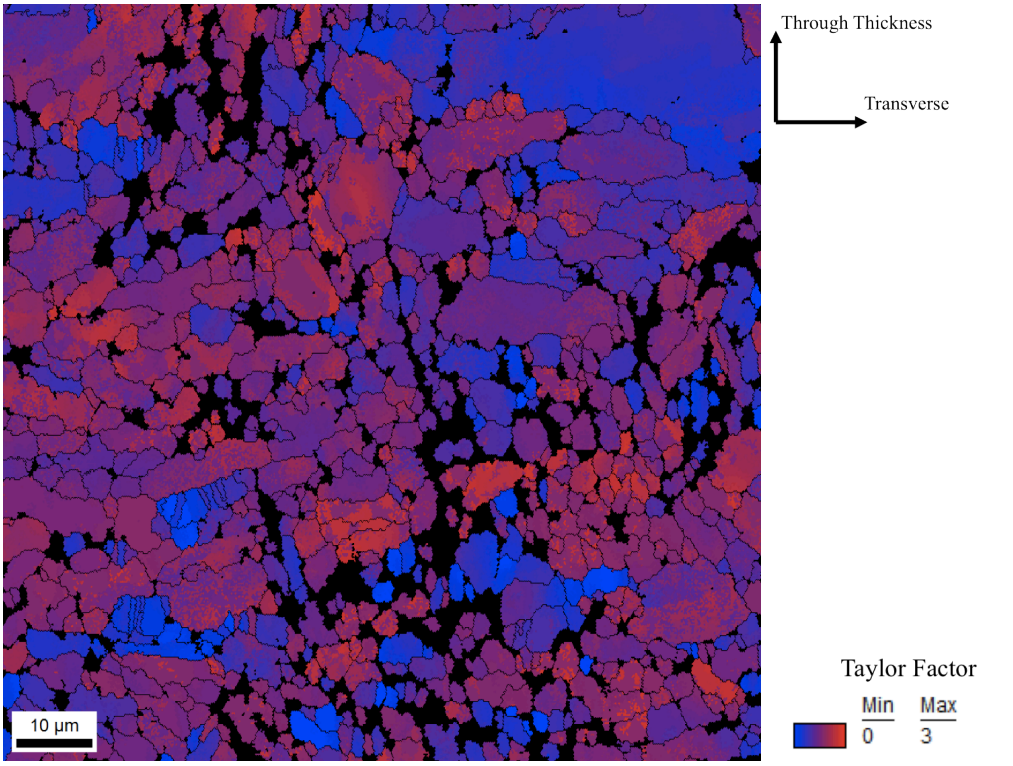


Figure 6.23 - Taylor factor map of the deformed transverse Taylor impact specimen from Plate 3

6.6.4 Discussion

Before beginning an in-depth discussion on the mechanisms of plastic deformation from the IPF maps shown in Figure 6.18, Figure 6.19, Figure 6.20 and Figure 6.21, it is first instructive to determine the final strains and strain path histories of the areas under investigation. From the analysis in the previous section, it can be shown that the area 200 μm from the impact face of the specimen cut from the longitudinal material orientation has a final true strain of ~18% with a peak strain rate of ~24,500 s^{-1} over the initial 5 μs. Similarly, it can be shown that the area 200 μm from the impact face of the specimen cut from the transverse material orientation has a final true strain of ~17% with a peak strain rate of ~19,500 s^{-1} over the initial 5 μs. However, it is worth noting that for the transverse specimen, high strain rates are maintained for longer, with the strain rate continuing at ~15,000 s^{-1} over the subsequent 5 μs, whereas in the longitudinal specimen, the strain rate quickly drops to 1000 s^{-1} over the subsequent 5 μs.

These differences in the strain path histories of the two specimens mean that it is not possible to directly compare the mechanisms of plastic deformation in the two specimens. However, comparisons can still be made between the overall deformations of the specimens to determine the effects of texture on the deformation history of the two specimens.

An initial qualitative comparison between the undeformed (Figure 6.18, Figure 6.22) and deformed (Figure 6.19, Figure 6.23) microstructure of the longitudinal specimen shows a number of very interesting results. Firstly, noting that the level of plastic strain correlates with the level of misorientation between measured lattice points within a grain, it can be seen that the majority of plastic deformation is accommodated by grains/laths that form part of α colonies or macrozones. It can also be seen that, despite being preferentially orientated for easy slip relative to direction of loading i.e. the ***c***-axis of the *hcp* unit cell is pointing out of

the page, allowing easy glide of dislocations along $\langle \boldsymbol{a} \rangle$ type slip systems, the primary α grains appear to have undergone little deformation, acting as hard particles in a deforming matrix.

Secondly, a number of twins can be observed in the deformed microstructure. It has been previously reported that at high strain rates the volume fraction of deformation twins increases significantly in Ti-6Al-4V, when compared with quasi-static strain rates [25]. The deformed microstructure in Figure 6.19 confirms these observations. However, the addition of the textural data given by EBSD allows for an interesting expansion of this hypothesis.

From the Taylor factor maps in Figure 6.22 and Figure 6.23, where "hard-orientated" grains with a high Taylor factor are colored red and "soft-orientated" grains with a low Taylor factor are colored blue, relative to the direction of loading, it can clearly be seen that twinning only occurs in grain/lath colonies preferentially orientated for easy slip, with cases of multiple twins occurring in one grain/lath. This has a profound impact on the role twinning plays in the deformation process. However, further analysis of the data in Figure 6.18 and Figure 6.19 is required to make any conclusions.

Using the data in Figure 6.18 and Figure 6.19, it is possible to construct plots of the observed grain-to-grain crystallographic misorientations. This data can then be used to determine what types of twins have been observed [9], [60]. Figure 6.24 shows the misorientations between grains in the undeformed microstructure. Due to the influence of α colonies and macro-zones, the initial 20° of misorientations are ignored. From Figure 6.24 it can be seen that the undeformed microstructure has a relatively random distribution of misorientations between grains.

This method was then applied to the deformed microstructure given in Figure 6.19. Figure 6.25 shows the misorientations between grains in the deformed microstructure. As with the previous undeformed microstructure, the initial 20° of misorientations between grains of the deformed microstructure must be ignored.

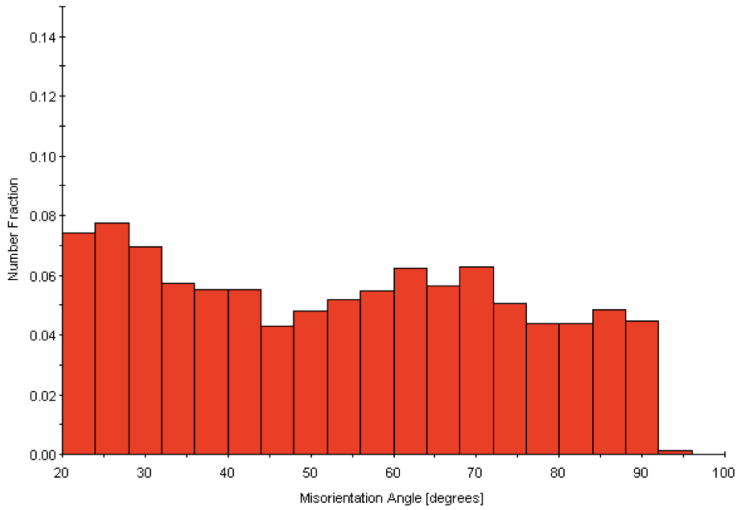


Figure 6.24 - Number fraction of misorientations between grains in an undeformed Taylor impact specimen cut from the longitudinal material orientation

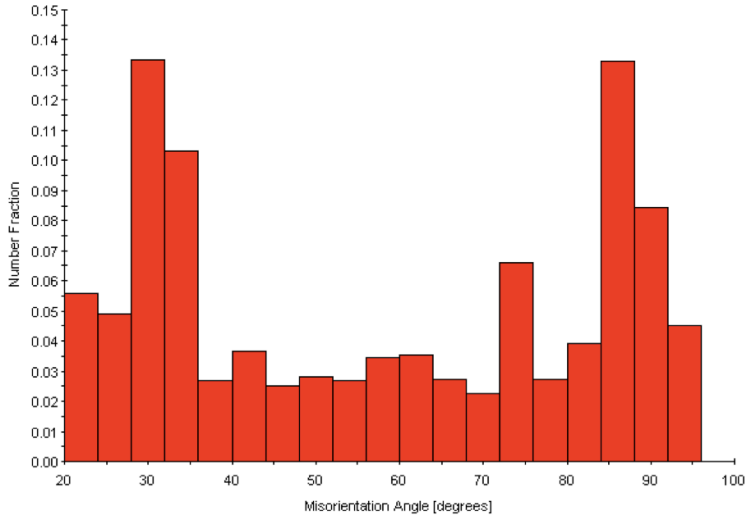


Figure 6.25 - Number fraction of misorientations between grains in a deformed Taylor impact specimen cut from the longitudinal material orientation

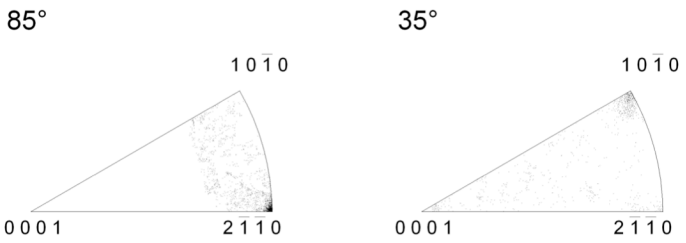


Figure 6.26 – IPF projections of "grain-to-grain" misorientations of a longitudinal Taylor impact specimen over the ranges of 35±5° and 85±5°

Comparison between the grain-to-grain misorientation plots of the undeformed and deformed microstructures show that significant microstructural evolution has occurred during the Taylor impact experiment. It is clear from the misorientation plot of the deformed microstructure that "grain boundaries" have preferentially been formed with misorientations in the range of 30-35° and 85-90°. These exactly correlate with the deformation twinning angles for so-called "tensile" twins [9], [60]. It is worth noting that the terminology of "compressive" and "tensile" twins can be slightly misleading, as compression in one orientation results in tension in the other orientation, relative to the twinning plane, and vice-versa. To confirm the presence of these twinning systems, the data between "grains" with misorientations of 35±5° and 85±5° were then projected back onto IPF plots to determine if these misorientations were acting over specific planes [24]. The IPF plots for this analysis are given in Figure 6.26.

The data presented in Figure 6.26 confirms that the additional grain-to-grain misorientations observed in the deformed microstructure of the longitudinal Taylor impact specimen are in fact deformation twins of the $\{10\bar{1}2\}$ and $\{10\bar{2}1\}$ type.

In terms of deformation, "tensile" twins of the $\{10\bar{1}2\}$ type result in a contraction along the direction of loading, or the longitudinal material orientation, and an extension in the transverse material orientation. For the case of the 85±5°, this results in a reorientation of the ***c***-axis of the *hcp* unit cell from pointing parallel to the transverse material axis, thus accommodating easy slip in the longitudinal material orientation, to pointing parallel to the longitudinal material orientation, thus accommodating easy slip in the transverse material orientation. The same is true for the 35±5° $\{10\bar{2}1\}$ type twinning but to a lesser extent.

To further analyse the deformed microstructure of the Taylor impact specimen cut from the longitudinal material orientation, another EBSD scan, this time with a higher-resolution, was completed on an area just above the previously scanned area. The results of

this analysis are presented in the form of an IPF map in Figure 6.27. From this plot it can clearly be seen that a significant number of deformation twins are present. The grain-to-grain misorientations were analysed as before and once again showed that the twins present were of the $\{10\bar{1}2\}$ type with an 85° misorientation. A further point-to-point analysis was carried out, the results of which are also shown in Figure 6.27. From this higher resolution EBSD analysis it can clearly be seen that a significant number of deformation twins have been nucleated. It is interesting to note that the relative number of visible twins has increased. There are two possible explanations for this increase; the area observed happens to be a highly deformed region with a higher number of twins or the increased resolution, and the resultant reduction in SEM spot size, has enabled the EBSD analysis to capture twinned regions which would have previously been unindexed. At lower resolutions the larger spot size may cause the interaction volume to cover the twinned and untwinned regions, resulting in dual Kikuchi patterns that cannot be indexed. This would explain the relatively large regions of unindexed material seen in Figure 6.19 and Figure 6.21. However, more regions would need to be analysed at high resolution to confirm/refute this point.

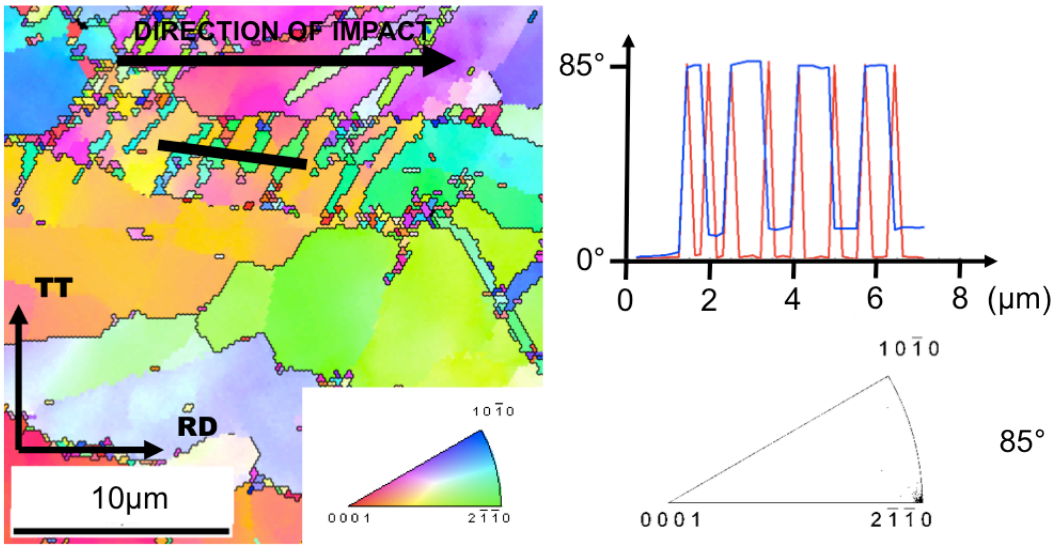


Figure 6.27 – High-resolution IPF map and misorientation profile for a deformed longitudinal Taylor impact specimen from Plate 3

A qualitative analysis of the undeformed and deformed microstructures of the Taylor impact specimens cut from the transverse material orientation proves to be far less fruitful than that of the longitudinal material orientation. No clear channels of flow can be seen. However, it is worth noting that as with the longitudinal specimen, twinning has occurred and appears to be preferentially occurring in grains orientated for easy slip. It is also worth noting that the material seems to be more "broken-up" than that of the longitudinal specimen. This may be due to the fact that the material has sustained high strain rates for a longer period of time. Further, the higher percentage of unindexed points may indicate that significant deformation twinning has occurred in those unindexed region. However, more high resolution EBSD would be required to confirm this hypothesis.

Using the data in Figure 6.20 and Figure 6.21, a grain-to-grain misorientation analysis was completed. The results of this analysis for the undeformed microstructure of Figure 6.20 is given in Figure 6.28. From this analysis it can be seen that the undeformed microstructure has a random misorientation distribution. Once again, it is worth noting that in Figure 6.28 the initial 20° of grain-to-grain misorientations are ignored due to the influence of α colonies.

A misorientation analysis was then carried out on the deformed microstructure seen in Figure 6.21 and is given in Figure 6.29. From the plot in Figure 6.29 it can be seen that, as with the longitudinal deformed microstructure, a peak occurs around 85±5°. Interestingly, no peak is observed around the 35±5° misorientations, indicating that only one type of twin is formed in the Taylor impact specimen cut from and loaded along the transverse material orientation.

To confirm the type of twin, the 85±5° misorientation were then projected onto an IPF plot to determine the plane the misorientations occurred around. The result of this analysis can be seen in Figure 6.30, where it is clear that the twins present are of the of the "tensile" $\{10\bar{1}2\}$ type with a 85° misorientation.

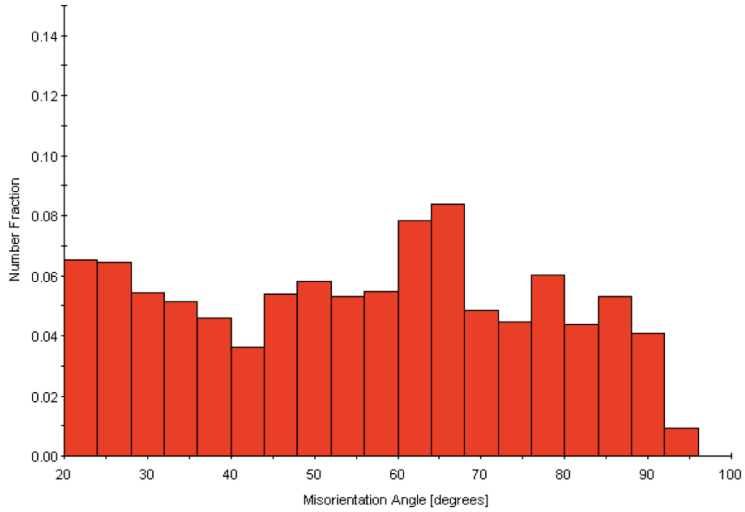


Figure 6.28 - Number fraction of misorientations between grains in an undeformed Taylor impact specimen cut from the transverse material orientation

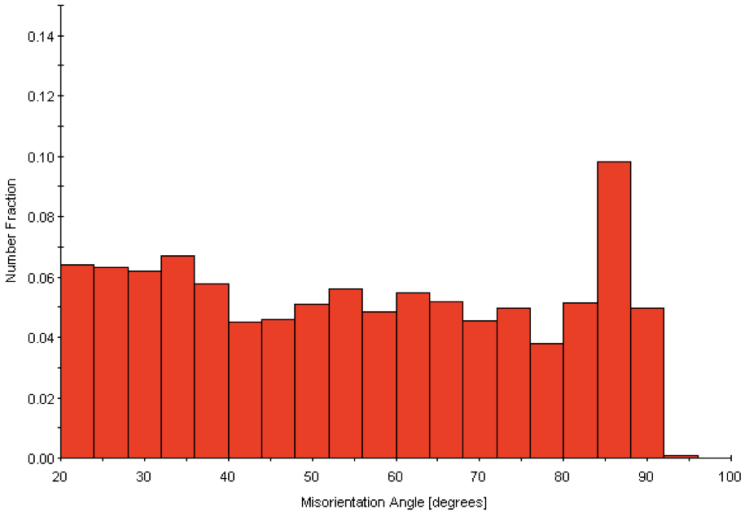


Figure 6.29 - Number fraction of misorientations between grains in a deformed Taylor impact specimen cut from the transverse material orientation

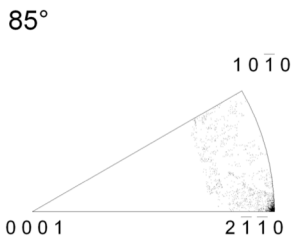


Figure 6.30 - IPF projections of "grain-to-grain" misorientations of a transverse Taylor impact specimen over the ranges of 85±5°

6.6.5 Conclusions

From the EBSD analysis of the undeformed and deformed Taylor impact specimens cut from the longitudinal and transverse material orientations of a previously characterised Ti-6Al-4V plate, it has been shown that the plastic deformation of Ti-6Al-4V is a complex process involving the interaction of numerous mechanisms of plastic deformation.

Qualitative analysis of the deformed microstructures indicated that micro-texture plays a key role in defining the mechanics of deformation. In the deformed longitudinal specimen it appears as though grains/laths of α colonies and macro-zones maintain plastic deformation by forming channels of flowing material. Further, primary α grains appear to undergo very little deformation and effectively act as hard particles in a deforming matrix. However, it should be noted that, due to the nature of this post-experiment observation, further *in-situ* investigations of this feature of the deformation process are required to conclusively prove this hypothesis.

Another feature clearly seen in the deformed microstructures is the presence of deformation twins. Interestingly, it appears as though these deformation twins only occur in grains/laths of α colonies and macro-zones preferentially orientated for slip in the direction of loading. Misorientation analysis was used to determine the type of deformation twins, with both material orientations showing “tensile” type twins. Such twins were shown to result in the reorientation of the grain’s crystal lattice to accommodate easy slip in the cross-sectional directions. Finally, it was noted that the $\{10\bar{1}2\}$ type twin with an 85° misorientation was observed in both loading orientations, whereas the $\{10\bar{2}1\}$ type twinning a 35±5° misorientation is only observed in the specimen loaded along the longitudinal material direction.

6.7 Conclusions

An extension of the classic Taylor impact test has been used to investigate the effects of macro and micro-texture on the deformation of Ti-6Al-4V under complex high strain rate loading scenarios.

The addition of an optical measurement and reconstruction technique to the classic Taylor impact test was outlined, with trials carried out on specimens cut form commercially pure Zirconium plate. The application of this technique was verified by comparison of the outputted results with those of a coordinate measurement machine. Excellent agreement was seen between the two methods. The application of this technique allowed key information to be obtained on the deformation of the Taylor impact specimens under investigation, such as; the major/minor axes of the deforming cross-sectional area as a function of time and axial position, the true strain as a function of time and axial position and the strain rate as a function of axial position.

The validated optical measurement and reconstruction technique was then used to study the effect of texture during Taylor impact testing of specimens cut from the in-plane material orientations of a heavily textured Ti-6Al-4V plate. Differences in the strain path and strain rate histories of the specimens cut from the longitudinal and transverse material orientations were highlighted. From this analysis it is clear that texture plays a significant role in defining the macroscopic deformation response of Ti-6Al-4V. However, to further understand these effects, the interactions of the underlying microscopic mechanisms of plastic deformation needed to quantified to fully understand the role of texture in the deformation of Ti-6Al-4V.

To facilitate this understanding, EBSD analysis of the undeformed and deformed microstructures of the previously analysed Ti-6Al-4V Taylor impact specimens was carried out. From this analysis a number of key features of the microscopic deformation of Ti-6Al-4V were observed and quantified where possible.

Firstly, it appears as though α colonies and macro-zones of grains/laths form flowing channels of plastic deformation. Conversely, primary α grains, even if well orientated for slip with respect to the direction of loading, appear to be relatively undeformed, acting as hard particles in a deforming matrix.

Another key feature of the deformed microstructures observed using EBSD analysis was the presence of deformation twins. Interestingly, the observed twins preferentially occur in α colonies of grains/laths that are orientated for easy slip relative to the direction of loading. A misorientation analysis was carried out, which showed that the twins were of the "tensile" type, resulting in a reorientation of the twinned regions to allow for easy slip in the cross-sectional directions.

7 MODELLING THE EFFECTS OF MICROSTRUCTURE AND TEXTURE ON THE FLOW STRESS OF Ti-6Al-4V

7.1 Overview

In this chapter a model will be developed to predict the flow stress of Ti-6Al-4V using parameters based on key microstructural and textural features that can be easily measured and quantified using widely available characterisation techniques. The intention is that the model be used to optimise the microstructure and texture of Ti-6Al-4V for use in specific applications.

A brief summary will be given of two key empirical and physically based material models that are currently in widespread use within both academia and industry before a general framework for the new Ti-6Al-4V model is outlined. The Ti-6Al-4V model will then be compared with experimental results and the effects of varying different microstructural features within the model studied. Finally, a brief overview will be given of the intended industrial applications of the model, with a number of general frameworks summarised.

7.2 Phenomenological Material Models

7.2.1 Overview

Over the last 50 years a number of empirically based constitutive equations have been developed to describe the plastic behaviour of metals over the range of strain rates and temperatures that are typically of interest to the general engineering community. By far the most widely used of these models is the so-called Johnson-Cook model.

7.2.2 Johnson-Cook Model

The Johnson-Cook model is based on a number of fundamental observations about the plastic behaviour of metals at low to moderate strain rates and low homologous temperatures. Firstly, it is well known that the initial onset of yield and strain hardening behaviour of metals at low temperatures can be described by an empirical equation of the form:

$$\sigma = \sigma_0 + K\varepsilon^n \tag{7.1}$$

where σ is the uniaxial flow stress, ε is the uniaxial strain, σ_0 is the uniaxial yield stress, K is the strengthening coefficient and n is the strain hardening exponent. Likewise, it has been shown that the strain rate dependence of the flow stress for most metals over a strain rate range, typically in the order of 10^{-4} - 10^{2} s^{-1}, can be expressed in the form:

$$\sigma \propto \ln \dot{\varepsilon} \tag{7.2}$$

where $\dot{\varepsilon}$ is the strain rate. Finally, it has been shown that the temperature dependence of the flow stress can be expressed by:

$$\sigma = \sigma_r \left[1 - \left(\frac{T - T_r}{T_m - T_r}\right)^m\right] \tag{7.3}$$

where T is the temperature, T_m is the melting temperature of the material, T_r is a reference temperature, σ_r is the flow stress at the reference temperature and m is the temperature dependent exponent.

Johnson and Cook [61], [62] combined these well known basic formulations for the strain, strain rate and temperature dependence of a metals yield and flow stress into the following constitutive equation:

$$\sigma = (\sigma_0 + B\varepsilon^n)\left(1 + C\ ln\frac{\dot{\varepsilon}}{\dot{\varepsilon}_0}\right)(1 - \ (T^*)^m) \tag{7.4}$$

where $\dot{\varepsilon}_0$ is the reference strain rate at which σ_0 is measured. T^* is given by:

$$T^* = \frac{T - T_r}{T_m - T_r} \tag{7.5}$$

Due to its ease of use and relative simplicity, the Johnson-Cook model has seen widespread use in the material modelling community. With only five experimentally determined parameters, all of which can be obtained using standard uniaxial compression or tension testing, the model is simple to calibrate and implement in modelling frameworks such as finite element analysis.

However, the Johnson-Cook model has a number of significant weaknesses. Firstly, it is not a physically based model. As a result, extrapolation of the model beyond the regime for which the model parameters were experimentally determined should be done with great caution and is not recommended. Further, it should be noted that the strain hardening, strain rate dependence and temperature dependence are experimentally coupled. This means changes of behaviour in the strain hardening, strain rate dependence and temperature dependence cannot be accounted for without affecting the others.

7.3 Physically Based Material Models

7.3.1 Overview

In the preceding section the strengths and weaknesses of the Johnson-Cook model, and phenomenological models in general, were detailed. From this analysis it is clear that a key weakness of phenomenological models of material behaviour is that the underlying mechanics of plastic deformation are ignored in favour of a simple modelling approach. Although this is of great use for providing a method to validate a materials response under well-understood conditions, this approach has little to offer in the way of predictive capability and provides no framework for understanding the fundamental mechanisms governing plastic deformation.

To understand the plastic behaviour of materials it is therefore necessary to incorporate the mechanisms of plastic deformation into a material modelling framework. This class of material models are often referred to as "physically based models", as the underlying physics of plastic deformation are used as a basis for their formulation.

The mechanisms of plastic deformation in metals were outlined in Chapter 2. These typically consist of the motion of dislocations through the crystal structure and/or deformation twinning. For the time being, deformation twinning shall be ignored, and the focus will be on the motion of dislocations through a crystal lattice structure.

7.3.2 Thermally Activated Dislocation Motion

Before a modelling framework for the thermally activated motion of dislocations through a crystal lattice can be developed, the underlying physics must be described. As briefly discussed in Chapter 2, if a shear stress of an appropriate magnitude is applied to a metal containing dislocations, those dislocations will begin to glide along preferential planes and in preferential directions. Opposing the motion of these dislocations, at an atomic level, is the Peirerls-Nabarro forces, which can be thought of as the inherent lattice resistance to

dislocation motion. As each of the dislocations move between atomic equilibrium positions, they must overcome the Peierls-Nabarro forces. The stress required to overcome the Peierls-Nabarro forces is know as the Peierls-Nabarro stress [17]. If a single dislocation was moving through an infinitely large perfect crystal (apart from the imperfection of the dislocation itself), the only barrier to that dislocations motion would be the Peierls-Nabarro forces and thus the yield stress of the material would simply be the Peierls-Nabarro stress. From this point onwards all stresses and strains will be considered to be resolved shear stresses and shear strains unless explicitly stated i.e. parallel to the slip direction and along the slip plane.

In reality, dislocations must overcome a number of short-range barriers to dislocation motion, such as solute atoms, interstitial atoms and vacancies in the crystal lattice, and/or long-range barriers to dislocation motion, such as grain boundaries and twin boundaries [17].

As thermal energy is added to the system, the amplitude of vibration of the atoms in the crystal lattice increases. Under mechanical load, added thermal energy increases the probability that a dislocation will overcome a given short-range barrier to its motion. Therefore, the stress required to overcome a short-range barrier reduces as temperature increases [5]. This is illustrated in Figure 7.1.

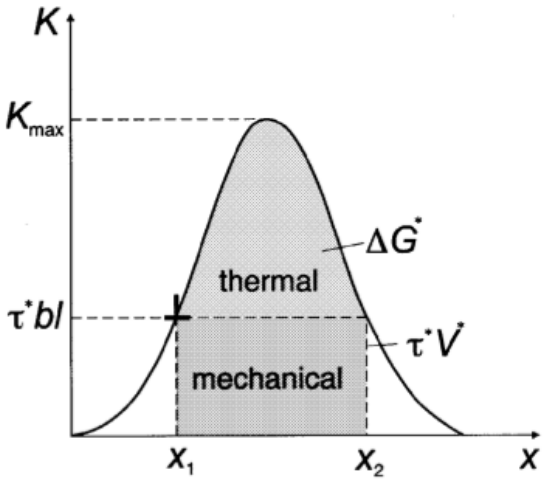


Figure 7.1 - Overcoming of short-range barriers to dislocation motion by thermal + mechanical energy [5]

A similar argument can be given for the effect of strain rate on the stress required to overcome a given short range barrier to dislocation motion. If the strain rate is increased, the time available for a dislocation to overcome a short-range barrier is reduced, thus the stress must increase to increase the probability that the dislocation will overcome that barrier to its motion and achieve the dislocation velocity required to maintain plastic flow at the increased strain rate [5], [17].

To describe these effects thermodynamically, it is instructive to consider a single dislocation gliding along a single slip plane in a given slip direction, designated the x direction, under an applied resolved shear stress, τ. The applied shear stress results in a force per unit length, F, to be generated on the dislocation line, which can be expressed as:

$$F = \tau b \tag{7.6}$$

where b is the Burgers vector.

If the considered dislocation were to encounter short-range obstacles to its motion, with spacing between obstacles along the dislocation line, l, each of which produced a resisting force, K. It can then be said that the driving force per obstacle is:

$$F_{obstacle} = \tau b l \tag{7.7}$$

From the analysis outlined above and as shown in Figure 7.1, at a temperature of 0 K, the dislocation will stop moving when $F_{obstacle}$ is greater than K_{max}. To overcome the barrier and move the dislocation line from x_1 to x_2, the required change in energy is the area under the curve between states x_1 and x_2 in Figure 7.1. This is known as the Helmholtz free energy change and can be calculated by integrating K with respect to x between the limits x_1 to x_2:

$$\Delta G_0 = \int_{x_1}^{x_2} K \, dx \tag{7.8}$$

Once again, as shown in Figure 7.1, the energy required to overcome the short-range barrier can be split into thermal and mechanical components. The work done by the mechanical load can be calculated from the applied load and the activation volume:

$$L = \tau V \tag{7.9}$$

where L is the mechanical work and V is the activation volume, which can be calculated from:

$$V = bl(x_2 - x_1) \tag{7.10}$$

The thermal component of the required change in energy is typically termed the free energy of activation and is the Gibbs free energy change between states x_1 and x_2:

$$\Delta G = \Delta G_0 - L \tag{7.11}$$

Assuming that a dislocation will overcome a short-range barrier to its motion if its energy is equal to or higher than the energy of the barrier, from the preceding analysis it can be shown that the frequency at which a dislocation overcomes that barrier is given by:

$$v = v_0 \exp\left(-\frac{\Delta G}{kT}\right) \tag{7.12}$$

where v is the frequency which a dislocation overcomes the barrier to its motion, v_0 is the vibrational frequency of the dislocation, ΔG is the shear stress-dependent Gibbs free energy of activation, k is Boltzmann's constant and T is the temperature. Based on the time waiting to overcome the barrier, it can be then shown that:

$$\dot{\gamma} = \dot{\gamma}_0 exp\left(-\frac{\Delta G}{kT}\right) \tag{7.13}$$

where $\dot{\gamma}$ is the applied strain rate and $\dot{\gamma}_0$ is a reference strain rate, defined as:

$$\dot{\gamma}_0 = v_0 \rho b l \tag{7.12}$$

where ρ is the dislocation density. Rearranging for ΔG it can then be shown that:

$$\Delta G = kT\ ln\left(\frac{\dot{\gamma}_0}{\dot{\gamma}}\right) \tag{7.13}$$

From this expression it can be seen that ΔG increases with increasing T and decreases with increasing $\dot{\gamma}$ [5].

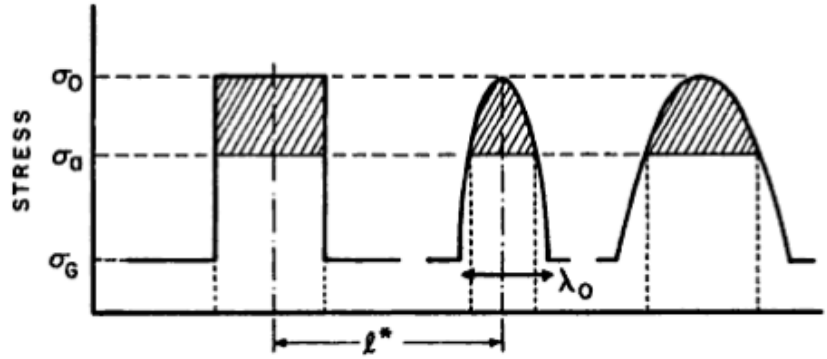


Figure 7.2 - Typical shapes of barriers to dislocation motion - rectangular, hyperbolic and sinusoidal [17]

Taking into account the shape of the barrier to dislocation motion, it can then be shown that:

$$\Delta G = \Delta G_0 \left[1 - \left(\frac{\tau}{\tau_0}\right)^p\right]^q \tag{7.14}$$

where τ_0 is the shear stress at 0 K and p and q define the shape of the barrier to dislocation motion [66], [5], [17]. A number of different barrier shapes are shown in Figure 7.2.

As long-range barriers to dislocation motion are relatively far from the dislocation, they cannot be overcome by thermal energy and instead create a back-stress that further resists the motion of dislocations. Taking this into consideration, it is instructive to separate the shear stress as follows:

$$\tau = \tau_{athermal} + \tau_{thermal} \tag{7.15}$$

where τ is the shear stress, $\tau_{athermal}$ is the temperature and strain rate independent shear stress due to long-range barriers to dislocation motion and $\tau_{thermal}$ is the temperature and

strain rate dependent shear stress required to overcome short-range barriers to dislocation motion [66], [5], [17].

Using this analysis of the thermally activated motion of dislocations as a basis, a number of physically based models have been developed to capture the plastic deformation behaviour of metals. The most general of these models, and one widely used within the high strain rate material modelling community, is the mechanical threshold stress model.

7.3.3 Mechanical Threshold Stress Model

Using the analysis of thermally activated dislocation motion outlined in the preceding section, Kocks and Mecking [63] developed a physically based model that captures the temperature and strain rate dependence of a materials yield stress. This model is based on the observation that metals have a threshold stress at 0 K that can be used as a reference stress in the framework outlined above, for that reason the model is known as the Mechanical Threshold Stress (MTS) model. This model has successfully been used as a basis for a wide range of material models [18], [63–65].

Normalising for the temperature dependent shear modulus, μ, the general framework for the MTS model can be written as:

$$\frac{\tau_{thermal}}{\mu} = S(T, \dot{\gamma}) \frac{\tau_0}{\mu} \tag{7.16}$$

where $\tau_{thermal}$ is the yield stress due to thermally activated dislocation motion and τ_0 is the mechanical threshold stress. S is a function that defines the ratio between the mechanical threshold stress and the temperature and strain rate dependent stress. Using the analysis of thermally activated dislocation motion outlined previously and a normalised activation energy, g_0, it can be shown that the function defining the ratio between the temperature and strain rate dependent shear stress and the mechanical threshold stress is given by:

$$S = \left[1 - \left(\frac{kT}{g_0 \mu b^3} ln\left(\frac{\dot{\gamma}_0}{\dot{\gamma}}\right)\right)^{1/q}\right]^{1/p} \tag{7.18}$$

Using this framework, the effect of different short-range barriers to dislocation motion can then be added to give the total resolved thermal yield stress, $\tau_{thermal}$. The effects of long-range barriers to dislocation motion can then be accounted for as part of the athermal stress component, $\tau_{athermal}$. As previously discussed, these can include grain boundaries, twin boundaries and many other obstacles to dislocation motion that result in a long-range stress field. Further, the effects of strain hardening through the accumulation/annihilation of dislocations can be included separately, typically with the dislocation density taken as an internal state variable.

For a comprehensive overview of the classical dislocation mechanics concepts discussed in this section, this author highly recommends the excellent works by Hull and Bacon [5], and Kocks, Argon and Ashby [66].

7.4 Ti-6Al-4V Model

7.4.1 Overview

A model will now be developed to capture the plastic deformation behaviour of Ti-6Al-4V with a bi-modal (duplex) microstructure using physically based parameters that relate to key microstructural and textural features of the alloy. Using the MTS model as its basis, the model will be developed to include the effects of temperature, strain rate, solute atom content (or percentage weight Aluminium), dislocation density and microstructural features such as volume fraction primary α, primary α grain size, macro-zones of micro-texture and macro-texture.

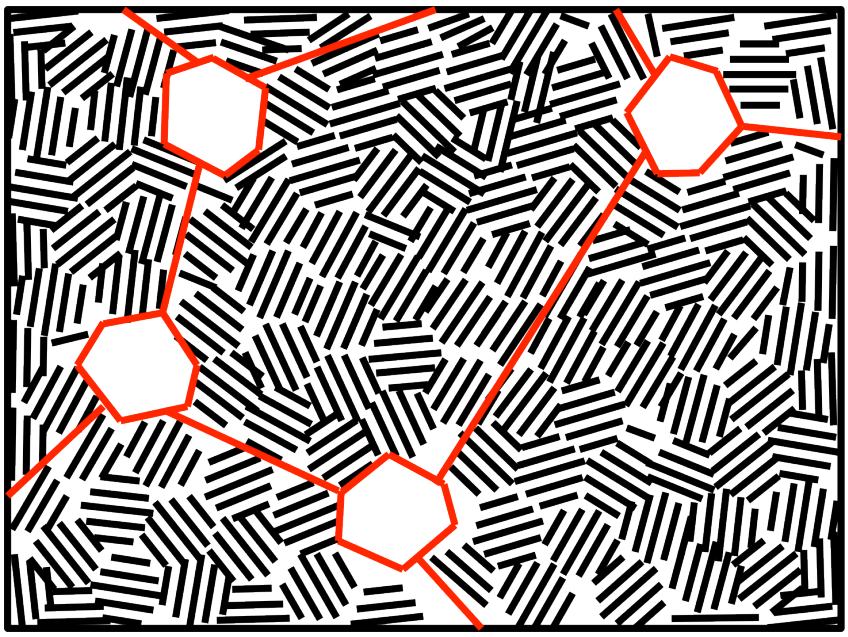


Figure 7.3 - Idealised Ti-6Al-4V bi-modal microstructure

The bi-modal Ti-6Al-4V microstructure will be idealised as shown in Figure 7.3, where the α/β lath structures are contained within colonies/macro-zones formed from prior β grains. The boundaries between these colonies are highlighted in red. Primary α grains are found at the triple-points between prior β grains.

It has been widely reported that primary α grains and α laths in the colony structures of bi-modal microstructures have different yield stresses due to the different concentrations of Aluminium found in the two structures [1], [2]. The yield stresses of these constituent structures will be considered separately and split into their thermal and athermal components.

The thermal component of the α grains and α lath colonies will be modelled using a MTS model, with the effect of Aluminium content on the yield stress of α phase Titanium included.

The athermal component of the α grains and α lath colonies will include the effects of grain boundaries and macro-zone boundaries using a Hall-Petch type relationship [5]. Strain hardening will be accounted for using a Taylor dislocation interaction model, with the total

dislocation density stored as an internal state variable for each of the constituent structures [67].

The volume fraction of each of the constituent structures will then be combined using a method of mixtures. The shear stresses will be scaled up to uniaxial stresses using a Taylor factor [5], with the effects of macro-texture taken into account [68].

Finally, it will be shown how the calculated uniaxial flow stresses can be implemented within an appropriate yield criterion for use in finite element analysis packages.

The complete Ti-6Al-4V model will take the form:

$$\sigma_i^y = M_i\left(V\tau_\alpha + [1-V]\tau_{\alpha/\beta}\right) \tag{7.19}$$

where i is the relevant orthogonal material orientation and the other parameters are as defined in Figure 7.4, which gives an outline of the basic structure of the new Ti-6Al-4V model.

The rest of this chapter will be dedicated to developing this modelling framework. The model will then be implemented in the technical computing software package MATLAB and compared with the mechanical characterisation results of Plate 1.

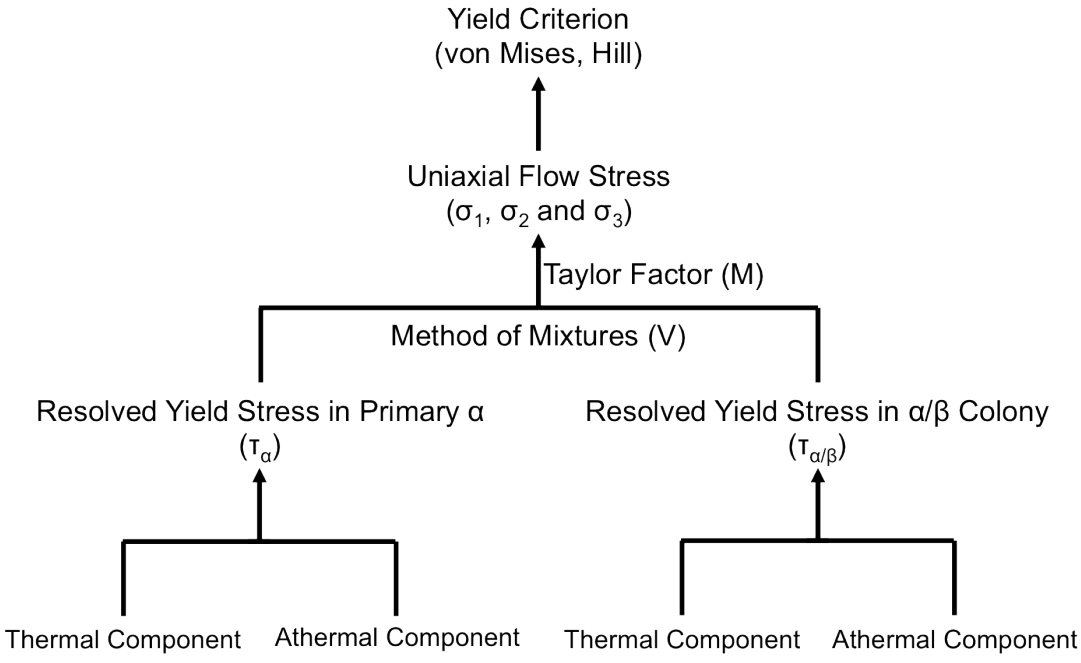


Figure 7.4 - Outline of Ti-6Al-4V modelling framework

7.4.2 Effect of Aluminium Content on the Yield Stress of α Phase Titanium

As discussed earlier in this chapter, solute atoms affect the flow stress of a metal by distorting the crystal lattice and acting as short-range barriers to dislocation motion. In the case of Ti-6Al-4V, Aluminium atoms stabilise the α phase of the alloy and Vanadium atoms stabilise the β phase. At room temperature, the volume fraction β phase is very low, of the order 5-10%, and it does not contribute to the deformation process [1]. As a result, the β phase shall be ignored in this model.

Paton *et al.* [11] have carried out an extensive investigation into the effects of Aluminium content on the yield stress of Titanium on specific slip systems over a wide range of temperatures. Using the data from this study, it is possible to determine the normalised activation energy, g_0, and the mechanical threshold stress, τ_0, for Aluminium contents of 3.5%, 6.9% and 10.2% by weight. The temperature dependent yield stress data from Paton *et al.* for prismatic slip is given in Figure 7.5. From this point the yield stress for all slip systems will be taken to be the same as that of Prismatic slip. Assuming at low temperatures the glide of dislocations only occurs along slip systems with a slip direction on the basal plane i.e. $\langle \boldsymbol{a} \rangle$ type dislocations, and noting that the difference between the resolved shear stress for the Prismatic and Basal slip systems is negligible, this is a valid assumption to make. The effect of increased temperature will be discussed later in this chapter. However, for the time being, it should be noted that the assumption of $\langle \boldsymbol{a} \rangle$ type slip means that the outlined model is only applicable in the temperature range of 0 K - 800 K.

It is possible to calculate the required parameters for the MTS model by plotting $\frac{\tau}{\mu}$ against $\left[\frac{kT}{\mu b^3} ln\left(\frac{\dot{\gamma}_0}{\dot{\gamma}}\right)\right]^2$ for the Ti-Al yield stress data from Paton *et al.* Using a linear fit to the data, τ_0 can be found from the intercept with the y-axis and g_0 from the gradient of the fitted line, as shown in Figure 7.6. Following Follansbee and Gray III [25], p and q taken to be 1 and 2 respectively, with $\dot{\gamma}_0$ taken as 10^{10}.

From Figure 7.6, τ_0 was found to vary with Aluminium content as follows:

$$\tau_0 \propto \sqrt{C_{Al}}$$

where C_{Al} is the concentration of Aluminium atoms.

The normalised activation energy, g_0, was found to vary slightly at the higher Aluminium content. However, a value of 0.9 was found to give a good fit to the lower two data sets, with the higher value of 10.2% Al content being out of the useful industrial range.

The contribution of Aluminium content to the yield stress in shear can then be formulated in terms of the MTS model as:

$$\frac{\tau_{Al}}{\mu} = \frac{\tau_0}{\mu}\left[1 - \left(\frac{kT}{g_0 \mu b^3} ln\left(\frac{\dot{\gamma}_0}{\dot{\gamma}}\right)\right)^{1/q}\right]^{1/p} \tag{7.20}$$

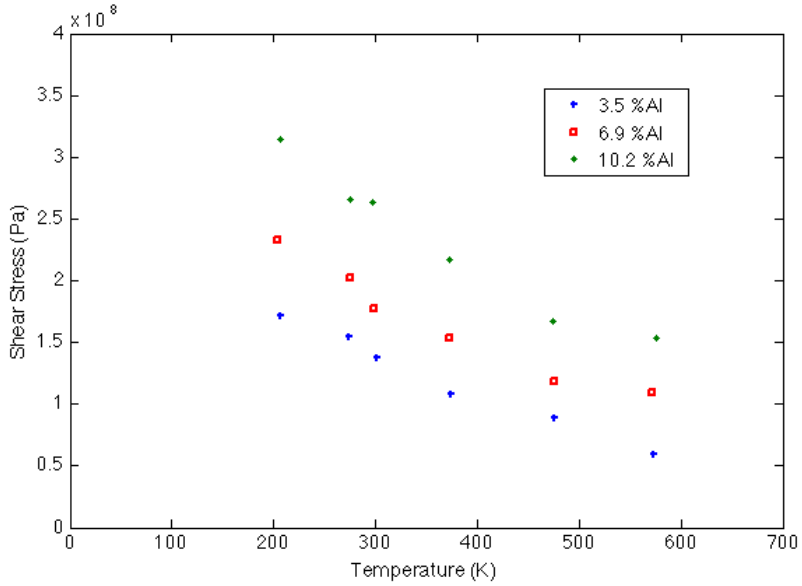


Figure 7.5 - Shear stress vs temperature for different contents of Aluminium in Titanium

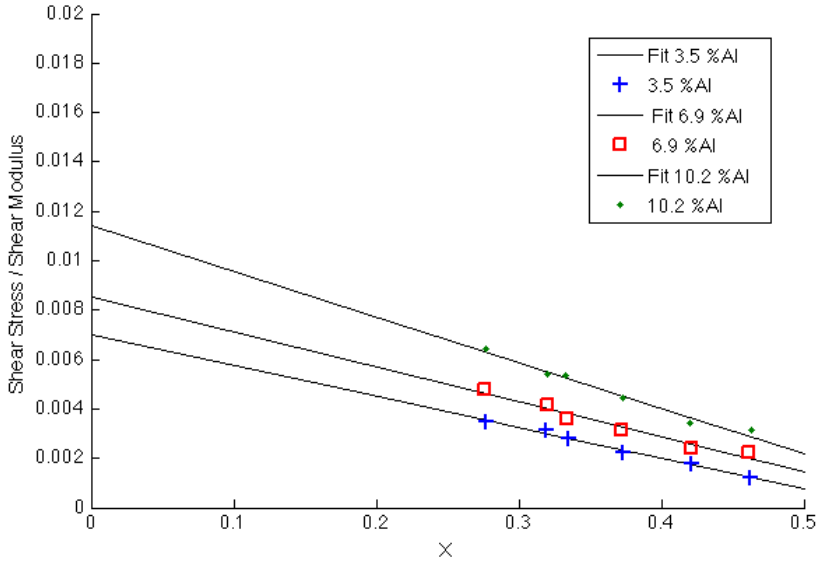


Figure 7.6 - Plot showing fit of yield stress data to MTS model

7.4.3 Effect of Dislocation Density on the Yield Stress of α Phase Titanium

The multiple slip systems observed in *fcc* and *bcc* crystal structures cause slip systems to intersect each other, resulting in a forest of dislocations lines for a given dislocation on any given slip system to overcome, acting as short-range barriers to dislocation motion. Therefore, in *fcc* and *bcc* metals, the interaction of mobile dislocations with other dislocations, and the overcoming of the barriers to motion they create, is often considered a thermally activated process [64].

As dislocations are generally free to glide along the basal and prismatic planes in *hcp* metals, this will not to be considered the case for Titanium [1], [11]. Instead, it will be assumed that dislocations are free to glide until they encounter strong barriers to their motion.

To model the back-stress caused by the long-range interactions with other dislocations, the classic Taylor hardening model [67] is used:

$$\tau_{dislocations} = A\mu b\sqrt{\rho} \tag{7.21}$$

where $\tau_{dislocations}$ is the back-stress due to long-range dislocation-dislocation interaction, A is a strain hardening coefficient, μ is the shear modulus, b is the Burgers vector and ρ is the total dislocation density. From Nabarro *et al.* [69], the strain hardening coefficient is taken as 0.2, assuming the close-packed *hcp* structure of Titanium follows the same relationship as the close-packed structure of *fcc* metals. The shear modulus is dependent on the temperature and the Burgers vector is $0.29\text{x}10^{-9}$ m [1].

The dislocation density can be shown to evolve as a function of strain using the geometric argument of Kocks and Mecking [63]:

$$d\rho = \frac{1}{b\lambda} d\gamma \tag{7.22}$$

where λ is the mean free path of the dislocations and γ is the shear strain. In the case of *fcc* and *bcc* metals, it is common to assume that the mean free path of any given dislocation is the distance between forest dislocations [17], [63], [69].

To determine the density of forest dislocations, it can be said that:

$$\rho_{forest} = B\rho \tag{7.23}$$

where ρ_{forest} is the density of forest dislocations and B is a coefficient that determines the density of forest dislocations from the total dislocation density, ρ, [67]. Assuming the forest dislocations are evenly spaced, it is then possible to calculate the mean free path between the forest dislocations:

$$\lambda = \frac{1}{\sqrt{\rho_{forest}}} \tag{7.24}$$

Due to the parallel slip direction of the easily activated $\langle \boldsymbol{a} \rangle$ type slip systems, it can be argued that these only act as a very weak barrier to dislocation motion and do not contribute to the dislocation forest density.

As discussed previously, to accommodate compatible plastic flow, a fifth independent slip system is required. Typically in Ti-6Al-4V this fifth independent slip system is accommodated by the so-called $\langle \boldsymbol{c}+\boldsymbol{a} \rangle$ type slip system. As can be seen from Figure 2.15, the $\langle \boldsymbol{c}+\boldsymbol{a} \rangle$ type slip system cuts through both the Prismatic and Basal slip systems and has a slip direction nearly orthogonal to $\langle \boldsymbol{a} \rangle$ type slip.

Due to this, dislocations of the $\langle \boldsymbol{c}+\boldsymbol{a} \rangle$ type act as strong barriers to dislocation motion in the $\langle \boldsymbol{a} \rangle$ type systems and are the sole contribution to the dislocations forest [70]. Numerous studies have documented the activation of a small number of $\langle \boldsymbol{c}+\boldsymbol{a} \rangle$ dislocations during the deformation of Ti-6Al-4V [71–73]. The low number of $\langle \boldsymbol{c}+\boldsymbol{a} \rangle$ type dislocations seen at low strains and low temperatures explains the low strain hardening seen in Ti-6Al-4V, when compared with *fcc* and *bcc* metals. This hypothesis, and the framework outlined above, will be used to calculate the strain hardening in the Ti-6Al-4V model.

Sensible approximations for this value of the ratio of $\langle \boldsymbol{a} \rangle$ to $\langle \boldsymbol{c}+\boldsymbol{a} \rangle$ type slip will be made, and used as a means of fitting the strain hardening response to the experimental data.

7.4.4 Resolved Yield Stress of Primary α Grains

The primary α grains will be modelled using the following framework:

$$\tau_{\alpha} = \tau_{\alpha\,(athermal)} + \tau_{\alpha\,(thermal)} \tag{7.25}$$

where $\tau_{\alpha(athermal)}$ is the temperature independent part of the flow stress given by the equation:

$$\tau_{\alpha\,(athermal)} = A\mu b\sqrt{\rho_{\alpha}} \tag{7.26}$$

with ρ_{α} stored as an internal state variable whose evolution is given by:

$$d\rho_{\alpha} = \frac{1}{b\lambda_{\alpha}} d\gamma \tag{7.27}$$

where λ_{α} is the mean free path of a dislocation in a primary α grain. Using the hypothesis outlined in the previous section, the mean free path for a dislocation in a primary α grain is the distance between the $\langle \boldsymbol{c} + \boldsymbol{a} \rangle$ type dislocations that make up the dislocation forest. This can be calculated from:

$$\lambda_{\alpha} = \frac{1}{\sqrt{\rho_{forest\,(\alpha)}}} \tag{7.28}$$

where $\rho_{forest\,(\alpha)}$ is the dislocation density of forest dislocations in a primary α grain.

The temperature dependent part of the flow stress, $\tau_{\alpha\,(thermal)}$, is given by the Aluminium concentration dependent MTS model developed in the preceding section:

$$\frac{\tau_{\alpha\,(thermal)}}{\mu} = S(T, \dot{\gamma}) \frac{\tau_{Al(\alpha)}}{\mu} \tag{7.29}$$

where $\tau_{Al(\alpha)}$ is the Aluminium concentration dependent mechanical threshold stress for primary α grains and $S(T, \dot{\varepsilon})$ is given by:

$$S(T, \dot{\varepsilon}) = \left[1 - \frac{kT}{g_0 \mu b^3} ln \frac{\dot{\gamma}_0}{\dot{\gamma}}\right]$$

7.4.5 Resolved Yield Stress of α/β Lath Colonies

The α/β lath colonies will be modelled using the same method as the primary α grains:

$$\tau_{\alpha/\beta} = \tau_{\alpha/\beta\ (athermal)} + \tau_{\alpha/\beta\ (thermal)} \tag{7.30}$$

where $\tau_{\alpha/\beta\ (athermal)}$ is the temperature independent part of the flow stress given by the equation:

$$\tau_{\alpha/\beta\ (athermal)} = A\mu b\sqrt{\rho_{\alpha/\beta}} \tag{7.31}$$

with $\rho_{\alpha/\beta}$ stored as an internal state variable whose evolution is given by:

$$d\rho_{\alpha/\beta} = \frac{1}{b\lambda_{\alpha/\beta}} d\gamma \tag{7.32}$$

where $\lambda_{\alpha/\beta}$ is the mean free path of a dislocation in an α/β lath colony. As with the analysis for a primary α grain, the mean free path for a dislocation in an α/β lath colony is the distance between the $\langle \boldsymbol{c} + \boldsymbol{a} \rangle$ type dislocations that make up the dislocation forest. This can be calculated from:

$$\lambda_{\alpha/\beta} = \frac{1}{\sqrt{\rho_{forest\ (\alpha/\beta)}}} \tag{7.33}$$

where $\rho_{forest\ (\alpha/\beta)}$ is the dislocation density of forest dislocations in an α/β lath colony.

The temperature dependent part of the flow stress, $\tau_{\alpha/\beta\ (thermal)}$, is given by the Aluminium concentration dependent MTS model developed in the preceding section:

$$\frac{\tau_{\alpha/\beta\ (thermal)}}{\mu} = S(T, \dot{\gamma}) \frac{\tau_{Al\ (\alpha/\beta)}}{\mu} \tag{7.34}$$

where $\tau_{Al\ (\alpha/\beta)}$ is the Aluminium concentration dependent mechanical threshold stress for an α/β lath colony and $S(T, \dot{\varepsilon})$ is given by:

$$S(T, \dot{\varepsilon}) = \left[1 - \frac{kT}{g_0 \mu b^3} ln \frac{\dot{\gamma}_0}{\dot{\gamma}}\right]$$

7.4.6 Effect of Primary α Grain Size and α/β Colony Size on Resolved Yield Stress

As noted in the analysis of the deformation induced during a Taylor impact test on a Ti-6Al-4V alloy with α colonies and macro-zones of micro-texture, these α colonies (or macro-zones) can have a significant effect of the mechanical behaviour of Ti-6Al-4V. In the preceding sections it was assumed that grain and lath boundaries within these α colonies are weak barriers to dislocation motion. This was based on the observation that dislocations can easily transfer between neighbouring grains and laths that are both well orientated for slip. However, at the boundaries of an α colony the grains/laths are typically poorly oriented relative to the neighbouring α colonies or primary α grains, resulting in pile-ups of dislocations at the edge of the α colony. This is exactly analogous to the pile up of dislocations commonly seen in grain-grain interactions in untextured polycrystalline metals. To account for the back-stress caused by the pile-up of dislocations at a grain boundary, it is common to use the so-called Hall-Petch relationship, which takes the form:

$$\tau_{HP} = kd^{1/2} \tag{7.35}$$

where is k is the strengthening coefficient due to the grain boundary and d is typically the grain boundary diameter [5]. However, in the case outlined above, d can be taken as the diameter of the α colony, with k = 12.7 MPa.mm$^{1/2}$ for a strong grain-grain interaction in α phase Titanium [74]. It can then be said that $\tau_{HP} = \tau_{macro}$, where τ_{macro} is the back-stress due to dislocation pile-ups at the interface of the α colonies.

The same approach will be used to account for the back-stress caused by dislocation pile-ups at the grain boundaries of primary α grains. In this case, d will be taken to be the primary α grain size. It can then be said that $\tau_{HP} = \tau_{\alpha-grain}$, where $\tau_{\alpha-grain}$ is the back-stress due to dislocation pile-ups at the primary α grain boundaries.

As both of these terms are athermal, they will be included in the athermal component of the primary α grain and α/β lath colony resolved yield stresses.

7.4.7 Effect of Volume Fraction Primary α on the Yield Stress of Ti-6Al-4V

It is noted by Lutering and Williams [1] that increasing the volume fraction primary α in Ti-6Al-4V with a bi-modal microstructure will have the effect of increasing the yield stress of the material. The physical mechanisms that underpin this behaviour are two fold. Firstly, primary α grains are nucleated at the triple points of prior β grains. The volume fraction primary α is therefore an indicator of the size of the α/β colony, which is typically of the same order as the prior β grains. As was discussed in the previous section, grains/laths within colonies of α/β have the same crystallographic orientation, thus the slip length of interest is the size of the α colony or macro-zone. This mechanism was accounted for in the previous section. The second mechanism that results in the increase in yield stress due to increasing volume fraction primary α is alloying element partitioning.

During thermo-mechanical processing, Aluminium preferentially locates in the primary α grains, resulting in an increased Aluminium content in the primary α grains relative to the α laths. This effect is observed to increase with increasing volume fraction primary α. Up to 20% volume fraction primary α, the α colony size dominates the mechanical response, with a peak in yield stress seen between 10-20% volume fraction primary α. Above 20% volume fraction primary α, the effect of alloying element partitioning dominates [1].

To account for the difference in strength of the primary α grains and the α/β lath colonies due to alloying element partitioning, a method of mixtures is used to give the cumulative flow stress of Ti-6Al-4V with a bi-modal microstructure. This results in the formulation:

$$\tau_{\alpha+\,\alpha/\beta} = V\tau_{\alpha} + [1 - V]\tau_{\alpha/\beta} \tag{7.36}$$

where $\tau_{\alpha\,+\,\alpha/\beta}$ is the cumulative flow stress due to the combination of primary α grains and α/β lath colonies and V is the volume fraction of primary α grains.

7.4.8 Effect of Macro-Texture on Uniaxial Flow Stress of Ti-6Al-4V

To account for the effect of macro-texture on the flow stress, and to scale the shear stresses up from shear stresses acting in the primary α grains and α/β laths to a uniaxial flow stress, a Taylor factor approach is used. A Taylor factor is calculated by assuming that during a uniaxial deformation, every grain in the polycrystalline material undergoes the same uniaxial strain. This rigidly imposes compatibility between the grains and results in a single scalar value that scales the shear stress up to a uniaxial flow stress [75]. This gives a simple scaling of the form:

$$\sigma = M\tau \tag{7.37}$$

where σ is the uniaxial flow stress, τ is the shear stress and M is the Taylor factor, typically the order of 2-3.

Using the EDAX EBSD Data Analysis software package, it is relatively simple to calculate the Taylor factor of a scanned microstructure for a given loading direction and given active slip systems, in this case the Prismatic and Basal slip systems.

However, care must be taken when using this approach with *hcp* metals such as Titanium, as they do not have the required five independent slip systems to accommodate compatible plastic deformation in a polycrystalline material, unless the $\langle \boldsymbol{c} + \boldsymbol{a} \rangle$ slip system is considered [7]. This will be discussed further in the following sections.

7.4.9 Complete Model Framework

Combining the constituent parts outlined above, the complete model framework for Ti-6Al-4V with a bi-modal microstructure can then be formulated as in Equation 7.19.

This can further be expanded to include the effects of anisotropy; due to the varying Taylor factors in the different material orientations. The yield stresses in the three orthogonal material orientations can be determined by calculating the Taylor factors in the three orthogonal material orientations:

$$\sigma_1^y = M_1\left(V\tau_\alpha + [1-V]\tau_{\alpha/\beta}\right)$$
$$\sigma_2^y = M_2\left(V\tau_\alpha + [1-V]\tau_{\alpha/\beta}\right)$$
$$\sigma_3^y = M_3\left(V\tau_\alpha + [1-V]\tau_{\alpha/\beta}\right) \quad (7.38)$$

where M_1, M_2 and M_3 are the Taylor factors for the three orthogonal material orientations and σ_1^y, σ_2^y and σ_3^y are the yield stresses in the three orthogonal material orientations, as shown in Figure 7.7.

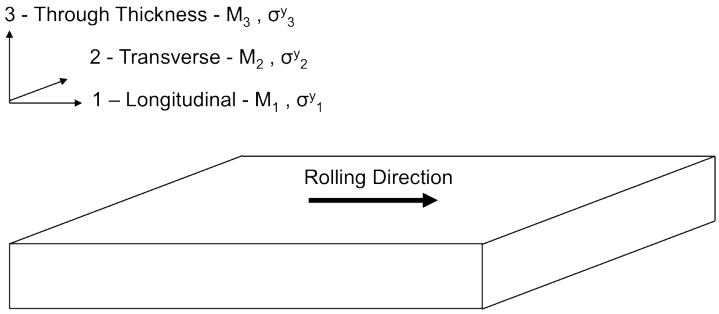


Figure 7.7 - Orthogonal material orientations and yield stresses relative to rolled plate

7.5 Comparison with Experimental Results

7.5.1 Overview

The Ti-6Al-4V model outlined in the previous section will now be compared with experimental data for the flow stress of textured Ti-6Al-4V with a bi-modal microstructure, over a range of strain rates at room temperature. Key microstructural and textural features of the material under investigation must be quantified before the model results can be compared with experimental results. Attempts were made to compare the model outputs with data from the literature. However, as previously noted, much of the literature on the flow behaviour of Ti-6Al-4V contains little information on the microstructure and texture of the material tested. As a result, comparisons will only be made with a selected plate of Ti-6Al-4V that was characterised in Chapters 4 and 5. Plate 1 was chosen, as this has a microstructure closest to that seen in commercially available Ti-6Al-4V plate, with a bi-modal microstructure and light texturing.

7.5.2 Physically Based Model Parameters

To compare the model with the mechanical characterisation results for Plate 1, the new Ti-6Al-4V model must be populated with measured microstructural data from Plate 1. The following sections will detail how the required data were obtained and the final values used in the model. It should be noted that some of the data required for the Ti-6Al-4V model need expertise of experimental techniques outwith the scope of this project. As a result, estimations for some of the parameters will need to be made and compared with similar data in the literature. When this is the case, the assumptions behind those estimations will be clearly outlined and references given to the relevant paper containing the data used.

7.5.3 Aluminium Content

The effect of Aluminium partitioning, which results in a higher Aluminium concentration in the primary α phase relative to the α/β colonies, can be captured using the outlined MTS based Ti-6Al-4V model. The Aluminium concentration can be calculated for Plate 1 from the compositional data generated from the material characterisation in Chapter 4. However, this compositional analysis is for the entire material and does not distinguish between the primary α and the α/β colonies. It was not within the scope of this project to carry out the required analysis to determine the Aluminium content in the primary α and the α/β colonies. Instead, sensible approximations were made for both these values based on the Aluminium content obtained from the compositional analysis.

7.5.4 Volume Fraction Primary α Grains

The volume fraction of primary α grains was measured using the image analysis software, ImageJ. The optical micrograph of Plate 1, as seen in Chapter 4, was first edited to increase the contrast between the primary α grains and the α/β lath structures before thresholding to highlight the primary α grains. It was found that the contrast between the primary α grains and the α laths was not high enough to provide good binary thresholding. The primary α grains were manually edited to increase contrast before thresholding. ImageJ was then used to fit ellipses around the primary α grains and measure their area, thus allowing the calculation of the volume fraction primary α grains in Plate 1. To qualify as a primary α grain it was decided the grains must have a major-to-minor ellipse axis ratio of 0.75-1.25. It should be noted that there are no clear guidelines as to determine what qualifies as a primary α grain from an optical micrograph. A step-by-step illustration of the process can be seen in Figure 7.8. The volume fraction primary α grains in Plate 1 was calculated as ~6%.

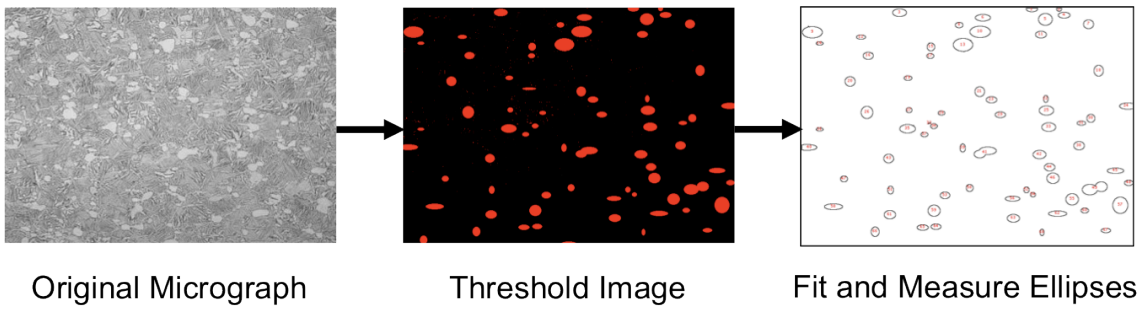


Figure 7.8 - ImageJ process used to measure the volume fraction of primary α grains in Ti-6Al-4V

7.5.5 Primary α Grain Size

The primary α grain size was measured using the data generated to calculate the volume fraction primary α grains, as outlined above. The mean grain diameter was calculated to be ~20μm.

7.5.6 α Colony Size

Very little data is available on the size and geometry of α colonies in Ti-6Al-4V. However, it is hoped that with the advent of EBSD as a widespread component in most SEM setups, the characterisation and effects of α colonies will be studied in more detail. No method of characterising the size and geometry of α colonies has been outlined in the literature.

For simplicity, it was assumed in the Ti-6Al-4V model that the α colonies seen in Plate 1 are effectively spherical. This is clearly not the case for all microstructures, as can be seen in the EBSD results for Plate 4. However, as a first approximation, the assumption of spherical α colonies is reasonable.

From the inverse pole figure maps of Plate 1 in Chapter 4, the α colonies were measured by inspection to have diameter of the order of ~100μm. This large α colony size is consistent with the low volume fraction of primary α seen in the previous section.

7.5.7 Dislocation Density

The initial density of dislocations in the primary α grains has been noted to be significantly lower than the dislocation density in the α laths. However, there are no appropriate numerical data in the literature relating to dislocation density in rolled Ti-6Al-4V plate. Due to a lack of data, it was assumed that the α laths had a dislocation density typical of a lightly deformed metal (~10^{14} m^{-2}) and that the primary α grains had a dislocation density slightly higher than a typical annealed metal (~10^{13} m^{-2}).

To fit with the observed experimental flow stress data, the required ratio of mobile dislocations to forest dislocations, or $\langle \boldsymbol{a} \rangle$ to $\langle \boldsymbol{c}+\boldsymbol{a} \rangle$ type dislocations, was calculated to be of the order of 0.001. This is an order of magnitude less than that experimentally observed ratio for geometrically necessary dislocations in Ti-6Al-4V deformed to 6% true strain by Littlewood *et al.* [72]. One explanation for this discrepancy is that if, as is typically observed in other metals, the $\langle \boldsymbol{c}+\boldsymbol{a} \rangle$ type dislocations group together to form localised slip bands, the forest of dislocations would no longer be evenly dispersed, as assumed in the Ti-6Al-4V model, effectively increasing the mean free path to a value closer to the one required for the model. Another explanation is that near α colony boundaries, the number of $\langle \boldsymbol{c}+\boldsymbol{a} \rangle$ type dislocations must increase to accommodate compatibility and subsequent strain gradients. This would result in the required lower $\langle \boldsymbol{c}+\boldsymbol{a} \rangle$ type dislocation density in the bulk of the grain but a higher average dislocation density in the bulk material. This feature has been observed experimentally by Britton *et al*. [73]. Further, it should be noted that the dislocations measured in both studies were geometrically necessary. It may be that the mobile dislocation density consists purely of $\langle \boldsymbol{a} \rangle$ type dislocations. If this were the case, the ratio of $\langle \boldsymbol{a} \rangle$ to $\langle \boldsymbol{c}+\boldsymbol{a} \rangle$ type dislocations would be reduced. Despite this slight discrepancy, it is reassuring to note that the ratio of $\langle \boldsymbol{a} \rangle$ to $\langle \boldsymbol{c}+\boldsymbol{a} \rangle$ type dislocations required to generate the observed strain hardening response is within a reasonable bound of the ratios observed experimentally.

7.5.8 Taylor Factor

As discussed previously, a Taylor factor can easily be calculated for loading in the three orthogonal material orientations using EBSD analysis software packages. The Taylor factor is calculated by assuming that a uniform strain is applied to the polycrystalline material under investigation i.e. all grains/laths in the material are strained by the same amount. The stress is then averaged over the material by considering the most favourable slip system for each of the grains/laths. The assumption of uniform strain rigidly imposes compatibility between the grains/laths [7], [75].

Due to the inherent anisotropy of plastic deformation in the *hcp* crystal structure, it is arguable that the Taylor factor is not an appropriate model for *hcp* polycrystalline materials, as this anisotropy results in large mismatches in stresses between grains/laths [7]. Further, the bi-modal nature of the Ti6Al-4V under investigation means that mismatches may also be present between the "hard" primary α grains and the "soft" α/β laths. It may even be possible that the strength differential between the primary α grains and the α/β laths is so large that the primary α grains undergo no deformation, as suggested in Chapter 6.

Considering these points, it was still decided to use a Taylor factor type model, due to its relative simplicity and the fact that, as grain/laths having the same orientation in an α colony, compatibility will be maintained in the majority of the material. However, it should be noted that other models are available and widely used in the literature, such as the self-consistent type family of models [67].

Taylor factors were calculated for Plate 1 considering only slip systems with a slip direction on the basal plane i.e. $\langle \boldsymbol{a} \rangle$ type slip, using the EBSD characterisation data from Chapter 4. From this analysis, M_1 and M_2 for Plate 1 were calculated as 2.46 and 2.54, respectively.

7.5.9 Comparison with Uniaxial Flow Stress Data

The physically based model parameters determined for Plate 1 were inputted into the Ti-6Al-4V model, with the initial dislocation density and the ratio of mobile dislocations to forest dislocations calibrated using the experimental tensile data for Plate 1 in the longitudinal material orientation at a strain rate of 10^{-3} s^{-1}, as described in Chapter 5. All subsequent flow stresses in different material orientations and at different strain rates are predicted using the new Ti-6Al-4V model.

The simulation conditions were set to room temperature at strain rates of 10^{-3} s^{-1} and 10^{3} s^{-1}, termed quasi-static (QS) and high strain rate (HR), respectively.

In Figure 7.9, comparisons are made between the model and the experimental results in the longitudinal material orientation at quasi-static and high strain rates. It can be seen that the model accurately predicts the flow stress, work hardening and strain rate dependence of Plate 1 in the longitudinal material orientation.

In Figure 7.10, the model results are compared with the experimental results for Plate 1 in the transverse material orientation. Once again, it can be seen that the model accurately predicts the flow stress, work hardening and strain rate dependence of Plate 1, this time in the transverse material orientation.

From Figure 7.9 and Figure 7.10, it can be seen that the model successfully captures the effect of texture on the yield stress, and subsequent flow stress and work hardening, of rolled Ti-6Al-4V plate, such as Plate 1, up to a final true strain of 10%. It should be noted that at larger strains and very high strain rates, where deformation twinning has been shown to be prevalent, significant texture evolution might occur, invalidating the constant Taylor factor approach assumed in this model.

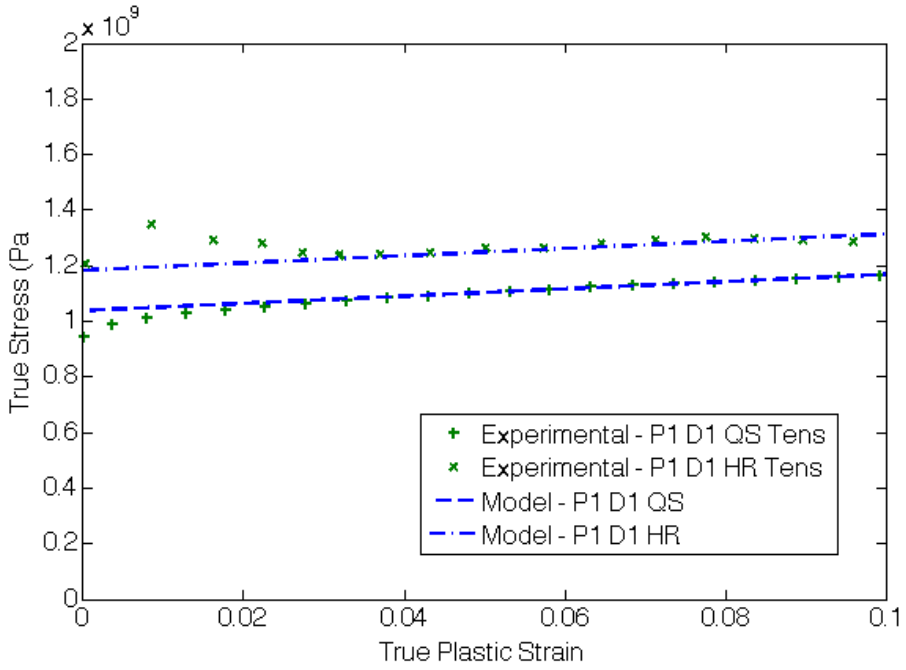


Figure 7.9 - Comparison of model results with experimental results for Plate 1 - Direction 1

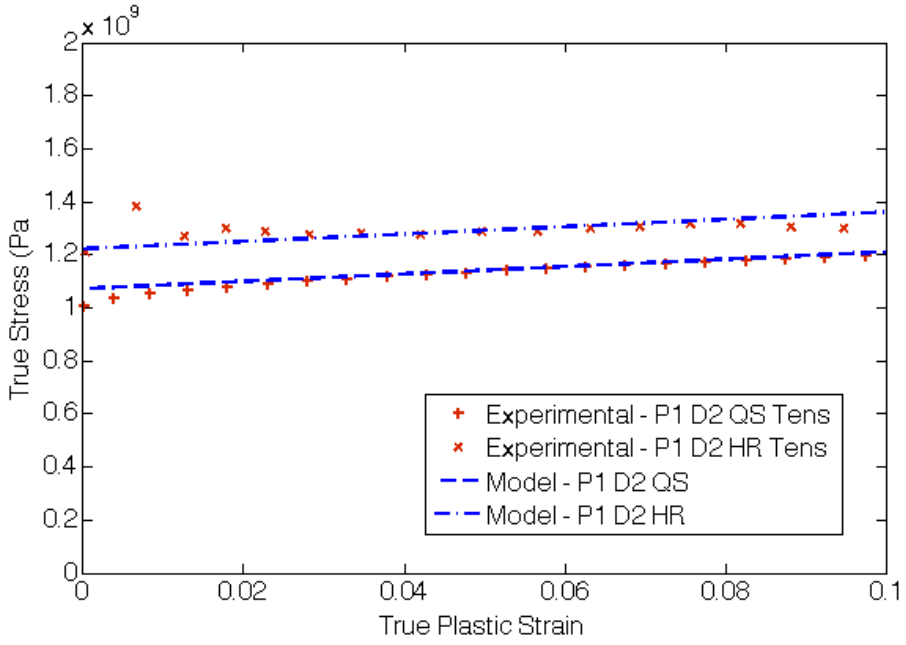


Figure 7.10 - Comparison of model results with experimental results for Plate 1 - Direction 2

7.5.10 Effect of Temperature on the Ti-6Al-4V Model

To simulate the effects of temperature on the flow stress calculated by the Ti-6Al-4V model, virtual tests were carried out at a number of different temperatures at a constant strain rate of 800 s^{-1}. As can be seen from the results in Figure 7.11, the effect of increasing temperature is to lower the calculated yield and flow stress.

Also plotted on Figure 7.11 are the experimental flow stress data obtained by Lee *et al.* [26] for a generic Ti-6Al-4V material at a number of different temperatures at a constant strain rate of 800 s^{-1}. Unfortunately, Lee *et al.* provide no data on the microstructure and texture of the material they tested. As a result, it was not possible to explicitly model the material tested using the new Ti-6Al-4V model outlined in this chapter. However, comparing the model for Plate 1 with the experimental data from Lee *et al*., it can be seen that the model closely approximates the temperature dependent flow stress behaviour at 25°C. The small deviation between the model and the experimental data is likely due to microstructural and textural differences between the material tested by Lee *et al*. and that of the modelled Plate 1.

Comparing the high temperature flow stress data from Lee *et al.* with the outputs from the Ti-6Al-4V model at the same conditions, it can be seen that although showing the correct trend, the model significantly under predicts the effects of temperature on the plastic flow stress of Ti-6Al-4V.

The under prediction of the temperature dependence of the plastic flow stress by the Ti-6Al-4V model is due to the assumption of a constant activation energy, which in turn is due to the assumption of a linear fit of the MTS model to the temperature dependent yield stress data of Paton *et al.* [11]. It is anticipated that the prediction of the temperature dependence of the plastic flow stress at high temperatures by the Ti-6Al-4V model could be significantly improved by including a temperature dependent activation energy term.

It should also be noted that the yield behaviour of Ti-6Al-4V significantly changes above 800 K, with Pyramidal slip becoming more prevalent. The outlined Ti-6Al-4V model does not consider this transition in the activation of slip systems. Further, the effect of temperature on the work hardening, through mechanisms such as dislocation annihilation, has not been considered in the Ti-6Al-4V model. These features of the high temperature deformation behaviour of Ti-6Al-4V would need to be included in the model to successfully capture the behaviour of Ti-6Al-4V at high temperatures

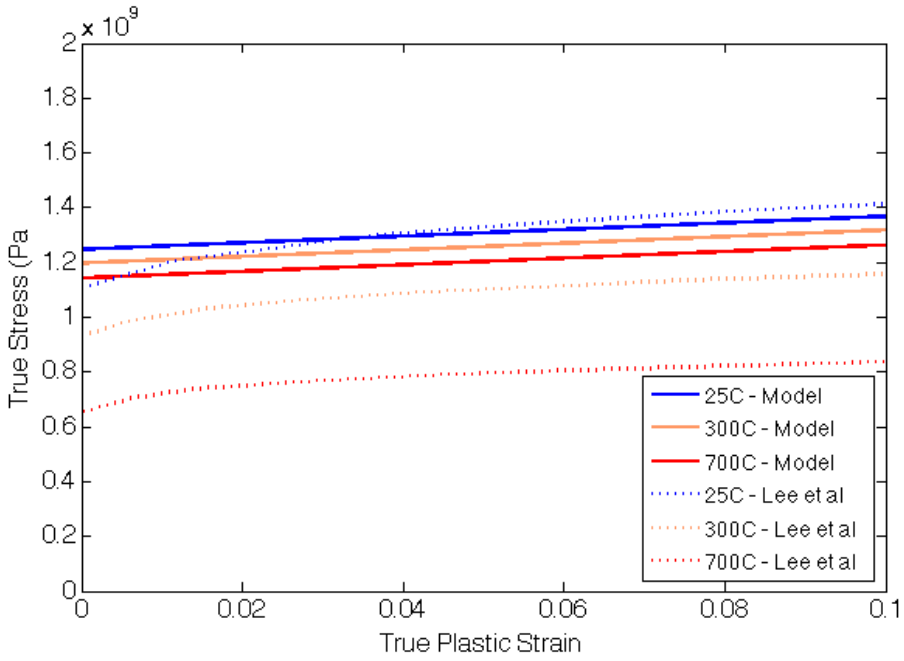


Figure 7.11 - Effect of temperature on model output compared with experimental results from literature

7.5.11 The Effect of Volume Fraction Primary α on the Ti-6Al-4V Model

To simulate the effects of varying volume fraction primary α on the flow stress calculated by the Ti-6Al-4V model, virtual tests were carried out with a number of different values for the volume fraction primary α. As can be seen from Figure 7.12, the effect of increasing the volume fraction of primary α is to increase the flow stress. The flow stress curves in Figure 7.12 were generated with the parameters used to model Plate 1 under quasi-static loading at room temperature in the longitudinal material orientation.

Comparing qualitatively with the literature, it is generally accepted that increasing the volume fraction primary α increases the flow stress up to a value of 20-30% primary α, after which alloying element partitioning becomes more pronounced, reducing the flow stress [1].

However, it should be noted that increasing the volume fraction primary α also affects a number of other parameters not considered for the flow curves in Figure 7.12. As discussed during the formulation of the model, the effect of increased volume fraction primary α also results in an increase in the Aluminium content in the primary α and a decrease in the Aluminium content in the α laths. Further, if the volume fraction primary α increases, it is expected that the size of the α colonies would decrease. Due to a lack of data, it is not possible to formulate the Ti-6Al-4V model to account for varying Aluminium content and α colony size for given primary α volume fractions. However, it is worth noting that it would be relatively simple to implement an empirical formulation given appropriate data. If given the thermo-mechanical processing history, it may be possible to formulate a physically based model capable of capturing the diffusion of solute atoms and the growth/reduction of β grains during processing.

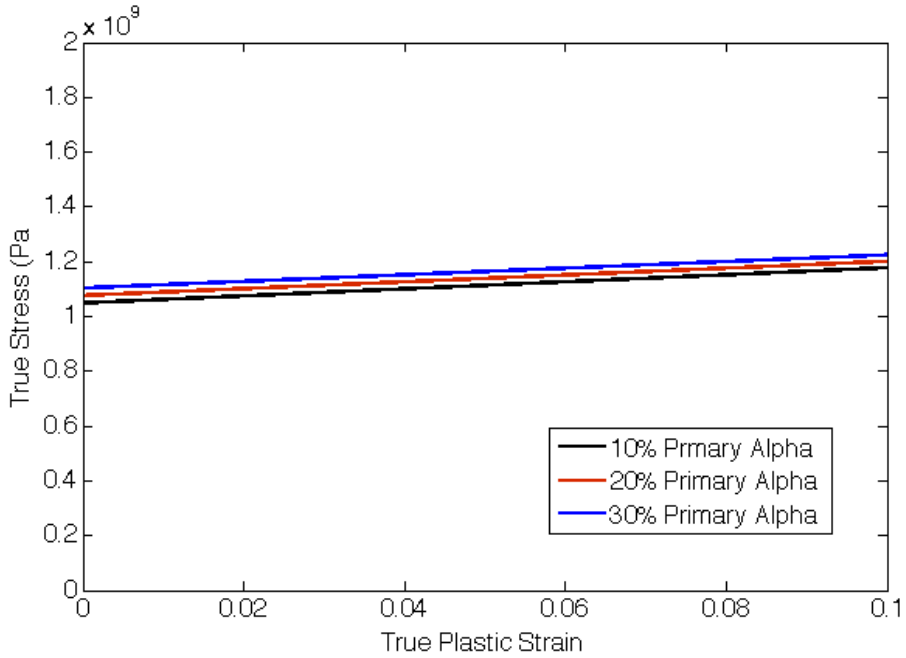


Figure 7.12 - Effect of volume fraction primary α on model output

7.5.12 Other Ti-6Al-4V Microstructures

As the outlined Ti-6Al-4V model is based on fundamental physical mechanisms that relate to specific microstructural features, the Ti-6Al-4V model can easily be extended to apply to nearly all microstructures seen in Ti-6Al-4V. For example, to model a fully lamellae microstructure, the volume fraction primary α simply needs to be set to zero. Likewise, to model a fully equiaxed primary α microstructure the volume fraction of the α/β colony structures simply needs to be set to zero.

Using the outlined dislocation interaction model, it would not be possible to capture a martensitic type, fine α/β lath structure. However, this could be overcome by changing the mean free path in the dislocation interaction section of the model from the distance between $\langle \boldsymbol{c}+\boldsymbol{a} \rangle$ type dislocations to the α lath thickness. This would result in the experimentally observed increase in yield stress and rate of strain hardening with decreasing lath thickness in fine α/β lath structures [1].

7.6 Implementation in a Finite Element Framework

7.6.1 Overview

For the outlined Ti-6Al-4V model to be useful to the engineering community, a framework is required for it to be implemented into commercial finite element (FE) packages such as ABAQUS, LS-DYNA and DEFORM. These packages are widely used within the engineering community to simulate the response of structures and components to applied boundary conditions. To be used in such packages, the Ti-6Al-4V model must be implemented within a framework that can capture the three-dimensional yield behaviour of the material. Typically this is done by means of a yield criterion. In this section a brief outline of possible implementation frameworks that can account for the observed macroscopic behaviour, and fit with the structure of the Ti-6Al-4V model, will be given.

7.6.2 Anisotropic Yield

As was clearly shown in Chapters 5 and 6, the yield and plastic flow stresses of the four development level Ti-6Al-4V plates are anisotropic. This anisotropy was explicitly modelled in the new Ti-6Al-4V model by measuring the Taylor factor for each of the orthogonal material orientations, as defined in the previous section. Varying Taylor factors in the orthogonal material orientations resulted in different yield stresses in the two orthogonal in-plane material orientations of Plate 1.

These yield stresses can be used to determine the yield surface of the material using the Hill yield criterion [76], an extension of the classic isotropic von Mises yield criterion [77], that accounts for anisotropy. In its quadratic form and excluding shear terms, the Hill yield criterion can be written as:

$$F(\sigma_{22}-\sigma_{33})^2+G(\sigma_{33}-\sigma_{11})^2+H(\sigma_{11}-\sigma_{22})^2=1 \tag{7.39}$$

where σ_{11}, σ_{22} and σ_{33} are the principal stresses and F, G and H can be written as:

$$F=\frac{1}{2}\left[\frac{1}{\left(\sigma_2^y\right)^2}+\frac{1}{\left(\sigma_3^y\right)^2}-\frac{1}{\left(\sigma_1^y\right)^2}\right]$$

$$G=\frac{1}{2}\left[\frac{1}{\left(\sigma_3^y\right)^2}+\frac{1}{\left(\sigma_1^y\right)^2}-\frac{1}{\left(\sigma_2^y\right)^2}\right]$$

$$H=\frac{1}{2}\left[\frac{1}{\left(\sigma_1^y\right)^2}+\frac{1}{\left(\sigma_2^y\right)^2}-\frac{1}{\left(\sigma_3^y\right)^2}\right] \tag{7.40}$$

where σ_1^y, σ_2^y and σ_3^y are the calculated yield stresses in the three orthogonal material orientations.

7.6.3 Tension/Compression Asymmetry of Yield Stress

The strain rate and material orientation dependent tension/compression asymmetry of the yield stress observed in the mechanical behaviour of the Ti-6Al-4V plates characterised in

Chapter 5 is not captured in the Ti-6Al-4V model. As discussed in Chapter 5, the large tension/compression asymmetries seen in the four development level Ti-6Al-4V plates, including Plate 1, are likely due to residual stresses locked in during thermo-mechanical processing.

The material orientation dependent tension/compression asymmetry of the yield stress of a material can be modelled using an extension of the previously discussed Hill yield criterion, know as the Caddell-Raghava-Atkins yield criterion [78]. In this model, the tension/compression asymmetry of yield is accounted for by including the effects of residual stresses in each of the material orientations. Written in its quadratic form and ignoring shear terms, the Caddell-Raghava-Atkins yield criterion can be written as:

$$F(\sigma_{22}-\sigma_{33})^2 + G(\sigma_{33}-\sigma_{11})^2 + H(\sigma_{11}-\sigma_{22})^2 + I\sigma_{11} + J\sigma_{22} + K\sigma_{33} = 1 \tag{7.41}$$

where all terms are the same as before and I, J and K are coefficients that determine the effect of residual stresses in the three orthogonal material orientations.

Using the Caddell-Raghava-Atkins yield criterion, the material orientation dependent tension/compression asymmetry of the yield stress can be accounted for by simply fitting the yield criterion to the mechanical characterisation data in Chapter 5, using the Ti-6Al-4V calculated tensile yield stresses as a reference.

Using the anisotropic and tension/compression dependent yield criterion proposed by Cazacu *et al.* [54], it is possible to account for the effect of deformation twinning induced texture evolution and the subsequent change in strain hardening response due to twinning planes acting as barriers to deformation motion.

The physical source of the strain rate dependent tension/compression asymmetry seen in all four Ti-6Al-4V plates is worthy of further study but outwith the scope of this project. One hypothesis that would account for the strain rate dependence of the tension/compression asymmetry is that at high strain rates, deformation twinning becomes significant under

compression loading but not tensile loading, possibly due to the additional residual stresses resulting in higher stresses in compression. If the observed strain rate dependent tension/compression asymmetry is due to increased twinning activity at high strain rates in compression, then the yield criterion proposed by Cazacu *et al.* could be used with an extension of the Ti-6Al-4V model which includes the effects of residual stresses and twinning on the yield stress and strain hardening, respectively. However, further mechanical and microstructural characterisation work is required to inform such a model.

7.7 Conclusions

A modelling framework has been developed and implemented that is capable of capturing the effects of temperature, strain rate, composition, microstructure, micro-texture and macro-texture on the plastic deformation of Ti-6Al-4V with a bimodal (duplex) microstructure.

Comparisons have been made between the model outputs and experimental results for a Ti-6Al-4V plate with a bimodal microstructure and crystallographic texturing, over a range of strain rates in the two in-plane material orientations in tension, with excellent agreement being shown in all cases.

The model's ability to capture the effect of temperature on the plastic behaviour of Ti-6Al-4V has not been verified due to a lack of available experimental data suitable for comparison. However, it is worth noting that the model should only be used up to temperatures of 800 K, as at this point significant changes in the modes of deformation in Titanium alloys occur.

Due to a lack of high quality experimental data for comparing with model outputs, the effects of varying different physically based parameters in the model were simply outlined by varying the parameters within sensible bounds and recording the results. A significant

program of focussed experimental work is required to provide data for a rigorous verification of the models ability to capture the effects of these varying microstructural features.

Finally, a number of anisotropic and tension/compression dependent yield criterion frameworks were briefly described, allowing the Ti-6Al-4V model to be implemented in FE analysis packages such as ABAQUS, LS-DYNA and DEFORM.

8 DISCUSSION

8.1 Outline

This chapter will discuss key research topics that were highlighted through the work carried out as part of this project. The discussion of these topics will be used to suggest possible future research topics, with particular focus on the effects of various microstructural and textural features on the flow stress of Ti-6Al-4V over a range of strain rates and temperatures.

8.2 The Effects of Microstructure and Texture

8.2.1 General

It is clear from the microstructural and mechanical characterisation work carried out in this research project (see Chapters 4 and 5), that understanding the effects of microstructure and texture on the plastic deformation behaviour of Ti-6Al-4V is a complex task. Many of the key microstructural features are closely intertwined and cannot be easily isolated. To obtain the required range of microstructures to suitably characterise their effects, the complete processing history of the material under investigation must be known and tightly controlled. For production standard material this is an almost impossible task, which would come at great monetary cost to the sponsor. To add further difficulty, even if the key microstructural features can be isolated, it is not guaranteed that the microstructural features can be isolated

from textural features, as at each stage of processing, changes to key processing variables may also result in changes to fundamental textural features, such as the macro-texture and micro-texture. Considering these difficulties, where does this leave the future of research into the effects of microstructure and texture on Ti-6Al-4V?

This author believes that the future of research into the effects of microstructure and texture on the plastic behaviour of Ti-6Al-4V is in developing new experimental techniques capable of isolating the underlying mechanisms of plastic deformation linked to key microstructural and textural features. The understanding gained can then be used to formulate physically based models that capture the experimentally observed behaviour of the bulk material. From the analysis contained in this thesis it is clear that this is not a simple task, as it requires an understanding of mechanisms of plastic deformation over a wide range of length scales and time scales with complex interactions occurring at all levels.

However, significant progress is being made on this front, with new mechanical testing techniques being used to isolate and understand mechanisms that were previously poorly understood or simply unknown. An excellent example of such methods is the recent work by Gong and Wilkinson [79], [80] studying the effects of solid solution strengthening and α/β laths on the plastic behaviour of Ti-6Al-4V using micro-cantilever testing.

The main advantage of this approach is that by providing a fundamental understanding of the physical mechanisms of plastic deformation, new advances in microstructural development can be quickly assessed using physically based models. Further, if a previously unseen behaviour is observed in-service, this understanding of the physical mechanisms of plastic deformation can be used to better understand that in-service behaviour. An example of this is the recent work by Dunne *et al.* [81] on the effects of grain-to-grain misorientation on facet nucleation during cold-dwell fatigue in Ti-6Al-4V.

Although a significant amount of work is currently being carried out in such areas, there is still a gap between the fundamental understanding of the mechanisms of plastic behaviour and the application of this understanding to practical models that can be used by engineers and material scientists on a daily basis. The new Ti-6Al-4V model outlined as part of this thesis is an attempt to bridge that gap. However, when looking to populate the new model with relatively fundamental data, it was found that there were significant holes in the required datasets that need to be filled for progress in this area to continue. Examples of key microstructural and textural features that need to be isolated and their effect on the plastic flow stress understood will be outlined in the next sections.

8.2.2 Solute Atom Content

From the modelling framework outlined in Chapter 7, it is clear that a key feature that effects the plastic flow stress behaviour of Ti-6Al-4V is the solute atom content of the different α structures. It is noted by Lutering and Williams [1] that as the volume fraction primary α increases the solute atom content in the primary α grains increases, whereas conversely, the solute atom content in the α laths decreases. This has a significant effect on the plastic flow stress behaviour of Ti-6Al-4V, particularly in bi-modal microstructures. However, this author could find no data available in the literature to quantify the solute atom content as a function of volume fraction primary α.

Using modern microscopy techniques such as wavelength dispersion spectroscopy (WDS), this would be a simple and highly useful research project to undertake. As a starting point, a simple empirical formulation could be obtained linking the volume fraction primary α with the solute atom content in the different α structures. However, it is conceivable that a physically based model could be developed to capture the diffusion process of solute atoms during the final primary α grain growth heat treatment. This would provide a powerful tool to understand the effects of processing on the plastic flow stress behaviour of the final product.

8.2.3 Micro-Mechanical Testing of Microstructural Features

Recent advances in micro-mechanical testing of materials have the potential provide significant understanding into the effects of constituent microstructural features on the plastic behaviour of Ti-6Al-4V. Key to gaining insight into the behaviour of Ti-6Al-4V under impact loading is the development of an understanding of the microstructural, textural, temperature and strain rate dependent plastic flow stress behaviour of Ti-6Al-4V. It has been shown that the "log linear" dependence of a metals yield stress on strain rate is typically maintained up to strain rates of 10^4 s^{-1}. This means that much of the high strain rate behaviour can be understood by testing as lower strain rates using micro-mechanical testing techniques. For strain rates above this regime, where dislocation drag and relativistic effects begin to become important, or when the microstructure significantly changes as a function of strain rate, such as the onset of deformation twinning in *hcp* metals, new techniques are required that are capable of capturing the microstructural mechanics of deformation at high speeds. This is not a simple task but the adoption of ultra-high speed digital photography with microscopic lenses for use on miniaturised split-Hopkinson pressure bars offers the potential to view such high-speed deformations for the first time.

8.2.4 Dislocation Density

Another key microstructural feature that significantly affects the flow stress of Ti-6Al-4V is the initial dislocation density and the evolution of that dislocation density as a function of strain, strain rate and temperature. The theory behind the evolution of dislocation density is relatively well understood, with many modelling frameworks available that are capable of capturing the observed behaviour. However, in the case of commercial Ti-6Al-4V products, there is a lack of data on initial dislocation densities and the subsequent evolution due to strain, strain rate and temperature.

Recent studies by Britton *et al.* [73] and Littlewood *et al.* [72] have begun to address the lack of information in this area, giving some very intriguing results. Work in this area needs to continue and be extended to high strain rate loading.

8.2.5 Micro-Texture

In Chapter 6, regions with preferred crystallographic orientation (or micro-texture) were shown to have a significant effect on the deformation behaviour of Ti-6Al-4V. Studies have shown that under cold-dwell fatigue conditions, macro-zones can lead to premature failure, due to facet nucleation and propagation along the length of macro-zones [82]. The effects of these macro-zones on key mechanical properties such as plastic flow stress, ductility and fracture toughness, must be studied in more detail.

A focussed study on microstructures with varying α colony/macro-zone size, and their affect on the plastic flow behaviour of Ti-6Al-4V at high strain rates, would be a significant step forward. In particular, it would be interesting to study the effects of α colonies on the formation of deformation twins. As has been shown in this study, micro-texture appears to be a strong factor affecting the formation of deformation twins at high strain rates.

8.2.6 Deformation Twinning

From the analysis carried out in Chapter 6, it is clear that deformation twinning has a significant effect on the mechanical behaviour of Ti-6Al-4V at very high strain rates. Progress has been made in modelling the effects of twinning at a macroscopic scale [22], [51], [83]. However, it is clear that deformation twinning is a highly complex deformation mechanism that the solid mechanics and material science community have yet to fully understand.

The lack of clear mechanisms for the activation of twinning systems makes deformation twinning difficult to model in any real physical sense. Part of the problem is that the onset of twinning in any given grain is very clearly dependent on the stress state of that grain. The by-

product of this is that a relatively simple one dimensional modelling framework, like the one used in this thesis, is not appropriate for the study of deformation twinning.

Instead, complex three-dimensional crystal plasticity finite element (CPFE) models need to be used [84]. However, for this approach to be successful, the strain gradients, and thus the dislocation densities and solute atom content, need to be spatially mapped for the all the grains in the polycrystalline material. This is obviously a very computationally intensive task that quickly becomes impractical in any sort of engineering sense. On a small scale, such an approach is useful for understanding the stress states needed to activate twinning under given deformation conditions. However, this approach does not address the issue of a required physical nucleation mechanism. The approach is further undermined by the observation that twins propagate at the speed of sound in the material, resulting in almost instantaneous reorientation and thus straining of the neighbouring grains, something not suited to the finite element (FE) method.

So-called "self-consistent" type models have had significant success in modelling the evolution of texture [67], and thus the evolution of the anisotropic plastic flow stress behaviour, of *hcp* metals due to deformation twinning. Such models typically use relatively simple resolved shear stress criterions for twin activation and model the plastic flow behaviour in a similar way to that done in this thesis, with the addition of an appropriate hardening rule to account for twin boundaries [22], [58], [83]. This can then be used to inform an anisotropic yield criterion, like those discussed in the preceding chapter, for use in engineering analysis [42]. However, such approaches gloss over the complex stress states seen in a three dimensional polycrystalline material and, to this authors knowledge, are not capable of modelling features such as macro-zones and localised strains/stresses, which clearly have an affect on the nucleation of deformation twins [60], [85].

Modelling aside, understanding will surely be gained from experimental work into the nucleation and propagation of deformation twins. The advent of EBSD as a relatively common tool, and the use of techniques such as high energy X-ray and neutron diffraction, offers significant opportunities to understand the mechanisms of deformation twinning under various conditions. In this author's opinion, the application of these measurement techniques, combined with micro-mechanical testing approaches, offers the best hope for understanding the complex nature of deformation twinning.

8.3 Conclusions

It is clear from the work completed as part of this thesis that the plastic deformation behaviour of Ti-6Al-4V is extremely complex, with multiple microstructural features affecting the activation of a number of interlocking deformation mechanisms, many of which are not fully understood. However, the application of new measurement and mechanical testing techniques offers significant opportunities to further understand how these features interact and affect the high strain rate plastic deformation behaviour of Ti-6Al-4V.

9 CONCLUSIONS

9.1 Overview

The principal aim of this research project was to better understand the roles of microstructure and texture on the high strain rate plastic deformation behaviour of the industrially important Titanium alloy, Ti-6Al-4V. This was facilitated by TIMET Corp. providing four rolled Ti-6Al-4V plates with different thermo-mechanical processing histories.

9.2 Microstructural Characterisation

The provided plates of Ti-6Al-4V were first characterised using optical microscopy, allowing the microstructure of the four plates to be studied. It was found that all four plates exhibit bi-modal (duplex) microstructures with varying volume fractions and sizes of primary α grains. The primary α grains were interspersed amongst colonies of α/β laths at different stages of microstructural development.

The four Ti-6Al-4V plates were then characterised using electron backscatter diffraction (EBSD), to study any macroscopic and microscopic crystallographic texturing (also known as preferred crystallographic orientation) that might be present.

From the pole figures (PF) calculated from the EBSD data, it was found that all four plates have a classic "basal-transverse" macroscopic texture i.e. for the majority of grains/laths, the ***c***-axis of the *hcp* unit cell is pointing in the transverse material orientation.

For Plates 2, 3 and 4, analysis showed that a second "peak" in the texture was present, with the remaining grains/laths orientated such that the ***c***-axis of the *hcp* unit cell points in the through-thickness material orientation. Plate 1 is the exception, with the remaining grain orientations smeared around the transverse material orientation, indicating a level of cross-rolling during secondary processing.

Inverse pole figure (IPF) maps of the EBSD data showed that all four plates have significant zones of micro-texture i.e. regions of α lath colonies with the same crystallographic orientation.

9.3 Mechanical Characterisation

Compression and tension specimens were cut from the four Ti-6Al-4V plates in the longitudinal, transverse and through-thickness orthogonal material orientations. Uniaxial mechanical characterisation tests were then carried out at quasi-static (10 s^{-3}) and high strain rates (10 s^{-3}) using a standard electro-mechanical test device and split-Hopkinson pressure bars (SHPB), respectively. From these characterisation tests a number general observations were made about the strain rate dependent, uniaxial plastic deformation behaviour of rolled Ti-6Al-4V plate with a basal/transverse macro-texture:

- The flow stress is material orientation dependent, with the flow stress in compression showing greater material orientation dependence than the flow stress in tension, at both quasi-static and high strain rates.

- The flow stress is strain rate dependent, with the flow stress in compression showing greater strain rate dependence than the flow stress in tension in the longitudinal, transverse and through-thickness material orientations.

- The flow stress is direction of loading dependent (tension/compression), with the flow stress in the transverse material orientation showing greater tension/compression asymmetry than the flow stress in the longitudinal material orientation. Tension/compression asymmetry of the flow stress increases with increasing strain rate in the transverse material orientation.

Fracture surfaces from recovered tensile tests were analysed in a scanning electron microscope (SEM). From this analysis it was noted that there was a correlation between the size and shape of the dimples on fracture surfaces of the quasi-statically tested specimens and the microstructures of the plates. At high strain rates there was evidence of smearing, indicating adiabatic shear banding had occurred.

It was also observed that all four plates failed along preferential planes relative to the orthogonal material orientations. This feature was attributed to the effect of anisotropic yield stresses causing an elliptical cross-section to form during deformation, forcing failure to occur along specific planes relative to the orthogonal material orientations.

9.4 Taylor Impact Experiments

The classic Taylor impact experiment was adapted to include an optical measurement and geometry reconstruction technique capable of calculating the strain path history of a Taylor impact specimen during the experiment. A novel experimental setup was designed that consists of a high speed camera and mirror arrangement, allowing the specimen to be viewed from multiple angles during deformation. Using the optical measurement and geometry reconstruction technique, it was then possible to gain valuable, previously unobtainable, data on the deformation history of Taylor impact specimens *in-situ*, such as the major/minor axes of the anisotropically deforming elliptical specimen cross-sections as a function of time and

axial position, true strain as a function of time and axial position and the true strain rate as a function of axial position.

The technique was verified by testing a specimen cut from the in-plane material orientation of a clock-rolled high purity Zirconium plate. Before testing, the Zirconium plate was microstructurally characterised using EBSD, with the results showing that the plate is heavily textured, with the majority of grains having their ***c***-axis pointing in the through-thickness material orientation. The Zirconium plate was mechanically characterised by cutting compression specimens from the in-plane and through-thickness orthogonal material orientations and testing them at a strain rate of 10^3 s^{-1}, using a SPHB. The results from these characterisations tests showed that the Zirconium plate has significant anisotropy, with the through-thickness material orientation having a flow stress nearly double that of the in-plane material orientations.

The output measurements from the optical measurement and reconstruction technique of a post-deformation image frame from a Taylor impact test at 206 m s^{-1} were compared with the measurements of the recovered specimen using a coordinate measurement machine (CMM), with analysis showing excellent agreement between the two techniques.

Interestingly, the results from the experiments on the clock-rolled high purity Zirconium plate showed that, despite there being significant anisotropy in the different material orientations under uniaxial conditions, there was very little difference in the major/minor axes of the final deformed elliptical cross-sections of the analysed Taylor impact specimen. This was attributed to the activation of deformation twinning during the initial stages of the Taylor impact. However, further work is required to confirm this hypothesis.

The adapted Taylor impact experiment was then carried out on specimens cut from the two orthogonal in-plane material orientations of one of the four Ti-6Al-4V plates (Plate 3) at a velocity of 160 m s^{-1}. Analysis of data from these experiments showed that macro-texture had

a significant effect on the deformation of Ti-6Al-4V in the longitudinal and transverse material orientations, in terms of both the final and evolving specimen geometry and the strain rate history.

Recovered Ti-6Al-4V specimens from the outlined Taylor impact experiments were sectioned along specific planes and microstructurally characterised using EBSD, with comparisons made between the pre and post-deformation microstructures. From this analysis, insight was gained into the effects of micro-texture on the general anisotropic plastic deformation behaviour of Ti-6Al-4V plate materials and in particular the role of micro-texture on the formation of deformation twins. It was shown that deformation twins occurred in zones of micro-texture with a crystallographic orientation preferentially aligned for $\langle \boldsymbol{a} \rangle$ type slip along the direction of loading. Further, a misorientation analysis showed that the twins formed were all of the "tensile" type, resulting in compression in the direction of loading and an extension in the transverse direction, in the case of the longitudinal Taylor impact specimen.

9.5 Modelling the Effects of Microstructure and Texture

A modelling framework has been developed that is capable of capturing the uniaxial plastic deformation behaviour of Ti-6Al-4V with a bimodal (duplex) microstructure. Using a mechanical threshold stress (MTS) model as its basis, the new Ti-6Al-4V model is capable of modelling the effects of temperature, strain rate, solute atom content (or percentage weight Aluminium), dislocation density and key microstructural features such as volume fraction primary α, primary α grain size, regions of micro-texture (or α colonies) and macro-texture, on the plastic flow stress behaviour of Ti-6Al-4V.

The new Ti-6Al-4V model was populated with microstructural data obtained from one of the development Ti-6Al-4V plates (Plate 1) then compared with the previously discussed

mechanical characterisation results for that plate at quasi-static (10^{-3} s^{-1}) and high strain rates (10^{3} s^{-1}) in the longitudinal and transverse material orientation in tension. Excellent agreement was shown between the model outputs and the uniaxial flow stress data.

9.6 Final Remarks

The development of new high strain rate experimental techniques and the application of various microstructural characterisation techniques have contributed new understanding to the plastic deformation behaviour of Ti-6Al-4V at high strain rates. This understanding has been combined with knowledge gained from a detailed literature review to inform the development of a new Ti-6Al-4V material model, capable of capturing the effects of key microstructural features on the strain rate and temperature dependent flow stress behaviour of Ti-6Al-4V. It is hoped that the understanding gained from this project, and application of the new Ti-6Al-4V model, can be used to optimise the design of Ti-6Al-4V components and structures for impact loading scenarios.

10 BIBLIOGRAPHY

[1] G. Lutjering and J. Williams, *Titanium (Engineering Materials and Processes)*, 2nd ed. Springer, 2007, p. 442.

[2] M. Donachie, *Titanium: a technical guide*, 2nd ed. ASM International, 2000, p. 381.

[3] C. Leyens and M. Peters, *Titanium and Titanium Alloys: Fundamentals and Applications*, 1st ed. Wiley VCH, 2003, p. 532.

[4] Rolls-Royce, *The Jet Engine*, 2nd ed. 2005.

[5] D. Hull and D. J. Bacon, *Introduction to Dislocations*, 4th ed. A Butterworth-Heinemann Title, 2001, p. 242.

[6] V. Randle and O. Engler, *Texture Analysis - Macrotexture, Microtexture and Orientation Mapping*. 2000.

[7] U. F. Kocks, C. N. Tome, H. R. Wenk, and H. Mecking, *Texture and Anisotropy: Preferred Orientations in Polycrystals and Their Effect on Materials Properties*, 1st ed. Cambridge University Press, 2000, p. 688.

[8] M. F. Ashby and D. R. H. Jones, *Engineering Materials 1: An Introduction to Properties, Applications and Design*, 3rd ed. A Butterworth-Heinemann Title, 2005, p. 448.

[9] M. H. Yoo, "Slip, twinning, and fracture in hexagonal close-packed metals," *Metallurgical Transactions A*, vol. 12, no. 3, pp. 409-418, Mar. 1981.

[10] E. Tenckhoff, "Review of deformation mechanisms, texture, and mechanical anisotropy in zirconium and zirconium base alloys," *Zirconium in the Nuclear Industry: 14th International Symposium*, vol. 1467, pp. 25-50, 2005.

[11] N. E. Paton, J. C. Williams, and G. P. Rauscher, "Deformation of alpha-phase Titanium," in *Titanium science and technology; Proceedings of the Second International Conference*, 1973, pp. 1049-1069.

[12] K. T. Ramesh, "Effects of high rates of loading on the deformation behavior and failure mechanisms of hexagonal close-packed metals and alloys," *Metallurgical and Materials Transactions a-Physical Metallurgy and Materials Science*, vol. 33, no. 3, pp. 927-935, 2002.

[13] D. R. Chichili, K. T. Ramesh, and K. J. Hemker, "The high-strain-rate response of alpha-titanium: Experiments, deformation mechanisms and modeling," *Acta Materialia*, vol. 46, no. 3, pp. 1025-1043, 1998.

[14] P. S. Follansbee and G. T. Gray, "AN ANALYSIS OF THE LOW-TEMPERATURE, LOW AND HIGH STRAIN-RATE DEFORMATION OF TI-6AL-4V," *Metallurgical Transactions a-Physical Metallurgy and Materials Science*, vol. 20, no. 5, pp. 863-874, 1989.

[15] H. A. Padilla, C. D. Smith, J. Lambros, A. J. Beaudoin, and I. M. Robertson, "Effects of Deformation Twinning on Energy Dissipation in High Rate Deformed Zirconium," *Metallurgical and Materials Transactions A*, vol. 38, no. 12, pp. 2916-2927, Nov. 2007.

[16] W. G. Johnston and J. J. Gilman, "Dislocation Velocities, Dislocation Densities, and Plastic Flow in Lithium Fluoride Crystals," *Journal of Applied Physics*, vol. 30, no. 2, p. 129, 1959.

[17] M. A. Meyers, *Dynamic Behavior of Materials*, 2nd ed. John Wiley and Sons, 1994, p. 668.

[18] P. FOLLANSBEE and U. KOCKS, "A constitutive description of the deformation of copper based on the use of the mechanical threshold stress as an internal state variable," *Acta Metallurgica*, vol. 36, no. 1, pp. 81-93, Jan. 1988.

[19] J. Harding, "TEMPERATURE AND STRAIN RATE SENSITIVITY OF ALPHA-TITANIUM," *Archives of Mechanics*, vol. 27, no. 5-6, pp. 715-732, 1975.

[20] M. A. Meyers, G. Subhash, B. K. Kad, and L. Prasad, "EVOLUTION OF MICROSTRUCTURE AND SHEAR-BAND FORMATION IN ALPHA-HCP TITANIUM," *Mechanics of Materials*, vol. 17, no. 2-3, pp. 175-193, 1994.

[21] A. A. Salem, S. R. Kalidindi, and R. D. Doherty, "Strain hardening of titanium: role of deformation twinning," *Acta Materialia*, vol. 51, no. 14, pp. 4225-4237, 2003.

[22] A. A. Salem, S. R. Kalidindi, and S. L. Semiatin, "Strain hardening due to deformation twinning in alpha-titanium: Constitutive relations and crystal-plasticity modeling," *Acta Materialia*, vol. 53, no. 12, pp. 3495-3502, 2005.

[23] A. A. Salem, S. R. Kalidindi, and R. D. Doherty, "Strain hardening regimes and microstructure evolution during large strain compression of high purity titanium," *Scripta Materialia*, vol. 46, no. 6, pp. 419-423, 2002.

[24] N. P. Gurao, R. Kapoor, and S. Suwas, "Deformation behaviour of commercially pure titanium at extreme strain rates," *Acta Materialia*, vol. 59, no. 9, pp. 3431-3446, May 2011.

[25] G. T. Gray and P. S. Follansbee, "An Analysis of the Low Temperature, Low and High Strain-Rate Deformation of Ti-6Al-4V." .

[26] W. S. Lee and C. F. Lin, "Plastic deformation and fracture behaviour of Ti-6Al-4V alloy loaded with high strain rate under various temperatures," *Materials Science and Engineering a-Structural Materials Properties Microstructure and Processing*, vol. 241, no. 1-2, pp. 48-59, 1998.

[27] D. A. S. Macdougall, "The measurement of specimen surface temperature in high-speed tension and torsion tests," *International Journal of Impact Engineering*, vol. 21, no. 6, pp. 473-488, Jun. 1998.

[28] H. Sarsfield, L. Wang, and N. Petrinic, "An experimental investigation of rate-dependent deformation and failure of three titanium alloys," *Journal of Materials Science*, vol. 42, no. 13, pp. 5085-5093, 2007.

[29] K. T. Ramesh, *Handbook of Experimental Solid Mechanics*. Springer, 2010.

[30] J. E. Field, S. M. Walley, W. G. Proud, H. T. Goldrein, and C. R. Siviour, "Review of experimental techniques for high rate deformation and shock studies," *International Journal of Impact Engineering*, vol. 30, no. 7, pp. 725-775, 2004.

[31] G. T. Gray, "Classic split-Hopkinson pressure bar testing," vol. 8, H. Kuhn and D. Medlin, Eds. ASM International, 2000, pp. 462-476.

[32] G. I. Taylor, "THE USE OF FLAT-ENDED PROJECTILES FOR DETERMINING DYNAMIC YIELD STRESS .1. THEORETICAL CONSIDERATIONS," *Proceedings of the Royal Society of London Series a-Mathematical and Physical Sciences*, vol. 194, no. 1038, pp. 289-299, 1948.

[33] A. C. Whiffin, "THE USE OF FLAT-ENDED PROJECTILES FOR DETERMINING DYNAMIC YIELD STRESS .2. TESTS ON VARIOUS METALLIC MATERIALS," *Proceedings of the Royal Society of London Series a-Mathematical and Physical Sciences*, vol. 194, no. 1038, pp. 300-322, 1948.

[34] W. E. Carrington and M. L. V. Gayler, "THE USE OF FLAT-ENDED PROJECTILES FOR DETERMINING DYNAMIC YIELD STRESS .3. CHANGES IN MICROSTRUCTURE CAUSED BY DEFORMATION UNDER IMPACT AT HIGH-STRIKING VELOCITIES," *Proceedings of the Royal Society of London Series a-Mathematical and Physical Sciences*, vol. 194, no. 1038, pp. 323-331, 1948.

[35] E. H. Lee and S. J. Tupper, "ANALYSIS OF PLASTIC DEFORMATION IN A STEEL CYLINDER STRIKING A RIGID TARGET," *Journal of Applied Mechanics-Transactions of the Asme*, vol. 21, no. 1, pp. 63-70, 1954.

[36] J. B. Hawkyard, "THEORY FOR MUSHROOMING OF FLAT-ENDED PROJECTILES IMPINGING ON A FLAT RIGID ANVIL USING ENERGY

CONSIDERATIONS," *International Journal of Mechanical Sciences*, vol. 11, no. 3, pp. 313-&, 1969.

[37] D. E. Eakins and N. N. Thadhani, "Analysis of dynamic mechanical behavior in reverse Taylor anvil-on-rod impact tests," *International Journal of Impact Engineering*, vol. 34, no. 11, pp. 1821-1834, 2007.

[38] L. C. Forde, W. G. Proud, and S. M. Walley, "Symmetrical Taylor impact studies of copper," *Proceedings of the Royal Society a-Mathematical Physical and Engineering Sciences*, vol. 465, no. 2103, pp. 769-790, 2009.

[39] D. J. Chapman, D. D. Radford, M. Reynolds, and P. D. Church, "Shock induced void nucleation during Taylor impact," *International Journal of Fracture*, vol. 134, no. 1, pp. 41-57, 2005.

[40] D. J. Chapman, "A history of the Taylor test and its present use in the study of lightweight materials."

[41] P. J. Maudlin, G. T. Gray, C. M. Cady, and G. C. Kaschner, "High-rate material modelling and validation using the Taylor cylinder impact test," *Philosophical Transactions of the Royal Society A: Mathematical, Physical and Engineering Sciences*, vol. 357, no. 1756, pp. 1707-1729, Jun. 1999.

[42] B. Plunkett, O. Cazacu, R. A. Lebensohn, and F. Barlat, "Elastic-viscoplastic anisotropic modeling of textured metals and validation using the Taylor cylinder impact test," *International Journal of Plasticity*, vol. 23, no. 6, pp. 1001-1021, 2007.

[43] S. Amelinckx and D. van Dyck, *Handbook of Microscopy - Applications in Materials, Science, Solid-State Physics and Chemistry*. 1997.

[44] A. J. Schwartz, M. Kumar, B. L. Adams, and D. P. Field, *Electron Backscatter Diffraction (EBSD) in Materials Science*, 2nd ed. 2009.

[45] T. Neeraj, M. F. Savage, J. Tatalovich, L. Kovarik, R. W. Hayes, and M. J. Mills, "Observation of tension-compression asymmetry in alpha and alpha/beta titanium alloys," *Philosophical Magazine*, vol. 85, no. 2-3, pp. 279-295, 2005.

[46] J. C. Williams, R. G. Baggerly, and N. E. Paton, "Deformation behavior of HCP Ti-Al alloy single crystals," *Metallurgical and Materials Transactions A*, vol. 33, no. 3, pp. 837-850, Mar. 2002.

[47] I. JONES and W. HUTCHINSON, "Stress-state dependence of slip in Titanium-6Al-4V and other H.C.P. metals," *Acta Metallurgica*, vol. 29, no. 6, pp. 951-968, Jun. 1981.

[48] P. J. Withers and H. K. D. H. Bhadeshia, "Residual stress. Part 2 – Nature and origins," *Materials Science and Technology*, vol. 17, no. 4, p. 10, 2001.

[49] P. J. Withers and H. K. D. H. Bhadeshia, "Residual stress. Part 1 – Measurement techniques," *Materials Science and Technology*, vol. 17, no. 4, p. 11, 2001.

[50] D. R. Chichili, K. T. Ramesh, and K. J. Hemker, "Adiabatic shear localization in alpha-titanium: experiments, modeling and microstructural evolution," *Journal of the Mechanics and Physics of Solids*, vol. 52, no. 8, pp. 1889-1909, 2004.

[51] A. A. Salem, S. R. Kalidindi, R. D. Doherty, and S. L. Semiatin, "Strain hardening due to deformation twinning in alpha-titanium: Mechanisms," *Metallurgical and Materials Transactions a-Physical Metallurgy and Materials Science*, vol. 37, no. 1, pp. 259-268, 2006.

[52] S. R. Kalidindi, A. A. Salem, and R. D. Doherty, "Role of deformation twinning on strain hardening in cubic and hexagonal polycrystalline metals," *Advanced Engineering Materials*, vol. 5, no. 4, p. 229-+, 2003.

[53] E. Wielewski et al., "A method for the in situ measurement of evolving elliptical cross-sections in initially cylindrical Taylor impact specimens," *The Journal of Strain Analysis for Engineering Design*, vol. 45, no. 6, pp. 429-437, Aug. 2010.

[54] O. Cazacu, B. Plunkett, and F. Barlat, "Orthotropic yield criterion for hexagonal closed packed metals," *International Journal of Plasticity*, vol. 22, no. 7, pp. 1171-1194, 2006.

[55] B. Plunkett, R. A. Lebensohn, O. Cazacu, and F. Barlat, "Anisotropic yield function of hexagonal materials taking into account texture development and anisotropic hardening," *Acta Materialia*, vol. 54, no. 16, pp. 4159-4169, 2006.

[56] M. R. Arthington, C. R. Siviour, N. Petrinic, and B. C. F. Elliott, "Cross-section reconstruction during uniaxial loading," *Measurement Science & Technology*, vol. 20, no. 7, 2009.

[57] M. R. Arthington, "Photogrammetric techniques for characterisation of anisotropic mechanical properties of Ti-6Al-4V," 2010.

[58] C. N. Tome, P. J. Maudlin, R. A. Lebensohn, and G. C. Kaschner, "Mechanical response of zirconium - I. Derivation of a polycrystal constitutive law and finite element analysis," *Acta Materialia*, vol. 49, no. 15, pp. 3085-3096, 2001.

[59] G. C. Kaschner et al., "Mechanical response of zirconium - II. Experimental and finite element analysis of bent beams," *Acta Materialia*, vol. 49, no. 15, pp. 3097-3108, 2001.

[60] L. Wang, Y. Yang, P. Eisenlohr, T. R. Bieler, M. A. Crimp, and D. E. Mason, "Twin Nucleation by Slip Transfer across Grain Boundaries in Commercial Purity Titanium," *Metallurgical and Materials Transactions A*, vol. 41, no. 2, pp. 421-430, Nov. 2009.

[61] G. R. Johnson and W. H. Cook, "A constitutive model and data for metals subjected to large strains, high strain rates and high temperatures," in *Proceedings of the 7th International Symposium on Ballistics*, 1983, pp. 541-547.

[62] G. R. Johnson and W. H. Cook, "Fracture characteristics of three metals subjected to various strains, strain rates, temperatures and pressures," *Engineering Fracture Mechanics*, vol. 21, no. 1, pp. 31-48, 1985.

[63] H. Mecking and U. F. Kocks, "Kinetics of flow and strain-hardening," *Acta Metallurgica*, vol. 29, no. 11, pp. 1865-1875, Nov. 1981.

[64] Y. ESTRIN and H. MECKING, "A unified phenomenological description of work hardening and creep based on one-parameter models," *Acta Metallurgica*, vol. 32, no. 1, pp. 57-70, Jan. 1984.

[65] U. F. Kocks, "Realistic constitutive relations for metal plasticity," *Materials Science and Engineering: A*, vol. 317, no. 1-2, pp. 181-187, Oct. 2001.

[66] U. F. Kocks, A. Argon, and M. F. Ashby, "Thermodynamics and kinetics of slip," *Progress in Materials Science*, vol. 19, 1975.

[67] ASM, Ed., *ASM Handbook Vol 22a: Fundamentals of Modeling for Metals Processing*. ASM International, 2009, p. 734.

[68] H. J. Bunge, "Some applications of the Taylor theory of polycrystal plasticity," *Kristall und Technik*, vol. 5, no. 1, pp. 145-175, 1970.

[69] F. R. N. Nabarro, Z. S. Basinski, and D. B. Holt, "The plasticity of pure single crystals," *Advances in Physics*, vol. 13, no. 50, pp. 193-323, Apr. 1964.

[70] B. Bhattacharya and M. Niewczas, "Work-hardening behaviour of Mg single crystals oriented for basal slip," *Philosophical Magazine*, vol. 91, no. 17, pp. 2227-2247, Jun. 2011.

[71] T. B. Britton, H. Liang, F. P. E. Dunne, and A. J. Wilkinson, "The effect of crystal orientation on the indentation response of commercially pure titanium: experiments and simulations," *Proceedings of the Royal Society A: Mathematical, Physical and Engineering Sciences*, vol. 466, no. 2115, pp. 695-719, Nov. 2009.

[72] P. D. Littlewood, T. B. Britton, and A. J. Wilkinson, "Geometrically necessary dislocation density distributions in Ti–6Al–4V deformed in tension," *Acta Materialia*, vol. 59, no. 16, pp. 6489-6500, Sep. 2011.

[73] T. B. Britton, S. Birosca, M. Preuss, and A. J. Wilkinson, "Electron backscatter diffraction study of dislocation content of a macrozone in hot-rolled Ti–6Al–4V alloy," *Scripta Materialia*, vol. 62, no. 9, pp. 639-642, May 2010.

[74] R. C. Picu and A. Majorell, "Mechanical behavior of Ti–6Al–4V at high and moderate temperatures—Part II: constitutive modeling," *Materials Science and Engineering: A*, vol. 326, no. 2, pp. 306-316, Mar. 2002.

[75] G. I. Taylor, "Plastic strain in metals," *Journal Of The Institute Of Metals*, vol. 62, no. 1, pp. 307-324, 1938.

[76] R. Hill, "A Theory of the Yielding and Plastic Flow of Anisotropic Metals," *Proceedings of the Royal Society A: Mathematical, Physical and Engineering Sciences*, vol. 193, no. 1033, pp. 281-297, May 1948.

[77] R. Hill, *The Mathematical Theory of Plasticity*. OUP Oxford; New Ed edition, 1998, p. 368.

[78] R. M. Caddell, R. S. Raghava, and A. G. Atkins, "A yield criterion for anisotropic and pressure dependent solids such as oriented polymers," *Journal of Materials Science*, vol. 8, no. 11, pp. 1641-1646, Nov. 1973.

[79] J. Gong and A. J. Wilkinson, "Micro-cantilever testing of ⟨a⟩ prismatic slip in commercially pure Ti," *Philosophical Magazine*, vol. 91, no. 7-9, pp. 1137-1149, Mar. 2011.

[80] J. Gong and A. J. Wilkinson, "A microcantilever investigation of size effect, solid-solution strengthening and second-phase strengthening for prism slip in alpha-Ti," *Acta materialia*, vol. 59, no. 15, pp. 5970-5981.

[81] F. P. E. Dunne, D. Rugg, and A. Walker, "Lengthscale-dependent, elastically anisotropic, physically-based hcp crystal plasticity: Application to cold-dwell fatigue in Ti alloys," *International Journal of Plasticity*, vol. 23, no. 6, pp. 1061-1083, Jun. 2007.

[82] I. Bantounas, T. C. Lindley, D. Rugg, and D. Dye, "Effect of microtexture on fatigue cracking in Ti-6Al-4V," *Acta Materialia*, vol. 55, no. 16, pp. 5655-5665, 2007.

[83] G. Proust, C. N. Tome, and G. C. Kaschner, "Modeling texture, twinning and hardening evolution during deformation of hexagonal materials," *Acta Materialia*, vol. 55, no. 6, pp. 2137-2148, Apr. 2007.

[84] F. Roters, P. Eisenlohr, L. Hantcherli, D. D. Tjahjanto, T. R. Bieler, and D. Raabe, "Overview of constitutive laws, kinematics, homogenization and multiscale methods in crystal plasticity finite-element modeling: Theory, experiments, applications," *Acta Materialia*, vol. 58, no. 4, pp. 1152-1211, Feb. 2010.

[85] Z. Jin and T. R. Bieler, "An in-situ observation of mechanical twin nucleation and propagation in TiAl," *Philosophical Magazine A*, vol. 71, no. 5, pp. 925-947, May 1995.